THE SPECTRAL PROPERTY OF GAMMA-RAY BURSTS AND GRB FORMATION RATE IN THE EARLY UNIVERSE

Daisuke Yonetoku

Division of Mathematical and Physical Sciences,
Kanazawa University, Kakuma, Kanazawa, Ishikawa 920-1192, Japan

Abstract

Gamma-Ray Bursts (hereafter GRBs) are the most energetic explosion in the universe and most of all occur at the cosmological distance. At the brightest case, the isotropic luminosity reaches 10^{54} erg s^{-1} in gamma-ray band, so we can explore the early universe such as $z \sim 20$ with the prompt emission of GRBs. At present, we know about 40 GRBs with known redshift and the most remote case is GRB 000131 at $z \sim 4.5$. However the number of GRBs measured their redshift is only a fraction of all GRBs detected with the *Compton Gamma-Ray Observatory* (*BATSE* detectors), *BeppoSAX* , *HETE-2* and *INTEGRAL* satellites. We could not know where the majority of GRBs come from, whether the nearby galaxy or the extremely early universe. The absence of informations about the distance scale for many GRBs restricts us to perform quantitative arguments about the cosmological history. According to the results of recent observations, it is established that GRBs occur when massive stars collapse into the black hole or some kind of compact object. Thus if we estimate the redshift for each GRB, we enable to probe the star formation history in the universe using the extremely bright emissions of GRBs.

In this thesis, we propose the "E_p–luminosity relation" as an empirical redshift indicator. We investigated the spectral properties of prompt emissions of 12 GRBs with known redshifts (GRB 970508, GRB 970828, GRB 971214, GRB 980326, GRB 980329, GRB980425, GRB 980703, GRB 990123, GRB 990506, GRB 990510, GRB991216, and GRB 000131) detected with the *BATSE* . We found a fine positive correlation between the isotropic peak luminosity and the spectral peak energy $E_p(1 + z)$. Here E_p is equivalent to the energy at the maximum flux of νF_ν spectrum. This relation can be described as $L = (2.34^{+2.29}_{-1.76}) \times 10^{-5}[E_p(1 + z)]^{2.0\pm0.2}$ which can be explained by the standard synchrotron radiation within the framework of the theoretical internal/external shock scenario. When we obtain the observed energy flux and the peak energy E_p, we can estimate the redshift for many GRBs without known distance using the E_p–luminosity relation. Then we performed spectral analyses for 689 brighter GRBs detected by *BATSE* and estimated their redshifts.

Based on the redshift distribution of the 689 samples, we derive the absolute GRB formation rate including the geometrical correction of the relativistic jets. The GRB formation rate rapidly increases at $z \leq 1$ and keeps rising toward the higher redshift up to $z \sim 12$. This result indicates that explosive massive star (population-III star) formation occurred in the early universe. Assuming the initial mass function calculated by the numerical simulations, we also estimated the absolute star formation rate. In this thesis, we discuss two fundamental issues; the early epoch reionization at $z = 17 \pm 5$ measured by the *WMAP* satellite and the uniform metal abundance in the intergalactic medium. We show the reionization can be realized within 10^7 yrs by the strong ultraviolet radiation from population-III stars. Moreover, estimating the amount of heavy elements produced by the explosion of massive stars at the final stage of their lifetime, we also show the metal pollution has been completed at the early universe before $z < 12$. This is the first work to estimate the absolute star formation rate at $z \sim 12$, and also to explain these two phase transitions of the vast universe.

Contents

List of Figures

List of Tables

Chapter 1

Introduction

1.1 Historical Background

The phenomena as Gamma-Ray Bursts (GRBs) are discovered by American satellite *Vela* in 1969 (Klebesadel et al., 1973). They generally show the short time duration and the rapid variability in the lightcurve, and the mean gamma-ray energy is about ~ 200 keV.

The distance and the origin of GRBs could not be confirmed because of poor technology of the instruments and observations for a long time. However, by the grace of large amount of GRB detections by the Compton Gamma-Ray Observatory (*CGRO* ; *BATSE* detectors), it was found that GRBs distribute isotropically in the celestial sphere as shown in figure 1.1. This fact indicates that the GRBs are cosmological origin because there is no construction along our galactic plane. One of the most important discovery is the X-ray afterglow following the prompt gamma-ray emission by the *BeppoSAX* satellite (Costa et al., 1997). Since the afterglow discovery, *BeppoSAX* and the Inter Planetary Network (IPN), which can determine the GRB coordinate with the time delay among a few satellites, the position of some GRBs were decided. Thanks to the afterglow observations, we could determine their precious position, and obtained a lot of properties about GRBs. Many ground based telescopes have tried to detect optical afterglows, and to measure their redshifts using the spectral absorption and/or emission lines caused by the gas in the GRB host galaxy. At present, we know about 30 GRBs with known redshift, and the most of them occur at cosmological distances such as the redshift of $z \geq 1$. The energy released while a GRB is about 1×10^{51} ergs in gamma-ray, which is corrected by the geometrical effect of the relativistic jet (Frail et al., 2001; Bloom et al., 2003), and the isotropic luminosity exceeds 10^{54} ergs s^{-1} in the prompt gamma-ray emission. Therefore, we can say that "*GRBs are the most energetic explosion in the universe*".

In this chapter, we briefly show the observed properties of GRBs and the cosmic star formation rate. First we show the temporal and the spectral properties of prompt emission of GRBs and afterglows. Based on the results of recent observations, we introduce the total energy released in a GRB event and the connections between GRBs and supernovae. Second, we show the cosmic star formation rate measured by the *Hubble* space telescope and the 8–10 m ground based telescopes. Finally, we introduce two fundamental topics, the early epoch reionization and the metal abundance in the intergalactic medium discussed in this thesis.

2704 BATSE Gamma-Ray Bursts
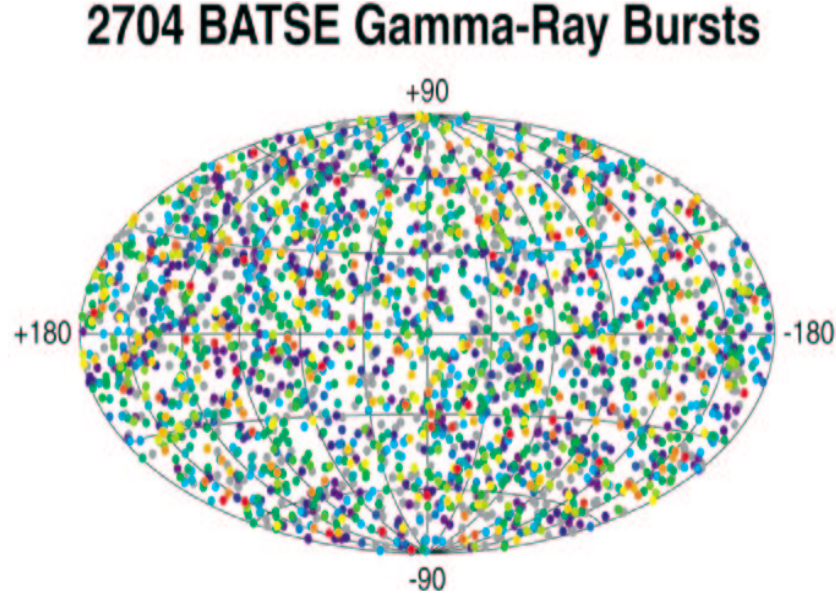
Figure 1.1: The sky distribution of GRBs detected by the *CGRO* -*BATSE* detectors. No clustering along the galactic plane was found, but GRBs isotropically distribute in the sky.

1.2   Observed Properties of GRBs

GRBs generally compose by the prompt gamma-ray emission phase and the following afterglow phase in X-ray, optical, infrared and radio bands. In this and next sections, noticing the time variability, spectrum and some important characteristics, we introduce the basic observed property of the GRBs and the afterglows, respectively.

1.2.1   Time Variability of GRBs

As shown in figure 1.2, the prompt gamma-ray emission of GRBs generally shows complex time profiles with rapid variability which drastically change from burst to burst. It is difficult to determine the pulse shape with a unified function because of their complexity, but the many pulses shows a "Fast Rise and Exponential Decay (FRED)" shape. Since the most rapid time variability is in order of 1 msec, the size of the GRB seems to be very small.

There are two populations in time duration such as short GRBs ($T_{90} < 2$ sec) and long GRBs ($T_{90} > 2$ sec) as shown in figure 1.3, where T_{90} is measured as the duration of the time interval during which 90 % of the total observed counts have been detected. The T_{90} duration is also various burst to burst. Some of the GRBs categorized as the long GRBs show brief duration with a few second, and the long cases exceed several hundred seconds. These durations are generally considered as the activity timescale of the GRB progenitor (central engine). As described below, the long GRBs are very bright, and their position could be determined by the past satellites. Thus, the properties of long GRBs are considerably studied while we have still few knowledge about short GRBs because they are much dimmer than the long GRBs because of their short duration. Therefore, in this thesis, we deal with only the long GRBs with the duration of $T_{90} > 2$ sec.
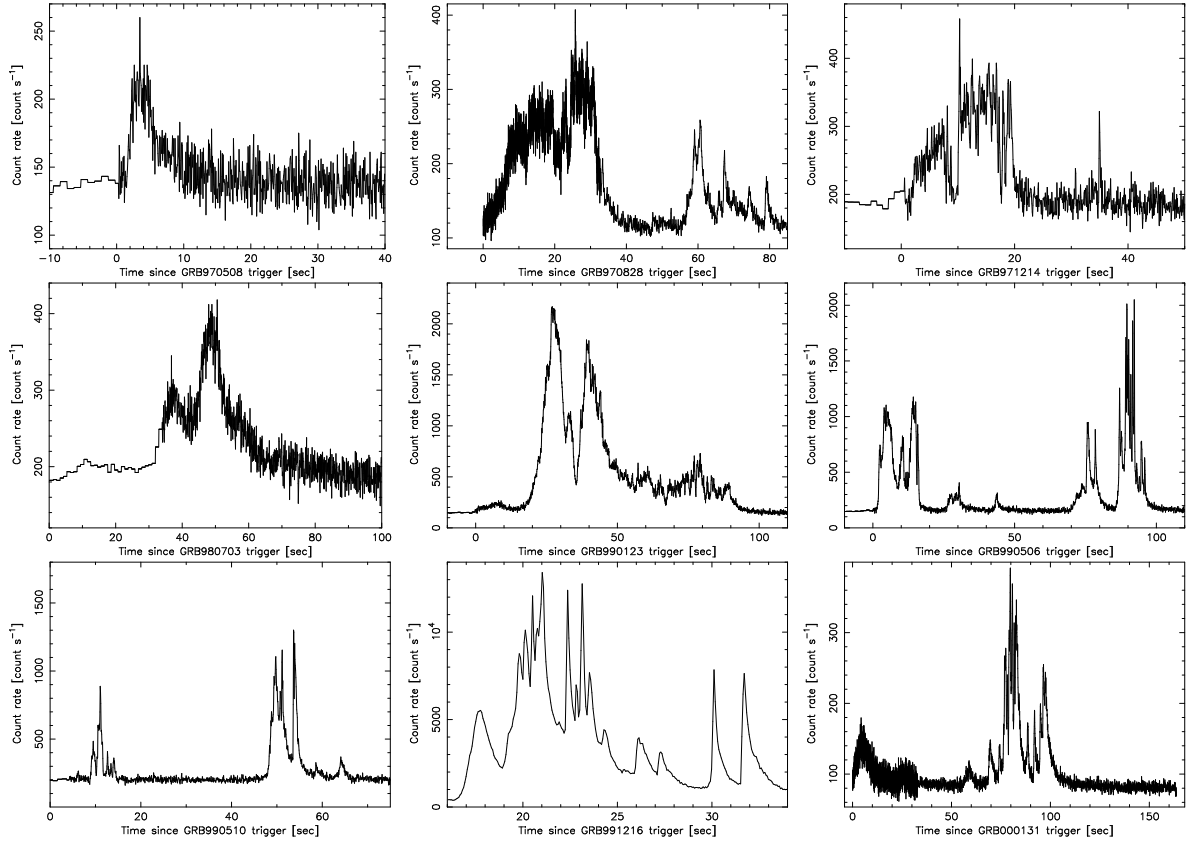
Figure 1.2: Examples of GRB lightcurves detected by *BATSE* .
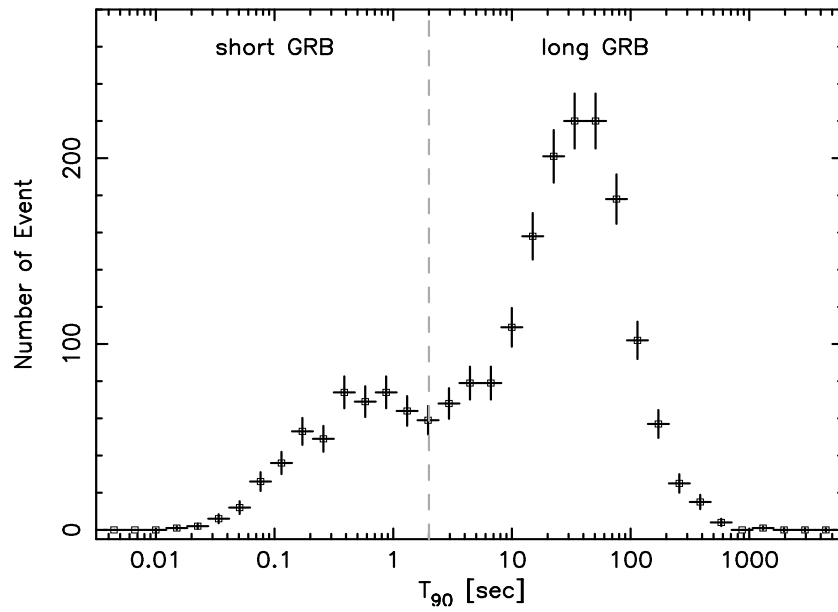
Figure 1.3: A distribution of T_{90} detected by *BATSE* . There are roughly two populations such as short GRBs ($T_{90} < 2$ sec) and long GRBs ($T_{90} > 2$ sec).

1.2.2   Spectral Property of GRBs

In figure 1.4, we show an example of the GRB spectrum detected by *BATSE* (Briggs et al., 1999).
The upper and lower panels are the photon spectrum and the νF_ν spectrum, respectively. The
spectrum is well represented by the smoothly broken power-law model with the functional form
described below (Band et al., 1993).

$$
N(E) = \begin{cases} A\left(\frac{E}{100\ \text{keV}}\right)^{\alpha} \exp\left(-\frac{E}{E_0}\right) & \text{for } E \leq (\alpha - \beta)E_0, \\ A\left(\frac{E}{100\ \text{keV}}\right)^{\beta} \left(\frac{(\alpha-\beta)E_0}{100\ \text{keV}}\right)^{\alpha-\beta} \exp(\beta - \alpha) & \text{for } E \geq (\alpha - \beta)E_0, \end{cases} \tag{1.1}
$$

where, $N(E)$ is in unit of photons $\text{cm}^{-2}\text{s}^{-1}\text{keV}^{-1}$, E_0 is the energy at the spectral break. α and
β is the low- and high-energy power-law index, respectively. For the case of $\beta < -2$ and $\alpha > -2$,
the peak energy can be derived as $E_p = (2 + \alpha)E_0$, which corresponds to the energy at the
maximum flux in νF_ν spectra as shown in the lower panel of figure 1.4. This power-law shape
in GRB spectra indicates that the emission mechanism of GRBs is a non-thermal emission such
as the synchrotron radiation via shock accelerated electrons.
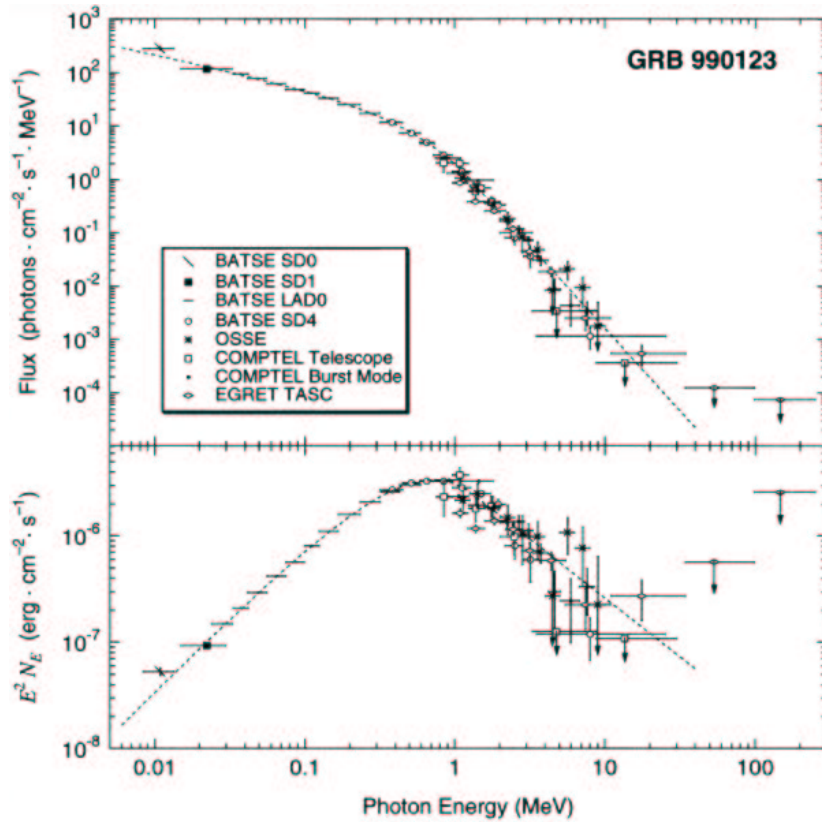
Figure 1.4:   An example of the GRB spectrum (GRB 990123) observed by the
CGRO satellite (Briggs et al., 1999). This spectrum is combined by the *BATSE* , *OSSE* ,
COMPTEL and *EGRET* detectors. The horizontal axis is correspond to the energy at the
GRB's rest frame. The upper panel is a photon spectrum in units of photon $\text{cm}^{-2}\text{s}^{-1}\text{MeV}^{-1}$
and the lower panel is νF_ν spectrum in units of erg $\text{cm}^{-2}\text{s}^{-1}$. GRB spectrum can be de-
scribed by the smoothly broken power-law in equation (1.1).
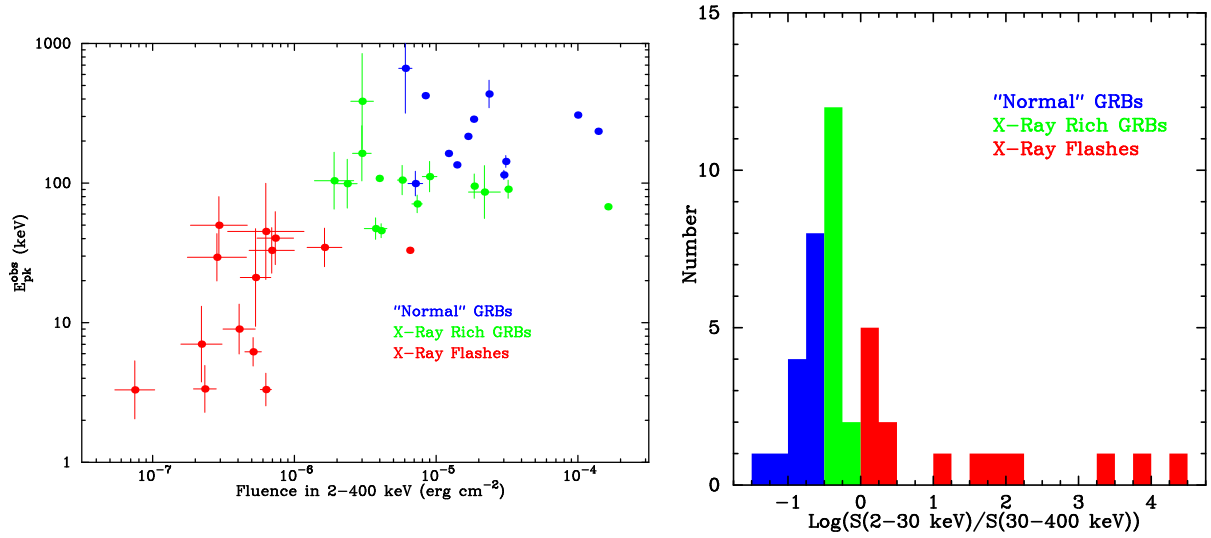
Figure 1.5: Left and right panel are the E_p–fluence diagram and the distribution of the hardness ratio of GRBs, XRFs and XRRs. (Lamb et al., 1999)

1.2.3 X-ray Flashes and X-ray Rich GRBs

Sakamoto (2004) summarized the observation results by the *HETE-2* satellite. A large fraction of entire 45 events are bright in the X-ray band of 2–30 keV. These events are very similar to the GRBs properties in time variability and the spectral shape, but the large amount of fluences are detected in X-ray range (2–30 keV). Sakamoto (2004) and Lamb et al. (1999) determined them as new categories of X-ray Flashes (XRFs) and X-ray Rich GRBs (XRRs), distinguishing the typical GRBs. In figure 1.5 (left), observed properties of three populations are plotted on the peak energy E_p and the fluence plane (Lamb et al., 1999). The distributions of the hardness ratio (fluence ratio of $S_X(2-30)/S_\gamma(30-400)$) are shown in figure 1.5 (right). Their distribution seems to be continuous, and we can consider the origins of GRBs, XRFs and XRRs may be same. At present, the numbers of these three populations detected by *HETE-2* are roughly comparable (XRFs : XRRs : GRBs = 15 : 20 : 10). This is one of the important results by *HETE-2* . In this thesis, we use the *BATSE* data whose energy range is about 30–2000 keV, so we do not include the XRFs and XRRs.

1.3 Observed Properties of Afterglows

The afterglows following the prompt gamma-ray emission of GRBs are observed in X-ray, optical, infrared and radio band. The X-ray afterglows are observed in almost all GRBs (~ 90 %) while the optical and the radio transient are found only in a fraction of 50 % or less. In this section, we briefly introduce the property of GRB afterglows.

1.3.1 Time Variability of Afterglows

An X-ray afterglow of GRB 970228 was discovered with the Italian-Dutch X-ray satellite *BeppoSAX* at first (Costa et al., 1997). The Gamma-Ray Burst Monitor (*GRBM*) and the Wide Field Camera (*WFC*) aboard the *BeppoSAX* satellite determined the position of GRB 970228
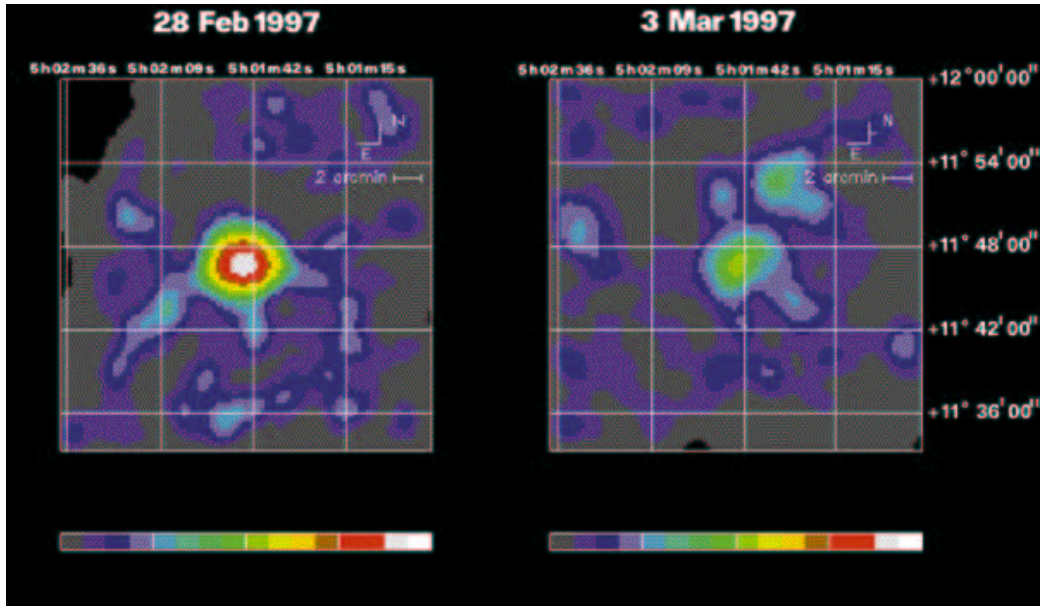
Figure 1.6: The images of the X-ray afterglow of GRB970228 detected with *NFI* aboard *BeppoSAX* (2–10keV) during the first and second Target of Opportunity observations Costa et al. (1997).

within the error of several arcmin. By the follow-up observations with the Narrow Field Instruments (*NFI*) 8 hours after the GRB trigger, a new X-ray source was discovered and its flux decayed about 1/20 at 3.5 days after the GRB. In figure 1.6, we show the image of the X-ray afterglow of GRB 970228. The left and right panel is the image at 8 hours and 3.5 days after the burst, respectively.

In figure 1.7 (left), we show an example of the afterglow lightcurve. The mainly brightening energy band changes from X-ray to radio, and the afterglow brightness in the fixed energy band generally shows the power-law decline in time. This decline is well adopted to the X-ray, infrared and radio lightcurves as well as optical ones.

By the grace of the *HETE-2* and *INTEGRAL* satellite, the GRB positions are rapidly announced all over the world, and a lot of observations are performed for the early optical afterglows. At the extremely early phase of the optical afterglows, such as 0.01 days after the GRB trigger, the flux decline with $\propto t^{-2}$ was observed in several GRBs, (for example GRB 021004 and GRB 021211 as well as GRB 990123). These decay indices are steeper than the typical value of t^{-1}, and they are interpreted as the decline of optical flashes which is generated in the reverse shock propagating into the GRB ejecta. At the case of GRB 990123, whose redshift is $z = 1.6$, its optical flash reaches $M_v \sim 9$ mag. in the visual magnitude (Akerlof et al., 1999). On the other hand, although the early epoch observations are performed, no optical transient is found in several cases. These events are generally called *optically dark GRBs*, and their origin is still in debate.
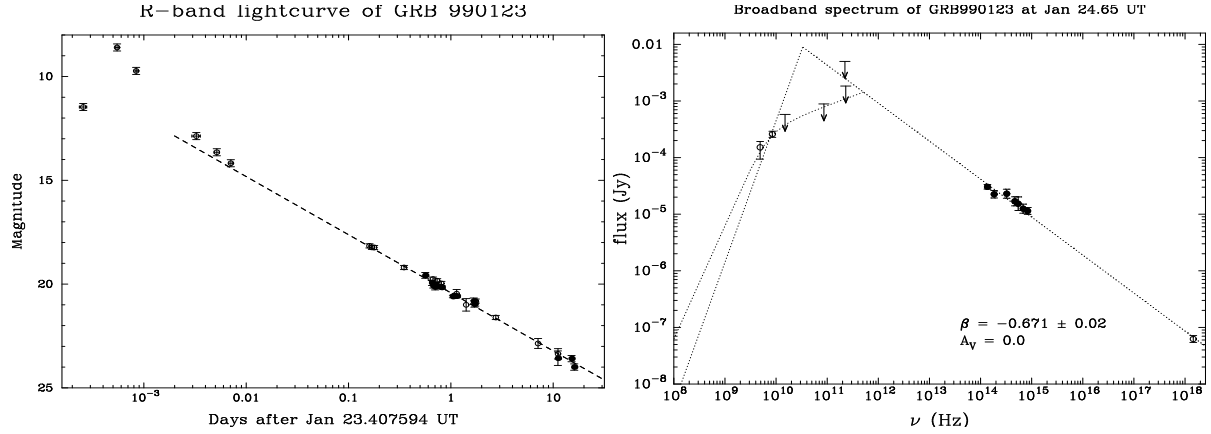
Figure 1.7: An example of the lightcurve (left) and the multi-band spectrum (right) of the afterglow (Galama et al., 1999). The lightcurve decays with the power-law in time, and the spectrum is well described by the synchrotron emission model from X-ray to radio.

1.3.2 Spectral Property of Afterglows

The multiband spectrum, from X-ray to radio, has been obtained for some bright GRBs. As shown in figure 1.7 (right), the spectral shape is well described by the synchrotron model (e.g., Galama et al., 1999). This fact indicates that the afterglow is non-thermal emission generated by the shock accelerated electrons as long as the prompt GRB.

One of the most important key to trace the GRB environment is the emission lines of heavy elements in the X-ray afterglow spectra. If such a emission feature is detected, it means that GRB progenitors exist in the dirty environment such as a star forming region. Piro et al. (1999) and Yoshida et al. (1999) independently reported the detection of the strong iron emission line in the X-ray afterglow of GRB 970508 and GRB 970828 with the *BeppoSAX* and *ASCA* satellite, respectively. From the *Chandra* observation of GRB 991216, the strong iron emission line was detected together with the radiative recombination edge (Piro et al., 2000). To represent the observed spectral features, Yoneotku et al. (2001) performed numerical simulations and interpreted the plasma condition around the GRB progenitor as the non-equilibrium ionization states. Reeves et al. (2002); Watson et al. (2003) revealed the existence of the emission lines of light elements by the *XMM-Newton* observation. These observations strongly support that the progenitor of GRBs are massive star origin, i.e. supernova/Hypernova.

On the other hand, Yoneotku et al. (2000) reported no spectral features in two X-ray afterglow of GRB 990123 and GRB 990704 with *ASCA* . Especially, by the observation of GRB 990123, we set an upper-limit flux of iron emission line as $EW < 100$ eV in 90 % confidence level. Yoshida, Namiki, Yonetoku et al. (2001); Reeves et al. (2002); Watson et al. (2003) suggest the time variability of the emission line fluxes, so the X-ray emission features are not detected at any time. It probably depends on the geometrical effects and the plasma condition near the GRB site. We continuously observed the X-ray afterglows with *ASCA* satellite, and systematic analyses have performed in Yonetoku Master Thesis (2001). The results of further analyses including *XMM-Newton* data are summarized in Appendix D.
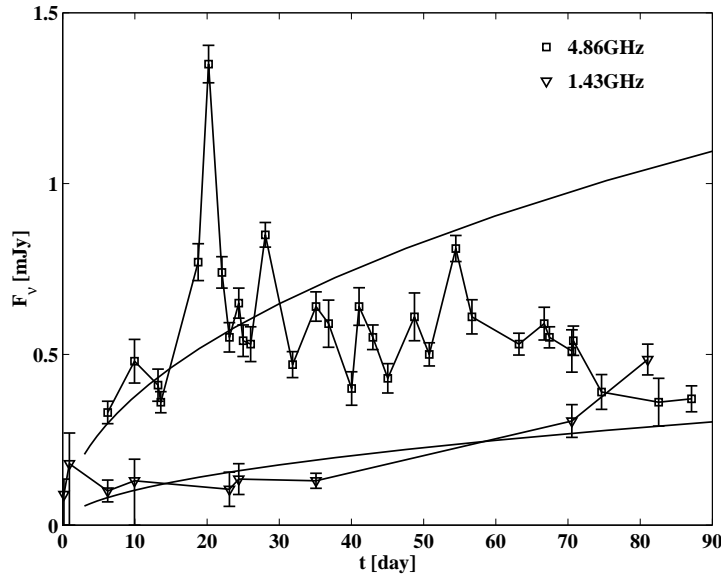
Figure 1.8: Light curve of the radio afterglow of GRB970508 at 4.86 GHz and 1.43 GHz. The solid lines are model functions due to adiabatic expansion.

1.3.3 Evidence of the Relativistic Jet

Waxman et al. (1998) observed the radio afterglow of GRB 970508, and found the quenching of diffractive scintillation at ~ 4 weeks delay as shown in figure 1.8. Based on this result, they provide a direct estimate of source size and expansion speed. The radiation of radio afterglow comes from $R \sim 10^{17}$ cm from the central engine and its expansion velocity is comparable to the speed of light (relativistic speed) at $t \sim 4$ weeks.

A lot of observations are held for afterglows in the world, and the continuous property of the decaying afterglow can be observed. As shown in figure 1.9 (left), the index of the power-law decline generally changes. It is more appropriate to describe the temporal evolution with the broken power-law in time. Typically, the flux decays with $\propto t^{-1}$ at the early epoch, and it changes as $\propto t^{-2}$ after the break time. It is interpreted that this property is caused by the geometrical effect of the relativistic jet as described below.

The observable emitting region of GRBs are restricted by the relativistic beaming effect, γ^{-1}, where γ is the Lorenz factor of the emitting material. Thus the observer cannot obtain the information of a entire sphere of the collimated jet. However, the relativistic matter expands and decelerates its Lorentz factor, and it will achieve $\gamma^{-1} > \theta_j$, where θ_j is the geometrical angle of the collimated jet. Then, the observed flux is free from the relativistic beaming effect, and its decline is completely determined by the geometrical effect. The break point shown in figure 1.9 (left) is determined as the time achieving $\gamma^{-1} \sim \theta_j$. When we measure the break time, the collimation angle can be determined, so the total energy emitted as gamma-ray photons can be also estimated. In figure 1.9 (right), we show the distribution of the geometrically-corrected gamma-ray energy by (Bloom et al., 2003). It is tightly clustering around the standard energy of $\sim 1 \times 10^{51}$ ergs, so the prompt emission of GRBs may enable to be used as a standard candle.
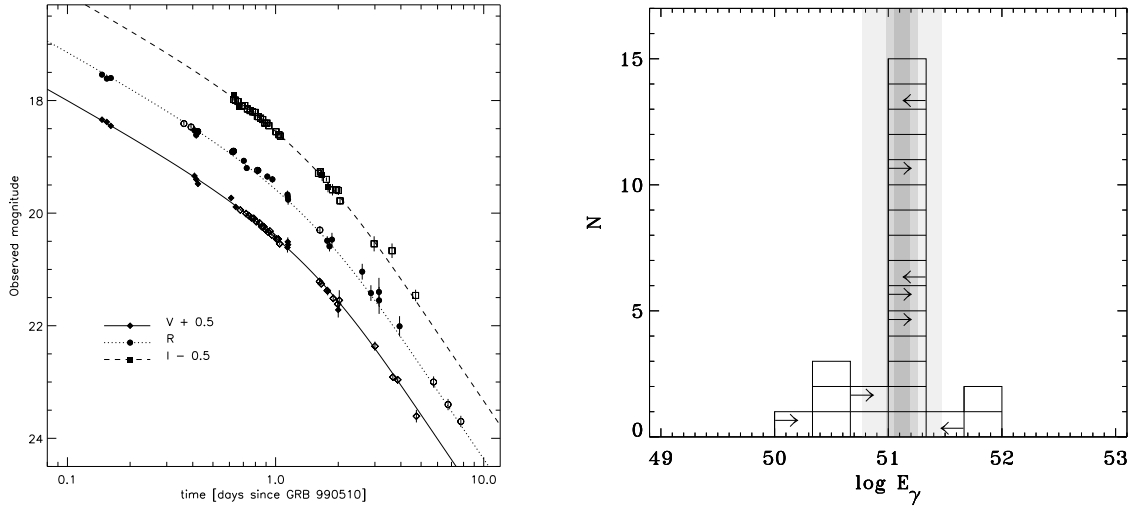
Figure 1.9: The left panel is an example (GRB 990510) of the jet-break in the afterglow lightcurve. The collimation angle of the relativistic jet is determined by the jet-break time. The right panel is the distribution of the total gamma-ray energy released in the jet opening angle (Bloom et al., 2003). It is tightly clustering around 1×10^{51} ergs.

1.4 Massive Star as a GRB Progenitor

On March 29, 2003, one of the most important event GRB 030329 occurred. Thanks to the rapid announce by the *HETE-2* committee, the afterglows are continuously observed around the world (e.g., Peterson & Price, 2003; Uemura, 2003; Torii, 2003; Sato et al., 2003; Murakami, Yonetoku et al., 2003). This GRB is the third closest event ever known, $z = 0.168$, and a supernova spectrum was observed by Hjorth et al. (2003) after 12 days since the GRB trigger (see, figure 1.10-left). This supernova is named as SN 2003dh. This is the first case to detect the spectral component of supernova in the late-epoch afterglow. We can say that we confirmed the GRB progenitor is the supernova by the GRB 030329/SN2003dh observation while the connection between GRB 980425 and SN 1998bw was marginal result.

In several cases of the afterglow, especially at the case with steep decline of $prop tot^{-2}$, rebrightening components are detected as shown in figure 1.10 (right). Comparing the lightcurve of bumping phase with one of SN 1998bw, these structures are interpreted as the supernova signatures (Bloom et al., 1999). Therefore these bumps are also direct detections of supernova, and strongly support that the GRB progenitors are massive stars.

Another evidence about the connection between GRBs and massive stars is the detection of emission lines in the X-ray afterglow spectra. Since emission lines are independently detected with four X-ray satellites (*ASCA* , *BeppoSAX* , *Chandra* and *XMM-Newton*) with above 3 σ significance, they really exists in the X-ray spectrum in some kind of afterglow. These emission lines are generated only in the metal-rich dense-gas environment. The origin of the line emitting gas may be stellar wind from massive stars before GRB explosions. However, the physical process to generate the emission lines is a puzzle.
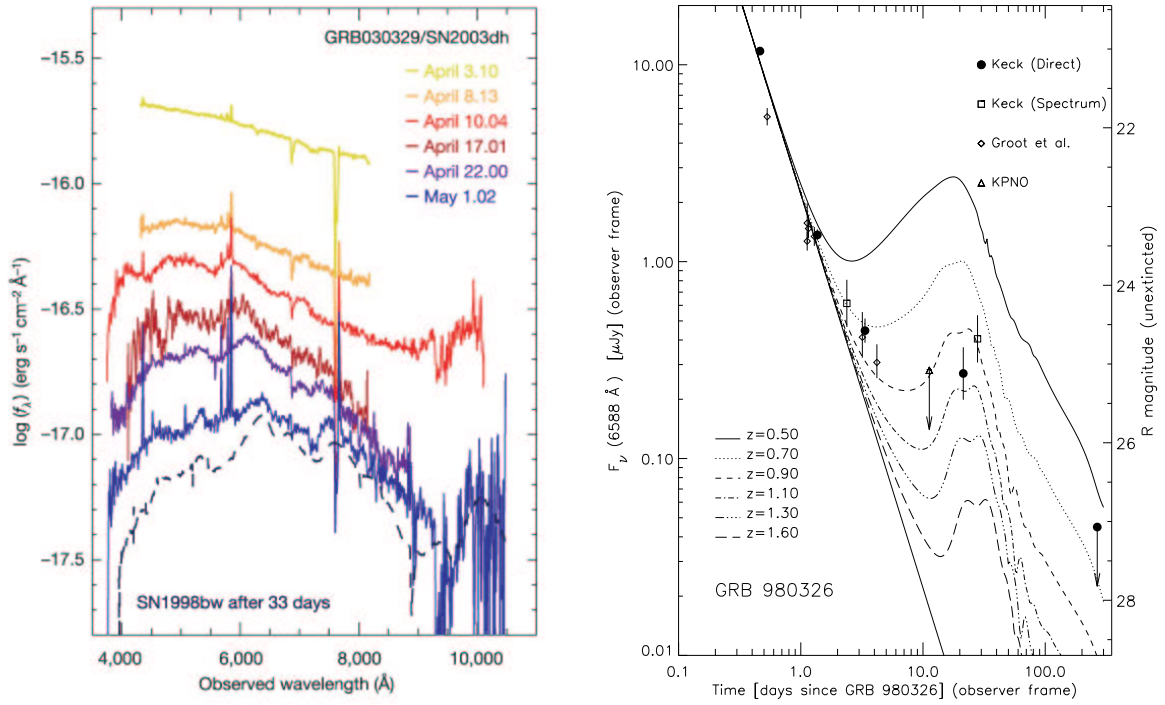
Figure 1.10: Left panel is the spectral evolution of the combined optical flux density of the afterglow of GRB030329, and the associated SN2003dh (Hjorth et al., 2003). The upper spectrum, which is observed at 12 days after GRB trigger, is rather well fitted by a power law, as usually seen in afterglow spectra. The middle spectra show clear deviations from a power-law, similar to SN1998bw at the same phase. The lower spectra, dominated by SN2003dh, reveal the supernova signatures. For comparison, the spectrum of SN1998bw after 33 days is shown (dashed line) shifted to the GRB030329 redshift. Right panel is lightcurve of the optical afterglow of GRB 980326. A supernova-like signature, SN bump structure, appears 10 days after the GRB trigger time.
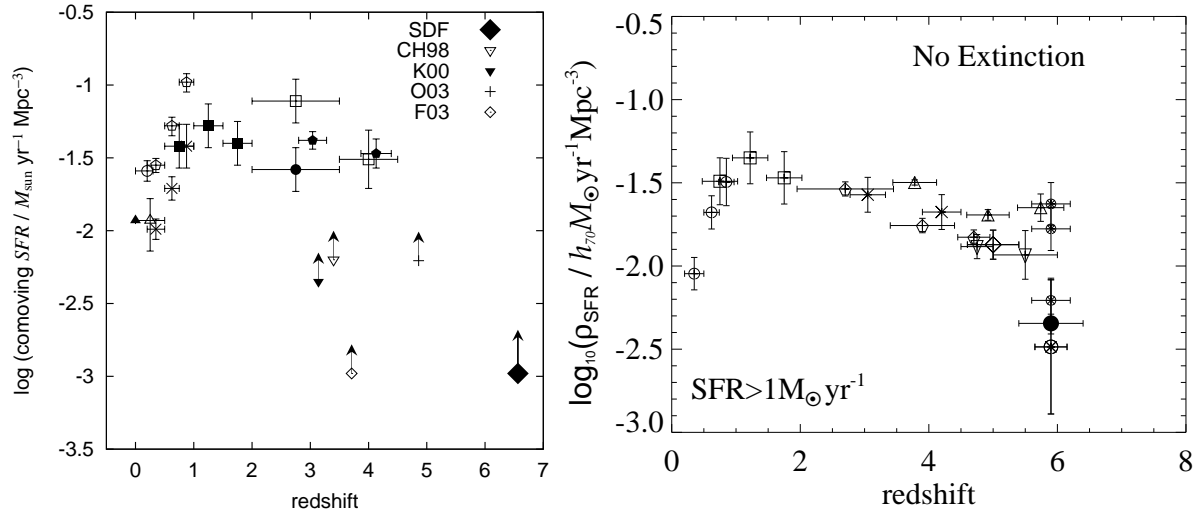
Figure 1.11: Star formation rate measured by the Subaru Deep Field (left) (Kodaira et al., 2003) and the Hubble Ultra Deep Field (right) (Bunker et al., 2004) with the past observations. The SFR reaches its maximum at $z \sim 1$ and decreases toward the higher redshifts. These plots are lower limit because the galactic and the intergalactic extinction are not corrected.

1.5 Star Formation Rate

Historically, the star formation rate (SFR) have been measured by UV, optical and infrared observation (e.g., Madau et al., 1996; Lilly et al., 1996; Barger et al., 2000; Stanway et al., 2003). In this section, we introduce the past observations.

Since the star's lifetime in the main sequence phase is as a function of its own mass as $T_{\mathrm{life}} \propto M^{-3}$. For example, the lifetime of the massive star, such as O-type star (~ 25 $M_{\odot}$), is about 10^6 yr while one of the M-type star (~ 0.5 $M_{\odot}$) is 5×10^{10} yr. Therefore, if we can observe the number distribution of the massive star, it is thought to well correlate to the *current* SFR. Generally, the massive stars categorized as OB-type stars are very bright in the rest ultraviolet band, so the UV observation is important to trace the amount of massive stars and the SFR. The Lyα emission line, the rest wavelength is 1216 Å, is one of the important tool to estimate the UV luminosities.

On the other hand, UV photons are considerably extincted by the galactic and the inter-galactic medium (IGM), such as dust, gas, and so on. When the UV photons are absorbed by the dust, the infrared photons are reprocessed. Therefore, the infrared luminosity also enable to trace the SFR indirectly. Additionally, the significant correction for the UV luminosity is needed, so the it is considerably difficult to measure the SFR only by the UV observations.

By the grace of the Hubble space telescope and the 8–10 m class ground-based telescopes, the SFR is measured beyond $z > 5$. Especially, several Lyα galaxies (Lyα emitters) are discovered in the Subaru deep field, and their redshifts exceed $z > 6$ (e.g. Kodaira et al., 2003, as the first report). Using the relation between the SFR and the Lyα luminosity as $SFR(\mathrm{Ly}\alpha) = 9.1 \times 10^{-43}$ Lyα $M_{\odot}\mathrm{yr}^{-1}$, the SFR at $z \sim 6.6$ was estimated. In figure 1.11 (left), we show one of the most distant SFR by Kodaira et al. (2003) together with the past observation results.
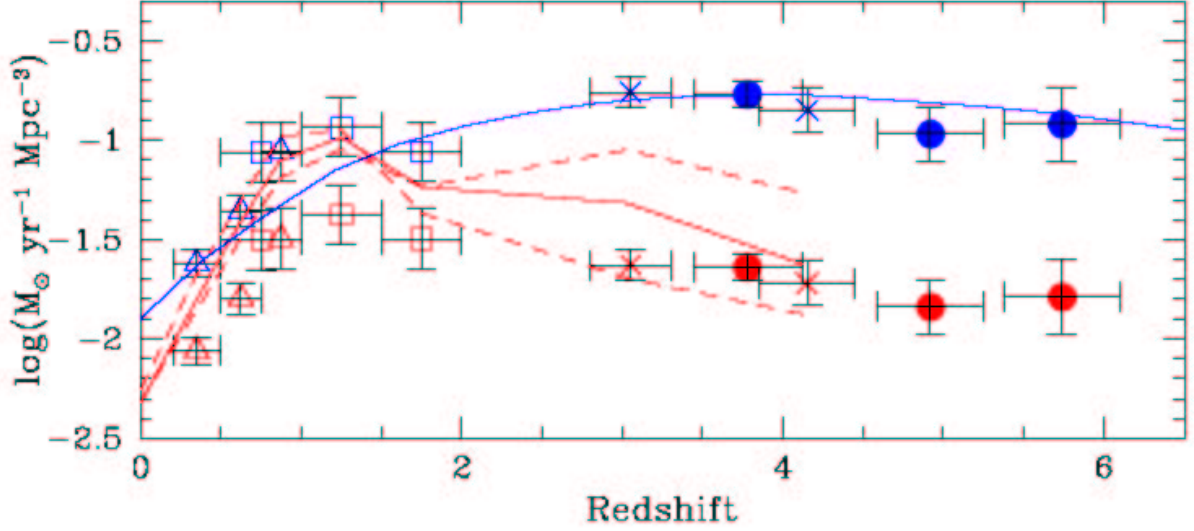
Figure 1.12: Star formation rate estimated from the Ly-break galaxies observed by the Hubble space telescope (Giavalisco et al., 2004). Red and blue points are the observed and the dust-corrected star formation rate, respectively. The star formation rate keeps flat toward higher redshift.

Additionally, in figure 1.11 (right), we show the SFR measured from the Hubble Ultra Deep Field (Bunker et al., 2004). According to these results, the SFR reaches its maximum at $z \sim 1$, and it may decrease toward the higher redshift. However one should pay attention that these SFRs are the lower limit, because the galactic and the intergalactic extinction is not corrected. In figure 1.12, we show the SFR corrected for the dust extinction (Giavalisco et al., 2004). The corrected SFR (blue line) keeps flat toward higher redshifts. However the correction factor of absorption degree considerably depends on some model parameters, such as a number density of Lyα cloud, temperature of IGM, column density in the star forming galaxy and so on. Therefore there are large ambiguities in the corrected SFR.

1.6   Cosmic Reionization

The *WMAP* satellite (Wilkinson Microwave Anisotropy Probe) observed the cosmic microwave background, and obtained the full-sky map of the oldest light in the universe with the high spacial resolution. The *WMAP* satellite resolves slight temperature fluctuations as shown in figure 1.13 [1]. These patterns are tiny temperature differences within an order of 10^{-5} K around the average temperature of about 2.73 K with complete blackbody spectrum.

Spergel et al. (2003) reported the determination of cosmological parameters measured from the *WMAP* observations combined with the past data. The parameter set is $(\Omega_m, \Omega_\Lambda, H_0) = (0.32, 0.68, 72)$ with the flat universe $\Omega_k = 0$ and $\Omega_r = 0$. Here, Ω_m, Ω_Λ, Ω_k and Ω_r are the cosmological parameters for the matter, the cosmological constant (dark energy), the curvature and the radiation, respectively. The value H_0 is the Hubble constant in units of km s^{-1}Mpc^{-1}. The *WMAP* satellite also revealed that the cosmic reionization started at $z = 17 \pm 5$. This

---

[1]from the *WMAP* web site: http://map.gsfc.nasa.gov/
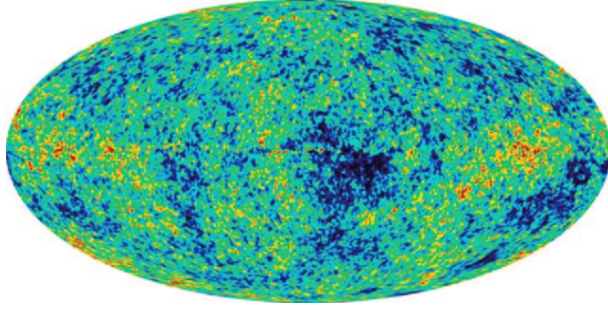
Figure 1.13: Temperature fluctuations of cosmic microwave background measured by the *WMAP* satellite. Colors indicate warmer (red) and cooler (blue) spots compared with the average temperature, respectively.

fact indicates that the first star has been brightened earlier than this epoch.

Cen (2003) summarized the recent observations about the cosmic reionization history. According to the up-to-date results, the universe is thought to be reionized twice. The first is the early epoch reionization at $z \sim 17$, which is measured by the *WMAP* satellite. The primary source of this reionization is uncertain, but the first generation objects may realize it. The second one is, so called, the final cosmological reionization at the $z \sim 3$. This is observed by the absorption (Lyα forest) in the quasar spectra. This reionization is realized by the UV photons emitted by the galaxies. In this thesis, we will discuss the early epoch reionization.

1.7 Metal Abundance in the Intergalactic Medium

The big bang can produce only the hydrogen and the other light-elements (stable elements are deuterium, helium, lithium and beryllium). Many isotopes are not stable. If their half-lives are shorter than the time of fusion collisions, the isotope will decay away before the next collision to use it to build the next heavier element. The ^{4}He constitutes nearly 25 % of the composition of the universe. But the next few stable elements, ^{6}Li, ^{7}Li and ^{9}Be had to go through several bottlenecks to be synthesized. Calculations predict that ^{7}Li makes up about 8×10^{-10} of the universe as a primordial element, ^{7}Be makes up 2×10^{-11}, and ^{9}Be is 8×10^{-15} compared to hydrogen. Then let us consider the amount of heavy elements in the diffuse intergalactic medium. We may think that the IGM far from galaxies is not contaminated by the heavy elements from the galactic winds, and conserves the metal abundance of the primordial gas.

However Cowie & Songaila (1998) suggested that the metallicity is roughly constant over a wide range of densities in the IGM. In figure 1.14, we show the relation between the optical depth of C$_{IV}$ and Lyα (Cowie & Songaila, 1998). The values of $\tau(\text{Ly}\alpha)$ and $\tau(\text{C}_{IV})$ are optical depth measured from the absorption in the spectra of quasars. The linear correlation between these two values indicates that the metallicity is roughly constant over the wide range of density in the IGM. This fact is quite different from the above descriptions about the nucleosynthesis in the big bang. Moreover Songaila (2001) reported the metal abundance of C$_{IV}$ and Si$_{IV}$ in the IGM measured from the metal absorption lines in quasar spectra. In figure 1.15, the evolution of metal abundance by Songaila (2001) is shown as a function of redshift. This figure shows that the large amount of heavy elements with the metallicity of $Z \sim 10^{-4} Z_\odot$ have been already set in the early universe at $z > 6$. Based on these facts, it is natural to consider that the metal pollution has spread over the wide scale IGM at the early universe.
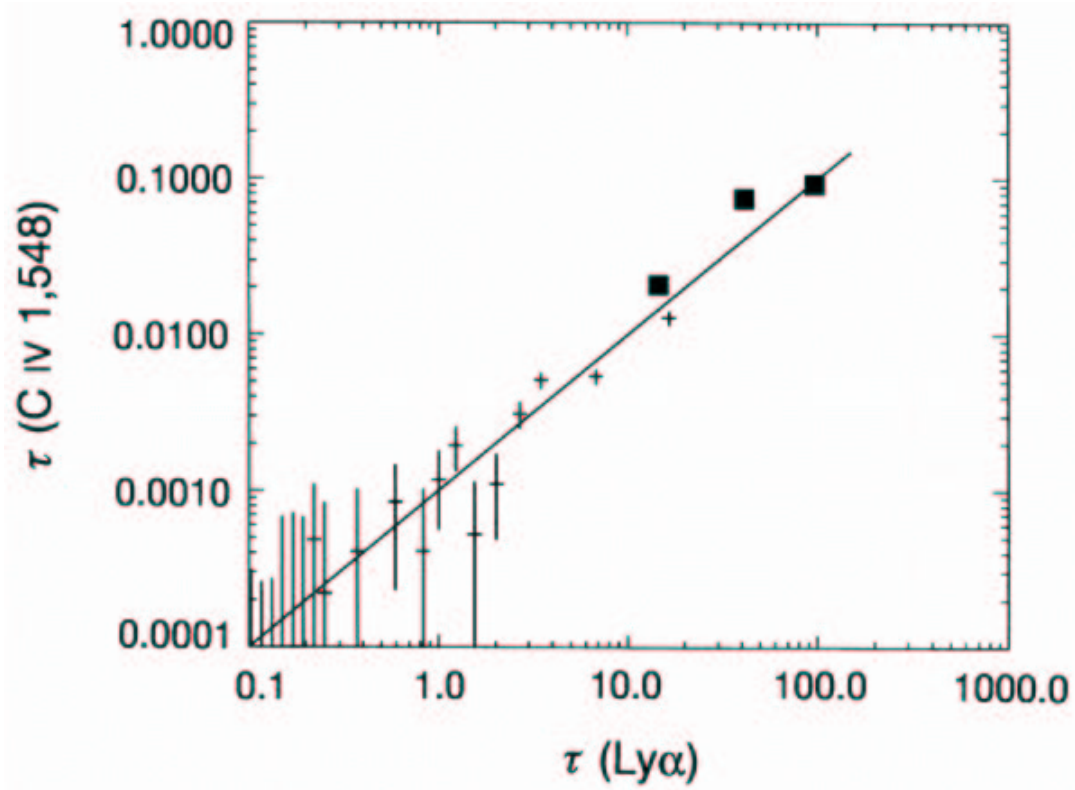
Figure 1.14: Relation between the optical depth of C_{IV} and $Ly\alpha$ (Cowie & Songaila, 1998). The values of $\tau(Ly\alpha)$ and $\tau(C_{IV})$ are optical depth measured from the absorption in the spectra of quasars. The linear correlation between $\tau(Ly\alpha)$ and $\tau(C_{IV})$ indicates that the metal abundance is roughly constant over the wide range of density in the IGM.
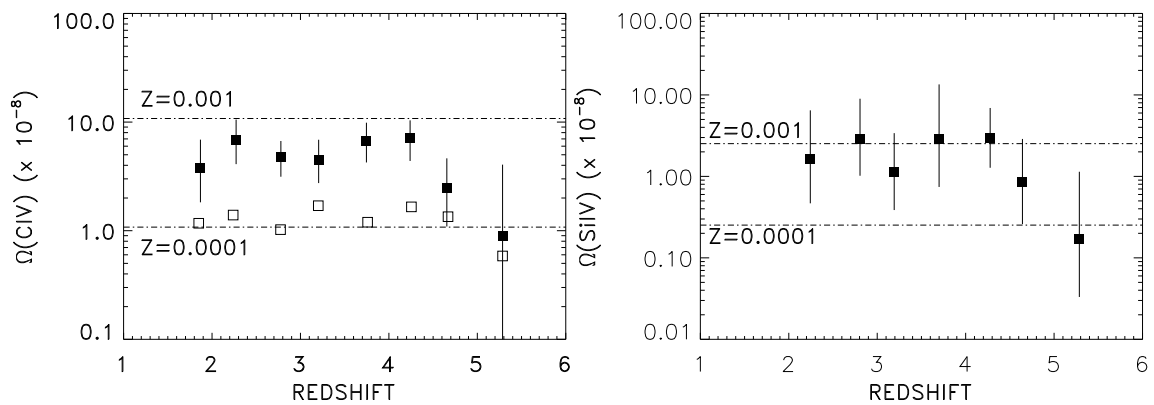
Figure 1.15: Metallicity as a function of redshift measured from the column density of C_{IV} (left) and Si_{IV} traced by the quasar light (Songaila, 2001). Two dot-dashed lines correspond to the metallicity of $Z = 10^{-4} Z_\odot$ and $10^{-3} Z_\odot$, respectively. At the redshift of $z = 5$, the metal abundance have already been $10^{-4} Z_\odot$ in the IGM.

This thesis is organized in the following order.

In Chapter 2, we introduce the theoretical model so called the relativistic fireball model to refer to the review by Piran (1999). We explain the energy conversion in the relativistic shock, the synchrotron emission from relativistic matter, and the temporal and spectral properties of GRBs and afterglows with the special relativity. In Chapter 3, we summarized the capability and the performance of four instruments aboard the *CGRO* observatory. Especially we note the *BATSE* instrument, whose data are used in this thesis, and show the background and the efficiencies of the instrument. Using the *BATSE* data, we performed the spectral and the temporal analysis of prompt emission of GRBs. We show the results in Chapter 4, and discuss an intrinsic property of "E_p–luminosity" relation. In Chapter 5, using the E_p–luminosity relation, we estimate the redshifts and lumionsities for large amount of GRBs without known distance. Based on the redshift distribution, we derived the GRB formation rate at the early universe toward $z = 12$. In Chapter 6, adopting the geometrical correction of the GRB jet, we estimate the absolute GRB formation rate at early universe. We discuss the early epoch reionization and the metal abundances in the IGM with the absolute GRB formation rate. Finally, we summarized about this thesis in Chapter 7.

The mathematical descriptions used in calculating the GRB formation rate are given in Appendix A. We correctly take into account the flux limited samples with this method. A table of all samples estimated the redshift and luminosity are listed in Appendix B. Additionally, we show the spectral and the temporal analysis of the X-ray afterglows observed with *ASCA* and *XMM-Newton* in Appendix D.

Chapter 2

Standard Scenarios of GRBs

As already mentioned in Chapter 1, the relativistic outflows with high Lorentz factor ($\gamma \sim 100$) is required to solve the compactness problem. It is widely believed that the prompt gamma-ray emission and the following afterglows are arisen by the internal–external shock of the relativistic outflows. This scenario is called a *Fireball Model* (Rees & Mészáros, 1992).

A basic stream of the fireball model is following:

1. A large amount of energy, such as $E = 10^{52}$ erg, closed in a compact volume are transferred into a kinetic energy of a small mass. Then, the small mass is accelerated to the relativistic velocities with the Lorentz factor of ~ 100, and a lot of outflows are generated. The total mass should be satisfied $M = E/\gamma c^2 \sim 10^{-5}\ M_\odot$ to achieve $\gamma = 100$.

2. One of the outflow with the high Lorentz factor catches up the slower outflow, and occurs an internal shock. A lot of internal shocks will be generated, and shock accelerated electrons in each internal shock emit gamma-ray photons via synchrotron radiation. This is the prompt gamma-ray burst.

3. The relativistic outflows merged into one and decelerate its Lorentz factor. This merged outflow through into the ISM and generate an external shock. The synchrotron radiation is emitted by the electrons accelerated in the external shock, and it is observed as an afterglow.

The above stream is drawn as a schematic image in figure 2.1. In this section, we briefly explain the standard scenarios of GRBs to refer to the review by Piran (1999).

2.1 Compactness Problem

The complex time profile and the rapid variability observed in the prompt gamma-ray emission indicates that the size of the central engine is considerably small. For example, the variability of $\delta T = 1$ msec corresponds to the source size of $R_i \sim 3 \times 10^7$ cm. The large amount of the gamma-ray photons are confined within such a small volume, electron–positron pair creations are dominated, and the gamma-ray photon cannot escape straightforwardly. An optical depth of the pair creation is estimated as

$$\tau_{\gamma\gamma} = \frac{f_p \sigma_T F D^2}{R_i^2 m_e c^2} = 10^{11} f_p \left(\frac{F}{10^{-7}\ \text{erg/cm}^2}\right)\left(\frac{D}{3\ \text{Gpc}}\right)^2\left(\frac{\delta T}{1\ \text{msec}}\right)^{-2}. \tag{2.1}$$
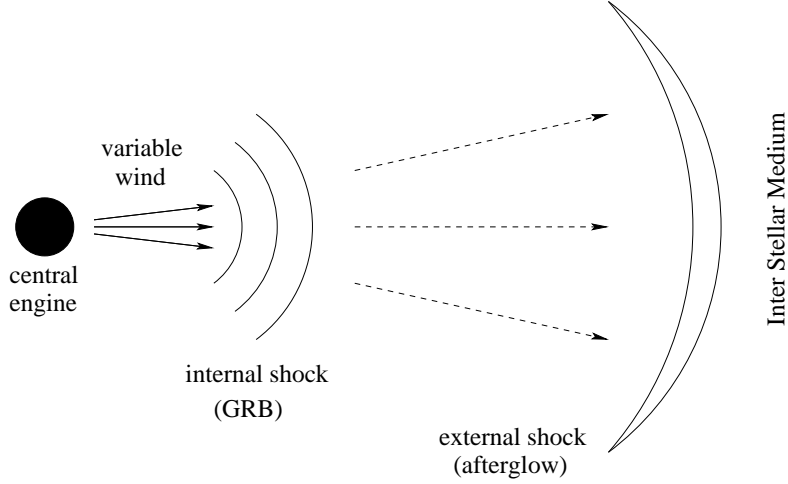
Figure 2.1: Outline of a fireball model. A large amount of shells with variable Lorentz factor is emitted by the central engine, and they interact with each other by the internal shocks, then prompt GRBs are generated. A merged shell propagates into the ISM, and the following afterglow occurs.

Here, F and D is the observed fluence and the distance to GRBs, and σ_T is the Thomson cross section. The value f_p is a fraction of the process $\gamma\gamma \rightarrow e^+ e^-$. This fact means that the gamma-ray photons should be scattered at least 10^{11} times, so the black-body spectrum should be observed from such a system. However, the GRBs are really observed with the non-thermal spectrum. This paradox is called "the compactness problem".

One solution for the compactness problem is given when we introduce the relativistic effect. If the source expands with the Lorentz factor γ, by the Lorentz contraction, the source size and the variable time scale is modified by the factor of $1/\gamma$ and γ, respectively. Moreover, since the observed gamma-ray photon is blueshifted, the intrinsic photon energy at the rest frame of the emitting material is reduced by the factor of $1/\gamma$, so the f_p is also modified as f_p/γ^2. Totally, the optical depth is improved $\tau' = \tau/\gamma^6$. Therefore, if the source has $\gamma \sim 100$, the photon can be escaped from the source, and the compactness problem can be solved. This scenario is named as the relativistic fireball model.

2.2   Energy Conversion

The cross section for a direct electromagnetic and/or nuclear interaction between the relativistic particles and the external particles (ISM or forward shell) is too small to convert the kinetic energy to radiation effectively. Therefore, we generally consider that the kinetic energy is converted to the thermal energy via collisionless shocks as in the supernova remnants (SNRs). Assuming the equipartition case, the energy density of the magnetic field may enable to be developed comparable to the energy density of accelerated electrons, and so the synchrotron radiation is expected in both case. Since it is difficult to consider a physical micro-process, we will avoid to explain it in this thesis. Hereafter, we discuss GRB phenomena as a relativistic analogues of SNRs. Even the total energy is comparable, but there are some differences between

them.

1. SNRs involve a solar mass or more with the corresponding velocity of $\sim 10^3$ km s^{-1} which is much less than the speed of light. On the other hand, in GRBs, the masses are smaller by several orders of magnitude with the same energy. The matter of GRBs attains ultra-relativistic velocities.

2. While SNRs result from the interaction of the ejecta with the ISM, prompt emission of GRBs results from internal collisions. The interaction of the ejecta with the ISM produces the afterglow that follows the prompt gamma-ray emission.

3. The interaction between the SNR ejecta ant the ISM takes place on scales of $\sim$ pc and it is observed for thousands of years. On the other hand, in GRBs, the internal interaction of the relativistic matter takes place at $\sim 10^{14}$–10^{18} cm and special relativistic effects reduce the observed time scale to several days.

Both of the prompt GRB and the afterglow are the synchrotron emission from relativistic materials, so both phenomena can be basically described by the same physics while they are different from each other in their locations, either. Therefore, in this chapter, first we show the shock property and the energy conversion in the relativistic shock. Second, we explain the synchrotron radiation from the relativistic shell. Finally, we summarize the properties of the internal and the external shock, respectively.

2.2.1 Relativistic Inelastic Collisions

Let us consider a rapid shell (mass ; m_r and Lorentz factor; γ_r) that catches up with a slower one (m_s and γ_s). Here the external shock can be described with the condition : $\gamma_s = 1$. The internal (thermal) energy of both shells is negligible compared to the rest mass. The two shells collide and merge to form a single mass (m_m and γ_m). In this case, energy and momentum conservation yield

$$
\begin{aligned}
m_r \gamma_r + m_s \gamma_s &= (m_r + m_s + \mathcal{E}/c^2)\gamma_m, & (2.2) \\
m_r \sqrt{\gamma_r^2 - 1} + m_s \sqrt{\gamma_s^2 - 1} &= (m_r + m_s + \mathcal{E}/c^2)\sqrt{\gamma_m^2 - 1}, & (2.3)
\end{aligned}
$$

where $\mathcal{E}$ is the internal energy generated in the collision (in the rest frame of the merged mass).

There are two interesting limits. First let m_s be at rest: $\gamma_s = 1$. This is the case in external shocks, or in a shock between relativistic ejecta and a non-relativistic material which was ejected from the source before it exploded (for example the stellar winds). The equation (2.2) and equation (2.3) reveal that a mass

$$
m_s \sim m_r/\gamma_r \quad (\ll m_r), \tag{2.4}
$$

is needed to yield $\gamma_m \sim \gamma_r/2$ and $\mathcal{E} \sim m_r c^2/2$ (for a conversion with high efficiency from the kinetic energy to the internal energy). The external mass (m_s) needed to be smaller than the original mass by a factor of γ_r, to convert half of the kinetic energy into the internal energy.

The second case corresponds to an internal collision between shells that are moving at different relativistic velocities $\gamma_r \geq \gamma_s \gg 1$ and merged velocity $\gamma_m \gg 1$. The equation (2.2) and equation (2.3) yield

$$\gamma_m \sim \sqrt{\frac{m_r\gamma_r + m_s\gamma_s}{m_r/\gamma_r + m_s/\gamma_s}}, \qquad \text{with} \quad \gamma_{rs} \sim \frac{1}{2}\Big(\frac{\gamma_r}{\gamma_s} + \frac{\gamma_s}{\gamma_r}\Big). \tag{2.5}$$

The internal energy of the merged mass measured from the external observers, $E_{int} = \gamma_m \mathcal{E}$, is the difference of the kinetic energies before and after the collision,

$$E_{int} = m_r c^2 (\gamma_r - \gamma_m) + m_s c^2 (\gamma_s - \gamma_m). \tag{2.6}$$

The conversion efficiency of kinetic energy into internal energy is

$$\epsilon = 1 - \frac{(m_r + m_s)\gamma_m}{(m_r\gamma_r + m_s\gamma_s)}. \tag{2.7}$$

As can be expected a conversion of a significant fraction of the initial kinetic energy to internal energy requires that the difference in velocities between the shells will be significant $\gamma_r \gg \gamma_s$ and that the two masses will be comparable $m_r \sim m_s$. However the external shocks with $\gamma_s = 1$ cannot reproduce prompt GRBs with variable temporal structures, so it is widely believed that the internal shocks originate the GRB.

2.2.2   Physical Conditions in Relativistic Shocks

In the previous two-mass model, faster shell overtakes slower one, then the relativistic shocks are generated by their collision. Here, we explain a physical condition of the shocked material. Note that the shocks are collisionless since the energy conversion has to take place in the optically thin region and the opacity to the Coulomb collision is considerably small.

Again, let us consider a situation that a relativistic cold shell (whose internal energy is negligible compared to the rest mass) which collides with another cold shell or moves into the cold ISM. Generally, two shocks are formed:

a "forward shock" that propagates into the outer shell or ISM, and

a "reverse shock" that propagates into the inner shell,

with a contact discontinuity between the shocked material. Therefore, we consider the four regions as shown in figure 2.2:

Region 1: the unshocked outer shell or ISM,

Region 2: the shocked outer shell or ISM,

Region 3: the shocked inner shell,

Region 4: the unshocked inner shell.

The quantities of region i, n_i, p_i, and e_i (number density, pressure, and internal energy density), are measured in the rest frame of each shell, while Lorentz factors γ_i are measured by the rest frame of region 1. The unshocked inner shell is ultra-relativistic, $\gamma_4 \gg 1$ (and therefore $\gamma_3 \gg 1$). The unshocked shells or ISM are cold and the shocked matter is extremely hot, so that,

$$e_1 = p_1 = e_4 = p_4 = 0, \quad p_2 = e_2/3. \tag{2.8}$$
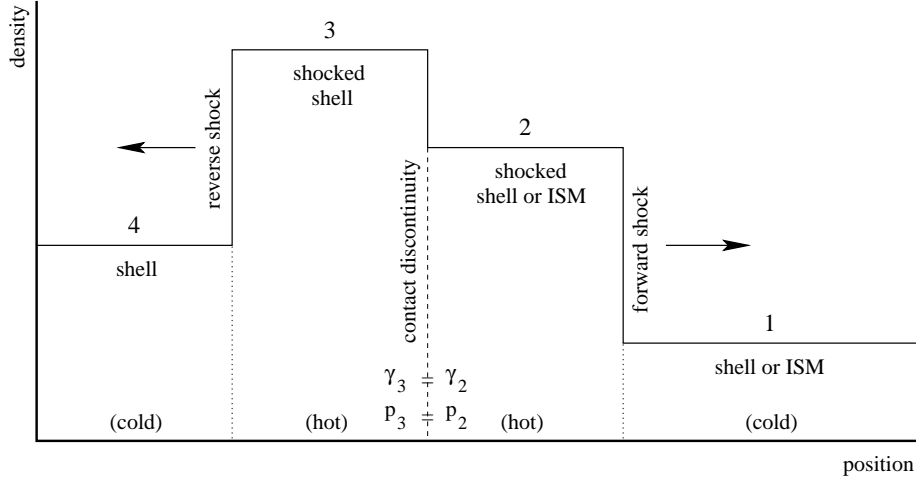
Figure 2.2: Schematic representation of shocked and unshocked region .

The equality of pressures and velocities across the contact discontinuity gives

$$e_2 = e_3, \quad \gamma_2 = \gamma_3, \tag{2.9}$$

and therefore,

$$\gamma_{34} = \gamma_{24} \sim \frac{1}{2}\Big(\frac{\gamma_2}{\gamma_4} + \frac{\gamma_4}{\gamma_2}\Big), \tag{2.10}$$

where γ_{ij} is the relative Lorentz factor between the shells in region i and j. The equations governing the strong shocks are calculated by Blandford & McKee (1976):

$$e_2/n_2 m_p c^2 = \gamma_{12} - 1 \quad , \quad n_2/n_1 = 4\gamma_{12} + 3, \tag{2.11}$$

$$e_3/n_3 m_p c^2 = \gamma_{24} - 1 \quad , \quad n_3/n_4 = 4\gamma_{24} + 3, \tag{2.12}$$

which can be written as an equation for γ_{12},

$$f \equiv n_4/n_1 = \frac{(4\gamma_{12} + 3)(\gamma_{12} - 1)}{(4\gamma_{24} + 3)(\gamma_{24} - 1)}. \tag{2.13}$$

Since $\gamma_{14} = \gamma_{12}\gamma_{24} - (\gamma_{12}^2 - 1)^{1/2}(\gamma_{24}^2 - 1)^{1/2}$, the quantity γ_{12} depends only on γ_{14} and f. Once γ_{12} is given in terms of γ_{14} and f, the energy, pressure, and density depend linearly on the third parameter n_1, from equation (2.11) and equation (2.12).

The time needed for the reverse shock to cross the inner shell with a width w is determined as

$$t_w = \frac{w}{c(\beta_4 - \beta_{rs})}, \gamma_{rs} = \gamma_2\Big(\frac{\gamma_4 + 2\gamma_2}{2\gamma_4 + \gamma_2}\Big)^{1/2}, \tag{2.14}$$

where γ_{rs} is the Lorentz factor of the reverse shock measured in the observer's frame. The time needed for the forward shock to collect a fraction γ_{14}^{-1} of the shell's rest mass is

$$t_d \sim f w/c, \tag{2.15}$$

which is the deceleration time deduced from the simple two mass model in equation (2.4).

1. Ultra-relativistic external reverse shock case: $\gamma_1 = 1$ and $\gamma_{14} \gg f^{1/2}$

   This case corresponds to the external shock [$\gamma_1 = 1$, and therefore $\gamma_{14} = \gamma_4$, $\gamma_{12} = \gamma_{13} = \gamma_3 = \gamma_2 \gg 1$, $\gamma_{24} \sim (\gamma_2/\gamma_4 + \gamma_4/\gamma_2)/2$], and the reverse shock is ultra-relativistic ($\gamma_{24} \gg 1$). The shock equations yield

   $$\gamma_{12} = \gamma_{14}^{1/2} f^{1/4}/\sqrt{2}, \quad \gamma_{24} = \gamma_{14}^{1/2} f^{-1/4}/\sqrt{2}, \tag{2.16}$$

   $$n_2 = 4\gamma_{12}n_1, \quad n_3 = 4\gamma_{24}n_4 = 4\gamma_{24}fn_1, \tag{2.17}$$

   $$e_2 = e_3 = 4\gamma_{12}^2 n_1 m_p c^2. \tag{2.18}$$

   In this case, since $\gamma_{12} \ll \gamma_{14}$, almost all of the initial kinetic energy is converted by the shocks into the internal energy after a single passage of the reverse shock through the shell. The crossing time is larger than the deceleration time.

   $$t_w = \gamma_{14} f^{1/2} w/2c \sim \gamma_{14} f^{-1/2} t_d \gg t_d. \tag{2.19}$$

   Since both shocked regions have comparable width and same internal energies $e_2 = e_3$, they release comparable amounts of energy. The outer shell mass swept by the forward shock at the time that the reverse shock crosses the shell is $\sim f^{-1/2}$ of the shell's mass.

2. Newtonian external reverse shock case: $\gamma_1 = 1$ and $\gamma_{14} \ll f^{1/2}$

   This case corresponds to the external shock [$\gamma_1 = 1$, and therefore, $\gamma_{14} = \gamma_4$, $\gamma_{12} = \gamma_{13} = \gamma_3 = \gamma_2 \gg 1$, $\gamma_{24} \sim (\gamma_2/\gamma_4 + \gamma_4/\gamma_2)/2$], and the reverse shock is Newtonian ($\gamma_{24} - 1 \ll 1$). The shock equations yield

   $$\gamma_{12} = \gamma_{14}(1 - 2\epsilon^{1/2}), \quad \gamma_{24} - 1 \sim 4\gamma_{14}^2 f^{-1}/7 \equiv 2\epsilon \ll 1, \tag{2.20}$$

   $$n_2 = 4\gamma_{12}n_1, \quad n_3 = 7n_4 = 7fn_1, \tag{2.21}$$

   $$e_2 = e_3 = 4\gamma_{12}^2 n_1 m_p c^2. \tag{2.22}$$

   The crossing time is smaller than the deceleration time.

   $$t_w = (9/14)^{1/2}\gamma_{14} f^{1/2} w/c \sim \gamma_{14} f^{-1/2} t_d \ll t_d. \tag{2.23}$$

   The reverse shock converts only a fraction $\epsilon^{1/2} \sim \gamma_{14} f^{-1/2} \ll 1$ of the kinetic energy into internal energy. The energy conversion takes place in the forward shock. The sound crossing time across the shell with the sound speed $(4p_3/3n_3 m_p)^{1/2}$ is $t_s = (3\sqrt{7}/4)\gamma_{14} f^{1/2} w/c \sim t_w \ll t_d$, so that the shell acts as a single fluid during the deceleration.

3. Internal shock case: $\gamma_1 \gg 1$ and $f \sim 1$

   This case corresponds to the internal shocks $\gamma_4 \geq \gamma_1 \gg 1$, where both shells have similar densities and the relative Lorentz factor γ_{14} is more than a few. We derive

   $$\gamma_{12} \sim \gamma_{24} \sim \frac{\gamma_1}{\sqrt{2}} \sim \sqrt{(\gamma_{14} + 1)/2} \sim \sqrt{\gamma_{14}/2}, \tag{2.24}$$

   $$n_2 = (4\gamma_{12} + 3)n_1 \sim 4\gamma_{12}n_1, \quad n_3 = 4\gamma_{24}n_4 = 4\gamma_{24}fn_1, \tag{2.25}$$

   $$e_2 = e_3 = 4\gamma_{12}^2 n_1 m_p c^2, . \tag{2.26}$$

   Since $\gamma_{rs} \sim \gamma_2 \sim 1$, the crossing time is $t_w \sim w/c \sim t_d$.

2.3 Synchrotron Emission from Relativistic Shocks

Based on the observed non-thermal spectrum, the most likely radiation process in GRBs is synchrotron emission. The parameters that determine the synchrotron emission are the magnetic field strength B and the energy distribution of accelerated electrons that is characterized by the minimal Lorentz factor $\gamma_{e,min}$ and the power-law index p. The electrons lose energy via synchrotron emission, and the critical energy $\gamma_{e,c}$ can be determined by the magnetic field strength, B, in the shocked material. The values $\gamma_{e,min}$ and $\gamma_{e,c}$ reflect the spectral break energy, such as the peak energy E_p. This is the most important key of this thesis. These parameters should be determined from the microscopic physical processes in the ultra-relativistic collisionless shocks. Although, at present, there are several attempts, it is difficult to estimate them from first principles. Instead, we define two dimensionless parameters, ϵ_B and ϵ_e, that incorporate our ignorance and uncertainties.

2.3.1 Energy Distribution of Accelerated Electrons

The dimensionless parameter ϵ_B measures the ratio of the magnetic field energy density to the total thermal energy density $e \equiv e_2$ in the shocked material, that is

$$\epsilon_B = \frac{U_B}{e} = \frac{B^2}{8\pi e_e}. \tag{2.27}$$

Let n_1 and γ_{sh} be the comoving density of unshocked material and the Lorentz factor of the shock that is measured in the rest frame of the unshocked material, respectively. Then, substituting the shock condition as already shown in Section 2.2.2, the total thermal energy is $e_2 = 4\gamma_{sh}^2 n_1 m_p c^2$, so we have

$$B = (32\pi\epsilon_B \gamma_{sh}^2 n_1 m_p c^2)^{1/2}. \tag{2.28}$$

As another parameter, we define ϵ_e that measures the fraction of $e \equiv e_2$ going into the accelerated electrons, that is,

$$\epsilon_e = \frac{U_e}{e}. \tag{2.29}$$

We generally consider the situation of $\epsilon_e \sim 1$ and $\epsilon_B \sim 0.05$ while the exact values for these two parameters have not been determined yet.

The Lorentz factor of typical electrons can be determined with ϵ_e:

$$< \gamma_e >= \frac{U_e}{4\gamma_{sh} n_1 m_e c^2} = \frac{U_e}{4\gamma_{sh}^2 n_1 m_p c^2}\frac{m_p}{m_e}\gamma_{sh} = \frac{m_p}{m_e}\epsilon_e\gamma_{sh}. \tag{2.30}$$

The electrons are assumed to be accelerated and develop a power-law distribution of Lorentz factors

$$N(\gamma_e)d\gamma_e = A\gamma_e^{-p}d\gamma_e \quad \text{for} \quad \gamma_e > \gamma_{e,min}, \tag{2.31}$$

where A is a normalization and γ_e is the electron's Lorentz factor measured in the rest frame of the shocked material. Then we can estimate the number density and the thermal energy of

the accelerated electrons:

$$n_e = \int_{\gamma_{e,min}}^{\infty} N(\gamma_e)d\gamma_e = \frac{A}{p-1}\gamma_{e,min}^{-p+1}, \tag{2.32}$$

$$U_e = \int_{\gamma_{e,min}}^{\infty} N(\gamma_e)m_e c^2 \gamma_e d\gamma_e = \frac{A}{p-2}m_e c^2 \gamma_{e,min}^{-p+2}. \tag{2.33}$$

From the above equations, a typical Lorentz factor of these electrons is given:

$$\frac{U_e}{n_e} = \frac{p-1}{p-2}m_e c^2 \gamma_{e,min}. \tag{2.34}$$

Here, n_e is the number density in the shocked region, so it is equivalent to $n_2 = 4\gamma_2 n_1$ from the shock jump condition. Using this fact, the value $\gamma_{e,min}$ is estimated as:

$$\gamma_{e,min} = \frac{p-2}{p-1}\frac{U_e}{n_2 m_e c^2} = \frac{p-2}{p-1}\frac{U_e}{4\gamma_2 n_1 m_e c^2} = \frac{p-2}{p-1} < \gamma_e >= \frac{p-2}{p-1}\frac{m_p}{m_e}\epsilon_e \gamma_{sh}. \tag{2.35}$$

2.3.2 Synchrotron Power and Synchrotron Frequency

Observed synchrotron frequency depends on γ_e and B. Since the emitting material moves with a Lorentz factor γ_E, the photons are blue shifted. The radiation power and the characteristic frequency measured by the observer are given by Rybicki & Lightman (1979):

$$P(\gamma_e)_{obs} = \frac{4}{3}\sigma_T c \gamma_e^2 U_B \gamma_E^2 \tag{2.36}$$

$$\nu(\gamma_e)_{obs} = \frac{q_e B}{2\pi m_e c}\gamma_e^2 \gamma_E, \tag{2.37}$$

where σ_T is the Thomson cross section. The synchrotron cooling time of the electron measured in the observer's frame is

$$T_{syn}(\gamma_e) = \frac{\gamma_e m_e c^2}{P(\gamma_e)_{obs}/\gamma_E^2}\gamma_E^{-1} = \frac{3m_e c}{4\sigma_T U_B \gamma_e \gamma_E}, \tag{2.38}$$

where additional factor of γ_E^{-1} comes from the Lorentz transformation.

The instantaneous synchrotron spectrum from a single electron with the energy $m_e c^2 \gamma_e$ is due to a power-law shape. The spectral power P_ν (in units of erg s^{-1}Hz^{-1}) varies as $\nu^{1/3}$ for $\nu < \nu(\gamma_e)$, and cuts off exponentially for $\nu > \nu(\gamma_e)$. The peak power occurs at $\nu(\gamma_e)$:

$$P_{\nu,max} \sim \frac{P(\gamma_e)}{\nu(\gamma_e)} = \frac{m_e c^2 \sigma_T}{3q_e}\gamma_E B, \tag{2.39}$$

and it is independent of γ_e. This electron with the energy $E(t) = m_e c^2 \gamma_e(t)$ becomes cool as it emits synchrotron photons

$$P = -\frac{dE}{dt} = -m_e c^2 \frac{d\gamma_e}{dt}. \tag{2.40}$$

Using equation (2.36)

$$\frac{d\gamma_e}{dt} = -\frac{4\sigma_T U_B \gamma_e^2(t)\gamma_E}{3m_e c}, \tag{2.41}$$

When we perform integration with the initial condition of γ_e at $t = 0$, we obtain

$$\frac{1}{\gamma_e(t)} = \frac{1}{\gamma_{e,c}(t)} + \frac{1}{\gamma_e}, \quad \text{with} \quad \gamma_{e,c}(t) = \frac{3m_e c}{4\sigma_T U_B \gamma_E t}. \tag{2.42}$$

Here, $\gamma_{e,c}$ is a critical Lorentz factor that determines whether the electrons are cooling fast or slow. In the case of $\gamma_e > \gamma_{e,c}$, the electrons are effectively cooling at the time scale of t, and rapidly achieve $\gamma_e \sim \gamma_{e,c}$. On the other hand, in the case of $\gamma_e < \gamma_{e,c}$, since radiative cooling is not efficient, the Lorentz factor of electrons remains initial value of γ_e. A detail description about the fast or the slow cooling is given in next section. As it cools, the frequency of the synchrotron emission varies as $\nu \propto \gamma_e^2$, the spectral power varies as $\nu^{-1/2}$ over the frequency range $\nu(\gamma_{e,c}) < \nu < \nu(\gamma_e)$.

The synchrotron self absorption may be important in the late time afterglow and typically in radio emission, while it is irrelevant during the prompt GRB phase. To estimate the self absorption frequency ν_a, we need the optical depth along the line of sight that is approximated as $\sim \alpha'_{\nu'} \gamma_E \Delta$, where Δ and $\alpha'_{\nu'}$ are the width of the emitting shell measured in the observer's frame and the absorption coefficient in the shocked shell frame given by

$$\alpha'_{\nu'} = \frac{p+2}{8\pi m_e \nu'^2} \int_{\gamma_{min}}^{\infty} d\gamma_e P'_{\nu',e}(\gamma_e) \frac{N(\gamma_e)}{\gamma_e}, \tag{2.43}$$

respectively. Here γ_{min} is usually $\gamma_{e,min}$ or $\gamma_{e,c}$. The self absorption frequency ν_a satisfies $\alpha'_{\nu'_0} \gamma_E \Delta \sim 1$. At the frequency below ν_a, the system is optically thick to self absorption, and the observer sees the Rayleigh-Jeans portion of the black body spectrum $P_\nu \propto \nu^2 \gamma_{typ}(\nu)$. If $\gamma_{typ}(\nu) = \gamma_{e,c}$ (or $\gamma_{e,min}$), one obtains $P_\nu \propto \nu^2$, which is different from the well known dependence $\nu^{5/2}$.

2.3.3 Integrated Synchrotron Spectrum

In order to calculate the net spectrum from a power-law distribution of electrons, we integrate over γ_e. There are two interesting cases, depending on the relation between $\gamma_{e,min}$ and $\gamma_{e,c}$.

1. Fast cooling case: $\gamma_{e,min} > \gamma_{e,c}$

   The internal shocks and early external shocks are in this regime. All electrons cool down to roughly $\gamma_{e,c}$ and the spectral power peaks at $\nu_c = \nu(\gamma_{e,c})$, which is smaller than $\nu_m = \nu(\gamma_{e,min})$. The observed spectrum is given by

$$F_\nu = F_{\nu,max} \times \begin{cases} (\nu_a/\nu_c)^{1/3}(\nu/\nu_a)^2, & (\nu < \nu_a), \\ (\nu/\nu_c)^{1/3}, & (\nu_a < \nu < \nu_c), \\ (\nu/\nu_c)^{-1/2}, & (\nu_c < \nu < \nu_m), \\ (\nu_m/\nu_c)^{-1/2}(\nu/\nu_m)^{-p/2}, & (\nu_m < \nu), \end{cases} \tag{2.44}$$

   where $F_{\nu,max}$ is the observed peak flux. Using equation (2.31), and the relation $\nu \propto \gamma_e^2$ in the cooling regime, the highest spectrum at $\nu > \nu_m$ is

$$F_\nu = N(\gamma_e) \times \gamma_e m_e c^2 \frac{d\gamma_e}{d\nu} \propto \nu^{-p/2} \tag{2.45}$$

   since electrons emit practically all their energy $\gamma_e m_e c^2$ at their synchrotron frequency.

2. Slow cooling case: $\gamma_{e,min} < \gamma_{e,c}$

   The late-time external shocks are in this regime. The flux at the observer is given by

$$F_\nu = F_{\nu,max} \times \begin{cases} (\nu_a/\nu_c)^{1/3}(\nu/\nu_a)^2, & (\nu < \nu_a), \\ (\nu/\nu_m)^{1/3}, & (\nu_a < \nu < \nu_m), \\ (\nu/\nu_m)^{-(p-1)/2}, & (\nu_m < \nu < \nu_c), \\ (\nu_c/\nu_m)^{-(p-1)/2}(\nu/\nu_c)^{-p/2}, & (\nu_c < \nu), \end{cases} \qquad (2.46)$$

where $\nu_m < \nu_c$. The spectrum at $\nu_m < \nu < \nu_c$ is from

$$F_\nu = N(\gamma_e)P(\gamma_e)\frac{d\gamma_e}{d\nu} \propto \nu^{-(p-1)/2}, \qquad (2.47)$$

where we use equation (2.31) and the relation $\nu \propto \gamma_e^2$ in the cooling regime.

The spectral shapes of above two cases are shown in figure 2.3 (upper-left and lower-left). According to equation (2.44) and equation (2.46), the spectral index β in equation (1.1) relates with the index "p" of the electron distribution.

2.3.4   Critical Radii

Let us consider where the energy conversion from the kinetic energy of the relativistic flow to the internal energy takes place. Since the observed spectrum is non-thermal, at least, kinetic energy should be converted at the larger distance than

$$R_e = \left(\frac{3\sigma_T E}{4\pi m_p c^2 \eta}\right)^{1/2} \sim 1 \times 10^{14} E_{52}^{1/2}(\eta/10^2)^{-1/2} \text{ cm}, \qquad (2.48)$$

here $\eta = E/Mc^2$ is the initial energy-to-mass ratio. This radius corresponds to the one of the matter being optically thin. The flow is characterized by the total energy E, the Lorentz factor γ, the total width Δ, and the scale length of density contrast $\delta(< \Delta)$.

Internal shocks take place when an inner shell catches up with a slower outer shell. For a fast inner shell with a Lorentz factor γ_r to overtake a slower shell with Lorentz factor γ_s running ahead by $\sim \delta$, it takes at the distance

$$R_\delta \sim \gamma^2 \delta \sim 10^{14} \; \delta_{10}\gamma_{100}^2 \text{ cm}, \qquad (2.49)$$

where $\delta_{10} = \delta/(10^{10} \text{ cm})$ and $\gamma_{100} = \gamma/100$.

Let us consider the external shock. The density of external ISM is n_{ism}, so the characteristic radius (Sedov length) where the external mass equals the mass of the shell is determined:

$$l \equiv \left(\frac{E}{n_{ism}m_p c^2}\right)^{1/3} \sim 2 \times 10^{18} \; E_{52}^{1/3}n_{ism}^{-1/3} \text{ cm}. \qquad (2.50)$$

The density ratio between the shell and ISM is given as $f = n_4/n_{ism} = l^3\gamma^{-2}R^{-2}\Delta^{-1}$ since $n_4 \sim E/(\gamma m_p c^2 R^2 \Delta\gamma)$. As the shell propagates outward, it is initially very dense and f is extremely large (more specifically $f > \gamma_{14}^2$ where $\gamma_{14} \sim \gamma_4 \sim \gamma$). The reverse shock is initially

Newtonian. Such a shock converts only a small fraction of the kinetic energy to thermal energy. As the shell propagates, f decreases like R^{-2} if the width of the shell is constant. Eventually when $f = \gamma^2$, the reverse shock becomes relativistic. This radius is given by

$$R_N = l^{3/2}/(\Delta^{1/2}\gamma^2) \sim 3 \times 10^{17} \ E_{52}^{1/2} n_{ism}^{-1/2} \Delta_{12}^{-1/2} \gamma_{100}^{-2} \ \text{cm}. \tag{2.51}$$

The question where is the kinetic energy converted depends on whether the reverse shock reaches the inner edge of the shell before or after it becomes relativistic.

There are three other important radii that should be considered. From the result of Section 2.2.2, the shock crossing time is given by $t_\Delta \sim \gamma f^{1/2}\Delta/c$, where Δ is substituted for w. Then the radius R_Δ where the reverse shock reaches the inner edge of the shell is determined by $t_\Delta \sim R_\Delta/c$, so that,

$$R_\Delta \sim l^{3/4}\Delta^{1/4} \sim 5 \times 10^{14} \ E_{52}^{1/4} n_{ism}^{-1/4} \Delta_{12}^{1/4} \ \text{cm}. \tag{2.52}$$

The second radius is R_γ where the forward shock collects an ISM mass of M/γ (a fraction γ^{-1} of the shell's mass). The initial mass of the shell is $M = E/c^2\gamma$, the above condition

$$m_p n_{ism} R_\gamma^3 = \frac{M}{\gamma} = \frac{E}{\gamma^2 c^2}. \tag{2.53}$$

Therefore we derive

$$R_\gamma \sim l\gamma^{-2/3} \sim 9 \times 10^{16} \ E_{52}^{1/3} n_{ism}^{-1/3} \gamma_{100}^{-2/3} \ \text{cm}. \tag{2.54}$$

Finally, we consider the radius $R_s^{(ext)}$ where the shell begins to spread. If the typical variation in γ is of the same order as γ, then the shell width behaves like $\Delta(R) \sim \max\{\Delta, R/\gamma^2\}$. Therefore, we derive

$$R_s^{(ext)} \sim \Delta\gamma^2 \sim 1 \times 10^{16} \ \Delta_{12}\gamma_{100}^2 \ \text{cm}. \tag{2.55}$$

The different radii are related by one dimensionless parameter:

$$\xi \ \equiv \ (l/\Delta)^{1/2}\gamma^{-4/3}, \tag{2.56}$$

$$R_s^{(ext)} \ = \ R_\Delta/\xi^{3/2} = R_\gamma/\xi^2 = R_N/\xi^3 = R_\delta/\zeta. \tag{2.57}$$

Here, $\zeta \equiv \delta/\Delta$ is the ratio δ to Δ as There are two possibilities in the external shocks.

1. Thin shell case: $\xi > 1$: $(R_s^{(ext)} < R_\Delta < R_\gamma < R_N)$
   The reverse shock remains Newtonian or mildly relativistic at best during the energy conversion, which will be completed at R_γ. However, if there are variation in the Lorentz factor γ, the shell is spreading, therefore the shell width evolves as $\Delta(R) \sim R/\gamma^2$ at $R > R_s^{(ext)}$. This effect reduces ξ, leading to $R_\Delta \sim R_\gamma \sim R_N$ with a significant energy conversion in the reverse shock as well. This means that due to the spreading, a shell which begins with $\xi > 1$ adjusts itself in order to satisfy $\xi \sim 1$.

2. Thick shell case: $\xi < 1 : (R_s^{(ext)} > R_\Delta > R_\gamma > R_N)$

   The radius $R_s^{(ext)}$ is larger than all other radii, and hence the spreading effect is unimportant. The reverse shock becomes relativistic very early, which converts very efficiently the kinetic energy of the shell to thermal energy. Each layer of the shocked shell effectively loses all its kinetic energy at once and the time scale of converting the shell's kinetic energy to thermal energy is the shell crossing time. The kinetic energy is consumed at R_Δ. At this radius R_Δ, the Lorentz factors in equation (2.16)

$$\gamma_{12} \sim \gamma\xi^{3/4} = (l/\Delta)^{3/8}, \gamma_{24} \sim \xi^{-3/4} = \gamma(l/\Delta)^{-3/8}. \tag{2.58}$$

   Note that the Lorentz factor of the shocked region in the observer's rest frame $\gamma_2 \sim \gamma_{12} \sim (l/\Delta)^{3/8}$ is independent of shell's Lorentz factor γ.

2.4   Internal Shocks – GRBs

2.4.1   Temporal Structure and Kinematic Considerations

The observed temporal structure and kinematic considerations sets a strong constraint on the energy conversion models.

1. Intrinsic duration: ΔT

   The time scale in which the central engine that produces the relativistic shells is active: $\Delta T \sim \Delta/c$. Here Δ is the width of the total relativistic flows measured in the observer's rest frame.

2. Intrinsic variability: δT

   The time scale on which the central engine varies and produces a substructures in total relativistic flows with a length of δ is $\delta T = \delta/c$.

3. Hydrodynamical time scales: T_{hydro}

   The time scale for a emitting shock with a Lorentz factor γ_E to cross the shell with the width W is $\sim 2\gamma^2 W/c$ in the shell frame. This time scale is shorten by a factor $\sim 1/2\gamma^2$ in the observer frame: $T_{hydro} \sim W/c$.

4. The angular spreading time scale: T_{ang}

   Because of the relativistic beaming effect, an observer sees up to solid angle of γ_E^{-1} from the line of sight. Two photons emitted at the same time at the radius R_E, one on the line of sight and the other at an angle of γ_E^{-1} away travel different distances to the observer. The difference lead to a delay in the arrival time by $T_{ang} \sim R_E/2\gamma_E^2 c$. Clearly this delay is relevant only if the angular width of the emitting region, $\Delta\theta$ is larger than γ_E^{-1}.

5. The cooling time scale: T_{cool}

   The synchrotron cooling time of the electron measured by an observer is $T_{cool} = e/P\gamma_E$, where e and P is an internal energy density and the power of the synchrotron radiation, respectively.

Each pulse in the prompt gamma-ray emission phase arises from the merged shell with width of W. Since the cooling time is extremely shorter than the others, the time scale of the rising and decaying part of each spike are determined by T_{hydro} and/or T_{ang}. The total duration of the GRB is equal to ΔT, and must be longer than T_{hydro} and T_{ang}.

2.4.2   Physical Condition and Emission from Internal Shocks

The condition that the internal shock occurs before the external shock is given by $\xi^{3/2} > \zeta$ from equation (2.57). Since The total duration is ΔT and the time scale of variable structures is δT, the number of pulses are roughly $\mathcal{N} = \Delta T / \delta T = 1/\zeta$. When we assume the case that the $\mathcal{N}_2 = \mathcal{N}/10^2$, we can give a restriction to the shell's Lorentz factor as

$$\gamma < 2800 \ \mathcal{N}_2^{1/2} T_{10}^{-3/8} l_{18}^{3/8} . \tag{2.59}$$

Here, $T_1 = T_{dur}/10^1 \ rms$ is the total duration of a single GRB. On the other hand, the internal shocks must occur at the optically thin radius. We can give another restriction to the Lorentz factor:

$$\gamma > \left(\frac{E\sigma}{4\pi m_p c^2 \delta^2}\right) = 130 \ T_1^{-2/5} \mathcal{N}_2^{2/5} E_{52}^{1/5} . \tag{2.60}$$

2.5   External Shocks – Afterglows

We consider the situation that the shell propagates into the ISM and sweeps up its mass. In this case, an external shock between the shell and ISM is generated by the collision, so electrons are accelerated to the relativistic velocity. As shown in the previous section, these electrons loss energy by emitting the synchrotron radiation.

We assume the shell with the rest mass of M and its Lorentz factor γ, and the initial condition of the shell as $E_0 = M_0 c^2 \gamma_0$. The shell collides with the surrounding ISM. We denote the mass of the ISM by $m(R)$ that has already collided with the shell. Then, the energy and the momentum conservation yield

$$\frac{dm}{M} = -\frac{d\gamma}{\gamma^2 - 1}, \tag{2.61}$$

$$dE = (\gamma - 1)dm. \tag{2.62}$$

Here, dE is the internal energy produced by the collision. When we define ϵ as the fraction of the shock generated thermal energy (radiation energy) to the initial kinetic energy, the incremental total mass is estimated as

$$dM = (1 - \epsilon)dE + dm = [(1 - \epsilon)\gamma + \epsilon]\left(-\frac{M d\gamma}{\gamma^2 - 1}\right). \tag{2.63}$$

Analytical solution can be given between the total mass M and the Lorentz factor γ:

$$\frac{(\gamma - 1)(\gamma + 1)^{1-2\epsilon}}{(\gamma_0 - 1)(\gamma_0 + 1)^{1-2\epsilon}} = \left(\frac{M}{M_0}\right)^{-2}, \tag{2.64}$$

and the relation between $m(R)$ and γ:

$$\frac{m(R)}{M_0} = -(\gamma_0 - 1)^{1/2}(\gamma_0 + 1)^{1/2-\epsilon} \int_{\gamma_0}^{\gamma} (\gamma' - 1)^{-3/2}(\gamma' + 1)^{-3/2+\epsilon} d\gamma'. \qquad (2.65)$$

These relations completely describe the hydrodynamical evolution of the shell.

We can estimate the ISM mass $m(R)$ that should be swept to get significant deceleration. Solving equation (2.65) with an upper limit $\gamma_0/2$ of the integration within the condition of $\gamma_0 \gg 1$, we obtain a well-known result: a mass $m \sim M_0/(2\gamma_0)$ is required to reach $\gamma = \gamma_0/2$. This result is independent of the cooling parameter ϵ. On the other hand, assuming the case of $\gamma_0 \ll \gamma \ll 1$, we can obtain another simple solution:

$$m(R) = \frac{M_0}{(2 - \epsilon)\gamma_0}\left(\frac{\gamma}{\gamma_0}\right)^{-2+\epsilon}. \qquad (2.66)$$

When we define a number density of the ISM as n_{ism}, the total mass swept till the radius R is

$$m(R) = \frac{4\pi}{3}R^3 n_{ism} m_p, \qquad (2.67)$$

so the evolution of the Lorentz factor is $\gamma \propto R^{-3/(2-\epsilon)}$. Adopting the initial condition of $E_0 = M_0 c^2 \gamma_0$ to the equation (2.66), we obtain the equation:

$$E_0 = \frac{4\pi}{3}R^3 n_{ism} m_p c^2 (2 - \epsilon)\gamma^{-2+\epsilon}\gamma_0^{\epsilon}. \qquad (2.68)$$

In the case of adiabatic expansion ($\epsilon = 0$) [1], equation (2.68) is

$$E_0 = \frac{8\pi}{3}R^3 n_{ism} m_p c^2 \gamma^2, \qquad (2.69)$$

so the Lorentz factor is evolved as $\gamma \propto R^{-3/2}$. On the other hand, fully radiative case ($\epsilon = 1$), equation (2.68) is

$$E_0 = \frac{4\pi}{3}R^3 n_{ism} m_p c^2 \gamma\gamma_0, \qquad (2.70)$$

so $\gamma \propto R^{-3}$. For the purpose of considering the time dependency of the Lorentz factor and the radius, we consider the observation time [2]:

$$t_{obs} = \frac{R}{2\gamma^2 c}. \qquad (2.71)$$

Then the equation (2.69) and equation (2.70) are rewritten:

$$R(t) = \begin{cases} (3E_0 t/4\pi n_{ism} m_p c)^{1/4} & \text{adiabatic case,} \\ (2ct/L)^{1/7} L, & \text{radiative case,} \end{cases} \qquad (2.72)$$

and

$$\gamma(t) = \begin{cases} (3E_0/64\pi n_{ism} m_p c^5 t^3)^{1/8} & \text{adiabatic case,} \\ (2ct/L)^{-3/7} & \text{radiative case.} \end{cases} \qquad (2.73)$$

Here, $l = (3E_0/4\pi n_{ISM} m_p c^2 \gamma_0)^{1/3}$ is the Sedov Length of which describes the radius where the external mass equals the mass of the shell.

---

[1] In the afterglow phase we generally consider the adiabatic case.

[2] the above time scale is valid only for emission along the line of sight from a shell that propagates with a constant velocity. $dt_{obs} = dR/2\gamma^2 c$ may be more reasonable formula.

2.6 Synchrotron Emission from a Decelerating Shell

It is important to consider an instantaneous spectrum of the synchrotron emission from a decelerating shell for the purpose of comparing the observational property. Assuming a relativistic shell propagating into the flat-isotropic ISM, we consider two limiting case, i.e. a completely adiabatic case and a fully radiative case.

As already shown in Section 2.3, the shape of the instantaneous synchrotron spectrum is determined by cooling frequency $\nu_c \equiv \nu(\gamma_{e,c})$ and typical frequency $\nu_m \equiv \nu(\gamma_{e,min})$. Hereafter, we assume that the spectral shape does not change within the observation time interval. In the fully adiabatic case, using the equation (2.72) and (2.73), the shock condition of equation (2.16), and the synchrotron frequency equation (2.37):

$$\nu_c = 2.7 \times 10^{12} \epsilon_B^{-3/2} E_{52}^{-1/2} n_1^{-1} t_d^{-1/2} \text{ Hz}, \tag{2.74}$$

$$\nu_m = 5.7 \times 10^{14} \epsilon_B^{1/2} \epsilon_e^2 E_{52}^{1/2} t_d^{-3/2} \text{ Hz}, \tag{2.75}$$

$$F_{\nu,max} = 1.1 \times 10^5 \epsilon_B^{1/2} E_{52} n_1^{1/2} D_{28}^{-2} \text{ } \mu\text{J}. \tag{2.76}$$

On the other hand, in the fully radiative case:

$$\nu_c = 1.3 \times 10^{13} \epsilon_B^{-3/2} E_{52}^{-4/7} n_1^{-13/14} \gamma_2^{4/7} t_d^{-2/7} \text{ Hz}, \tag{2.77}$$

$$\nu_m = 1.2 \times 10^{14} \epsilon_B^{1/2} \epsilon_e^2 E_{52}^{4/7} n_1^{-1/14} \gamma_2^{-4/7} t_d^{-12/7} \text{ Hz}, \tag{2.78}$$

$$F_{\nu,max} = 4.5 \times 10^3 \epsilon_B^{1/2} E_{52}^{8/7} n_1^{5/14} \gamma_2^{-8/7} D_{28}^{-2} t_d^{-3/7} \text{ } \mu\text{J}. \tag{2.79}$$

Since we obtain the time dependency of ν_m, ν_c and $F_{\nu,max}$, we can also describe lightcurves at a given frequency. In both the adiabatic and radiative case, ν_m decrease more rapidly with time than ν_c. Therefore at sufficiently early times we have $\nu_m > \nu_c$ (fast cooling). At late times we have $\nu_m < \nu_c$ (fast cooling). The transition between the two occurs when $\nu_m = \nu_c$ at t_{fs}. At $t = t_{fs}$, the spectrum changes from fast cooling to slow cooling (from upper-left to lower-left in figure 2.3).

Let us consider the fixed frequency $\nu = \nu_{15}/10^{15}$ Hz, from equation (2.74) and (2.75) for adiabatic case or equation (2.77) and (2.78) for radiative case, we can see two critical times, t_c and t_m, when the break frequencies, ν_c and ν_m, cross the observed frequency ν:

$$t_c = \begin{cases} 7.3 \times 10^{-6} \ \epsilon_B^{-3} E_{52}^{-1} n_1^{-2} \nu_{15}^{-2} \text{ days}, & \text{adiabatic}, \\ 2.7 \times 10^{-7} \ \epsilon_B^{-21/4} E_{52}^{-2} n_1^{-13/4} \gamma_2^2 \nu_{15}^{-7/2} \text{ days}, & \text{radiative}. \end{cases} \tag{2.80}$$

$$t_m = \begin{cases} 0.69 \ \epsilon_B^{1/3} \epsilon_e^{4/3} E_{52}^{1/3} \nu_{15}^{-2/3} \text{ days}, & \text{adiabatic}, \\ 0.29 \ \epsilon_B^{7/24} \epsilon_e^{7/6} E_{52}^{1/3} n_1^{-1/24} \gamma_2^{-1/3} \nu_{15}^{-7/12} \text{ days}, & \text{radiative}. \end{cases} \tag{2.81}$$

There are only two orders among t_c, t_m and t_{fs}, i.e. $t_{fs} \geq t_m \geq t_c$ and $t_{fs} \leq t_m \leq t_c$. Then, we define the critical frequency, $\nu_0 \equiv \nu_c(t_{fs}) = \nu_m(t_{fs})$:

$$\nu_0 = \begin{cases} 1.8 \times 10^{11} \ \epsilon_B^{-5/2} \epsilon_e^{-1} E_{52}^{-1} n_1^{-3/2} \text{ Hz}, & \text{adiabatic}, \\ 8.5 \times 10^{12} \ \epsilon_B^{-19/10} \epsilon_e^{-2/5} E_{52}^{-4/5} \gamma_2^{4/5} n_1^{-11/10} \text{ Hz}, & \text{radiative}. \end{cases} \tag{2.82}$$
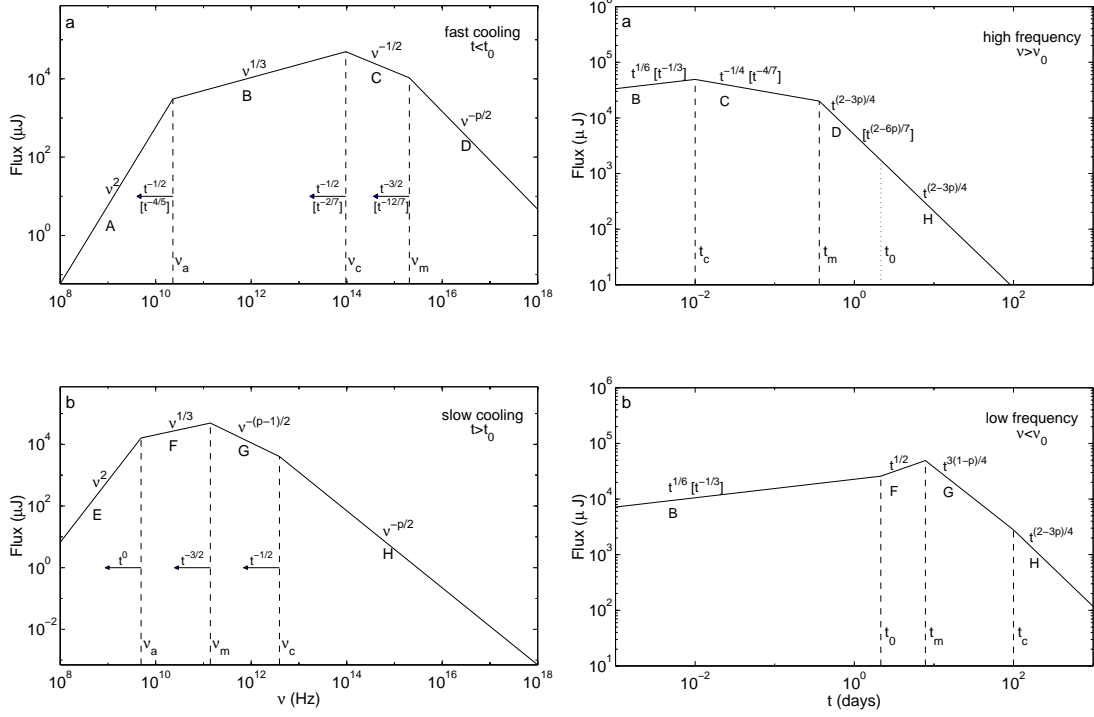
Figure 2.3: Theoretical synchrotron spectrum from a relativistic shock with a power-law distribution of electron energy.

In the case of $\nu > \nu_0(t_{fs} \geq t_m \geq t_c)$, the corresponding lightcurve is called *high-frequency lightcurve*, and one of $\nu < \nu_0(t_{fs} \leq t_m \leq t_c)$ is *low-frequency lightcurve*. As shown in equation (2.80), however, t_c is extremely small value, so the high-frequency case may appear only in the prompt GRB phase even if such a case is realized. The time dependency of the flux is:

$$F_\nu \propto \begin{cases} t^{1/6}, & t \leq t_c, \\ t^{-1/4}, & t_c \leq t \leq t_m, \\ t^{(2-3p)/4}, & t_m \leq t \leq t_0, \\ t^{(2-3p)/4}, & t_0 \leq t. \end{cases} \qquad (2.83)$$

$$F_\nu \propto \begin{cases} t^{1/6}, & t \leq t_0, \\ t^{1/2}, & t_0 \leq t \leq t_m, \\ t^{3(1-p)/4}, & t_m \leq t \leq t_c, \\ t^{(2-3p)/4}, & t_c \leq t. \end{cases} \qquad (2.84)$$

We show each lightcurve in figure 2.3 (upper-right and lower-right). As shown in the figure, there are four phases in lightcurve.

Chapter 3

Instruments
$-$ *Compton Gamma-Ray Observatory* $-$

We use the *CGRO* data to study the spectral property of the prompt emission of GRBs and the GRB formation rate at the early universe. In this chapter, we introduce the properties of detectors aboard the Compton Gamma Ray Observatory (*CGRO*). The large portion of descriptions, figures, and tables are referred to the *CGRO* web page (http://cossc.gsfc.nasa.gov/cossc/).

3.1   *CGRO* Overview

The *CGRO* satellite was launched on April 5, 1991 from the Kennedy Space Center on board the Space Shuttle Atlantis. The *CGRO* was successfully deployed on April 7, 1991 at an orbital altitude of 450 km with an orbital inclination angle of 28.5 degrees respecting to the Earth's equator. The weight of the spacecraft is 17 ton which is the most massive scientific satellite ever launched by the space shuttle. It is a sophisticated satellite observatory dedicated to observing the high-energy universe. *CGRO* carries a collection of four instruments which together can detect an unprecedented broad range of gamma-rays. These instruments are the Burst And Transient Source Experiment (*BATSE*), the Oriented Scintillation Spectrometer Experiment (*OSSE*), the Imaging Compton Telescope (*COMPTEL*), and the Energetic Gamma Ray Experiment Telescope (*EGRET*), respectively, and they are arranged as shown in figure 3.1. The combination of these instruments can detect photon energies from 20 keV to more than 30 GeV.

3.2   *BATSE* (Burst and Transient Spectrometer Experiment)

3.2.1   Detector Configuration

The *BATSE* consist of eight uncollimated detector modules arranged on the corners of the *CGRO* satellite to provide the maximum unobstructed view of the celestial sphere. As shown in figure 3.2, each detector module contains two NaI(Tl) scintillation detectors: a Large-Area Detector (LAD), optimized for sensitivity and directional response, and a spectroscopy detector (SD) optimized for broad energy coverage and energy resolution. The eight planes of the *LADs* are parallel to the eight faces of a regular octahedron, with the orthogonal primary axes of the octahedron aligned with the coordinate axes of the *CGRO* spacecraft.
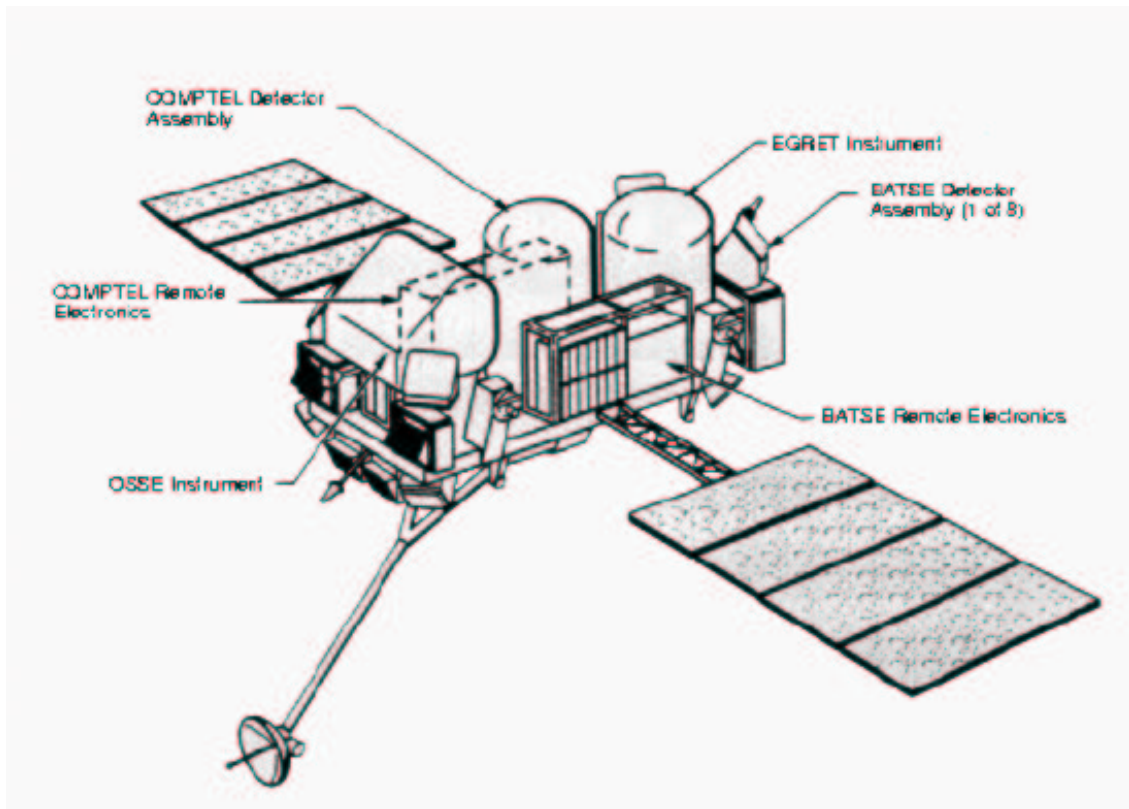
Figure 3.1: The schematic view of the *CGRO* satellite.
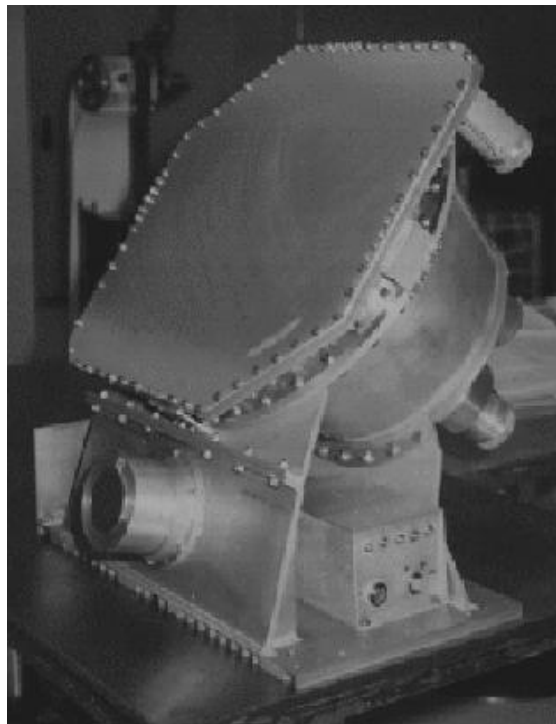
Figure 3.2: One of the eight identically configured *BATSE* detector modules. Each module contains a Large Area Detector (LAD) and a Spectroscopy Detector (SD).

3.2.2   LAD (Large Area Detector)

The LAD detector is a disk of NaI(Tl) scintillation crystal with 20 inches in diameter and one-half inch in thick, mounted on a three-quarter inch layer of quartz. The large diameter-to-thickness ratio of the scintillation crystal produces a detector angular response similar to that of a cosine function at low energies. This is because the crystal is opaque to the low-energy radiation ($\sim 100\%$ absorbed) and the surface area decreases with $\cos\theta$, where θ is an angle measured from the vertical axis of the detector surface. At energies above 300 keV, the angular response is flatter than a cosine because the photo-ionization efficiency is a function of detector thickness.

A light collector housing on each detector brings the scintillation light into three 5-inch diameter photo-multiplier tubes (PMTs). The signals from the three tubes are summed at the detector. A quarter-inch plastic scintillation detector in front of the LAD is used as an anti-coincidence shield to reduce the background due to charged particles. A thin lead and tin shield inside the light collector housing reduces the amount of background and scattered radiation entering the back side.

3.2.3   SD (Spectroscopy Detector)

The spectroscopy detector is an uncollimated NaI(Tl) scintillation detector 5 inches in diameter and 3 inches in thick. A single 5 inch photo-multiplier tube is directly coupled to the scintillation detector window. The housing of the PMT has a passive lead/tin shield similar to that of the LADs. The crystal housing has a 3-inch diameter 0.05-inch thickness beryllium window on its front face in order to provide high efficiency down to 10 keV for exposures near detector normal. The axis of symmetry of an SD is offset from by 19 degrees from the LAD axis for mechanical reasons. This offset is toward the spacecraft x-y plane.

3.2.4   CEU (Central Electronics Unit)

Each of the eight *BATSE* detector modules sends data to the Central Electronics Unit (CEU). The CEU contains hardware and software that accumulates the data into several large RAM memory buffers. Extensive use of commandable parameters, plus the capability to reprogram the flight software, insures that *BATSE* will have the flexibility to respond to unforeseen conditions in orbit or newly discovered gamma-ray phenomena. Signals from the pulse-height converters are used to construct 128-channel spectra from the LADs and 256-channel spectra from the SDs. Each of the spectra are subdivided into ranges with different dispersions to increase the dynamic range and to efficiently use the available telemetry space. These energy channels are also mapped into 16 coarse energy channels using programmable lookup tables, one for the LADs and one for the SDs. This permits a tradeoff of time resolution for energy resolution in several of the data types. Discriminator events are accumulated in the hardware every 64 ms. The CEU hardware constructs various data types from the discriminators, 16-channel, 128-channel, and 256-channel spectral data. The CEU produces data for telemetry at a uniform rate of one packet every 2.048 seconds. Each of these packets contains LAD and SD discriminator rates, 16-channel LAD spectra, and housekeeping information.

3.2.5   Burst Determination and Data Storing

BATSE detects GRBs on-board when the count rates of each of the eight LADs is significantly greater than the background level on each of three time scales: 64 ms, 256 ms, and 1024 ms. The discriminator rates in channels 2 and 3 (approximately 60 to 325 keV) are used. The background rate is determined for each detector over a time-interval of 17.4 sec. The statistical significance required for a burst trigger is set separately for each of the three time scales, with a quantization of 0.0625s. At least two detectors must exceed threshold ($\sim 5.5\ \sigma$) for a burst trigger to occur.

When a GRB is detected, the CEU enters a fast data acquisition mode and rapidly stores a variety of data types into memory. Over a interval of 45 to 105 minutes (depending on burst intensity) the normally scheduled output of pulsar data and high resolution spectra is suspended, and the collected burst data is read out in the variable portion of the data packets. While the burst memories are being telemetered, the trigger thresholds are temporarily revised to values corresponding to the maximum rates detected during the burst. Thus, a stronger burst will terminate the readout of a weaker burst and overwrite the burst memories. The data available from a overwritten burst is timing dependent, but includes at a minimum the 64 ms resolution discriminator data (DISCSC).

3.2.6   System Performances of *BATSE*

The system performances of *BATSE* are summarized in table 3.1. The burst sensitivity is 3×10^{-8} ergs/cm^2 for 1 sec duration burst. The burst location is determined by comparing count rates among separate detectors. Significant corrections are needed to account for the effects of atmospheric scattering. The burst location accuracy is estimated to be approximately 4 degrees for strong bursts, being limited by systematic errors. This estimate is based on the computed location of solar flares and from gamma-ray bursts located by the current interplanetary network (IPN).

As shown in table 3.1, the effective area of SD detectors is only 6% of that of LAD detectors while the energy coverage of SD detectors is wider than LAD's one. Since the number of high energy photons, such as a few MeV, are intrinsically small, SD detectors are not useful for dim GRBs because of its small effective area. Moreover the wide energy range is covered by several SD detectors, we have to take into account systematic errors among them, but it is highly depend on the burst location and the spectral parameters. On the other hand, single LAD detector can cover the energy range of 20–1900 keV, so the data of LAD detectors are usually analyzed. In this thesis we try to perform time resolved spectral analysis and investigate a properties of continuum spectra. Therefore we prefer to use the data set of LAD detectors in view of photon counting.

3.2.7   Trigger and Exposure Efficiency

BATSE will generate a burst trigger if the count rate in two or more detectors exceeds a threshold specified in units of standard deviations above background (nominally 5.5 σ). The

Description	LAD	SD
Number of Detectors	8	8
Field of View	Full Sky	Full Sky
Sensitive Area	2025 cm^2/LAD	127 cm^2/SD
Energy Range	20–1900 keV	10–10^5 keV

Table 3.1: The Characteristics of *BATSE* instrument.

rates are tested on three time scales: 64 msec, 256 msec and 1024 msec. The energy range is nominally 50 keV to 300 keV. These efficiencies apply only to the nominal thresholds and energy range. A history of the thresholds and energy range settings is provided in table 3.2. The threshold in flux units depends on the background rate and the sky location relative to the detector normals. The following table gives the efficiency for generating a burst trigger as a function of peak flux on each of the three trigger time scales. An efficiency of 100trigger if it is above the horizon and burst triggering is enabled.

The fraction of the time that a burst at a particular point on the sky is restricted by the earth blockage, SAA (South Atlantic Anomaly) passages, times when the burst trigger is disabled, and times when a burst readout is in progress. According to the 4B catalogue of *BATSE* , the average fraction of the sky coverage is 0.483.

64 ms		256 ms		1024 ms	
Threshold (ph/cm^2 sec)	Efficiency (%)	Threshold (ph/cm^2 sec)	Efficiency (%)	Threshold (ph/cm^2 sec)	Efficiency (%)
0.798	0.525	0.399	0.374	0.200	0.345
0.825	1.126	0.412	0.962	0.206	0.874
0.854	2.659	0.427	2.515	0.214	2.282
0.886	7.692	0.443	7.510	0.221	6.864
0.921	14.102	0.461	13.807	0.230	12.464
0.960	22.307	0.480	21.900	0.240	19.757
1.003	30.268	0.502	29.879	0.251	26.950
1.051	39.003	0.526	38.654	0.263	35.085
1.106	48.173	0.553	47.720	0.276	43.495
1.168	57.535	0.584	57.144	0.292	52.898
1.240	67.035	0.620	66.693	0.310	62.781
1.324	76.202	0.662	76.024	0.331	72.333
1.424	84.271	0.712	84.092	0.356	80.937
1.546	88.856	0.773	88.775	0.386	86.426
1.696	92.777	0.848	92.696	0.424	91.100
1.890	96.059	0.945	96.012	0.473	95.123
2.152	98.886	1.076	98.857	0.538	98.281
2.527	99.951	1.263	99.944	0.632	99.696
3.124	99.996	1.562	99.996	0.781	99.988
6.247	100.000	3.124	100.000	1.562	100.000

Table 3.2: *BATSE* trigger efficiency.

3.3   BATSE Data Types

Every day the BATSE data packets for the previous day are electronically transmitted to MSFC. This day's worth of data is unpacked and sorted into a group of files called a Daily Data Set. After a set of routine analyses are performed upon the Daily Data Set it is archived.

The data within the Daily Data Set can be grouped into three classes; burst data, scheduled data, and background data. The high time resolution burst data is gathered when a GRB, solar flare, or other event meets the BATSE burst trigger condition. The scheduled data is available from orbits during which no burst trigger occurred. It consists of high resolution spectra and data from the on-board folding of pulsars. Its content is flexible and needs to be pre-planned. The background data consists of discriminator rates and medium resolution LAD spectra that are collected continuously. In this thesis we use only the burst data, so we summarized several data-types categorized in the class in table 3.3.

Data Type	Detectors	Energy Channel	Time Resolution
DISCSC	2-4 LADs	4	64 ms
PREB	8 LADs	4	64 ms
DISCLB	8 LADs	4	1.024 s
TTE	2-4 LADs	4	2 ms
STTE	2-4 SDs	256	128 ms
TTS	2-4 LADs	4	2 ms
MER	2-4 LADs	16	16-64 ms
HERB	4 LADs	128	64 ms
SHERB	4 SDs	256	128 ms

Table 3.3: Data Types of BATSE detector.

1. DISCSC: The output of Discriminator Science Data (DISCSC) begins immediately after a burst trigger and continues for the whole burst acquisition. DISCSC consist of 64 ms discriminator data summed from each of the LAD's that were triggered by the burst.

2. PREB: The Pre-Burst (PREB) data consists of discriminator counts from the eight LADS immediately before a burst trigger. In the normal operating mode the LAD discriminator rates are stored in a ring buffer. This makes available the 64 ms resolution LAD discriminator rates for the 2.048 seconds immediately prior to a burst trigger.

3. DISCLB: Discriminator data from the eight LAD's collected to compensate for the loss of DISCSC and DISCLA data during telemetry gaps. This consists of 16.384 s of pre-trigger data with 2.048 second resolution and 49.154 s of post-trigger data with 1.024 second resolution.

4. TTE: Time-Tagged Event (TTE) data provide the time of occurrence, discriminator channel, and detector number of 32,768 individual LAD events. The time resolution is 2 ms. The memory is organized as a continually running ring buffer. When the burst trigger

occurs, data are entered only from the LADs that trigger the burst. Accumulation of data halts after three-fourths of the memory fills. The other one-fourth of the memory then contains data from all eight LADs immediately prior to the trigger.

5. STTE: Spectroscopy Time-tagged Event (STTE) data provide similar data for the SDs with a time resolution of 128 s. There are four memory buffers of 16,384 event capacity each. A selectable subset (currently two) run continually and the others are filled successively if a burst occurs. With the current settings the STTE data available from before the burst trigger can range from 16,384 to 32768 events. Normally the pre-trigger STTE includes all eight detectors, however if a subset of SD detectors were being used for on-board pulsar folding when the burst occurred, only data from this subset are included. The post STTE data are from the triggered detectors.

6. TTS: The Time-to-Spill (TTS) data provide the time to accumulate a specified number of discriminator events from the LADs. The number of events is nominally 64, but can also be commanded to either 16 or 256. Discriminator events are summed from those detectors that trigger the burst. The time resolution is 1 s for the shortest times, but increases at longer times to allow a satisfactory dynamic range. Each discriminator energy channel operates independently and has a capacity for 16,384 entries.

7. MER: Medium Energy Resolution (MER) data consist of 4,096 16-channel spectra summed from triggered detectors. The nominal accumulation time is 16 ms for 2,048 spectra, followed by 64 ms for the remaining 2,048 spectra for a total duration of about 164 s. These accumulation times are commandable software parameters.

8. HERB: The High Energy Resolution Burst (HERB) data consist of 128 separate HER spectra stored during a burst. The selection of detectors and storage times is under software control. Nominally, the accumulation time will be rate-dependent. Spectra from four LADs will be stored, with the more brightly illuminated detectors stored more often.

9. SHERB: The Spectroscopy High Energy Resolution Burst (SHERB) data provide the same function for the SDs, the only difference being that a total of 192 256-channel spectra can be stored.

In this thesis we use DISCSC and HERB data for temporal and spectral analysis, respectively. A background spectrum is extracted from the same data set with each GRB event.

3.4 Background Spectrum

A background rate in gamma-ray band shows high variability, and it is depend on the satellite orbit and its position. Generally, a gamma-ray source photons are remarkably dominated by background particles and photons. However the prompt gamma-ray emissions of GRBs are much brighter than the background rate, so we can perform spectral analyses for them with high signal-to-noise ratio. Moreover, since the durations of GRBs are very short (~ 20 sec), the

background variability in such a short time scale is not so significant when we perform spectral analyses.

In figure 3.3, we show examples of background spectra. The left panel contains two background spectra at different epoch 1991 and 2000, and we can recognize some differences between both spectral shape. This fact caused by the satellite's orbit and the internal background of the NaI material activated by the charged particles (mainly proton). For example, a spectral feature at ~ 511 keV comes from the activated ^{22}Na (generated by the action: ^{23}Na$(p, pn)^{22}$Na) in NaI scintillator. In the right panel of figure 3.3, we show background spectra extracted from same data set. The black and red points are correspond to the background spectra before and after GRB, respectively. We can recognize that the spectral shape and the background rate is not changed, so we use an average background spectrum in both before and after the burst[1].
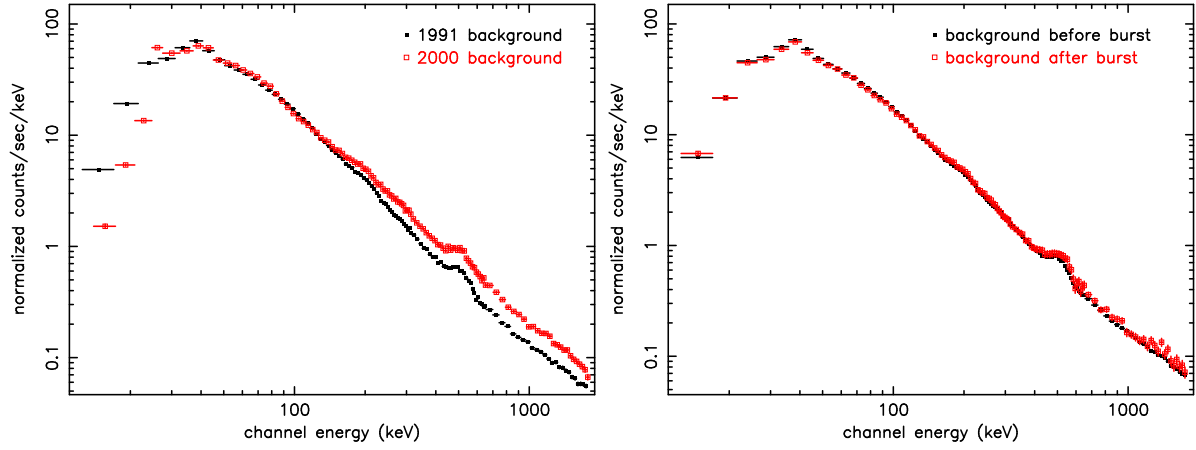
Figure 3.3: Example of the background spectra of BATSE detector. The left panel shows two background spectra in different epochs 1991 (black) and 2000 (red). The right panel shows two background spectra, before and after GRB, extracted from same data set. There is no significant discrepancy in two spectra.

---

[1] We use the background data pre- or past-GRB epoch when we cannot obtain stable background spectra.
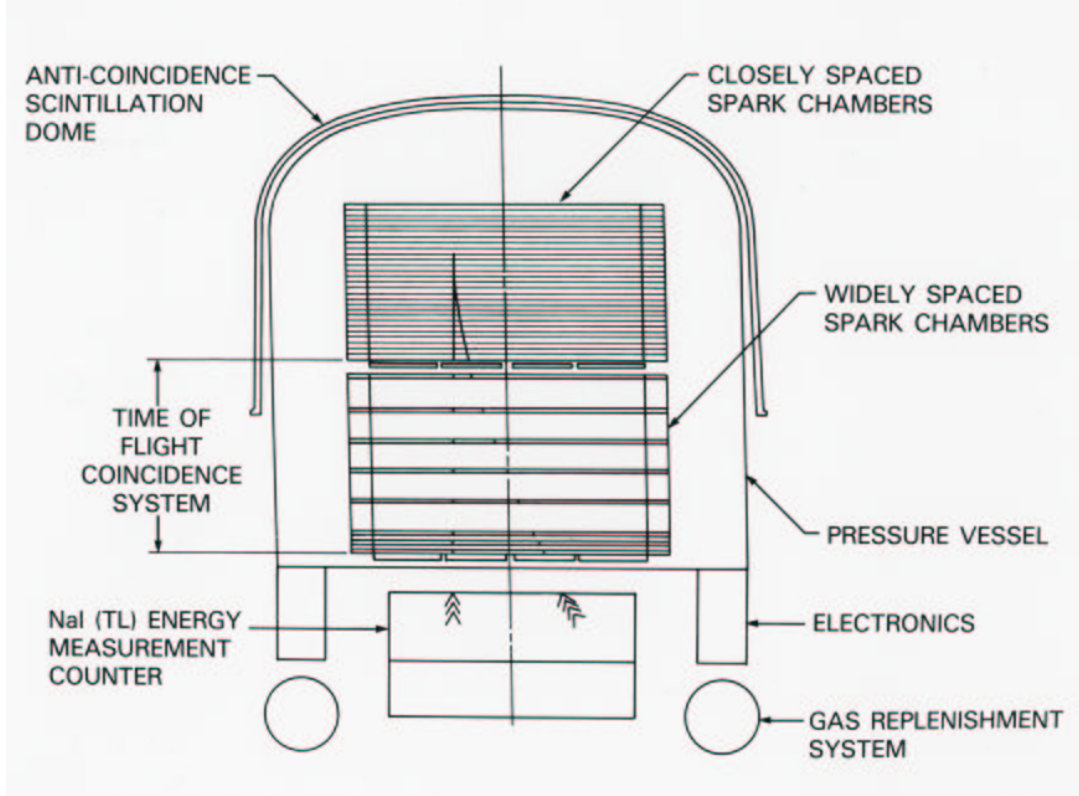
Figure 3.4: The detector configurations of *EGRET* .

3.5 Other Instruments

The *CGRO* satellite contains the other three detectors. Although we do not use these data in this thesis, we introduce the detector performance briefly.

3.5.1 *EGRET* (Energetic Gamma-Ray Experiment Telescope)

EGRET detected gamma-rays in the 20 MeV–30 GeV range, using a spark chamber for direction measurement and a NaI(Tl) calorimeter, the Total Absorption Shower Counter (TASC), for energy measurement (figure 3.4). The spark chamber had interleaved tantalum foils and tracking layers. A fraction of the incoming gamma rays (about 35 % above 200 MeV) interacted in the foils to produce high-energy positron-electron pairs, which were tracked through subsequent layers of the spark chamber and absorbed by the TASC at the bottom of the tracker. Reconstruction of the energies and directions of the positron-electron pairs yielded the energies and directions of the incident photons. *EGRET* had a very large field of view, approximately 80 degrees in diameter. The bright gamma-ray sources can be localized with approximately 10' accuracy in on-axis of *EGRET* . The energy resolution of *EGRET* was 20–25 % over most of its range of sensitivity.
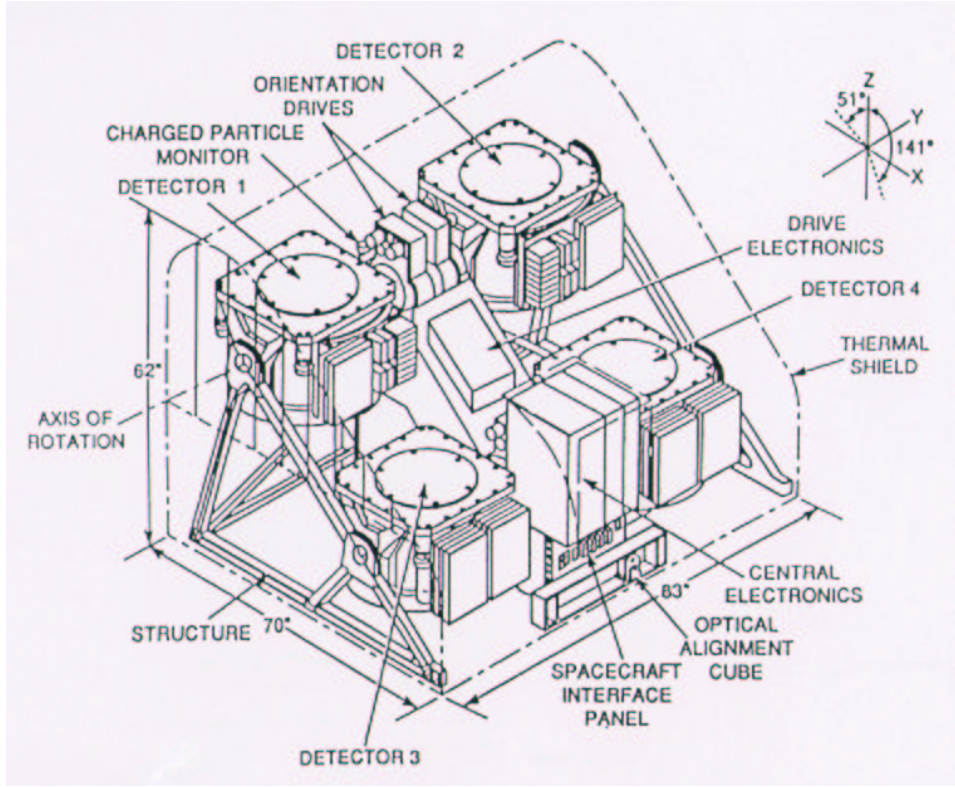
Figure 3.5: The detector configurations of *OSSE* .

3.5.2   *OSSE* (Oriented Scintillation Spectrometer Experiment)

The *OSSE* has been designed to undertake comprehensive observations of astrophysical sources in the 0.05–10 MeV energy range. Secondary capabilities for gamma-ray and neutron observations above 10 MeV have also been included, principally for solar flare studies. The use of NaI(Tl) scintillation techniques provides large area and high sensitivity in the 0.05–10 MeV region.

As shown in figure 3.5, the primary element of each detector system is the NaI(Tl) portion of a 330-mm diameter NaI(Tl)–CsI(Na) phoswich consisting of a 102-mm thick NaI(Tl) crystal optically coupled to a 76-mm thick CsI(Na) crystal. Each phoswich is viewed from the CsI face by seven 89-mm diameter PMTs, providing an energy resolution of 8 % at 0.662 MeV. Utilizing the differing scintillation decay time constants of NaI(Tl) and CsI(Na), the detector event processing electronics incorporates pulse-shape analysis for the discrimination of events occurring in the NaI crystal from those occurring in the CsI, allowing the CsI portion of the phoswich to act as anti-coincidence shielding for the NaI portion. A tungsten alloy passive slat collimator, located directly above the NaI portion of each phoswich, defines the gamma-ray aperture of the phoswich detector, providing a 3.8 × 11.4 FWHM rectangular field-of-view throughout the 0.1–10 MeV energy range.
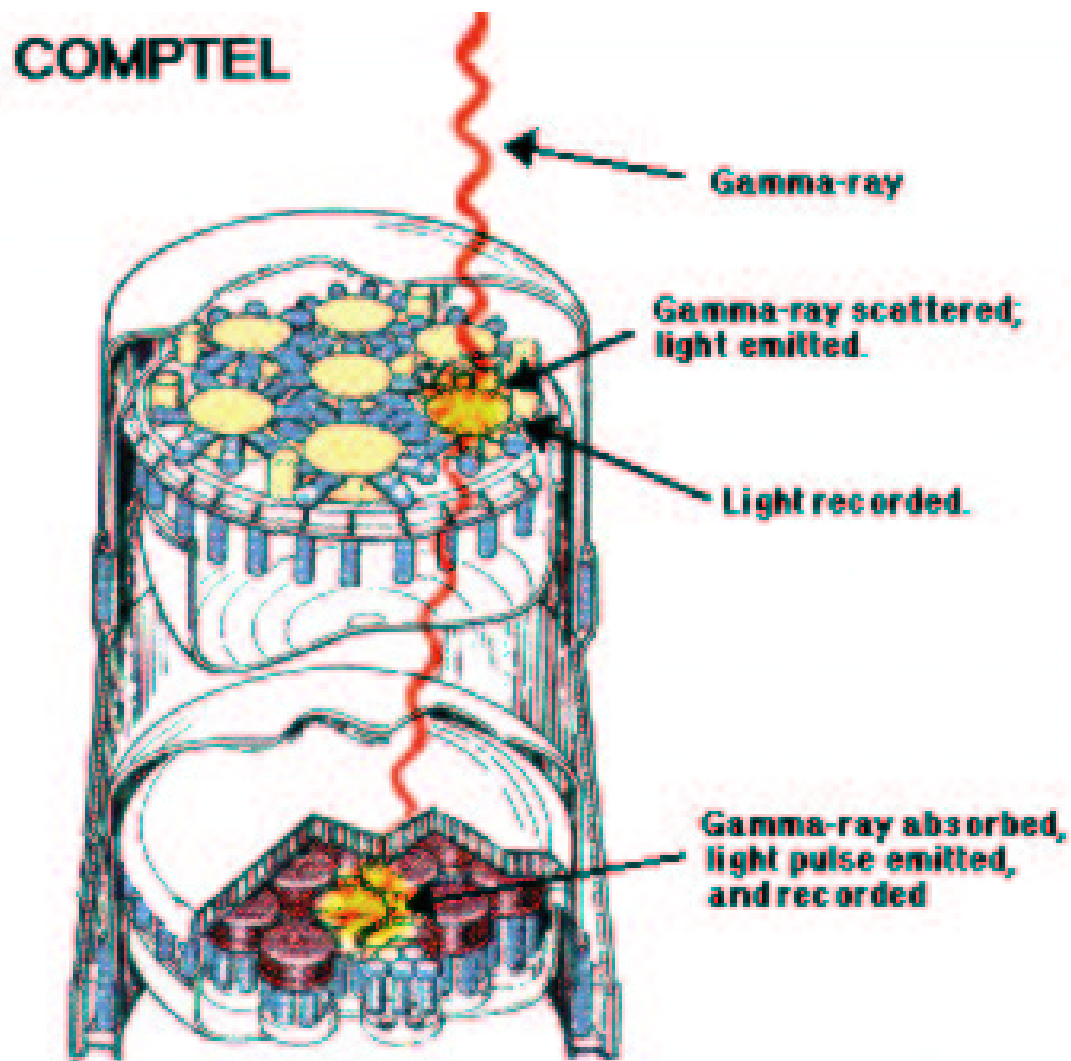
Figure 3.6: The detector configuration of *COMPTEL* .

3.5.3   *COMPTEL* (Compton Telescope)

The *COMPTEL* is capable of imaging 1 steradian of the sky in the 0.8-30 MeV range. As shown in figure 3.6, it consists of two detector arrays. In the upper one, a liquid scintillator (NE 213A) is used, and in the lower, NaI crystals. Gamma-rays are detected by two successive interactions: an incident cosmic gamma-ray is first Compton scattered in the upper detector, then totally absorbed in the lower. The locations of the interactions and energy losses in both detectors are measured. The accuracy in the measurement of these parameters determines the overall energy and angular resolution of the telescope. Solving the Compton kinematics, we can reconstruct sky images over a wide field of view with a resolution of a few degrees. The geometric area is 4188 cm^2 and 8620 cm^2 for the upper and the lower detector, respectively. The total effective area is 20–50 cm^2.

Chapter 4

Data Analysis

In this chapter, we investigate spectral and temporal properties of long duration GRBs with $T_{90} > 2$ sec. We used 10 GRBs with known redshifts (970508, 970828, 971214, 980425, 980703, 990123, 990506, 990510, 991216 and 000131) and 2 GRBs with photometrically measured redshifts (980326 and 980329). Basic informations of our samples are summarized in table 4.1. Since the *BATSE* detectors are not sensitive for soft gamma-ray photons below 30 keV, we do not deal with X-ray Flash and X-ray Rich GRBs (Sakamoto, 2004).

First, we investigate spectral properties averaged over the entire duration of T_{90} for each event. We suggest a strong correlation between the spectral peak energy E_p and the 1 sec peak luminosity at the rest frame of GRBs. Next, we perform the time-resolved spectral analysis for the individual pulses which are thought to be generated by each internal shock. Then we probe the physical condition of each internal shock. Through this thesis, when we estimate the physical values at the rest frame of GRBs, we assume the flat-isotropic universe with $\Omega_m = 0.32$, $\Omega_\Lambda = 0.68$ and $H_0 = 72$ km s^{-1}Mpc^{-1} (Bennett et al., 2003; Spergel et al., 2003). Here, Ω_m and Ω_Λ is a cosmological parameter associated with the mass and the cosmological constant, respectively. H_0 is the Hubble constant at the observer's rest frame.

GRB	*BATSE* ID	Redshift	Trigger Time	T_{90}	R.A.	DEC.
970508	6225	0.835	1997 May 08.904	23.1	$06^h53^m49^s.45$	$+79^o16'19".5$
970828	6350	0.9578	1997 Aug 28.739	—	$18^h08^m31^s.62$	$+59^o18'51".3$
971214	6533	3.418	1997 Dec 14.973	31.2	$11^h56^m26^s.35$	$+65^o12'00".7$
980326	6660	0.9–1.1	1998 Mar 26.888	9	$08^h36^m34^s.28$	$-18^o51'23".9$
980329	6665	2.0–3.9	1998 Mar 29.156	18.6	$07^h02^m38^s.02$	$+38^o50'44".0$
980425	6707	0.0085	1998 Apr 25.909	34.8	$19^h35^m03^s.17$	$+52^o50'46".1$
980703	6891	0.966	1998 Jul 03.184	411.6	$23^h59^m06^s.67$	$+08^o35'06".7$
990123	7343	1.600	1999 Jan 23.408	63.4	$15^h25^m30^s.53$	$+44^o46'00".5$
990506	7549	1.300	1999 May 06.475	130.0	$11^h54^m52^s.92$	$-26^o43'39".9$
990510	7560	1.619	1999 May 10.423	68.0	$13^h38^m07^s.62$	$-80^o29'48".8$
991216	7906	1.020	1999 Dec 16.672	15.2	$05^h09^m31^s.20$	$+11^o17'07".2$
000131	7975	4.5	2000 Jan 31.624	—	$06^h13^m31^s.00$	$-51^o56'40".0$

Table 4.1: The basic informations of our known redshift samples. The duration T_{90} cannot be determined for GRB 970828 and GRB 000131 because a part of data lacks. The coordinates of *R.A.* and *DEC.* are determined by optical or radio observations.

4.1 Model Functions

In this section, we introduce model functions of the spectral shapes and the temporal behaviors of GRBs. The GRB spectrum is well represented by the smoothly broken power-law model as the function (Band et al., 1993):

$$N(E) = \begin{cases} A\left(\frac{E}{100 \text{ keV}}\right)^{\alpha} \exp(-\frac{E}{E_0}) & \text{for } E \leq (\alpha - \beta)E_0, \\ A\left(\frac{E}{100 \text{ keV}}\right)^{\beta} \left(\frac{(\alpha-\beta)E_0}{100 \text{ keV}}\right)^{\alpha-\beta} \exp(\beta - \alpha) & \text{for } E \geq (\alpha - \beta)E_0. \end{cases} \tag{4.1}$$

Here $N(E)$ is in units of photons $\text{cm}^{-2}\text{s}^{-1}\text{keV}^{-1}$, E_0 is the energy at the spectral break. α and β are the low- and high-energy power-law indices, respectively. For the case of $\beta < -2$ and $\alpha > -2$, the peak energy can be derived as $E_p = (2 + \alpha)E_0$, which corresponds to the energy at the maximum flux in the νF_ν spectra. The νF_ν spectrum is proportional to $E^2 N(E)$, so the peak of νF_ν spectrum is determined at the energy where the differential coefficient of $E^2 N(E)$ is equivalent to be zero. We use the model function of equation (4.1) in the spectral analysis.

Generally, the pulse profiles of GRBs are due to "*Fast Rise and Exponential Decay (FRED)*", and well described by the function of

$$C(t) \propto \exp\left(-\left|\frac{t - t_{max}}{\tau_{r,d}}\right|^{\nu}\right). \tag{4.2}$$

Here, $C(t)$ is the count rate as a function of time and t_{max} is the time giving the maximum count rate. The value τ_r and τ_d are time-constants of the rising- and decaying-phase, and ν describes the "spikeness" of each pulse, respectively. This function can describe the *FRED* shape more flexibly, and it was adopted many pulses of GRBs (e.g. Norris et al., 1996; Crider et al., 1999). When we perform the spectral analyses of the individual pulses, we should avoid the contamination from the neighboring pulses. Therefore, if necessary, we quantify an independence of each pulse using equation (4.2), and we estimate the contamination flux.

When we measure the observed energy flux F_γ in units of ergs $\text{cm}^{-2}\text{s}^{-1}$, we integrate the spectrum between 30–10000 keV in the observer's rest frame to cover the hard emission beyond the peak energy. Assuming the cosmological parameter set of $(\Omega_m, \Omega_\Lambda, H_0) = (0.32, 0.68, 72)$ (Bennett et al., 2003; Spergel et al., 2003), we can determine a luminosity distance as

$$d_L = (1 + z)\frac{c}{H_0} \int_0^z \frac{dz'}{\sqrt{\Omega_\Lambda + (1 + z')^3 \Omega_m}}. \tag{4.3}$$

We calculate the isotropic luminosity L (ergs s^{-1}) at the rest frame of GRBs with the observed flux F_γ (ergs $\text{cm}^{-2}\text{s}^{-1}$) as $L = 4\pi d_L^2 F_\gamma k_c$. Here k_c is the k-correction factor, and we deal with k_c appropriately in this thesis [1].

---

[1]Multiplying by $(1 + z)$ the ENERG_LO and ENERG_HI columns in the MATRIX extension and the E_MIN and E_MAX columns of the EBOUNDS extension of the response matrix, we can obtain the redshift corrected spectra. The k-correction factor can be estimated by comparing the above spectrum and the spectrum at the observer's rest frame.

4.2 Average Property of GRBs

In this section, we show the average spectral properties of 12 GRBs with known redshifts as listed in table 4.1. In figure 4.1, we show the lightcurves of these 12 samples at the energy range between 110–320 keV. As shown in figure 4.1, we can recognize the various temporal behavior of GRBs, such as single pulse event, multiple pulses, existence of the long quiescent time, and so on. To take into account all the data with the single criteria, we extracted the spectral data of the *BATSE* –LAD detectors within the time interval of T_{90}, and performed spectral analyses for them.
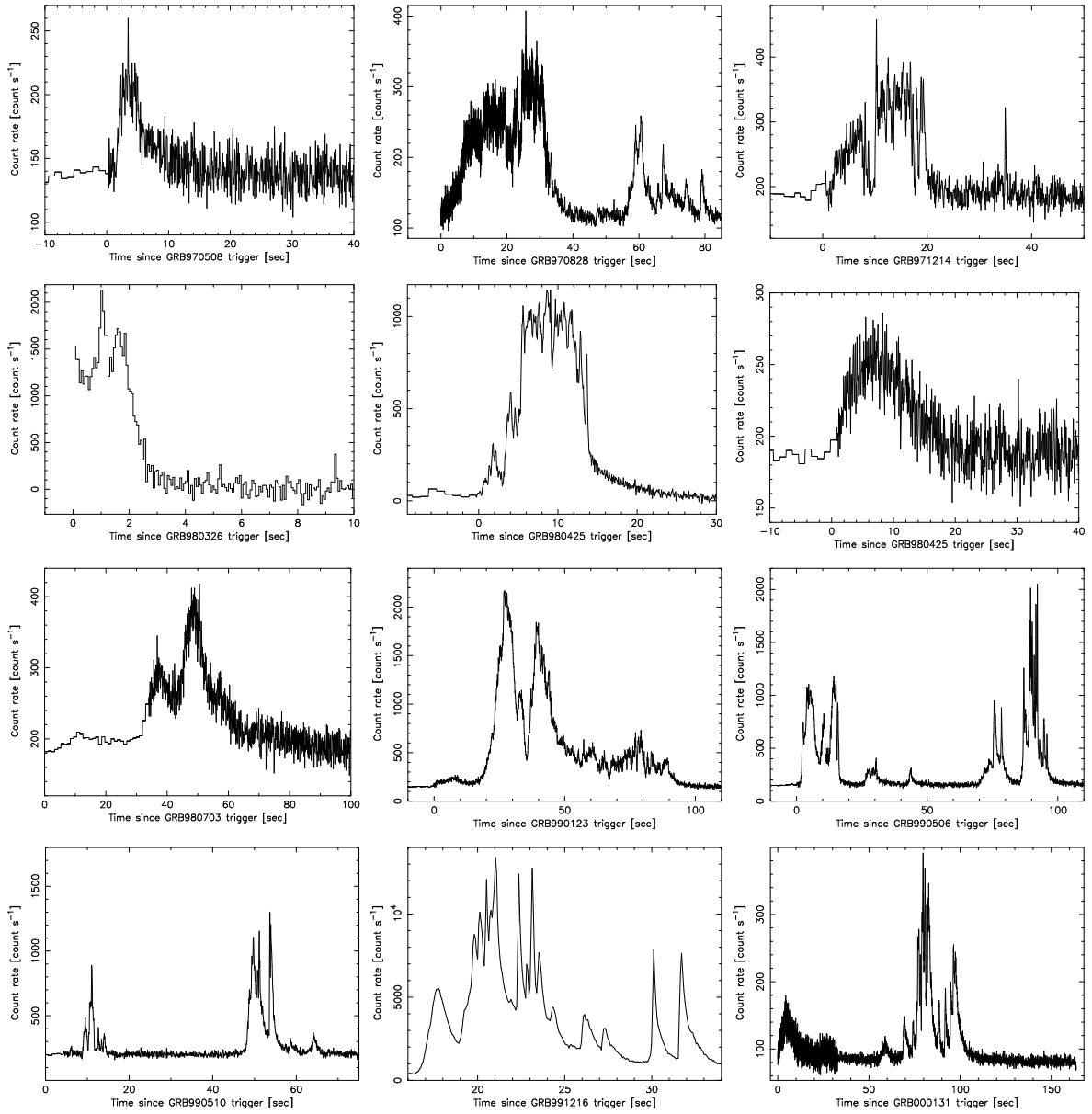
Figure 4.1: The lightcurves of 12 GRBs with known redshift.

The data analyses were performed with the standard data reduction technique[2]. First we extracted the burst data within the $\sim T_{90}$ duration for each burst with the *bcmppha* command[3], and subtracted the background spectrum derived from the average spectrum before and after the GRB in the same data set. The background stability, in such a short time scale, has been already discussed in Section 3.4. Next we generated an appropriate detector response file (including the angular response) for each event with the *fbdrm2rmf* command. Combined with the spectral data and the detector response matrices, we performed spectral fitting with the spectral model of smoothly broken power-law by Band et al. (1993) in equation (4.1).

In figures 4.2 and 4.3, we show the observed νF_{ν} spectra of these 12 GRBs. They are well described by the spectral model of equation (4.1), and we can calculate the peak energy, $E_p = (2 + \alpha)E_0$, for each event. In the case of GRB 980703, we failed to obtain the E_p value because of $\beta > -2.0$. The background level remarkably varies within the T_{90} duration of this event, as shown in figure 4.26. The detailed description about this point will be found in the latter section. The best-fit results for the spectral parameters are summarized in table 4.2.

GRB	redshift	α	β	E_p keV	F_{γ} 10^{-6} erg cm^{-2}s^{-1}	χ^2/d.o.f
970508	0.835	$-1.03^{+1.51}_{-0.06}$	$-2.20^{+0.10}_{-0.11}$	$48.9^{+21.1}_{-16.2}$	0.11 ± 0.01	43.8/40
970828	0.9578	$-0.45^{+0.06}_{-0.06}$	$-2.06^{+0.08}_{-0.10}$	$379.3^{+15.0}_{-16.4}$	4.74 ± 0.20	96.0/82
971214	3.418	$-0.36^{+0.14}_{-0.14}$	$-2.10^{+0.52}_{-6.90}$	$182.6^{+11.0}_{-14.3}$	0.40 ± 0.06	68.9/66
980326	0.9–1.1	$-0.93^{+0.09}_{-0.08}$	$-2.96^{+0.21}_{-0.51}$	$35.5^{+18.0}_{-18.0}$	0.14 ± 0.02	55.7/48
980329	2.0–3.9	$-0.79^{+0.03}_{-0.03}$	$-2.27^{+0.04}_{-0.05}$	$239.2^{+32.8}_{-43.2}$	6.22 ± 0.18	121.1/112
980425	0.0085	$-0.97^{+0.16}_{-0.16}$	$-2.06^{+0.09}_{-0.09}$	$54.6^{+11.5}_{-11.5}$	0.22 ± 0.04	36.4/33
980703	0.966	$-0.80^{+0.22}_{-0.16}$	$-1.60^{+0.06}_{-0.09}$	> 76.3	1.97 ± 0.18	89.6/91
990123	1.600	$-0.18^{+0.08}_{-0.07}$	$-2.33^{+0.08}_{-0.09}$	$513.0^{+19.2}_{-21.9}$	10.2 ± 0.01	134.1/112
990506	1.30	$-0.90^{+0.19}_{-0.13}$	$-2.08^{+0.08}_{-0.10}$	$320.7^{+30.1}_{-38.2}$	4.25 ± 0.20	108.3/103
990510	1.619	$-0.71^{+0.12}_{-0.12}$	$-2.79^{+0.51}_{-6.21}$	$205.5^{+9.6}_{-12.3}$	1.35 ± 0.05	89.9/111
991216	1.020	$-0.66^{+0.04}_{-0.04}$	$-2.44^{+0.12}_{-0.17}$	$536.5^{+18.5}_{-20.4}$	39.3 ± 0.02	125.8/102
000131	4.5	$-0.91^{+0.20}_{-0.15}$	$-2.02^{+0.18}_{-0.32}$	$168.4^{+17.7}_{-15.1}$	1.68 ± 0.02	115.1/97

Table 4.2: Observed spectral parameters for 12 known-redshift GRBs of *BATSE* . The value F_{γ} is the observed flux integrating between 30–10000 keV.

Using these spectral parameters, we calculated the peak energy-flux F_p of the energy range of 30–10000 keV from the 1 sec peak photon flux $P_{\gamma,1}$ (50–300 keV):

$$F_p = P_{\gamma,1} \times \frac{\int_{30}^{10000} E \times N(E)dE}{\int_{50}^{300} N(E)dE} \times 1.602 \times 10^{-10} \quad \text{ergs cm}^{-2}\text{s}^{-1} , \qquad (4.4)$$

where additional factor of 1.602×10^{-10} comes from the unit transformation from keV to ergs. The 1 sec peak luminosity is calculated as $L_p = 4\pi d_L^2 F_p k_c$, where k_c is the k-correction factor measured by the same method by Amati et al. (2002). In table 4.3, we summarized the rest

---

[2]http://cossc.gsfc.nasa.gov/analysis/index.html

[3]Since a part of data lacks for GRB 980326, GRB 980329, and GRB000131, we performed the spectral analysis for the *observed* entire interval for them.
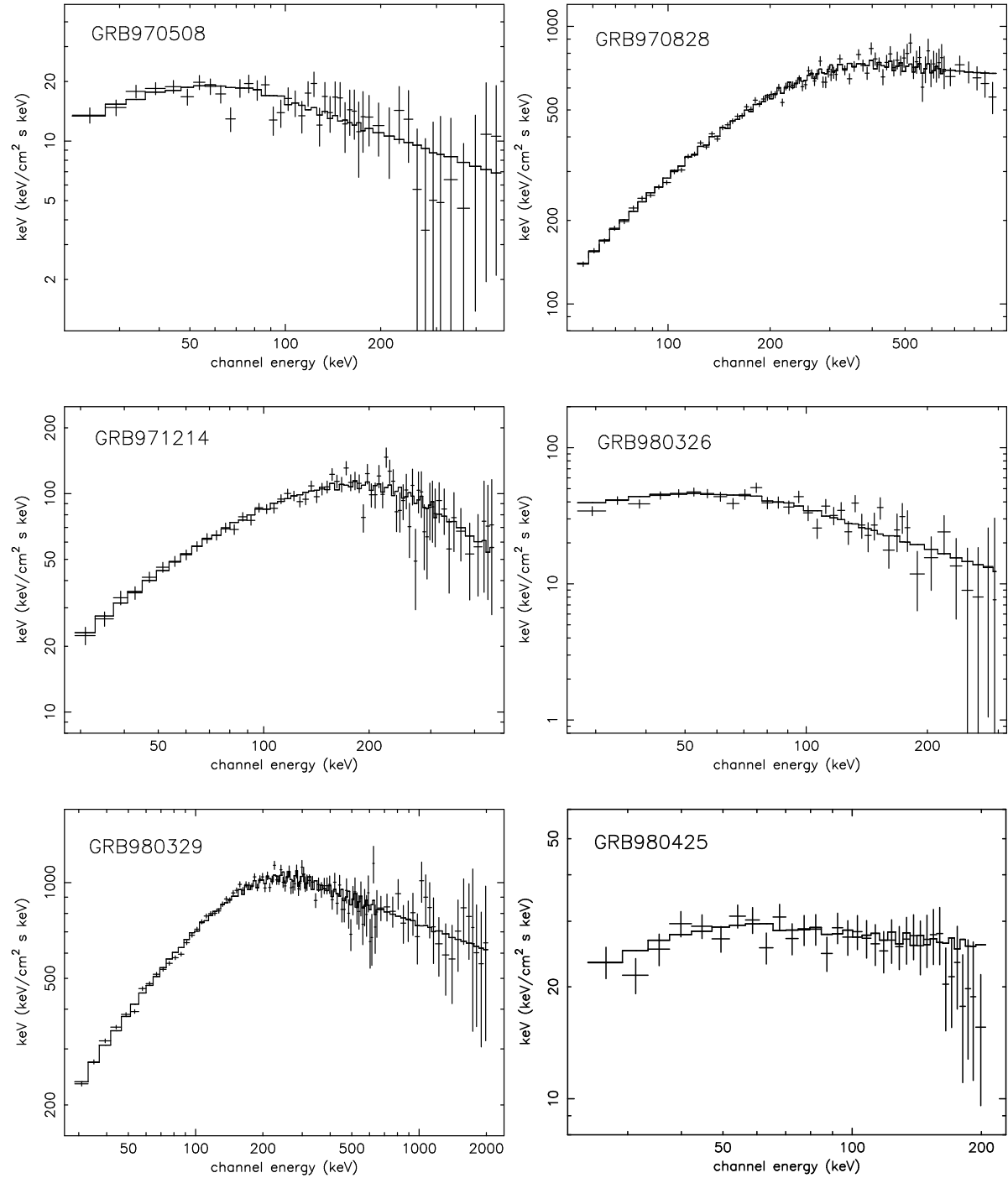
Figure 4.2: The νF_ν Spectrum of the GRBs with known redshift – (1).
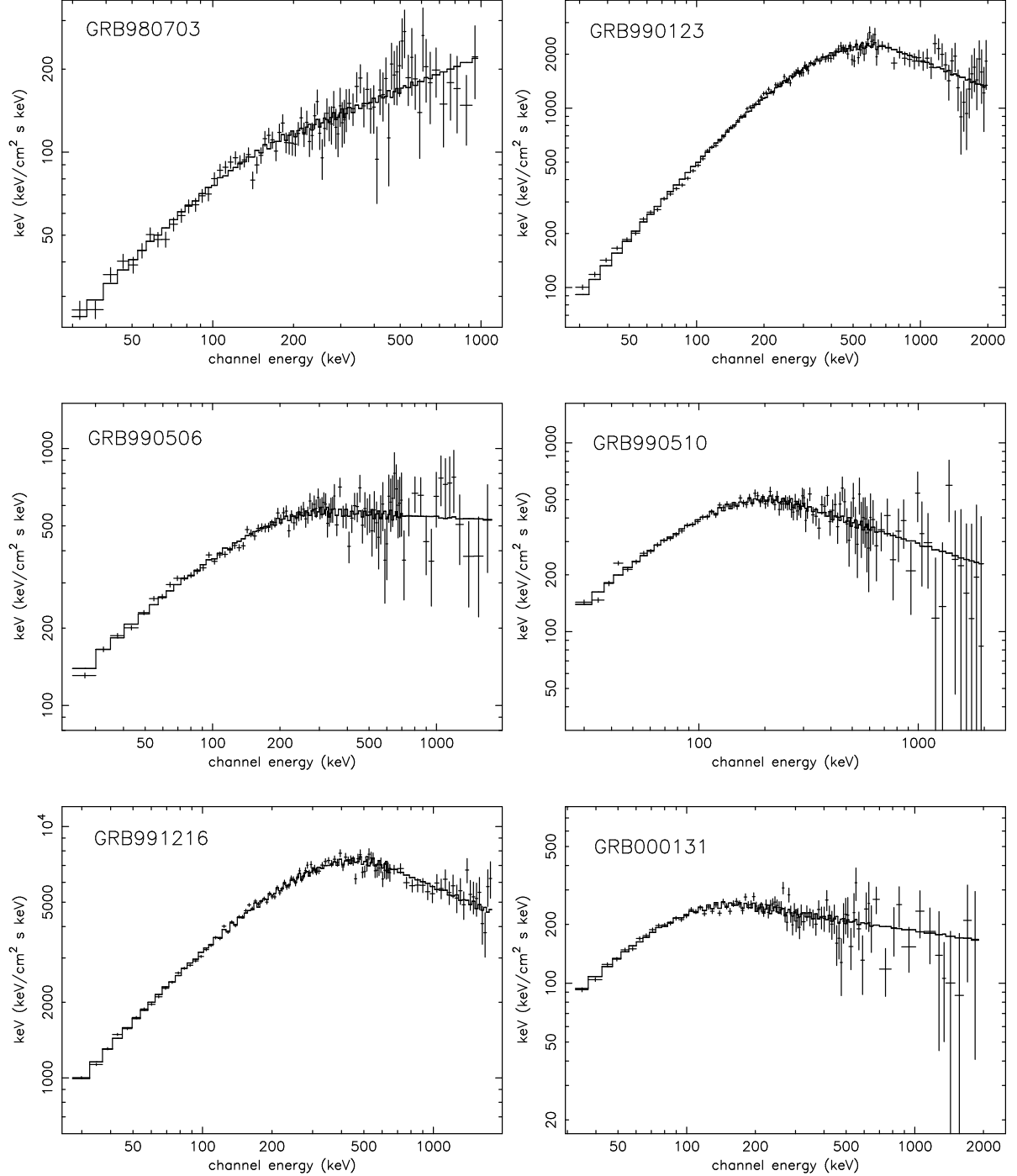
Figure 4.3: The νF_ν Spectrum of the GRBs with known redshift – (2).

GRB	$E_p(1+z)$ keV	F_p 10^{-6} erg cm^{-2}s^{-1}	L_p 10^{52} erg s^{-1}	k_c
970508	$89.8^{+37.8}_{-29.7}$	0.45 ± 0.10	0.14 ± 0.01	1.6
970828	$742.6^{+29.4}_{-32.1}$	5.93 ± 0.34	3.67 ± 0.15	1.5
971214	$806.7^{+48.6}_{-63.2}$	5.54 ± 0.28	19.51 ± 0.17	1.2
980326	$46\text{–}139$	0.17 ± 0.15	$0.2 - 0.4$	1.4
980329	$785\text{–}1085$	5.79 ± 4.17	$12.5 - 72.4$	1.3
980425	$55.1^{+11.6}_{-11.6}$	0.47 ± 0.031	$(7.15 \pm 0.47)^*$	1.0
980703	> 150.0	2.64 ± 0.51	1.76 ± 0.05	1.3
990123	$1333.7^{+49.8}_{-56.9}$	19.6 ± 0.04	31.22 ± 0.23	1.2
990506	$737.6^{+69.2}_{-87.8}$	9.36 ± 0.20	13.28 ± 0.10	1.3
990510	$538.4^{+22.3}_{-32.1}$	2.98 ± 0.18	6.19 ± 0.06	1.4
991216	$1083.7^{+37.3}_{-41.3}$	105.4 ± 1.21	32.36 ± 0.11	1.2
000131	$926.0^{+97.5}_{-83.1}$	2.67 ± 0.41	51.35 ± 7.88	1.4

Table 4.3: Spectral parameters for 12 known-redshift GRBs at the rest frame of each event. The value F_p and L_p is the 1 second peak flux and the 1 second peak luminosity, respectively. The peak luminosity of GRB 980425 (*) is in units of 10^{46} ergs s^{-1} . The parameter k_c is the k-correction factor, and does not exceed 2, because of the wide energy coverage by *BATSE* detectors.

frame values of $E_p(1 + z)$, L_p as well as the observed value of F_p and k_c. As listed in table 4.3, the k-correction factors show small values and do not exceed 2. This is because the observable energy range of *BATSE* is wide as 30–2000 keV. Therefore k-correction is not so important in our analyses.

4.3 E_p–Luminosity Relation

The redshifts are determined for these 12 samples, so we can investigate the intrinsic properties for them. The rest frame peak-energy can be described as $E_p(1 + z)$, and the intrinsic peak-luminosity (L_p) is calculated as $L_p = 4\pi d_L^2 F_p k_c$. We can compare each event on the same plane of $E_p(1 + z)$ with L_p in the rest frame of them. In figure 4.4, we show a relation between $E_p(1 + z)$ and L_p. The results with *BeppoSAX* by Amati et al. (2002), as summarized in table 4.4, are also included on the same plane of figure 4.4, after converting the same energy range (30–10,000 keV) of our analyses.

There is a high positive correlation between the $E_p(1+z)$ and the L_p. The linear correlation coefficient including the weighting factors is 0.958 for 14 degree of freedom (16 samples with firm redshifts [4]; open and filled squares in figure 4.4–top) for the $\log[E_p(1 + z)]$ and the $\log[L_p]$. The chance probability shows extremely low value of 5.31×10^{-9}. When we adopt the power-law model to the E_p–luminosity relation, the best-fit function is

$$\frac{L_p}{10^{52} \text{ ergs s}^{-1}} = (2.34^{+2.29}_{-1.76}) \times 10^{-5} \left[\frac{E_p(1 + z)}{1 \text{ keV}} \right]^{2.0 \mp 0.2} \tag{4.5}$$

where the uncertainties are 1 σ error. However GRB 980425 is apart from the other populations

---

[4]Since there are 4 samples detected by both *BATSE* and *BeppoSAX* , so the independent sample is 12.

on the E_p and luminosity plane as shown in figure 4.4 (bottom). The redshift of GRB 980425 is $z = 0.0085$, which is two orders of magnitude closer than the other samples. One possible interpretation will be given in Chapter 6.

We suggested that this E_p–luminosity relation becomes a redshift indicator for GRBs without known distance (Yoneotku et al., 2004). Once we obtain the E_p and the 1 sec peak flux at the observer's rest frame, we can numerically calculate the redshifts of many GRBs. In Chapter 5, we try to estimate the redshift of each GRBs based on the E_p–luminosity relation, and also derive the cosmological GRB formation rate from the redshift distribution. Amati et al. (2002) reported a similar relation between the E_p and the isotropic gamma-ray energy E_{iso} only from the *BeppoSAX* observations. Lamb et al. (1999) and Sakamoto (2004) extended the E_p–E_{iso} relation toward the X-ray Flashes and the X-ray Rich GRBs as shown in figure 4.5. Although this relation is also useful as the redshift indicator, we use our original work of E_p– luminosity relation. The reasons why we use the E_p–luminosity relation as the redshift indicator are described below.

1. For the remote GRBs, we may enable to observe only the brightest pulse and cannot detect the other dimmer pulses. Then we misunderstand not only the total duration of T_{90} but also the total energy of E_{iso}. On the other hand, as long as we consider the brightest 1 sec interval, we are free from the T_{90} uncertainty.

2. If the prompt emissions of GRBs are composed by multiple sub-jets, it is hard to deal with the off-axis viewing effect. In such a case, the off-axis effect must give smaller influences for the brightest pulse than the other dimmer pulses. Then the time integrated value of E_{iso} is mixed by several sub-jets with different off-axis angle while the peak luminosity is much closer to the on-axis emission.

GRB	redshift	α	β	$E_p(1+z)$	F_p	L_p
970228	0.695	-1.54 ± 0.08	-2.5 ± 0.4	195 ± 64	3.7 ± 0.1	1.27 ± 0.03
970508	0.835	-1.71 ± 0.10	-2.2 ± 0.25	145 ± 43	0.34 ± 0.01	0.22 ± 0.01
971214	3.418	-0.76 ± 0.17	-2.7 ± 1.1	685 ± 133	0.68 ± 0.07	13.7 ± 1.41
980326	0.9–1.1	-1.23 ± 0.21	-2.48 ± 0.31	71 ± 36	0.245 ± 0.015	0.16–0.26
980329	2.0–3.9	-0.64 ± 0.14	-2.2 ± 0.08	935 ± 150	3.1 ± 0.1	26–130
980613	1.096	-1.43 ± 0.24	-2.7 ± 0.6	194 ± 89	0.16 ± 0.04	0.16 ± 0.04
990123	1.600	-0.89 ± 0.08	-2.45 ± 0.97	2030 ± 161	17.0 ± 5.0	116 ± 34
990510	1.619	-1.23 ± 0.05	-2.7 ± 0.4	423 ± 42	2.47 ± 0.21	6.70 ± 0.65
990705	0.843	-1.05 ± 0.21	-2.2 ± 0.1	348 ± 28	3.7 ± 0.1	2.40 ± 0.06
990712	0.43	-1.88 ± 0.07	-2.48 ± 0.56	93 ± 15	6.5 ± 0.53	0.16 ± 0.01
000214	0.37–0.47	-1.62 ± 0.13	-2.1 (fix)	> 117	14.2 ± 0.4	0.38–0.67
010222	1.437	-1.35 ± 0.19	-1.64 ± 0.02	> 886	92.5 ± 2.8	42.9 ± 1.00

Table 4.4: The *BeppoSAX* results of the spectral parameters reported by Amati et al. (2002).
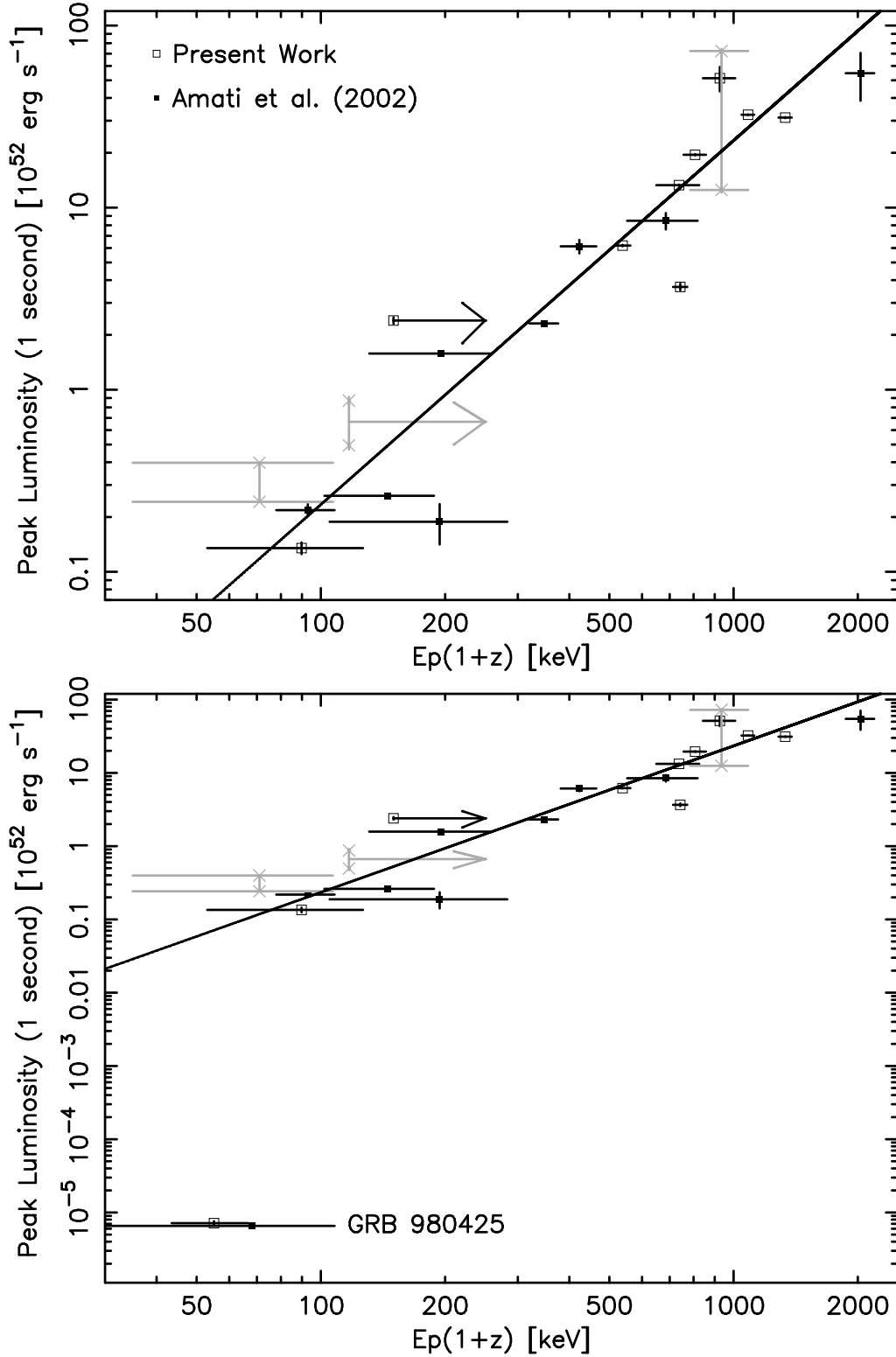
Figure 4.4: The upper panel is the observed E_p–luminosity relation for the average spectrum, except for GRB 980425. The *BeppoSAX* result for GRB 980425 by Frontera et al. (2000) is also plotted. The lower panel is the same of the upper one, but including GRB 980425. The luminosity of GRB 980425 is 4 orders of magnitude apart from the other population while the E_p is consistent with the lowest value of the other population.
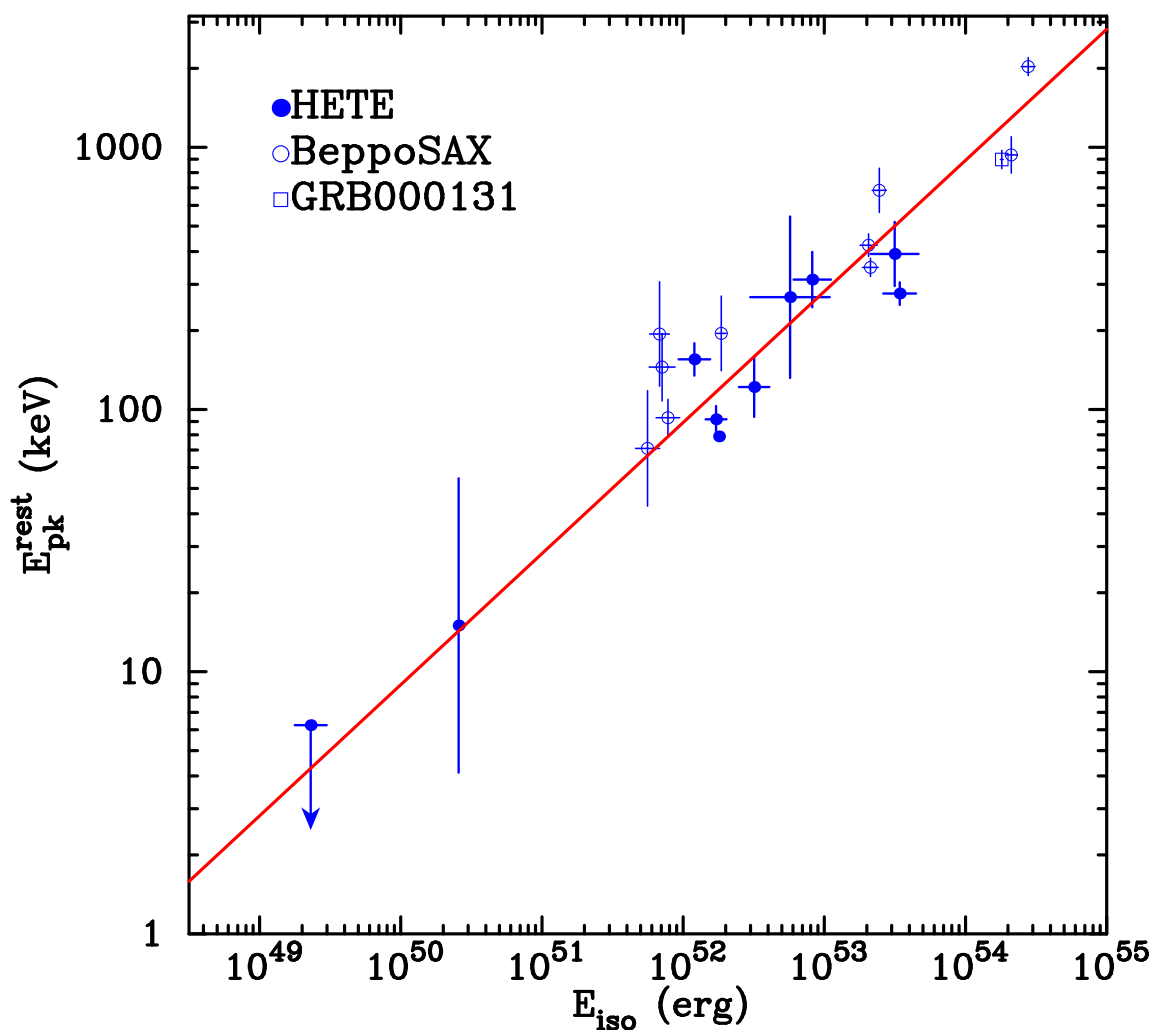
Figure 4.5: E_p–E_{iso} relation measured by *BeppoSAX* and *HETE-2* (Lamb et al., 1999; Sakamoto, 2004), where E_{iso} is the isotropic total energy radiated in gamma-ray band. Amati et al. (2002) reported this relation at first with the *BeppoSAX* data, and Lamb et al. (1999) and Sakamoto (2004) extend this relation toward the low-energy and the low-luminosity band with the *HETE-2* data.

4.3.1   Deviations of E_p–Luminosity Relation

We showed the E_p–luminosity relation in figure 4.4 and gave the best formula describing the relation. We suggested to use the E_p–luminosity relation as the redshift indicator. Then it is very important to estimate data deviations around the best functional form, because the deviations directly reflect the ambiguity of the redshift estimation. In figure 4.6, we again show the E_p–luminosity relation. From the 16 samples with known redshifts (open and filled squares), we estimate the sample deviations around the best-fit E_p–luminosity relation. Two dotted lines in figure 4.6 show the 1 σ standard deviations. The normalization of the upper (lower) dotted line is different from one of the best-fit function with the factor of 1.56 (0.64). We conclude the data deviation is a factor of 2.5 within 1 σ significance.
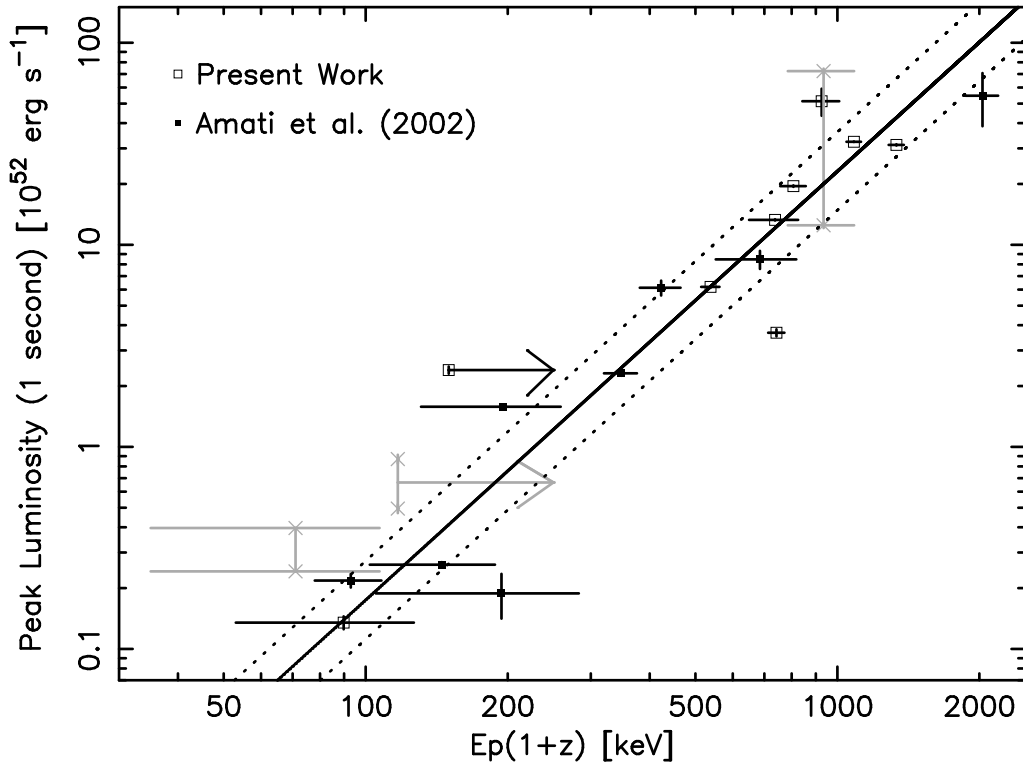
Figure 4.6: Deviations of the E_p–luminosity relation around the best-fit power-law model. Two dotted lines are equivalent to the 1 σ standard deviations. The normalization of the upper (lower) dotted line is different from one of the best-fit function with the factor of 1.56 (0.64).

4.4   Spectral property of the individual internal shock

In the previous section, we performed the time-averaged spectral analyses. We found the tight correlation between the $E_p(1 + z)$ and the 1s peak luminosity, and we have succeeded in combining the results of *BeppoSAX* and *BATSE* into the single formula of equation (4.5). Although Amati et al. (2002) have already suggested a similar correlation between $E_p(1 + z)$ and E_{tot} (the total gamma-ray energy released in the prompt gamma-ray emission), we prefer to use the E_p–luminosity relation as a redshift indicator rather than the E_p–E_{tot} relation by Amati et al. (2002).

However, it is not appropriate to discuss about the physical conditions in the internal shocks based on the above E_p–luminosity relation. This is because the time-averaged E_p–luminosity relation is the information mixed with the several internal shocks. When we would like to know and obtain the physical conditions in the internal shocks, we had better perform the time-resolved spectral analyses. In this section, as the next step, dividing each event into the individual pulses which are thought to be generated by the individual internal shocks, we perform the time-resolved spectral analyses. Since a lot of pulses can be resolved from GRB 991216, GRB 990506, and GRB 990510, first we show these properties. The events which is hard to resolve the individual pulses because of poor photon statistics and the complex pulse mixing are shown later.

4.4.1   GRB 991216

GRB 991216 began with a weak precursor pulse lasting about 3 seconds, followed about 16 seconds later by an intense multi-peaked complex. This burst is one of the brightest event ever detected by *BATSE* . An X-ray afterglow was observed with the *Chandra* satellite about 37 ksec after the GRB trigger, and the intense iron emission line with $\sim 4\ \sigma$ confidence level and the radiative recombination edge were detected by the High Energy Transmission Grating (Piro et al., 2000). Yoneotku et al. (2001) interpreted the plasma condition emitting the strong iron line and the recombination edge as a non-equilibrium ionization states.

The lightcurve of GRB 991216 is shown in figure 4.7 (top), which corresponds to the main emission phase, and we extracted 13 pulses from the entire lightcurve as shown in it. We could not analyze the X-ray precursor because of poor photon statistics. First, we performed time-resolved spectral analyses. A time history of the spectral parameters (α, β and E_p) are also shown in figure 4.7. The α and E_p are dramatically changed within the T_{90} duration while the β keeps almost constant. When we trace the physical property of the internal shocks, it is preferred to notice the individual pulses. Therefore, secondly, we used the spectral data for each pulse within the *FWHM* time interval. Since each pulse is contaminated from neighboring pulse, we have to treat this effect appropriately.

As already shown in figure 4.7, comparing the lightcurve with the E_p values, we can recognize the hard-to-soft trend in individual pulse. Based on the results, we may enable to assume the spectral shape of the contaminated flux from the previous pulse. Then we have some assumptions described below.

1. The ratio of the contamination flux to one of the pulse interval is estimated from the 50–
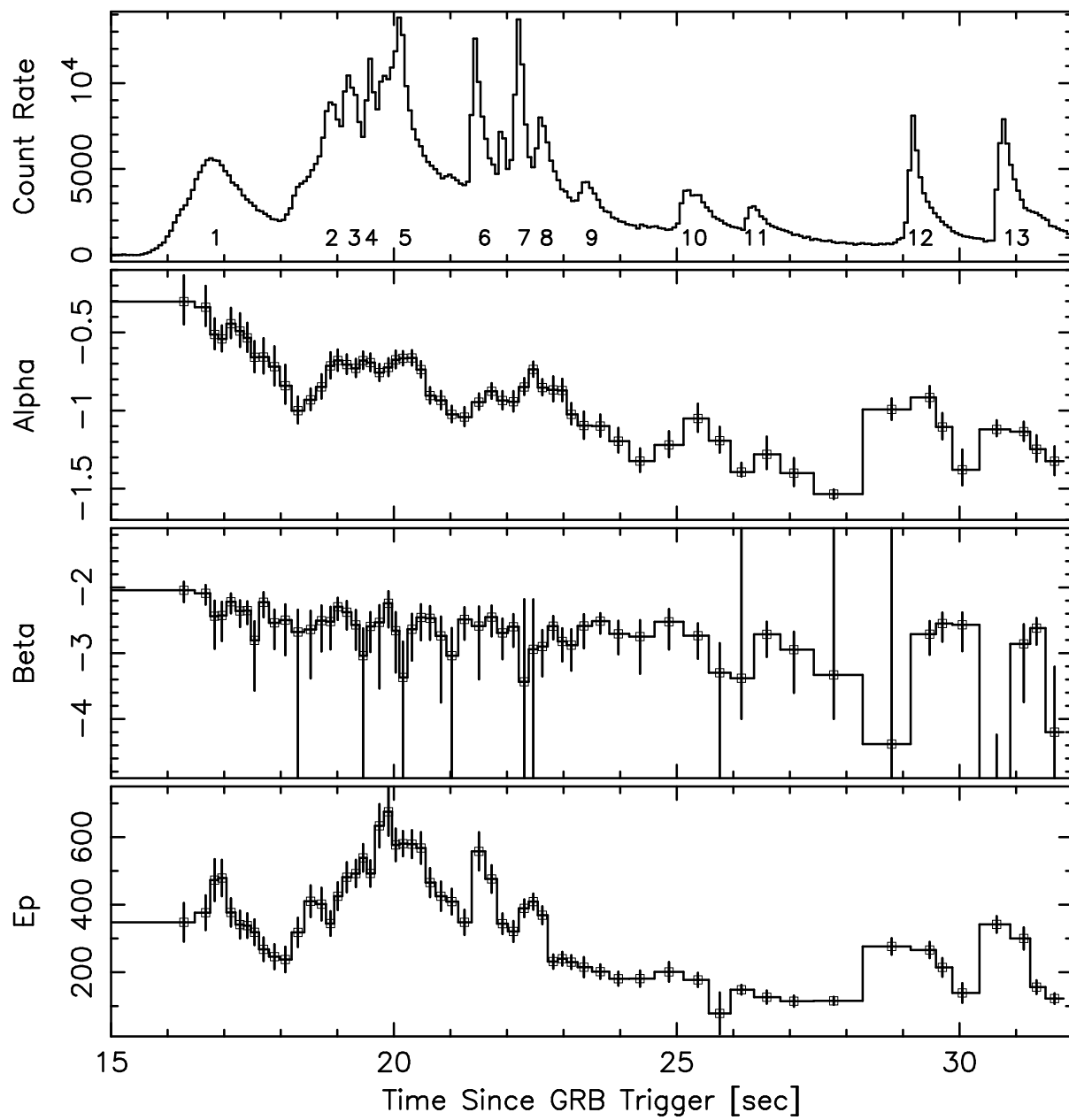
Figure 4.7: Top panel is the lightcurve of GRB 991216, which is enlarged for the purpose of clarity of the main emission phase. The spectral analyses are performed for 13 pulses as shown with number. Second, third and bottom panel are the time history of the spectral index α, β and E_p in the observer's rest frame.

300 keV lightcurve. This is because the detector response is rather flat, and considerably symmetry within the energy range.

2. We assume α and E_p values of contaminated pulse at the time just before the start time of remarking pulse.

3. We assume $\beta = -2.6$ which is the average value of this event as shown in figure 4.7 (third panel).

We used the above fixed-parameters to describe the off-set spectrum, and we could successfully fit all 13 spectra with the spectral model of equation (4.1). The νF_ν spectra for 13 pulses with the contaminated spectra we assumed are shown in figure 4.8 with the best fit model. The assuming spectral parameters of contaminated flux is rather rough, therefore the calculated pulse-averaged fluxes of individual pulses typically accompany ~ 30 % errors comes from the spectral shapes. We include this error for F_γ. The fitting results and the assuming parameters of off-set flux are summarized in table 4.5 and table 4.6, which also contains the pulse-averaged isotropic luminosity $L_{\gamma,52}$.

GRB	α	β	$E_p(1+z)$ keV	F_γ ergs cm^{-2}s^{-1}	L_γ ergs s^{-1}	χ^2/ν
991216-1	-0.58 ± 0.06	-2.17 ± 0.06	726.1 ± 87.3	21.89 ± 1.47	11.50 ± 0.77	$107.4/105$
991216-2	-0.69 ± 0.06	-2.25 ± 0.11	828.8 ± 105.7	35.55 ± 2.09	18.66 ± 1.10	$116.4/104$
991216-3	-0.29 ± 0.11	-2.51 ± 0.32	1178.2 ± 203.5	45.15 ± 3.31	23.7 ± 2.82	$114.6/106$
991216-4	-0.70 ± 0.09	-2.12 ± 0.86	1723.6 ± 482.7	71.72 ± 5.37	37.65 ± 2.82	$106.9/109$
991216-5	-0.57 ± 0.11	-2.20 ± 0.86	1255.0 ± 260.4	44.36 ± 2.82	23.29 ± 1.48	$116.5/99$
991216-6	-0.78 ± 0.06	-2.29 ± 0.19	1001.1 ± 161.5	41.55 ± 2.73	21.82 ± 1.43	$121.1/109$
991216-7	-0.77 ± 0.05	-3.46 ± 0.56	836.2 ± 93.2	37.34 ± 2.01	19.61 ± 1.05	$112.2/109$
991216-8	-0.81 ± 0.21	-4.04 ± 2.10	298.5 ± 83.6	6.52 ± 1.78	3.42 ± 0.93	$110.8/105$
991216-9	-1.12 ± 0.20	-2.46 ± 0.23	264.2 ± 108.7	4.37 ± 1.50	2.30 ± 0.79	$100.7/90$
991216-10	-0.91 ± 0.23	-2.45 ± 0.20	296.4 ± 115.2	4.68 ± 1.62	2.46 ± 0.85	$80.5/68$
991216-11	-0.82 ± 0.28	-2.72 ± 0.57	354.7 ± 143.9	6.51 ± 1.42	3.42 ± 0.74	$90.6/78$
991216-12	-1.15 ± 0.07	-2.71 ± 0.25	504.9 ± 86.0	7.85 ± 0.62	4.12 ± 0.32	$112.4/103$
991216-13	-1.24 ± 0.05	-2.92 ± 0.79	555.9 ± 93.3	11.16 ± 0.79	5.86 ± 0.41	$121.8/109$

Table 4.5: Fitting results of GRB 991216 spectra

In figure 4.9 (left), we superposed 4 spectra of the pulse (4), (6), (8) and (11) on the same figure for visual comparison. We can recognize that the brighter pulse shows higher E_p value. In figure 4.9 (right), we also show a hysteresis of the pulse properties in E_p–$L_{\gamma,52}$ plane, where $L_{\gamma,52}$ is the pulse averaged luminosity in units of 10^{52} ergs s^{-1} . A strong positive correlation between E_p and $L_{\gamma,52}$ are recognized, and their values dramatically change in one event. The linear correlation coefficient is 0.972 for 11 degree of freedom (d.o.f.), and the chance probability is 2.58×10^{-8}. The best fit relation is $L_{\gamma,52} \propto [E_p(1+z)]^{1.91\pm0.21}$. As a well known property of GRBs, the spectral shapes show *hard-to-soft* evolution in time which means the spectrum is hard in early epoch and transforms to the soft one in the end of event (e.g. Norris et al., 1986;
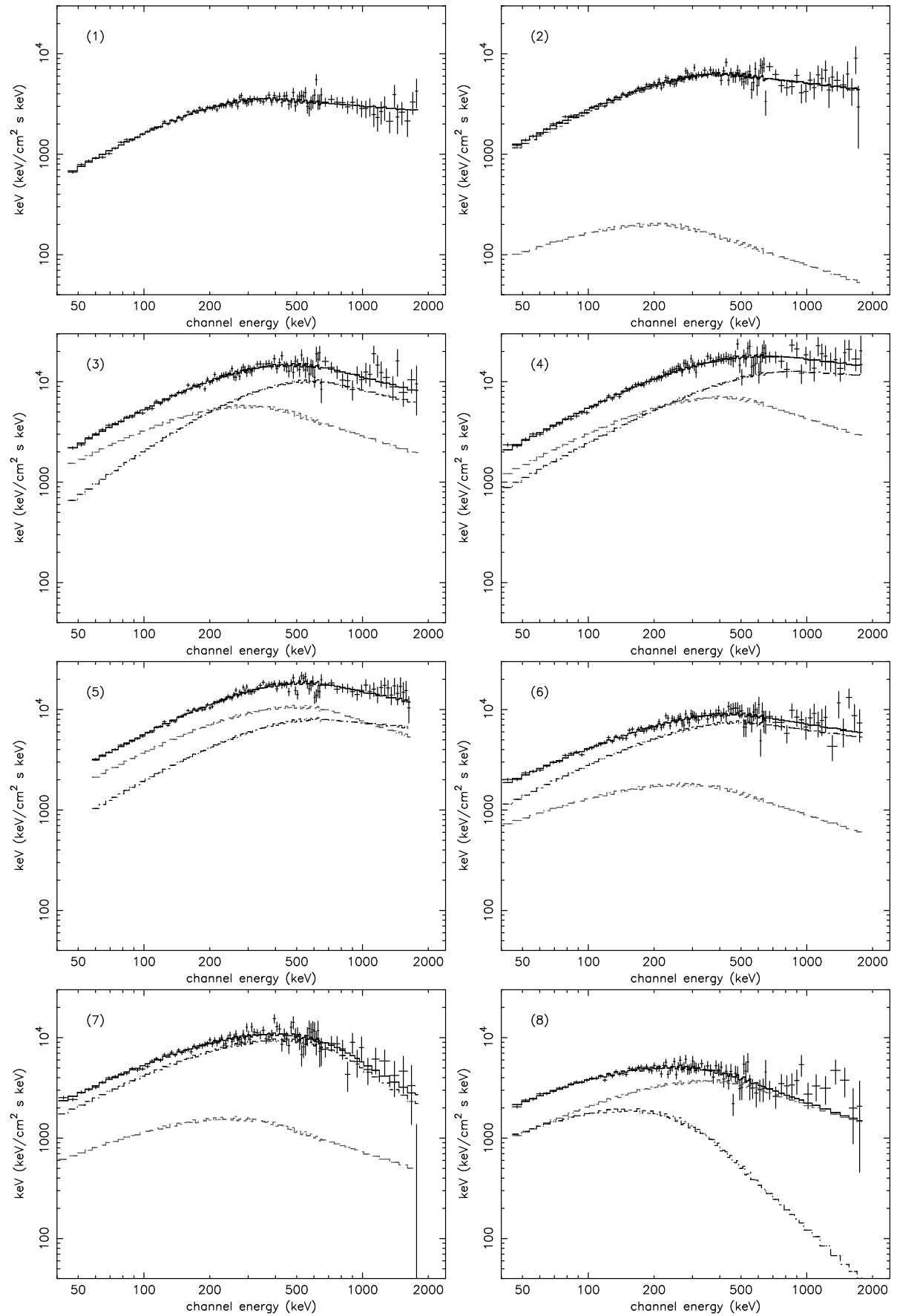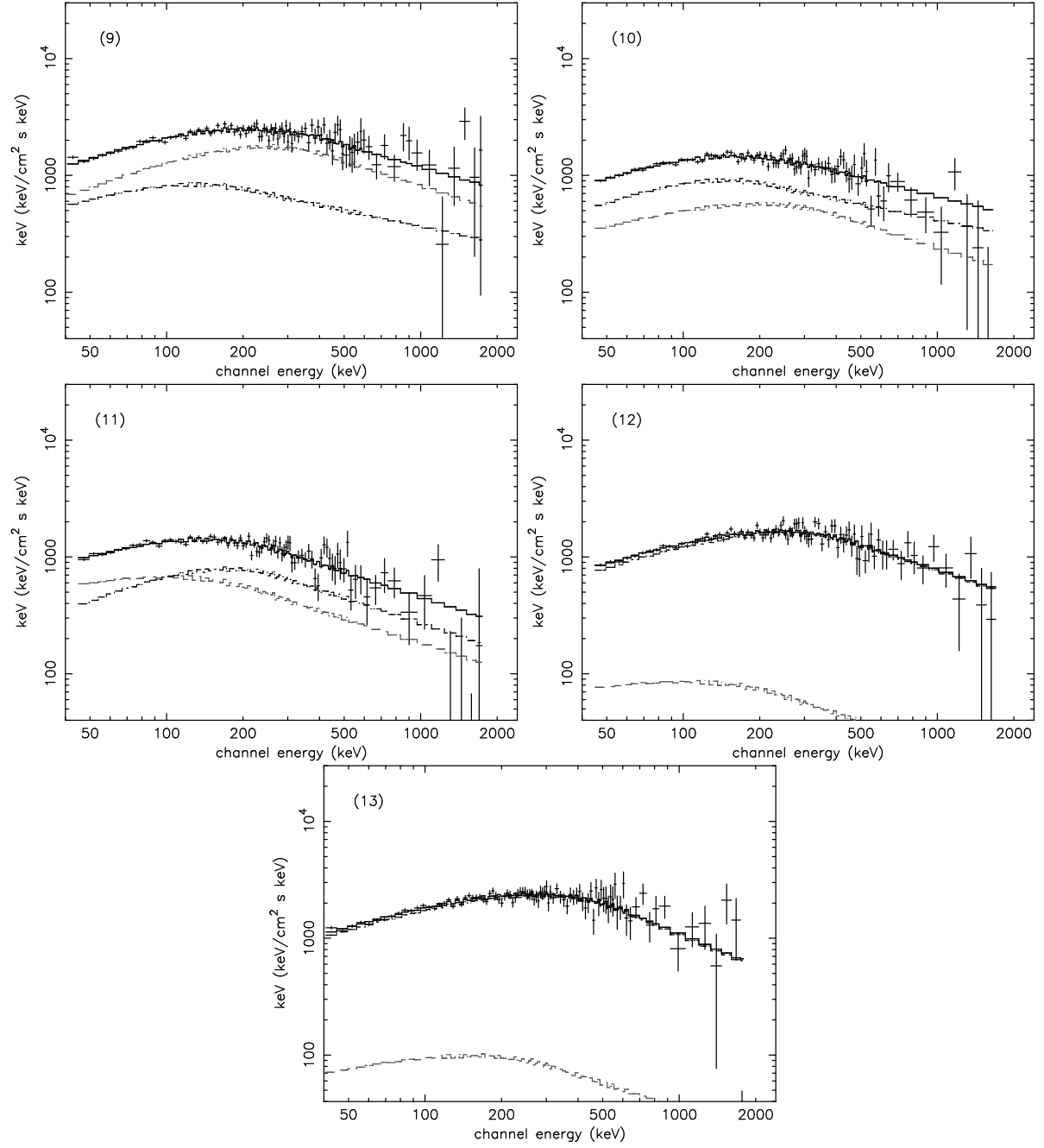
Figure 4.8: The spectra of GRB 991216 which correspond to 13 peaks as shown in figure 4.7. The black and gray dotted lines are the pulse and the contamination spectrum, respectively.

GRB	α	β	E_p keV	F_{cont}/F_{tot}	t_{max} sec	τ sec	$norm$ count
991216-1	—	—	—	—	16.98	0.98	5050
991216-2	-1.0	-2.6	200	8 %	18.92	1.06	8646
991216-3	-0.7	-2.6	300	62 %	19.32	0.63	8783
991216-4	-0.7	-2.6	400	52 %	19.64	0.58	9620
991216-5	-0.7	-2.6	500	47 %	20.08	0.09	11774
					20.28	1.24	7105
991216-6	-1.1	-2.6	300	32 %	21.41	0.33	13409
991216-7	-1.0	-2.6	250	28 %	22.20	0.23	14052
991216-8	-0.9	-2.6	350	61 %	22.61	0.54	7783
991216-9	-1.0	-2.6	250	61 %	23.39	0.33	3135
					—	—	1488 (const)
991216-10	-1.3	-2.6	200	46 %	25.24	0.91	3758
991216-11	-1.4	-2.6	100	44 %	26.33	1.03	26377
991216-12	-1.5	-2.6	100	9 %	29.14	0.32	8574
991216-13	-1.4	-2.6	150	9 %	30.69	0.35	10120

Table 4.6: Assuming spectral parameters for contaminated fluxes of GRB991216. F_{cont}/F_{tot} is the photon contamination fraction in 50–300 keV. The values t_{max}, τ and $norm$ is the pulse maximum time, the decay constant and the peak photon count in 50–300 keV, respectively.

Crider et al., 1999; Briggs et al., 1999). As shown in figure 4.9 (right), GRB 991216 roughly shows such a trend, but the spectral evolution is more complicated. The spectrum gradually becomes harder toward the brightest epoch of pulse (4), and turns hard-to-soft trend. In the final epoch of this event, it turns soft-to-hard evolution again. However, the evolution conserves the correlation between E_p and $L_{\gamma,52}$.
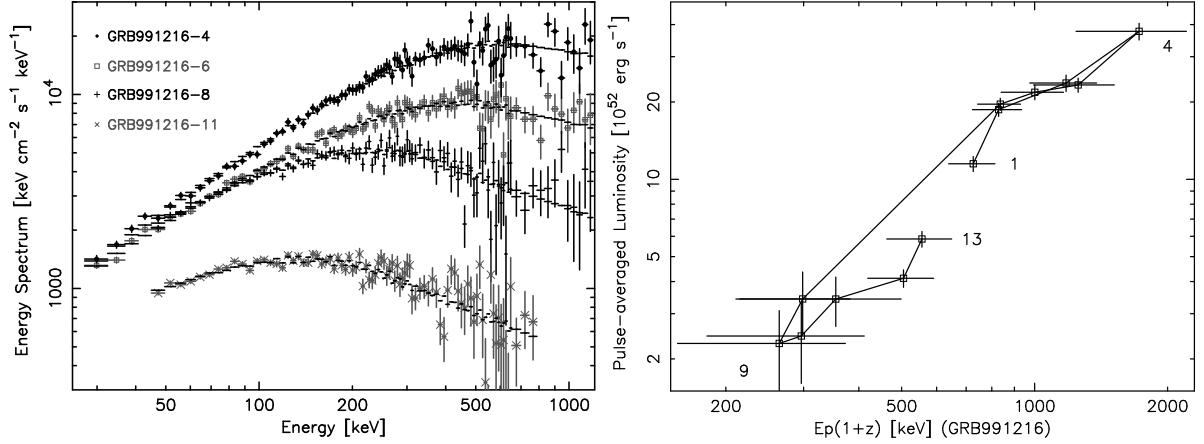
Figure 4.9: Left panel shows four νF_ν spectra of GRB 91216. There is a correlation between observed E_p and $L_{\gamma,52}$. Right panel is the hysteresis in a correlation between E_p and $L_{\gamma,52}$ of GRB 991216. There is a positive correlation between E_p and $L_{\gamma,52}$, and roughly a *hard-to-soft* trend.

4.4.2   GRB 990506

The lightcurve of GRB 990506 is shown in figure 4.10 (top). This event is composed by multiple peaks, and there are long quiescent times which has no significant signal compared with the background level and/or the Poisson fluctuation. We performed time-resolved spectral analyses. The time history of the spectral parameters (α, β and E_p) are also shown in figure 4.10.

As already described in the previous section of GRB 991216, using the same method, we extracted 8 pulses from the entire lightcurves as shown in figure 4.10 (top). Since the spectral data after 89.3 sec since the GRB trigger time are not present for the *LAD* detectors, we performed spectral analyses before 89 sec. Moreover, both two pulses between 20 and 60 sec are poor in photon statistics, so we cannot include them in our pulse samples. All spectra can be fitted by the function of equation (4.1). In figure 4.11, we show these 8 νF_ν spectra with the best-fit function. The fitting results and the contamination assumptions are summarized in table 4.7 and table 4.8, respectively.

GRB	α	β	$E_p(1+z)$	F_γ	$L_{\gamma,52}$	χ^2/ν
990506-1	-1.05 ± 0.01	-2.10 ± 0.25	1523.0 ± 629.0	17.60 ± 1.51	16.84 ± 1.50	$110.2/100$
990506-2	-0.74 ± 0.09	-2.48 ± 0.33	1073.9 ± 281.9	4.40 ± 1.29	4.20 ± 1.23	$103.5/100$
990506-3	-0.81 ± 0.14	-3.27 ± 0.64	1171.4 ± 268.8	7.34 ± 0.98	7.00 ± 0.94	$112.9/104$
990506-4	-1.13 ± 0.06	-2.08 ± 0.17	827.3 ± 222.2	5.33 ± 0.50	5.09 ± 0.47	$115.6/108$
990506-5	-1.23 ± 0.08	-2.21 ± 0.16	596.2 ± 160.7	2.59 ± 0.31	2.48 ± 0.28	$115.4/106$
990506-6	-0.81 ± 0.10	-2.38 ± 0.11	409.5 ± 70.0	4.86 ± 0.74	4.64 ± 0.70	$111.6/102$
990506-7	-0.95 ± 0.05	-2.78 ± 0.26	705.3 ± 93.1	7.90 ± 0.55	7.54 ± 0.53	$107.6/101$
990506-8	-0.54 ± 0.10	-9.37 ± 4.14	649.4 ± 99.0	3.12 ± 0.37	2.98 ± 0.35	$105.4/101$

Table 4.7: Fitting results of GRB 990506 spectra
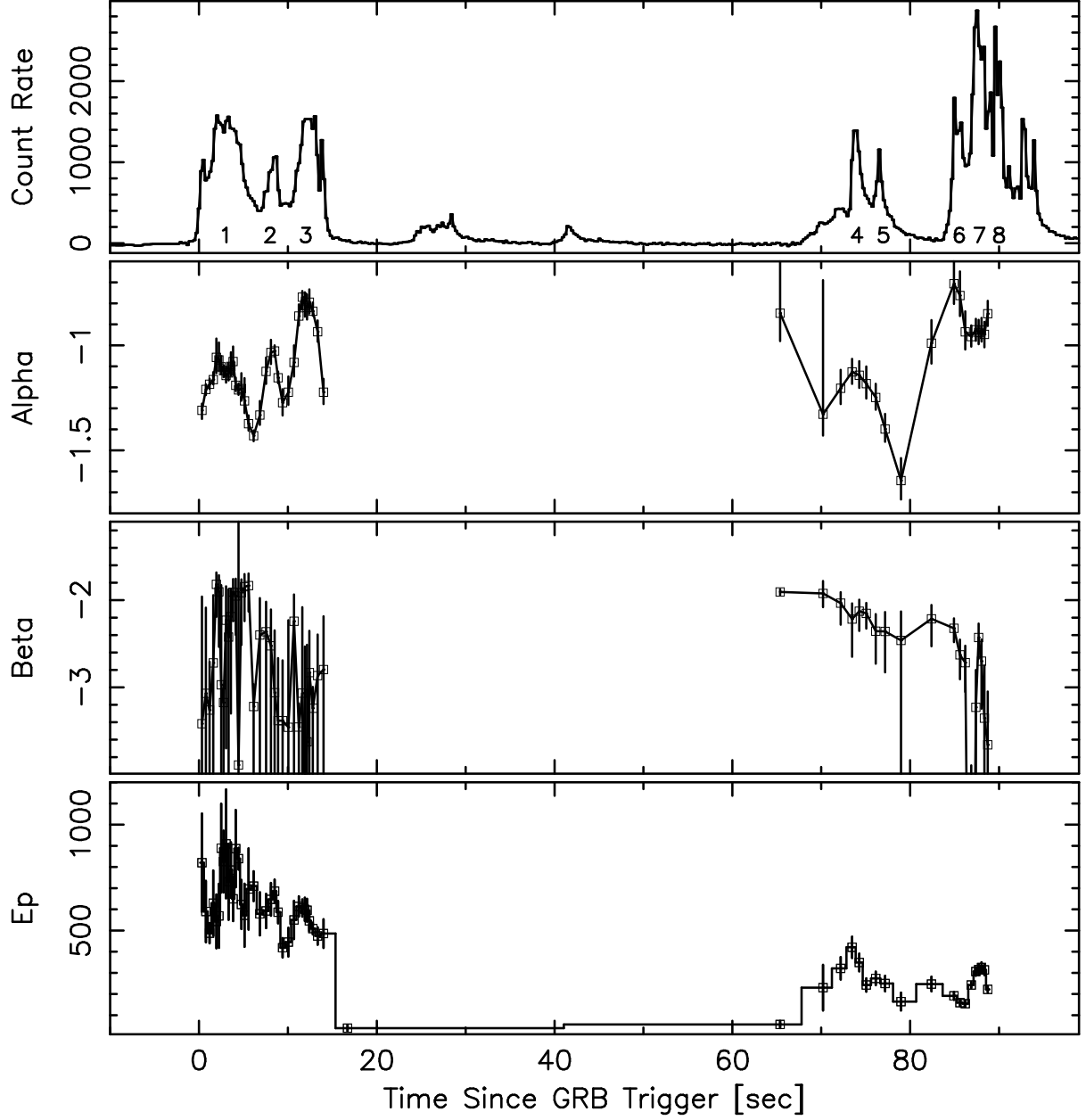
Figure 4.10: Top panel is the lightcurve of GRB 990506. The spectral analyses are performed for 7 pulses as shown with number (The spectral data are absent after 89.344 sec). There are long quiescent times with dim pulses. Because of poor photon statistics, we could not analyze spectra in the time interval. Second, third and bottom panel are the time history of the spectral index α, β and E_p in the observer's rest frame.
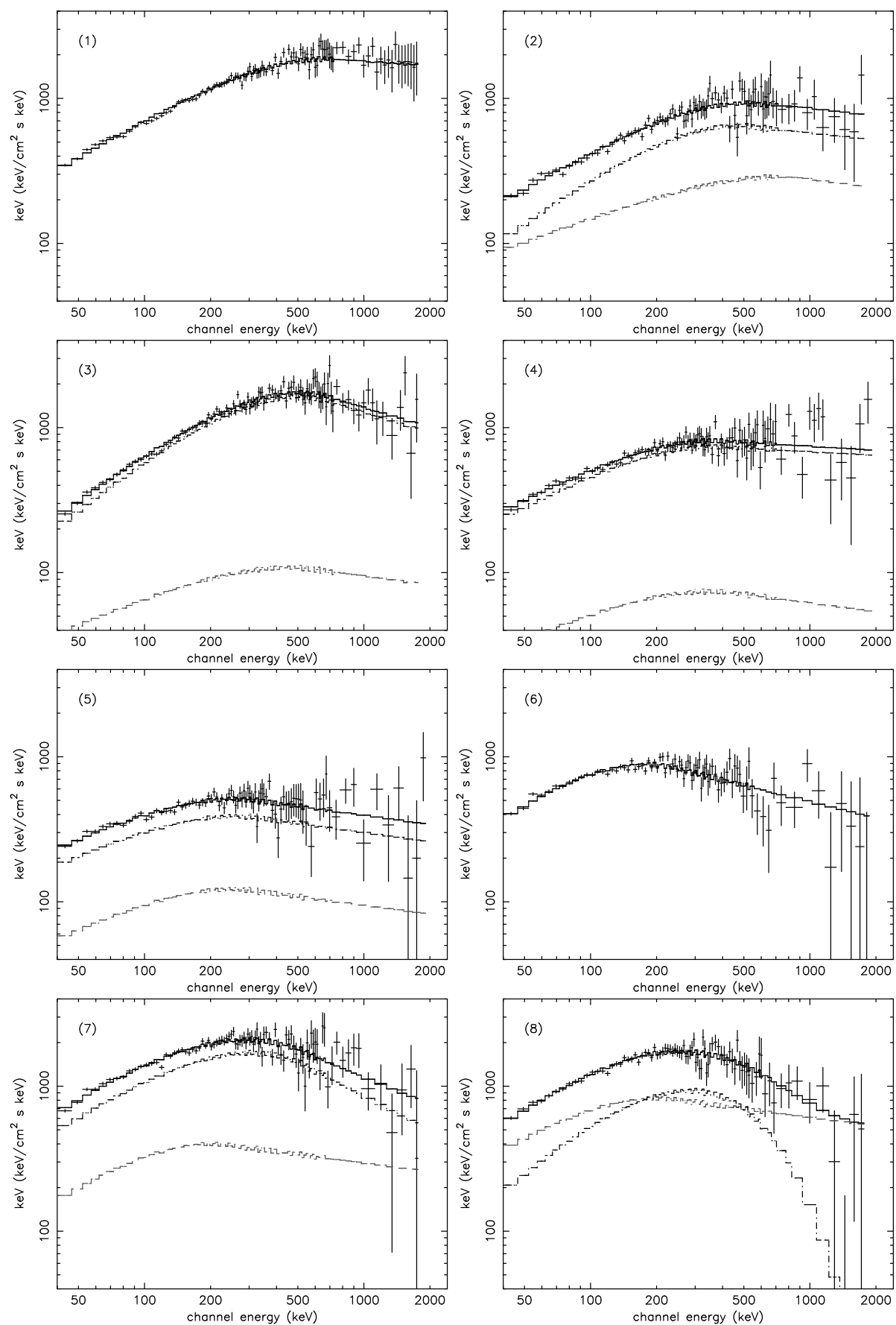
Figure 4.11: The νF_ν spectra of GRB 990506.

GRB	α	β	E_p keV	F_{cont}/F_{tot}	t_{max} sec	τ sec	*norm* count
990506-1	—	—	—	—	3.29	2.79	1594
990506-2	-1.4	-2.2	600	35 %	8.57	0.19	1156
					—	—	470 (const)
990506-3	-1.3	-2.2	450	10 %	12.86	1.03	1835
990506-4	-1.3	-2.2	400	10 %	73.98	1.37	1337
990506-5	-1.2	-2.2	250	24 %	76.36	1.00	1264
990506-6	—	—	—	—	83.68	2.41	2950
990506-7	-0.9	-2.2	200	23 %	87.48	2.33	2915
990506-8	-1.0	-2.2	200	56 %	89.55	1.44	2626

Table 4.8: Assuming spectral parameters for contaminated fluxes of GRB990506
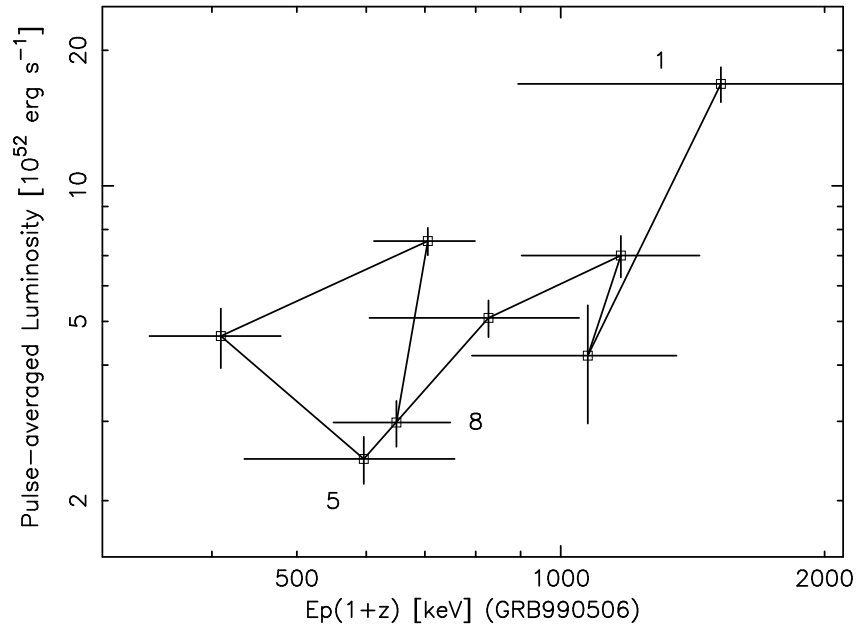
Figure 4.12: Hysteresis curve in the E_p–F_γ plane of GRB 990506. There is weak correlation and the hard-to-soft trend.

In figure 4.12, we show the hysteresis curve of the spectral evolution of GRB 990506 in $E_p(1+z)$–$L_{\gamma,52}$ plane. We find a weak positive correlation between them and the slightly hard-to-soft evolution in GRB 990506. The linear correlation coefficient for $\log[E_p(1+z)]$ and $L_{\gamma,52}$ is 0.569 for 6 d.o.f. with the significance of about 90 %. The best fit relation can be described as $L_{\gamma,52} \propto [E_p(1+z)]^{3.0\pm1.5}$. Observed E_p values are clustering within the factor of 3 and the error is quite large, we cannot conclude the existence of the strong correlation as similar to the sample of GRB 991216 in figure 4.9.

4.4.3   GRB 990510

In figure 4.13 (top), we show the lightcurve of GRB 990510. This event was strong and consisted of a complex series of pulses with two major episodes lasting > 100 sec. There is a long quiescent time between 11 and 44 sec since GRB trigger time. We performed the time-resolved spectral analyses. The results are also shown in figure 4.13 together with the lightcurve.

The spectral analyses were performed for individual 7 pulses. There are three weak pulses in the time interval denoted as (3). We could not separate them from the LAD spectral data. Therefore, we show the result of spectral analysis only for the purpose of the reference value, and will not include single pulse samples. The spectra and the fitting results are shown in figure 4.14. All spectra can be well fitted with the model function of equation (4.1). The best-fit parameters and the assumed function describing the contamination flux are summarized in table 4.9 and table 4.10, respectively.

In figure 4.15, we show the hysteresis curve on the $E_p(1+z)$–$L_{\gamma,52}$ plane. The E_p is strongly correlated with the pulse-averaged luminosity, and shows zig-zag evolution with keeping its correlation. The linear correlation coefficient is 0.971 for 5 d.o.f., and the chance probability is 2.36×10^{-4}. The best-fit result is $L_{\gamma,52} \propto E_p^{1.7\pm0.8}$.

GRB	α	β	$E_p(1+z)$	F_γ	$L_{\gamma,52}$	χ^2/ν
990510-1	-0.34 ± 0.38	-2.96 ± 0.26	209.5 ± 109.6	0.55 ± 0.08	0.91 ± 0.15	39.1/36
990510-2	-0.78 ± 0.16	-3.28 ± 0.35	280.5 ± 57.6	0.98 ± 0.25	1.62 ± 0.42	65.8/58
990510-3	-0.87 ± 0.06	-3.70 ± 0.71	164.8 ± 46.8	0.39 ± 0.28	0.64 ± 0.46	35.2/31
990510-4	-1.04 ± 0.07	-2.53 ± 0.05	788.5 ± 139.3	2.81 ± 0.47	4.60 ± 0.77	84.8/78
990510-5	-0.65 ± 0.23	-2.46 ± 0.18	469.2 ± 133.6	1.46 ± 0.42	2.40 ± 0.69	100.1/92
990510-6	-0.84 ± 0.19	-2.47 ± 0.17	457.3 ± 135.4	1.80 ± 0.43	2.96 ± 0.70	75.2/80
990510-7	-1.56 ± 0.09	-9.37 ± 5.22	138.3 ± 38.3	0.19 ± 0.06	0.32 ± 0.10	42.1/38

Table 4.9: Fitting results of GRB 990510 spectra

GRB	α	β	E_p keV	F_{cont}/F_{tot}	t_{max} sec	τ sec	*norm* count
990510-1	—	—	—	—	2.45	0.55	871
990510-2	-0.6	-3.0	100	4 %	4.00	0.47	1541
990510-3	-0.5	-3.0	50	17 %	—	—	—
990510-4	—	—	—	—	42.59	1.10	1855
990510-5	-1.0	-3.0	200	39 %	44.14	0.48	1315
					—	—	357 (const)
990510-6	-1.0	-3.0	150	10 %	46.92	0.62	1927
					—	—	110 (const)
990510-7	—	—	—	—	57.19	1.09	492

Table 4.10: Assuming spectral parameters for contaminated fluxes of GRB990510
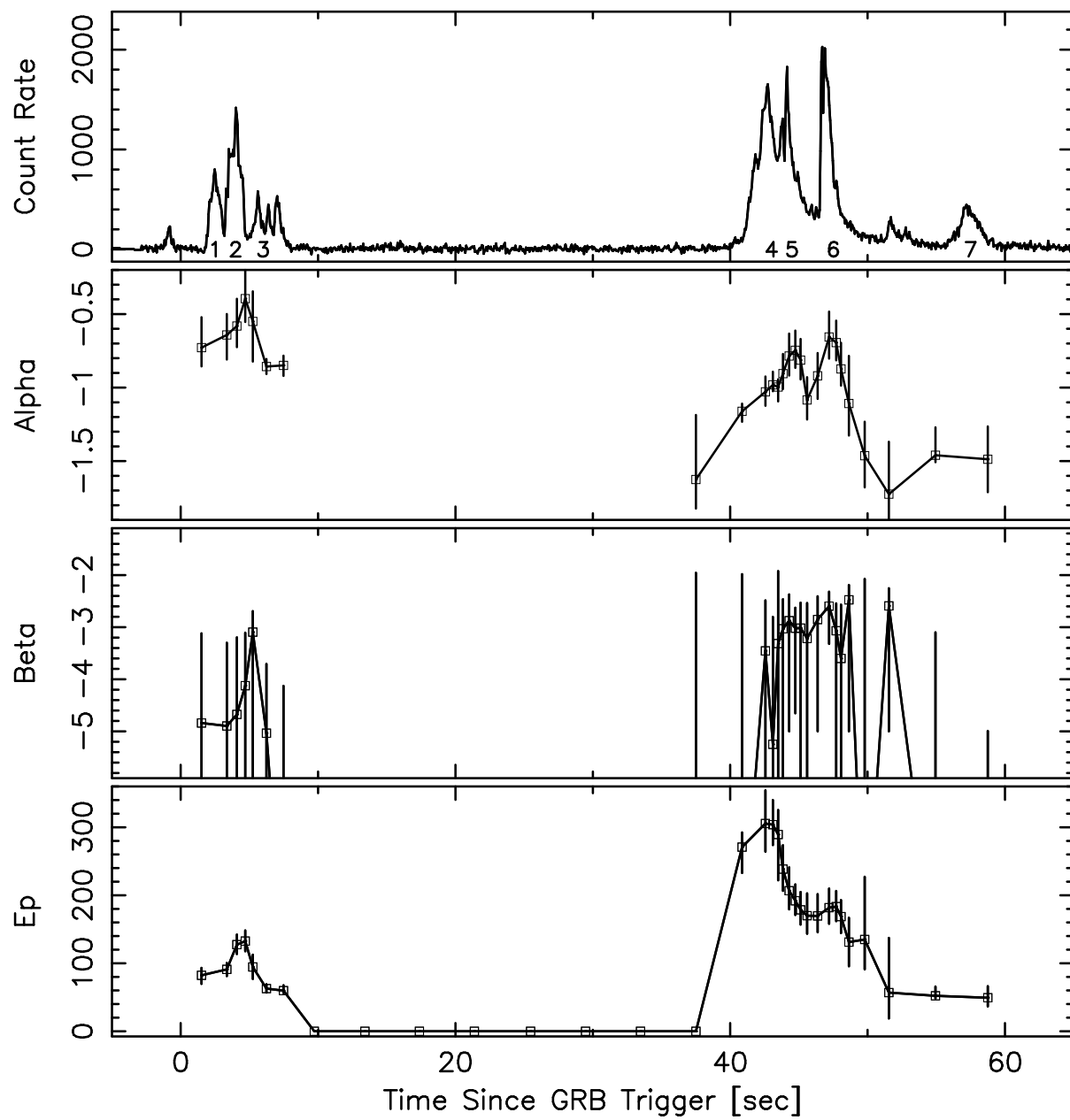
Figure 4.13: Top panel is the lightcurve of GRB 990510. The spectral analyses are performed for 7 pulses as shown with number. There are long quiescent times as well as GRB 990506. Second, third and bottom panel are the time history of the spectral index α, β and E_p in the observer's rest frame.
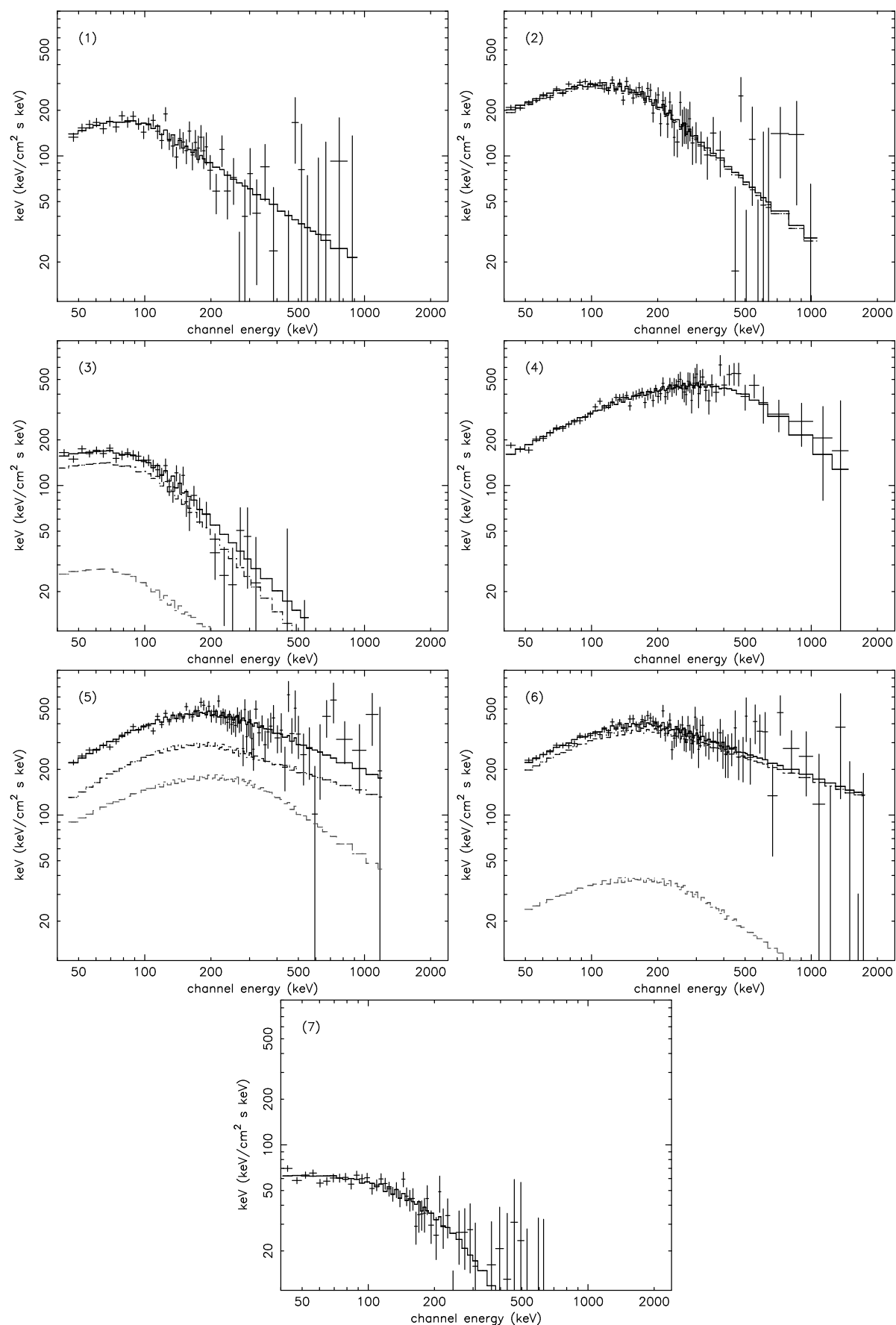
Figure 4.14: The spectra of GRB 990510 which correspond to 7 pulses divided by dotted lines as shown in figure 4.13.
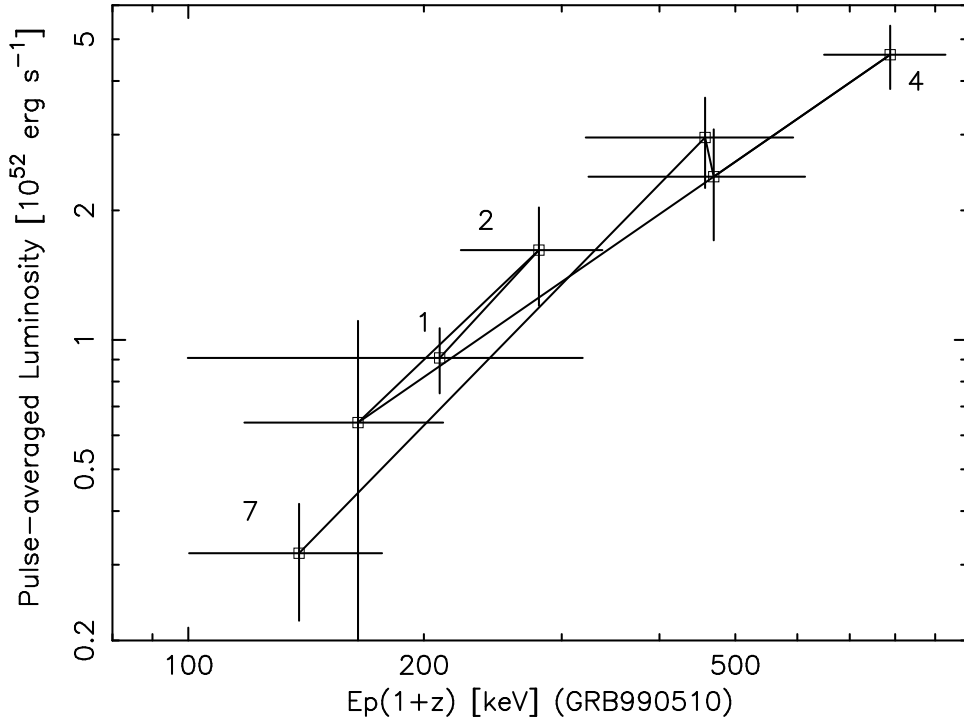
Figure 4.15: Hysteresis in a correlation between $E_p(1 + z)$ and $L_{\gamma,52}$ of GRB 990510.

4.5 E_p–Luminosity Relation of Individual Pulses

We have already shown the relation between $E_p(1 + z)$ and $L_{\gamma,52}$ for each event. Since these are the rest frame values, we can directly compare them on the same plane. In figure 4.16, we show the E_p–luminosity relation combining with three GRBs. Totally, the linear correlation coefficient for $\log[E_p(1+z)]$ and $L_{\gamma,52}$ is 0.907 for 26 d.o.f., and the chance probability is 2.94×10^{-11}. We have already shown the best fit function of $L_{\gamma,52} = 1.83 \times 10^{-5}[E_p(1 + z)]^{2.0\pm0.2}$ in the same figure. In view of each event, the data show one-sided distribution compared to the best fit function. For example, the luminosities of GRB 991216 samples slightly distribute above the average property. On the other hand, GRB 990506 samples systematically distribute lower than the model function. As a whole, all pulses distributes arround the univarsal function within the deviation of factor 5 (peak-to-peak).

In the previous works, Ford et al. (1995); Crider et al. (1999); Borgonovo & Ryde (2001) found the correlation between E_p and observed flux for bright GRBs without known redshift. Because of the limited information in distance, they can compare each data only on the E_p–flux plane at the observer's rest frame. Our results of the known redshift samples are consistent with their work, and we succeeded to describe the relation at the rest frame of GRBs with the universal formula of $L_{\gamma,52} = 1.83 \times 10^{-5}[E_p(1 + z)]^{2.0}$. Moreover, according to the hysteresis curve of each events, the pulse properties show *zig-zag* evolution on $E_p(1 + z)$–$L_{\gamma,52}$ plane to keep the E_p–luminosity relation.
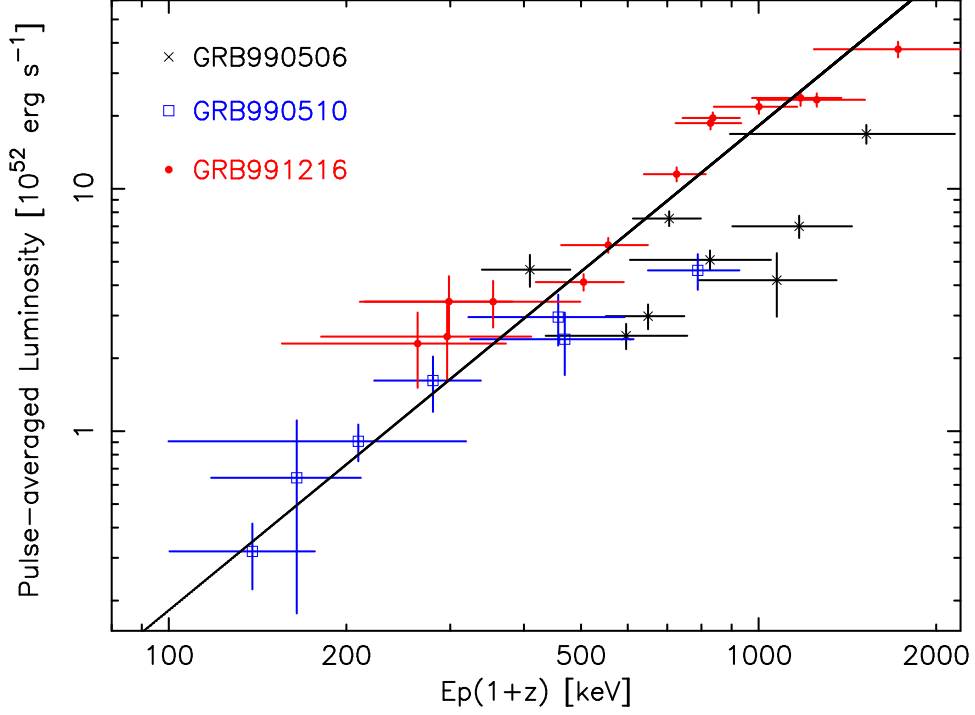
Figure 4.16: E_p–luminosity relation of individual pulses for three events GRB 990506, GRB 990510 and GRB 991216. The strong correlation enable us to describe these average property as $L_{\gamma,52} \propto [E_p(1+z)]^{2.0}$

4.6   Other Samples

In previous section, we have shown the E_p–luminosity relation at the rest frame of GRBs. Hereafter, we investigate the pulse properties for the other samples with known redshift, and test whether the E_p–luminosity relation is really univarsal or not. As shown in figure 4.1, the temporal histories of GRB lightcurves are quite variable, for example, single pulse structure, multiple pulses, the existence of long quiescent time, and so on.

4.6.1   GRB 970508 and GRB 980425

We show lightcurves of GRB 970508 and GRB 980425 in figure 4.17. Each event is faint burst and contain a single pulse. GRB 980425 is one of the closest sample of all GRBs, and its redshift is $z = 0.0085$. Especially, the discovery of a supernova SN 1998bw associated with GRB 980425 revealed that the origin of GRB is a massive star collapse. Therefore, this event is one of the most important event. The spectral analyses are performed between the time interval divided by two dotted lines as shown in figure 4.17. The spectra have been already shown in figure 4.2.

GRB 970508

Adopting the spectral model of equation (4.1) to the spectrum, we obtained the best-fit results with 1 σ uncertainty of $\alpha = -1.0 \pm 0.3$, $\beta = -2.2 \pm 0.1$ and $E_0 = 50.1 \pm 8.4$, respectively. We obtained the acceptable fit with the χ^2 value of 43.8 for 40 degrees of freedom (d.o.f).
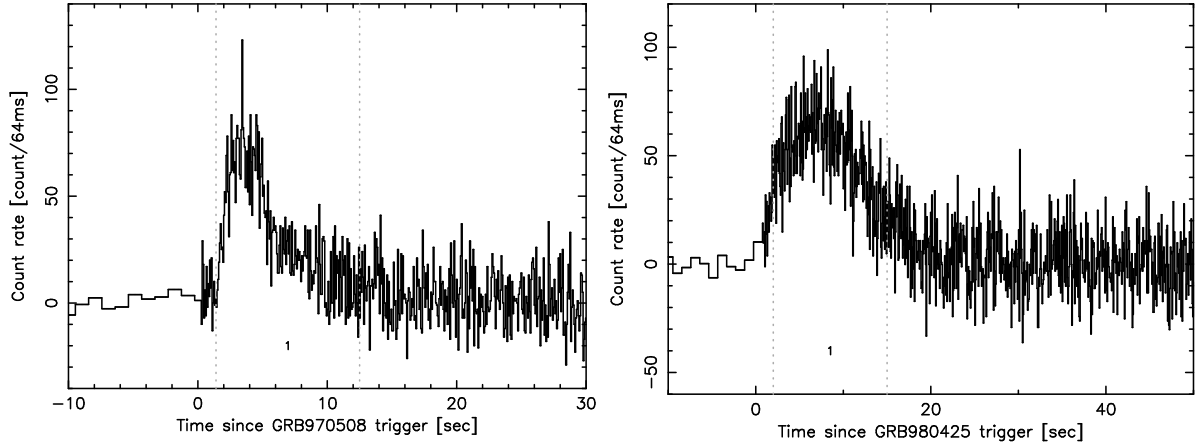
Figure 4.17: Lightcurve of GRB 970508 (left) and GRB 980425 (right), which are composed by a single pulse structure. The spectral analysis is performed between the time interval divided by two dotted lines.

The observed energy flux is $F_\gamma = (0.13 \pm 0.04) \times 10^{-6}$ ergs cm^{-2}s^{-1} , which is integrated from 30–10000 keV. The isotropic luminosity is $L_{\gamma,52} = 0.04 \pm 0.01$ ergs s^{-1} .

GRB 980425

The best-fit results are $\alpha = -0.97 \pm 0.16$, $\beta = -2.06 \pm 0.09$ and $E_0 = 53.3 \pm 6.5$ keV (therefore, $E_p(1 + z) = 55.1 \pm 11.6$ keV). This is an acceptable fit with the χ^2 value is 36.4 for 33 d.o.f. The observed flux is $F_\gamma = (0.28 \pm 0.04) \times 10^{-6}$ ergs cm^{-2}s^{-1} . Because of the close distance of GRB 980425, the isotropic luminosity is $L_{\gamma,52} = (4.37 \pm 0.47) \times 10^{-6}$ ergs s^{-1} which is about 5 orders of magnitude smaller than the typical events. A possible interpretation of the low E_p and the extremely low brightness is discussed in Chapter 6.

4.6.2   GRB 970828

An optical counterpart of GRB 970828 was not detected, so this event is categorized into "dark GRB". Based on a discovery of a weak radio flare associated with this event, a host galaxy was found and the redshift was measured as $z = 0.9578$ (Djorgovski et al., 2001). Therefore, GRB 970828 may become a key event to understand the optically dark GRBs. On the other hand, an X-ray afterglow of GRB 970828 was observed with *ASCA* , and an emission feature[1] was detected (Yoshida, Namiki, Yonetoku et al., 2001). Based on the redshift of $z = 0.9578$, we interpreted the emission feature as a radiative recombination edge and continuum of fully ionized iron (Yoneotku et al., 2001). This result indicates that the GRB progenitor exists in the dirty environment such as a star-forming region and/or a dense stellar wind. Therefore, we can assume that the GRB is triggered by the massive star collapses.

The lightcurve of GRB 970828 is shown in figure 4.18 (left). It shows multiple pulses at the early epoch of this event. Thus, we try to fit the pulse profiles with the equation (4.2), and devide into three pulses. We show the fitting results in figure 4.18 (right). There are

---

[1]At first, Yoshida et al. (1999) interpreted the emission feature as the He-like iron, and the redshift was estimated as $z = 0.33$. However, based on the discovery of the host galaxy, we interpreted it as the radiative recombination edge of fully ionized iron in Yoshida, Namiki, Yonetoku et al. (2001) and Yoneotku et al. (2001).

significant residual after the pulse (2). However we cannot extract the spectral data because of its weakness, and did not include it to the individual pulse-sample.
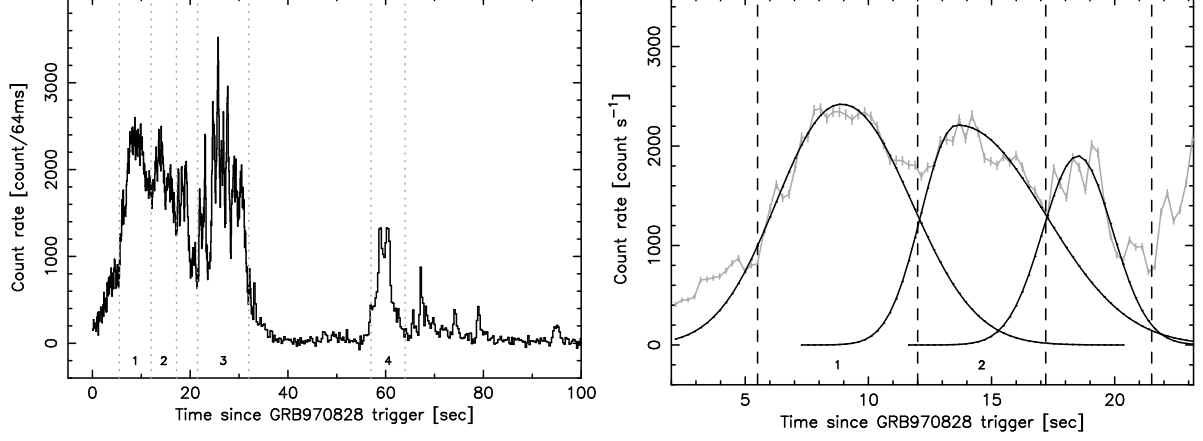
Figure 4.18: The left and the right panel is the lightcurve of GRB 970828 and the fitting curves with equation (4.2). The spectral analyses are performed for 4 pulses as divided by the dotted lines.

GRB	α	β	$E_p(1+z)$	F_γ	$L_{\gamma,52}$	χ^2/ν
970828-1	0.14 ± 0.07	-2.22 ± 0.09	759.2 ± 62.3	4.80 ± 0.23	2.16 ± 0.10	$116.0/106$
970828-2	-0.20 ± 0.09	-1.91 ± 0.10	625.9 ± 89.5	5.97 ± 0.53	2.69 ± 0.24	$99.7/100$
970828-3	-0.71 ± 0.06	-2.12 ± 0.07	604.6 ± 72.3	4.11 ± 0.21	1.85 ± 0.10	$106.3/90$
970828-4	-0.61 ± 0.12	-1.66 ± 0.05	> 358.6	3.01 ± 0.42	1.35 ± 0.19	$105.6/96$

Table 4.11: Fitting results of GRB 970828 spectra

The spectral analysises were performed for 4 pulses. The νF_ν spectra are shown in figure 4.19, and the fitting results are summarized in table 4.11. The high-energy spectral index of the pulse (4) spectrum is $\beta > -2.0$, so we could not determine the peak of νF_ν spectrum. Therefore, we set only the lower limit of $E_p(1+z)$ for the pulse (4) spectrum.

4.6.3 GRB 971214

We show the lightcurve of GRB 971214 in figure 4.20 (left). Although the shape of this burst is slightly anomalous (not *FRED*), we try to fit the each main pulse with equation (4.2). The fitting results are also shown in figure 4.20 (right). As shown in the figure, the contamination from the neighboring pulses is not significant with below 1 %. Therefore we divided the entire lightcurve into 3 parts, and performed the spectral analysises for them. In figure 4.21, we show the νF_ν spectra of these 3 pulses. The fitting results are summarized in table 4.12. The shape of pulse (2) is terribly strange similar to the trapezoid structure, so one may assume that this pulse is multiplied by a lot of short-duration spikes. However such short-duration spikes has the emission power weaker than the main structures, and they may enable to be physically
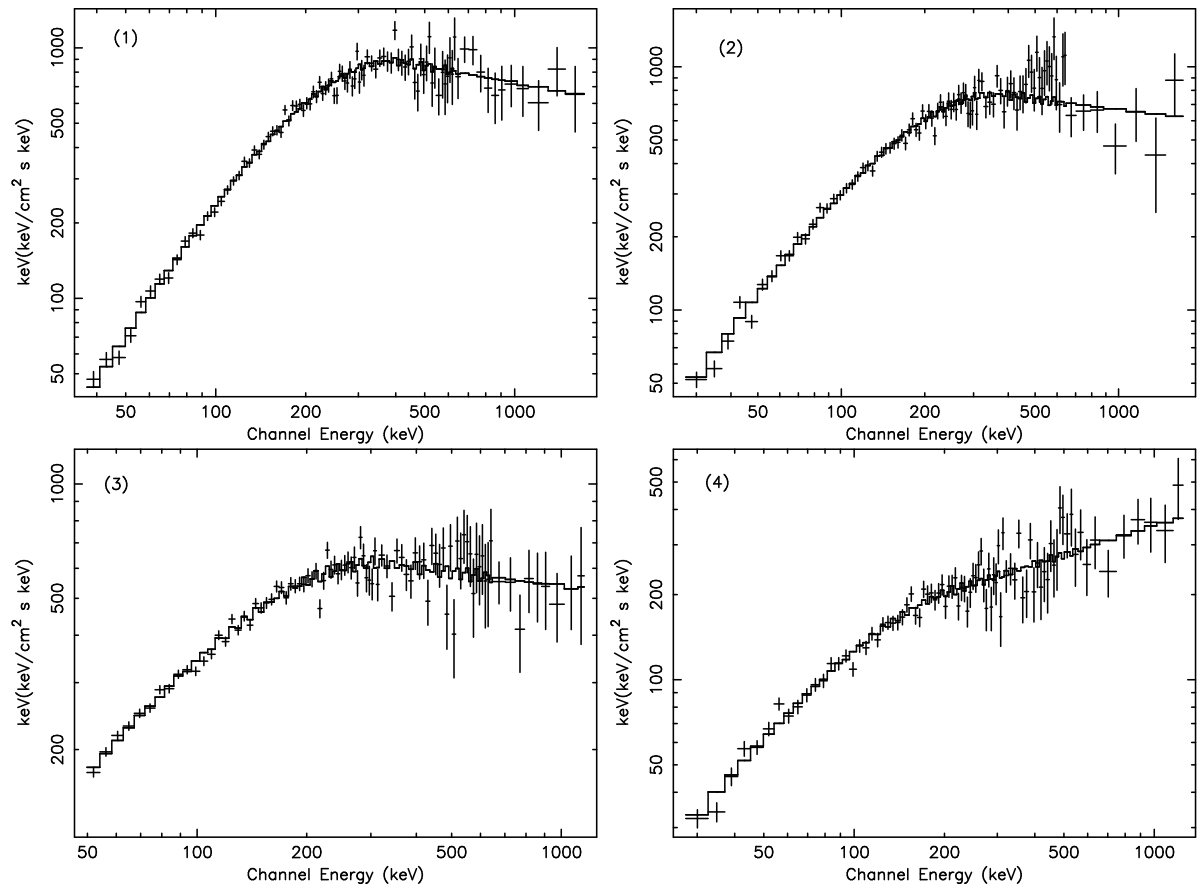
Figure 4.19: The spectra of GRB 970828 which correspond to 4 peaks divided by dotted lines as shown in figure 4.18.

interpreted as the fluctuation of internal shock. Therefore we deal with the pulse (2) as the average property of internal shock, and include individual pulse list.
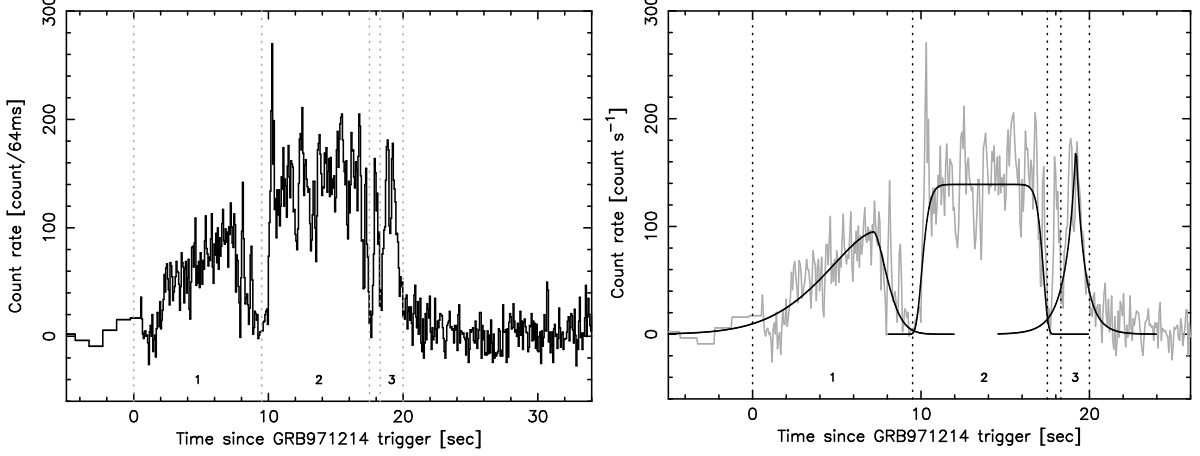
Figure 4.20: The left panel is the entire lightcurve of GRB 971214. The spectral analysises were performed for 3 pulses. The right panel is the results of a pulse fitting with equation (4.2). Scarcely any pulses were contaminated by the other pulses.

GRB	α	β	$E_p(1+z)$	F_γ	$L_{\gamma,52}$	χ^2/ν
971214-1	-0.46 ± 0.47	-2.05 ± 3.12	555.6 ± 176.0	0.52 ± 0.03	5.17 ± 0.28	$40.5/44$
971214-2	-0.56 ± 0.07	-9.37 ± 2.72	913.9 ± 109.8	0.53 ± 0.05	5.30 ± 0.47	$74.8/69$
971214-3	-0.14 ± 0.10	-2.04 ± 0.15	446.4 ± 309.1	0.58 ± 0.03	5.78 ± 0.32	$54.6/49$

Table 4.12: Fitting results of GRB 971214 spectra

4.6.4 GRB 980326 and GRB 980329

The redshift are determined based on the photometric measurement, so only the redshift interval are given as $0.9 \le z \le 1.1$ for GRB 980326, and $2.0 \le z \le 3.9$ for GRB 980329, respectively (Lamb et al., 1999). Although the redshift ambiguity might limit the informations of the intrinsic behavior, they are also important samples, and we briefly summarized the spectral properties of these two GRBs. The lightcurves of both events are shown in figure 4.22. Since a part of data of GRB 980326 lacks, we simply perform the spectral analysis for all arrival data. The νF_ν spectra of GRB 980326 and GRB 980329 are shown in figure 4.23. The fitting results are summarized in table 4.13.

4.6.5 GRB 980703

The lightcurve of GRB 980703 is shown in figure 4.24 (left), and we can recognize two adjacent peaks in the lightcurve. The fitting curves with the model function of equation (4.2) are also shown in figure 4.24 (right). These two pulses are clearly separated with contaminations
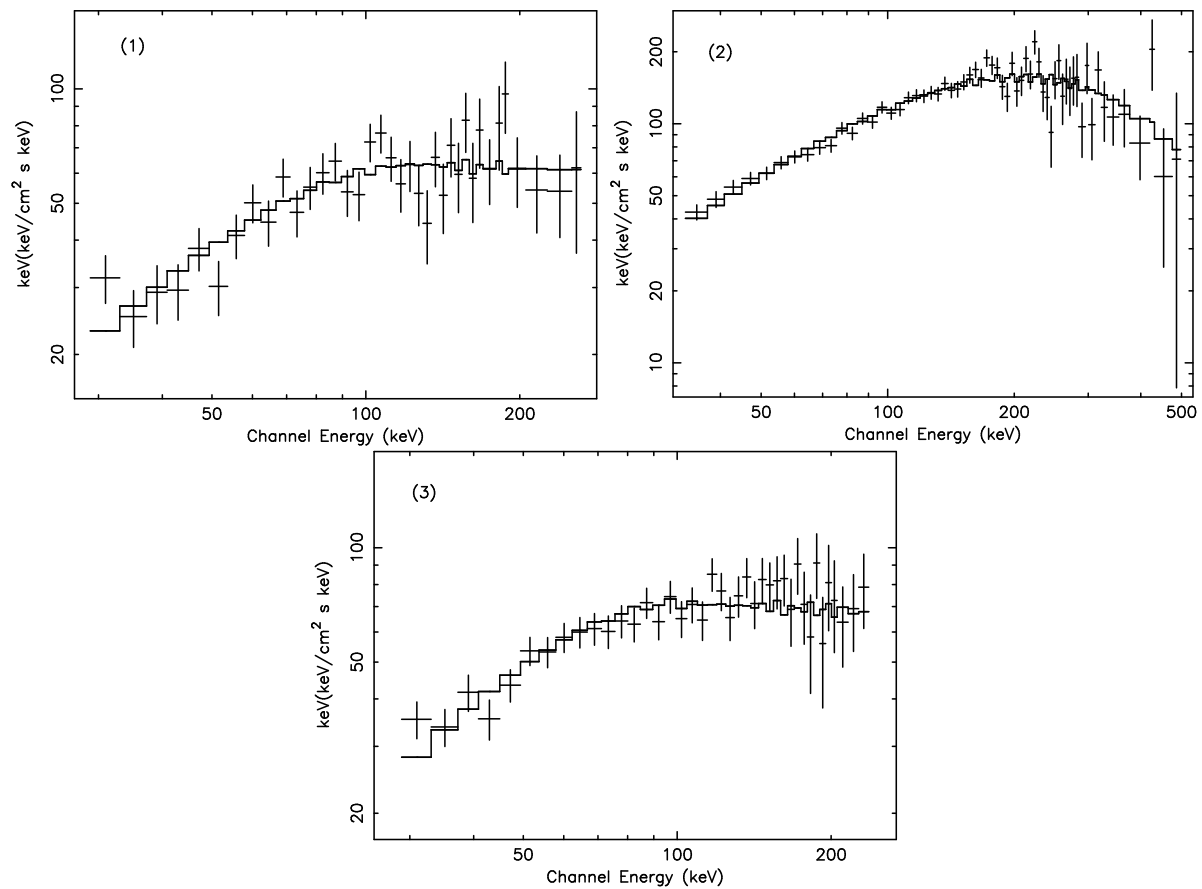
Figure 4.21: The spectra of GRB 971214 which correspond to 3 peaks divided by dotted lines as shown in figure 4.20.
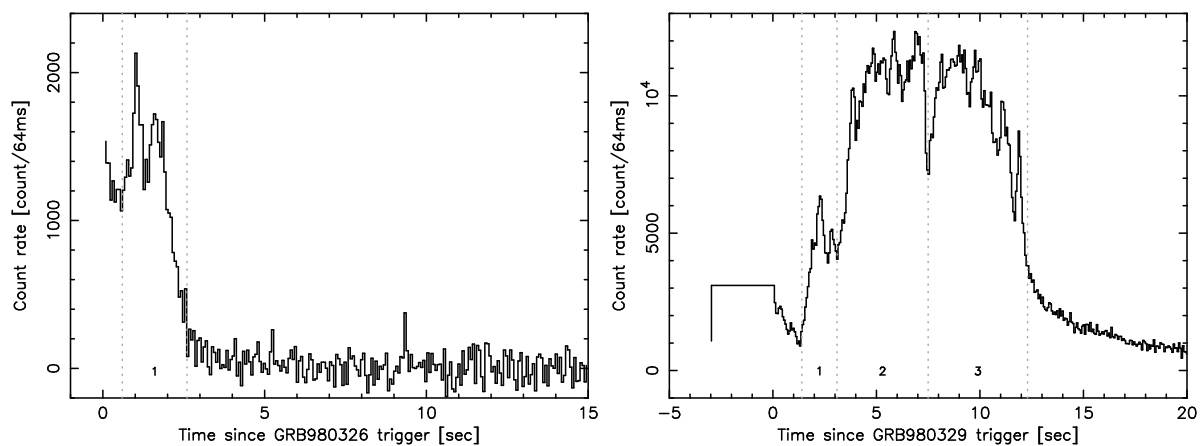
Figure 4.22: The lightcurves of GRB 980326 (left) and GRB 980329 (right). The spectral analysises are performed for 1 pulse and 3 pulse of each GRBs.
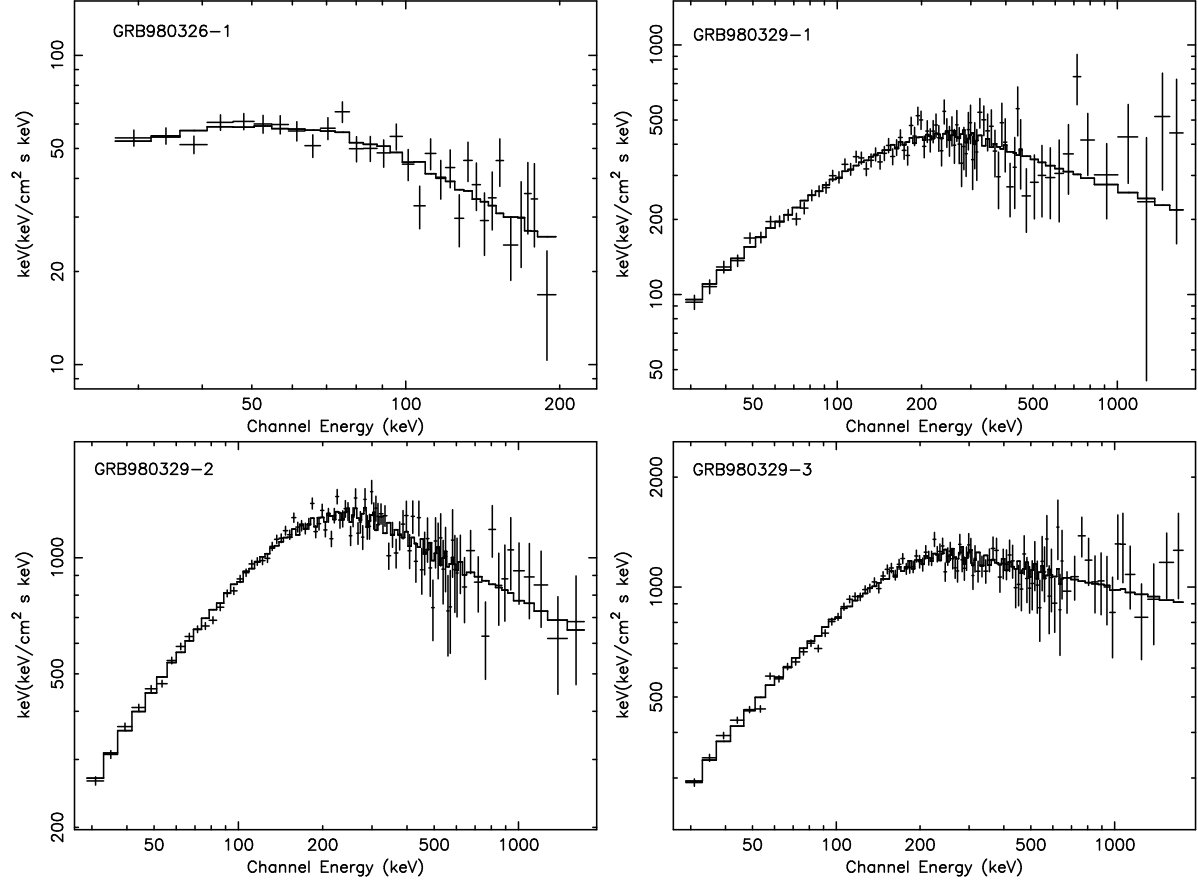
Figure 4.23: The spectra of GRB 980329 (upper-left) and GRB 980329 (the other 3 panels)

GRB	α	β	$E_p(1+z)$	F_γ	$L_{\gamma,52}$	χ^2/ν
980326-1	-1.13 ± 0.42	-2.94 ± 2.79	$[44.0, 174.2]$	0.23 ± 0.12	$[0.09, 0.21]$	$31.6/29$
980329-1	-0.76 ± 0.08	-2.40 ± 0.17	$[647.7, 861.0]$	2.39 ± 0.19	$[6.56, 32.73]$	$109.2/109$
980329-2	-0.12 ± 0.30	-2.34 ± 0.05	$[510.8, 846.5]$	7.17 ± 1.13	$[19.70, 98.30]$	$122.7/105$
980329-3	-0.88 ± 0.03	-2.17 ± 0.04	$[739.4, 849.4]$	8.26 ± 0.27	$[22.70, 113.28]$	$101.9/106$

Table 4.13: Fitting results of GRB 980326 and GRB 980329 spectra

below 15 % each other. However, there are significant residuals after the second pulse. When we adopted the additional component to describe the residuals, we could improve the fitting. However, the contamination from the pulse (2) was above 30 %, and we did not recognize this residual as the individual pulse sample.
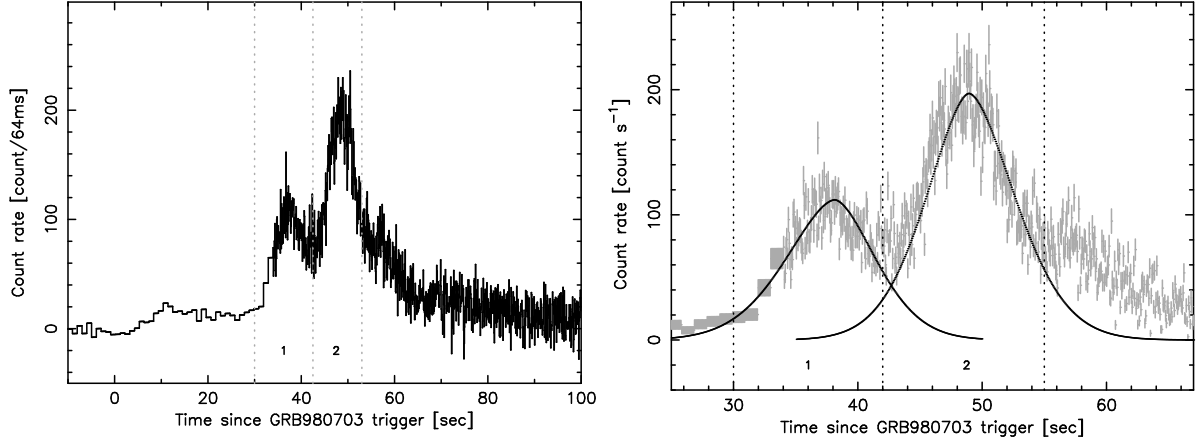
Figure 4.24: The left panel is the lightcurve of GRB 980703, and the right one is the fitting results with equation (4.2) for two pulses. There were significant residuals after the pulse (2), but we did not recognize it as an individual pulse because more than 30 % of the residuals were contaminated by the pulse (2). Therefore, the spectral analysises were performed for two pulses.

We performed the spectral analysis for these two pulses. The νF_ν spectra were shown in figure 4.25. These spectra could be described by the GRB spectral model of equation (4.1) and we could obtain the acceptable fit, but the high-energy spectral indices β of both spectra are $\beta > -2.0$. Therefore, we could not determine the E_p, and set only the lower limit as E_0 for these two pulses. The best-fit results were summarized in table 4.14. In figure 4.26, we show the background lightcurve before/after the GRB event. Since the background rate obviously changes and it has energy dependence, it is too difficult to model the variation. This kind of continuous variation is caused by the satellite environment, e.g. South Atlantic Anomaly. We should exclude this event from individual pulse list because the background modeling cannot be made correctly.

GRB	α	β	$E_p(1+z)$	F_γ	$L_{\gamma,52}$	χ^2/ν
980703-1	0.63 ± 0.45	-1.54 ± 0.11	> 128.6	1.28 ± 0.05	0.59 ± 0.02	$93.5/84$
980703-2	-0.63 ± 0.17	-1.73 ± 0.10	> 300.8	2.24 ± 0.43	1.03 ± 0.20	$68.7/60$

Table 4.14: Fitting results of GRB 980703 spectra
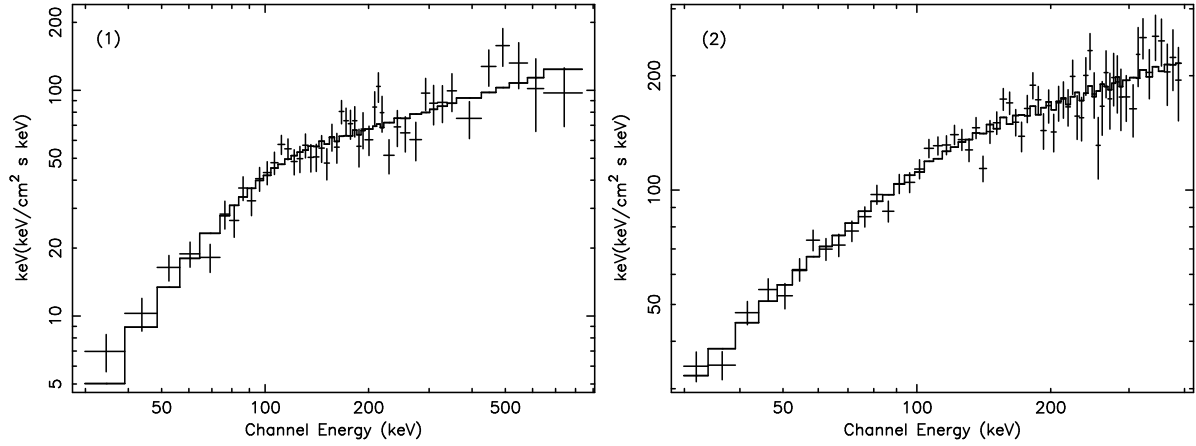
Figure 4.25: The spectra of GRB 980703 which correspond to 2 peaks divided by dotted lines as shown in figure 4.24.
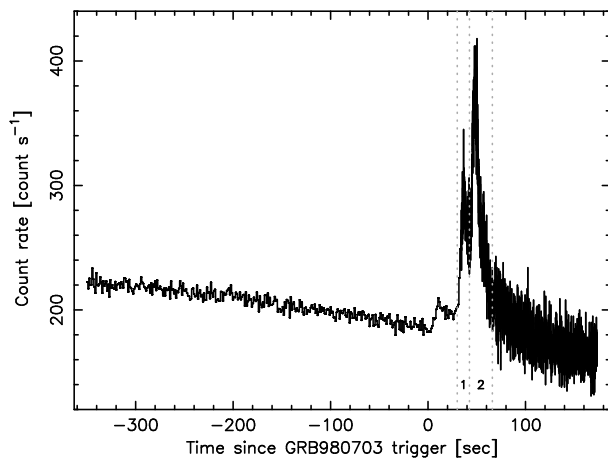
Figure 4.26: Background lighrcurve of GRB 980703. The background level significantly changes within the event interval.

4.6.6 GRB 990123

GRB 990123 is one of the most energetic event of all GRBs, and the isotropic equivalent energy radiated in gamma-ray band exceeds 10^{54} ergs (Amati et al., 2002). The existence of a collimated jet was established by the detail observation of an afterglow of this event (Kulkarni et al., 1999), and the released energy was modified as $\sim 10^{51}$ ergs with a geometrical correction (Frail et al., 2001; Bloom et al., 2003). Performing the time resolved analysis, the detail gamma-ray properties of GRB 990123 observed with *BATSE* were reported by Briggs et al. (1999). The X-ray afterglow was observed by the *ASCA* satellite after 54 hrs since GRB trigger time. The decline of X-ray flux is expressed as $F_X \propto t^{-1.4}$ which is the standard temporal behavior of the other X-ray afterglows. The spectrum is well fitted by the absorbed power-law with a photon index of 1.8 ± 0.1. The detail analysis is reported as Yoneotku et al. (2000).

The lightcurve of GRB 990123 is shown in figure 4.27 (left). The fitting curves for two bright peaks in the lightcurve are also shown in figure 4.27 (right). Although a sub-peak is found between the peak (1) and the peak (2), we did not include it as the independent sample because the contamination from the neighboring pulses was above 60 % of its count rate. Therefore, we performed the spectral analysis for two peaks as shown in figure 4.27.

The νF_ν spectra of these two pulses are shown in figure 4.28, and the best-fit results are summarized in table 4.15. The $E_p(1 + z)$ of the peak (1) reported by Briggs et al. (1999) is 1470 ± 110 keV, and the BeppoSAX results reported by Amati et al. (2002) is 2030 ± 161 which is the average value of the entire duration. Our results are consistent with these previous works within 1 σ uncertainty.
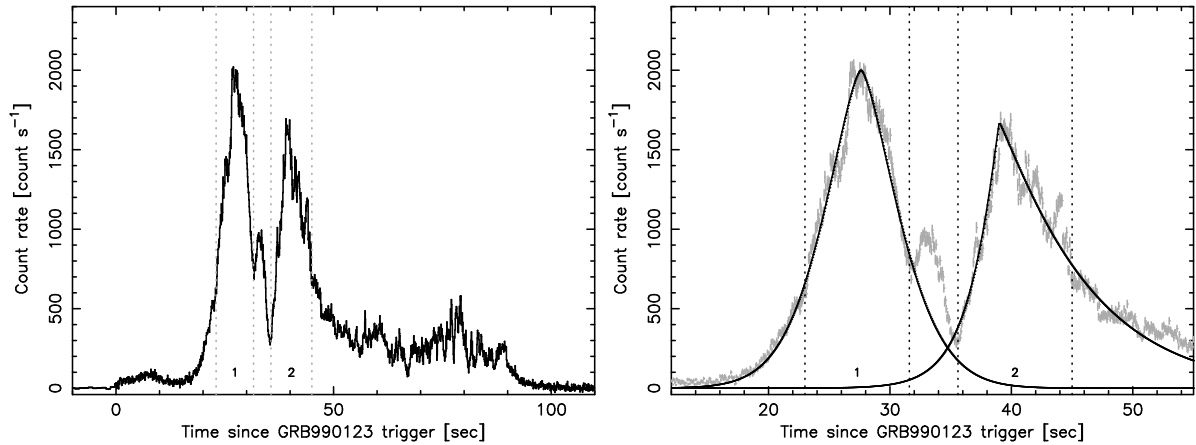
Figure 4.27: The left and right panel is the lightcurve of GRB 990123 and the fitting results with equation (4.2), respectively. The spectral analysises are performed for two pulses.

GRB	α	β	$E_p(1 + z)$	F_γ	L	χ^2/ν
990123-1	-0.25 ± 0.11	-2.08 ± 0.20	1929.2 ± 392.0	31.67 ± 3.47	50.42 ± 5.52	$112.9/108$
990123-2	-0.25 ± 0.08	-2.42 ± 0.19	1500.1 ± 194.9	20.29 ± 0.61	32.31 ± 0.97	$109.6/108$

Table 4.15: Fitting results of GRB 99023 spectra
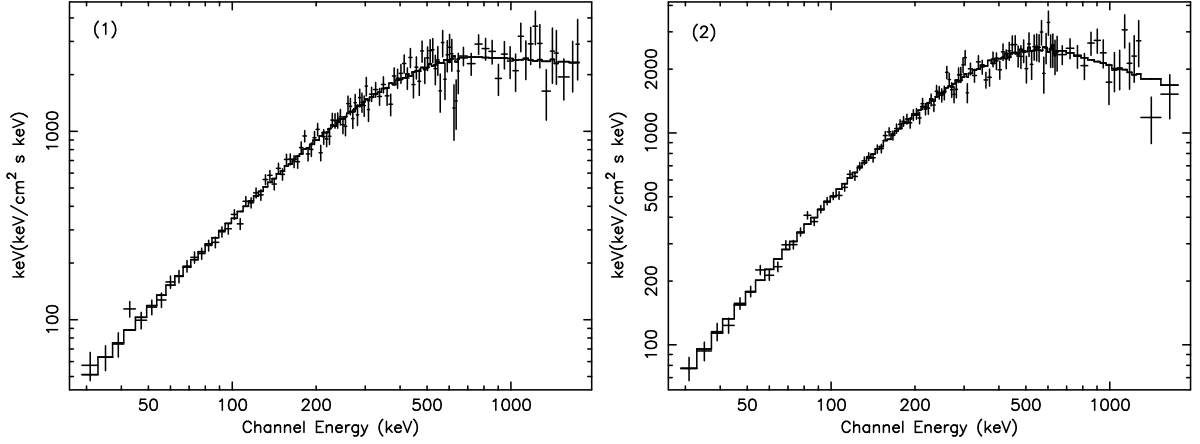
Figure 4.28: The spectra of GRB 990123. The left and right panel is correspond to the pulse (1) and (2), respectively.

4.6.7   GRB 000131

The redshift of GRB 000131 is measured as $z \sim 4.5$, which is the current record holder in distance, with the Lyα-break by the VLT observation (Andersen et al., 2000). The lightcurve of GRB 000131 is shown in figure 4.29. Although GRB 000131 occurred at the very cosmological distance as $z \sim 4.5$, it was enough bright. We selected 5 pulses from the entire lightcurve as shown in figure 4.29. The other dim pulses could not be analyzed because of poor statistics. We show the spectrum of these 5 pulses in figure 4.31, and the best-fit results are summarized in table 4.16. We set only the lower limit of $E_p(1+z)$ for the pulse (1), because the high-energy spectral index was $\beta > -2.0$.
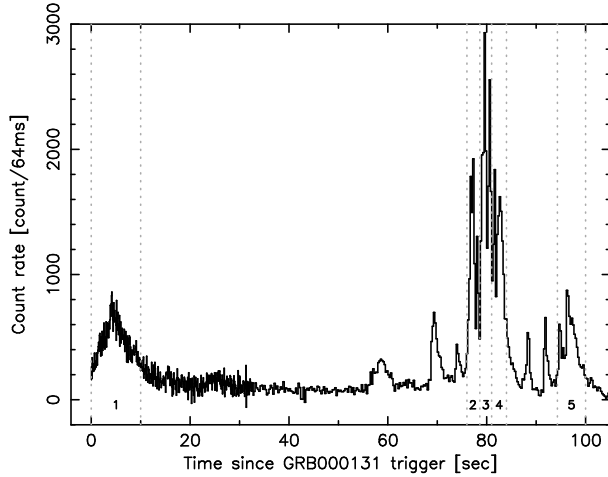
Figure 4.29: The lightcurve of GRB 000131. The spectral analysises are performed for 5 pulses divided by dotted lines.
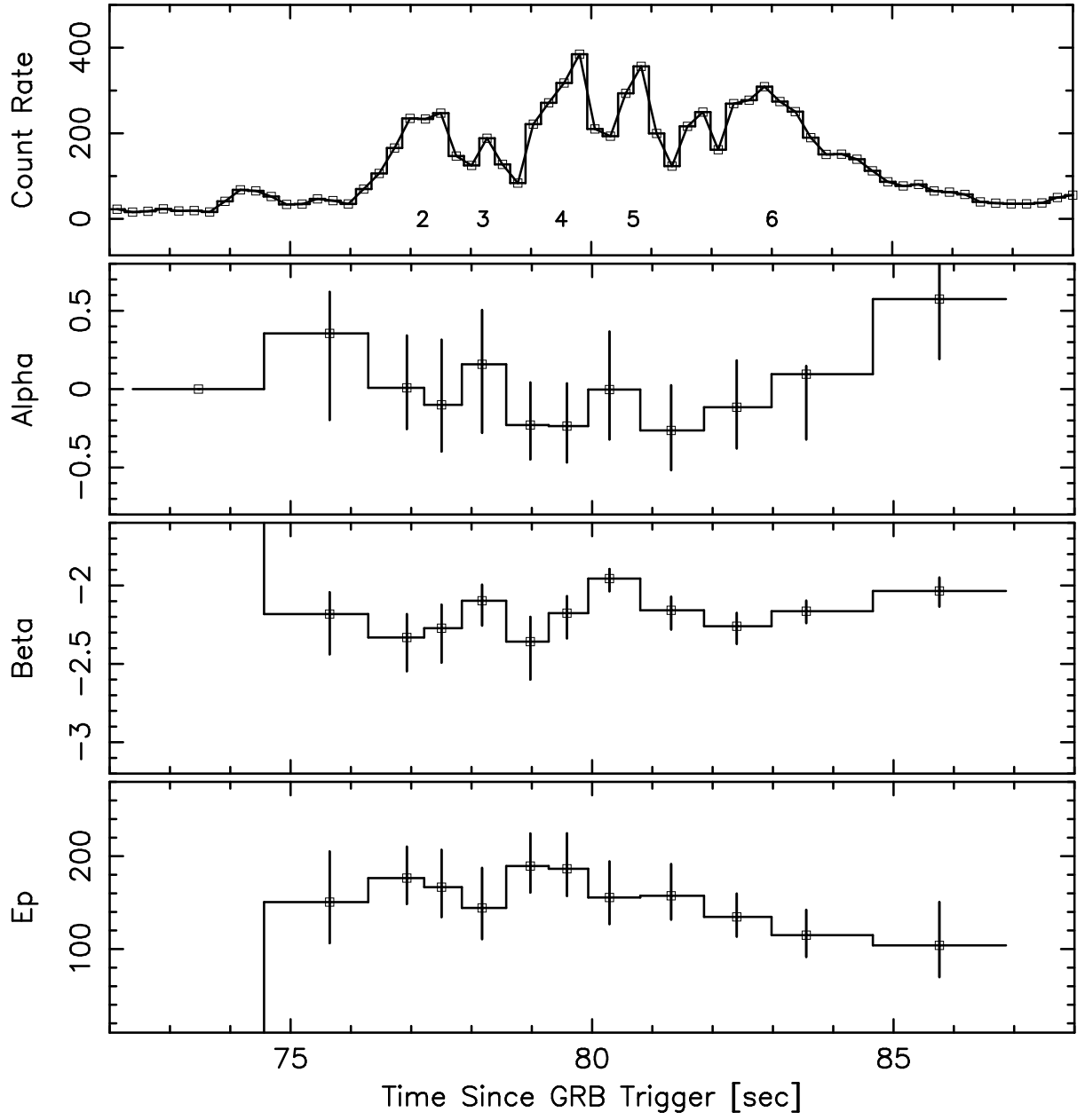
Figure 4.30: Top panel is the lightcurve of GRB 000131, which is enlarged for the purpose of clarity of the main emission phase. Second, third and bottom panel are the time history of the spectral index α, β and E_p in the observer's rest frame.

GRB	α	β	$E_p(1+z)$	F_γ	L	χ^2/ν
000131-1	-0.93 ± 0.14	-2.19 ± 0.26	1656.4 ± 263.5	0.72 ± 0.24	13.9 ± 2.62	$59.8/57$
000131-2	-0.22 ± 0.28	-2.23 ± 0.15	933.4 ± 299.6	1.87 ± 0.72	35.9 ± 13.8	$89.9/86$
000131-3	-0.41 ± 0.35	-2.41 ± 0.27	969.2 ± 209.7	1.45 ± 0.85	27.8 ± 16.4	$104.5/110$
000131-4	-0.47 ± 0.20	-2.18 ± 0.12	1072.5 ± 302.7	2.52 ± 0.61	48.5 ± 11.7	$123.6/108$
000131-5	-0.51 ± 0.28	-2.18 ± 0.09	768.7 ± 277.1	1.57 ± 0.68	30.2 ± 13.1	$97.1/108$
000131-6	-0.34 ± 0.16	-2.48 ± 0.07	501.1 ± 68.8	0.43 ± 0.19	8.32 ± 3.59	$97.1/108$

Table 4.16: Fitting results of GRB 000131 spectra
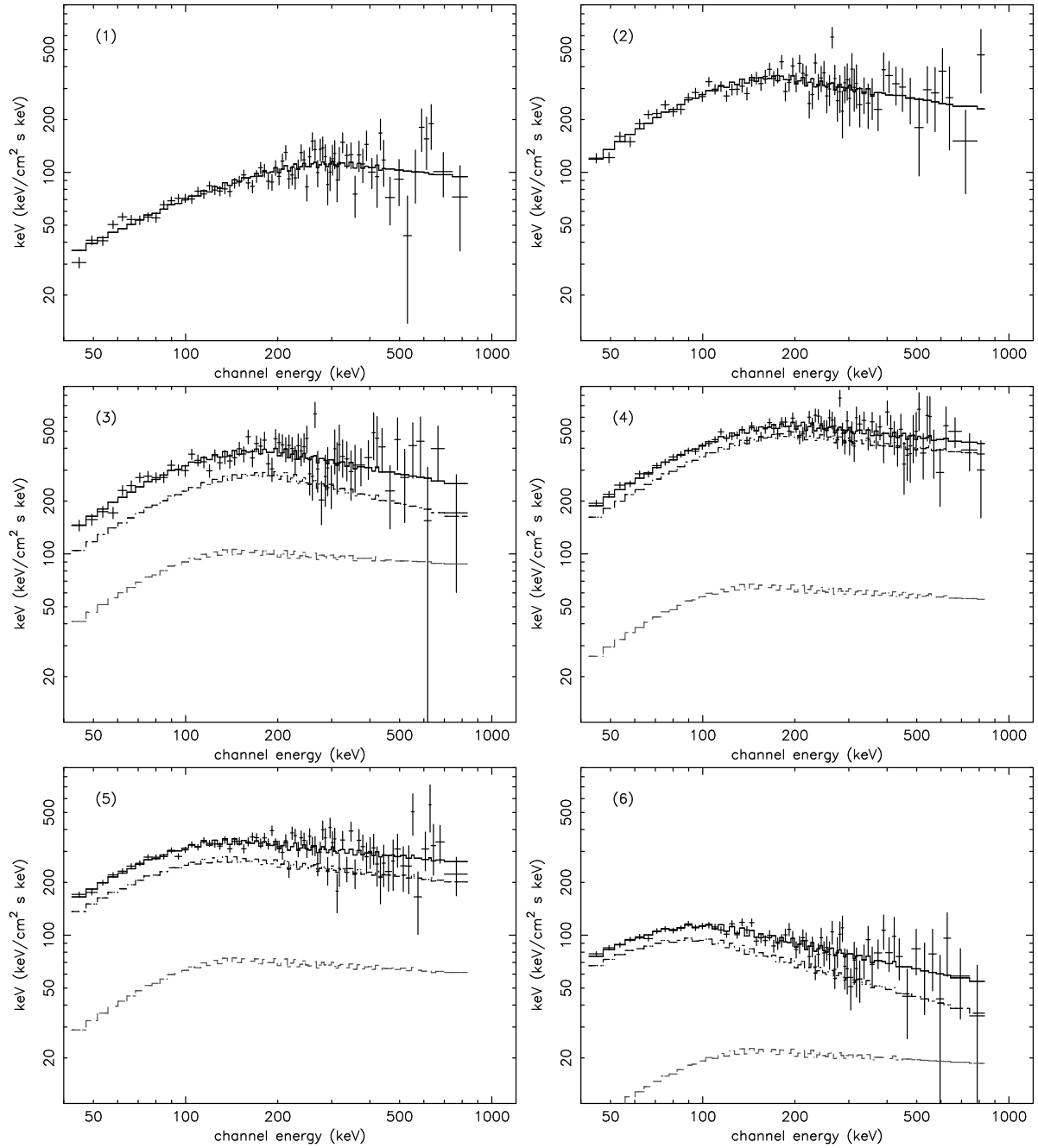
Figure 4.31: The spectra of GRB 000131 which correspond to 7 peaks divided by dotted lines as shown in figure 4.29.
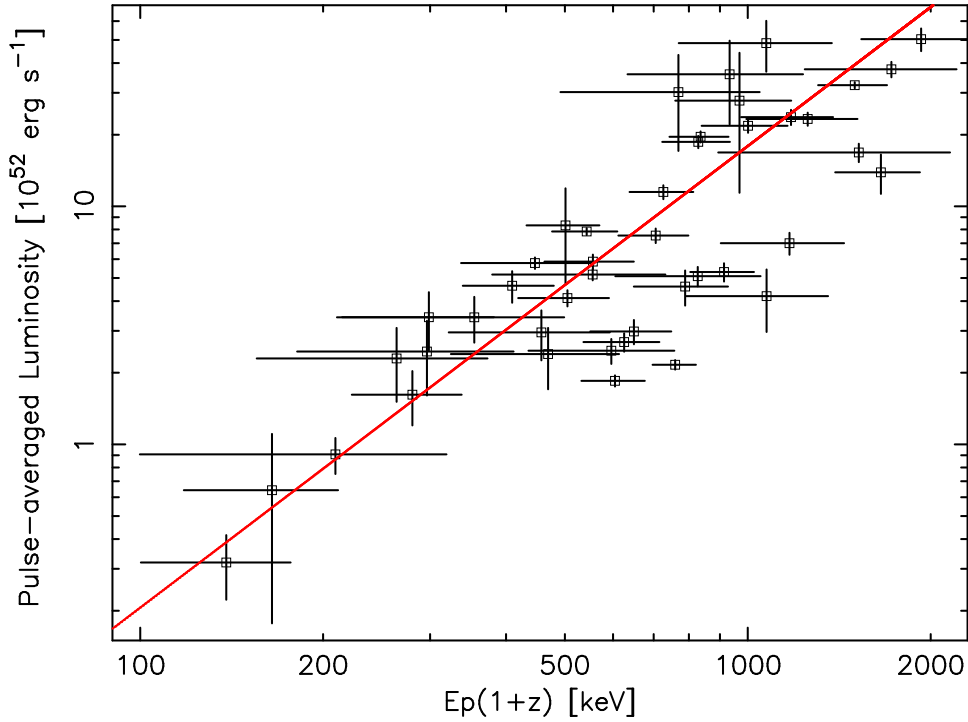
Figure 4.32: E_p–luminosity relation. The open squares are results the samples with firm redshift, and the cross points represent the unbiguous redshift samples (GRB 980326 and GRB 980329). The uncertainties of all data points is 1 σ error. The solid line is the best-fit power-law model of $L_{\gamma,52} \propto [E_p(1+z)]^{1.94}$.

4.7 Universal Formula of E_p–Luminosity Relation

We extracted 51 pulses from 12 GRBs detected by *BATSE* with known redshifts, and performed the spectral analysises for them. We could determin the $E_p(1+z)$ for 48 pulses, and set lower-limits for remaining 3 pulses because the high-energy spectral indices were $\beta > -2$ within 1 σ uncertainty. Only the case of GRB 980703, because of the background instability, could not be determined the E_p even if we used all pulse events. The fitting results for 48 pulses are summalized again in table 4.17.

In figure 4.32, we show the observed isotropic pulse-averaged luminosity in the unit of 10^{52} erg s^{-1} as a function of the $E_p(1+z)$ at the rest frame of GRBs. There is a fine positive correlation between $E_p(1+z)$ and $L_{\gamma,52}$ similarly to figure 4.16. A linear correlation coefficient including the weighting factors is 0.888 for 41 d.o.f. (except for GRB 980326, GRB 980329 and GRB 980425) for $\log[E_p(1+z)]$ and $\log[L/10^{52}$ erg s$^{-1}]$, and the chance probability is 2.02×10^{-15}. When we adopt the power-law model to the E_p–luminosity relation, we obtained the best-fit function is

$$\frac{L_\gamma}{10^{52} \text{ ergs s}^{-1}} = (2.72 \pm 0.15) \times 10^{-5} \left[\frac{E_p(1+z)}{1 \text{ keV}} \right]^{1.94 \mp 0.19} \tag{4.6}$$

Where the uncertainties are 1 σ error. The deviations of data distribution arround the best fit function are factor 3 in $E_p(1+z)$ and 10 in $L_{\gamma,52}$.
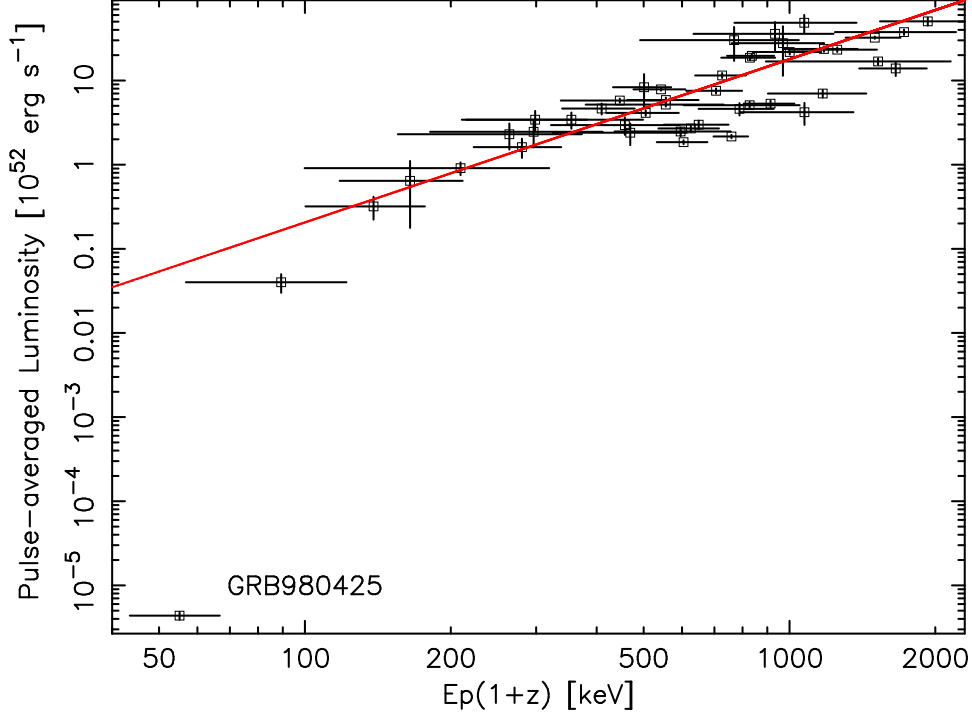
Figure 4.33: E_p–luminosity relation including the closest sample of GRB 980425. The marks are the same of figure 4.32.

We have shown the E_p–luminosity relation for firmly identified pulse samples of three GRB events (GRB 990506, GRB 990510 and GRB 991216) in figure 4.16. Although the temporal properties are considerably different from event by event and do never show same structures, we confirmed that this E_p–luminosity relation is universally established for all pulses in 12 GRBs with known redshifts. This observed property must refrect the individual internal shock physics. Using this result, in Chapter 6, we will give a probable interpretation for this formula within the frame work of the standard synchrotron shock model, and estimate the physical condition of the internal shocks.

In figure 4.33, we again show the E_p–luminosity relation but including the results of GRB 980425. This event is remarkably apart from the other populations. The redshift of GRB 980425 is $z = 0.0085$, which is two orders of magnitude closer than the other GRBs. Therefore, there is a possibility that GRB 980425 could be detected because of the close distance, although it was too much dimer than the others. We will also discuss about this point in Chapter 6.

GRB	α	β	$E_p(1+z)$	F_γ	$L_{\gamma,52}$	χ^2/ν
970508-1	-1.03 ± 0.31	-2.20 ± 0.08	89.3 ± 32.5	0.13 ± 0.00	0.04 ± 0.01	$43.8/40$
970828-1	0.14 ± 0.07	-2.22 ± 0.09	759.2 ± 62.3	4.80 ± 0.23	2.16 ± 0.10	$116.0/106$
970828-2	-0.20 ± 0.09	-1.91 ± 0.10	625.9 ± 89.5	5.97 ± 0.53	2.69 ± 0.24	$99.7/100$
970828-3	-0.71 ± 0.06	-2.12 ± 0.07	604.6 ± 72.3	4.11 ± 0.21	1.85 ± 0.10	$106.3/90$
971214-1	-0.46 ± 0.47	-2.05 ± 3.12	555.6 ± 176.0	0.52 ± 0.03	5.17 ± 0.28	$40.5/44$
971214-2	-0.56 ± 0.07	-9.37 ± 2.72	913.9 ± 109.8	0.53 ± 0.05	5.30 ± 0.47	$74.8/69$
971214-3	-0.14 ± 0.10	-2.04 ± 0.15	446.4 ± 309.1	0.58 ± 0.03	5.78 ± 0.32	$54.6/49$
980326-1	-1.13 ± 0.42	-2.94 ± 2.79	$[44.0, 174.2]$	0.23 ± 0.12	$[0.09, 0.21]$	$31.6/29$
980329-1	-0.76 ± 0.08	-2.40 ± 0.17	$[647.7, 861.0]$	2.39 ± 0.19	$[6.56, 32.73]$	$109.2/109$
980329-2	-0.12 ± 0.30	-2.34 ± 0.05	$[510.8, 846.5]$	7.17 ± 1.13	$[19.70, 98.30]$	$122.7/105$
980329-3	-0.88 ± 0.03	-2.17 ± 0.04	$[739.4, 849.4]$	8.26 ± 0.27	$[22.70, 113.28]$	$101.9/106$
980425-1	-0.97 ± 0.16	-2.06 ± 0.09	55.1 ± 11.6	0.28 ± 0.04	4.37×10^{-6}	$36.4/33$
990123-1	-0.25 ± 0.11	-2.08 ± 0.20	1929.2 ± 392.0	31.67 ± 3.47	50.42 ± 5.52	$112.9/108$
990123-2	-0.25 ± 0.08	-2.42 ± 0.19	1500.1 ± 194.9	20.29 ± 0.61	32.31 ± 0.97	$109.6/108$
990506-1	-1.05 ± 0.01	-2.10 ± 0.25	1523.0 ± 629.0	17.60 ± 1.51	16.84 ± 1.50	$110.2/100$
990506-2	-0.74 ± 0.09	-2.48 ± 0.33	1073.9 ± 281.9	4.40 ± 1.29	4.20 ± 1.23	$103.5/100$
990506-3	-0.81 ± 0.14	-3.27 ± 0.64	1171.4 ± 268.8	7.34 ± 0.98	7.00 ± 0.94	$112.9/104$
990506-4	-1.13 ± 0.06	-2.08 ± 0.17	827.3 ± 222.2	5.33 ± 0.50	5.09 ± 0.47	$115.6/108$
990506-5	-1.23 ± 0.08	-2.21 ± 0.16	596.2 ± 160.7	2.59 ± 0.31	2.48 ± 0.28	$115.4/106$
990506-6	-0.81 ± 0.10	-2.38 ± 0.11	409.5 ± 70.0	4.86 ± 0.74	4.64 ± 0.70	$111.6/102$
990506-7	-0.95 ± 0.05	-2.78 ± 0.26	705.3 ± 93.1	7.90 ± 0.55	7.54 ± 0.53	$107.6/101$
990506-8	-0.54 ± 0.10	-9.37 ± 4.14	649.4 ± 99.0	3.12 ± 0.37	2.98 ± 0.35	$105.4/101$
990510-1	-0.34 ± 0.38	-2.96 ± 0.26	209.5 ± 109.6	0.55 ± 0.08	0.91 ± 0.15	$39.1/36$
990510-2	-0.78 ± 0.16	-3.28 ± 0.35	280.5 ± 57.6	0.98 ± 0.25	1.62 ± 0.42	$65.8/58$
990510-3	-0.87 ± 0.06	-3.70 ± 0.71	164.8 ± 46.8	0.39 ± 0.28	0.64 ± 0.46	$35.2/31$
990510-4	-1.04 ± 0.07	-2.53 ± 0.05	788.5 ± 139.3	2.81 ± 0.47	4.60 ± 0.77	$84.8/78$
990510-5	-0.65 ± 0.23	-2.46 ± 0.18	469.2 ± 133.6	1.46 ± 0.42	2.40 ± 0.69	$100.1/92$
990510-6	-0.84 ± 0.19	-2.47 ± 0.17	457.3 ± 135.4	1.80 ± 0.43	2.96 ± 0.70	$75.2/80$
990510-7	-1.56 ± 0.09	-9.37 ± 5.22	138.3 ± 38.3	0.19 ± 0.06	0.32 ± 0.10	$42.1/38$
991216-1	-0.58 ± 0.06	-2.17 ± 0.06	726.1 ± 87.3	21.89 ± 1.47	11.50 ± 0.77	$107.4/105$
991216-2	-0.69 ± 0.06	-2.25 ± 0.11	828.8 ± 105.7	35.55 ± 2.09	18.66 ± 1.10	$116.4/104$
991216-3	-0.29 ± 0.11	-2.51 ± 0.32	1178.2 ± 203.5	45.15 ± 3.31	23.7 ± 2.82	$114.6/106$
991216-4	-0.70 ± 0.09	-2.12 ± 0.86	1723.6 ± 482.7	71.72 ± 5.37	37.65 ± 2.82	$106.9/109$
991216-5	-0.57 ± 0.11	-2.20 ± 0.86	1255.0 ± 260.4	44.36 ± 2.82	23.29 ± 1.48	$116.5/99$
991216-6	-0.78 ± 0.06	-2.29 ± 0.19	1001.1 ± 161.5	41.55 ± 2.73	21.82 ± 1.43	$121.1/109$
991216-7	-0.77 ± 0.05	-3.46 ± 0.56	836.2 ± 93.2	37.34 ± 2.01	19.61 ± 1.05	$112.2/109$
991216-8	-0.81 ± 0.21	-4.04 ± 2.10	298.5 ± 83.6	6.52 ± 1.78	3.42 ± 0.93	$110.8/105$
991216-9	-1.12 ± 0.20	-2.46 ± 0.23	264.2 ± 108.7	4.37 ± 1.50	2.30 ± 0.79	$100.7/90$
991216-10	-0.91 ± 0.23	-2.45 ± 0.20	296.4 ± 115.2	4.68 ± 1.62	2.46 ± 0.85	$80.5/68$
991216-11	-0.82 ± 0.28	-2.72 ± 0.57	354.7 ± 143.9	6.51 ± 1.42	3.42 ± 0.74	$90.6/78$
991216-12	-1.15 ± 0.07	-2.71 ± 0.25	504.9 ± 86.0	7.85 ± 0.62	4.12 ± 0.32	$112.4/103$
991216-13	-1.24 ± 0.05	-2.92 ± 0.79	555.9 ± 93.3	11.16 ± 0.79	5.86 ± 0.41	$121.8/109$
000131-1	-0.93 ± 0.14	-2.19 ± 0.26	1656.4 ± 263.5	0.72 ± 0.24	13.9 ± 2.62	$59.8/57$
000131-2	-0.22 ± 0.28	-2.23 ± 0.15	933.4 ± 299.6	1.87 ± 0.72	35.9 ± 13.8	$89.9/86$
000131-3	-0.41 ± 0.35	-2.41 ± 0.27	969.2 ± 209.7	1.45 ± 0.85	27.8 ± 16.4	$104.5/110$
000131-4	-0.47 ± 0.20	-2.18 ± 0.12	1072.5 ± 302.7	2.52 ± 0.61	48.5 ± 11.7	$123.6/108$
000131-5	-0.51 ± 0.28	-2.18 ± 0.09	768.7 ± 277.1	1.57 ± 0.68	30.2 ± 13.1	$97.1/108$
000131-6	-0.34 ± 0.16	-2.48 ± 0.07	501.1 ± 68.8	0.43 ± 0.19	8.32 ± 3.59	$97.1/108$

Table 4.17: Summary of the fitting results of GRB spectra

Chapter 5

GRB Formation Rate

Many ground based telescopes have tried to detect optical afterglows of GRBs and to measure their redshifts by using the spectral absorption and/or emission lines of the interstellar matter in the host galaxy. However, the number of GRBs with measured redshift is only a fraction of all GRBs detected with *BATSE* , *BeppoSAX* , *HETE-2* and *INTEGRAL* satellites; we have still only about 40 GRBs with the known redshifts. The most of them occur at the cosmological distance, and the current record holder is GRB 000131 at $z = 4.5$ (Andersen et al., 2000). According to the brightness distribution of GRBs with the known redshifts, the above satellites should have already detected much more distant GRBs, such as at $z \sim 20$ (Band, 2003). If we can establish a method for estimating the intrinsic brightness from the characteristics of the prompt gamma-ray emission, we can use the brightness of the GRB as a lighthouse to determine the unknown redshifts of majority of GRBs, which enables us to explore the early universe out to $z \sim 20$.

Several authors tried to establish a method for estimating the isotropic luminosity from the observed GRB properties. Using the lightcurves of the prompt gamma-ray emissions, a pioneering work has been done; the variability–luminosity relation reported by Fenimore & Ramirez-Ruiz (2000), which indicates that the variable GRBs are much brighter than the smooth ones (figure 5.1). The spectral time-lag, which is the interval of the peak arrival times between two different energy bands, also correlates with the isotropic luminosity (Norris et al., 2000) (figure 5.2). These properties based on the time-series data might be due to the effect of the viewing angle from the GRB jet (e.g., Ioka & Nakamura, 2001; Norris, 2002; Murakami et al., 2003).

On the other hand, based on the spectral analyses with the k-correction (Bloom et al., 2001), Amati et al. (2002) found the correlation between the isotropic-equivalent energy radiated in GRBs and the peak energies E_p, which is the energy at the peak of νF_ν spectrum. Atteia (2003) suggested a possibility to use this as the empirical redshift indicator.

In this Chapter, applying the E_p–luminosity relation of equation (4.5) to the GRBs without known redshifts, we estimate their redshifts from the observed peak energy (E_p) and the energy flux (F_γ). Although the E_p–E_{iso} relation by Amati et al. (2002) may be useful to estimate the unknown redshifts, our E_p–luminosity relation is an order of magnitude tighter than the previous E_p–E_{iso} relation. Therefore, we choose to use the E_p–luminosity relation. Then, we demonstrate the GRB formation rate out to $z \sim 12$ and the luminosity evolution using the
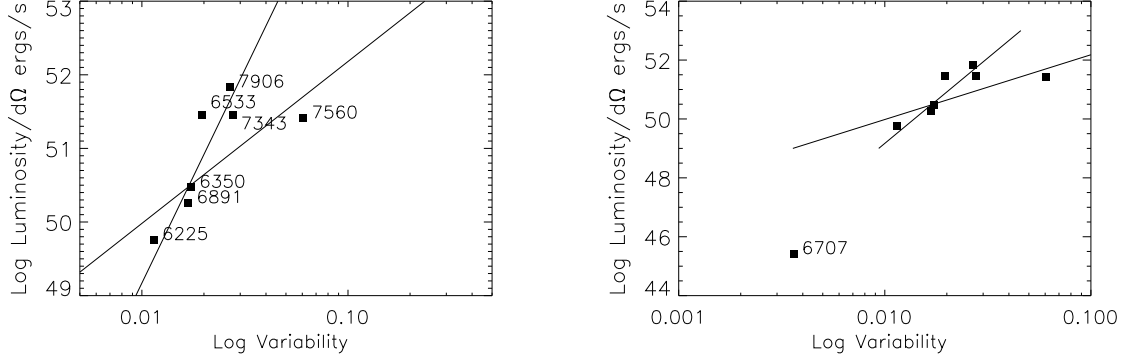
Figure 5.1: The variability–luminosity (V-L) relation of Fenimore & Ramirez-Ruiz (2000). The left panel is the V-L relation of the cosmological GRB samples. The right one is the same of the left one, but the GRB 980425 is included. There is a positive correlation between the degree of the variability and the source luminosity.
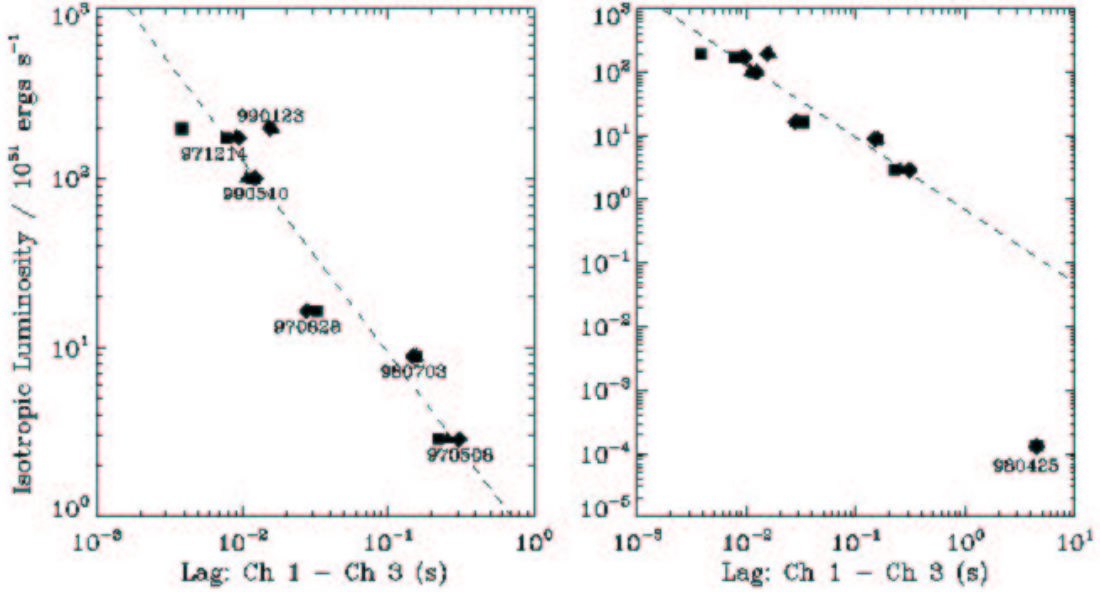
Figure 5.2: The spectral time lag–luminosity relation of Norris et al. (2000). The left panel is the V-L relation of the cosmological GRB samples. The right one is the same of the left one, but the GRB 980425 is included. There is a negative correlation between the time-lag and the isotropic luminosity. Although GRB 980425 is apart from the other population, this can be explained as the off-axis model by Ioka & Nakamura (2001); Murakami et al. (2003). There are two types of plot, filled-squares and the filled-diamonds, and they are the fitting results with the different model functions.

non-parametric method (Lynden-Bell, 1971; Efron & Petrosian, 1992; Petrosian, 1993; Maloney & Petrosian, 1999) which is summarized in Appendix A. Some part of results in this chapter are published by Yoneotku et al. (2004).

5.1 Spectral properties of GRBs with unknown redshifts

We first selected about 1000 GRBs in a class of the long duration of $T_{90} > 2$ sec detected by *BATSE* , and extracted the spectrum in $\sim T_{90}$ for each GRB. We performed the spectral analysis for these samples with the same method described in Chapter 4. Then we do not include k-correction factor (k_c) because it is almost unity as shown in table 4.3. The GRB spectra are described by the smoothly broken power-law model of equation (4.1) suggested by Band et al. (1993). In this section, we show the distributions of the spectral parameters of the low-energy and the high-energy power-law indices α and β, and the peak energy E_p. In order to have better S/N, we set a flux limit of $F_{\mathrm{limit}} = 2.0 \times 10^{-7}$ ergs cm^{-2}s^{-1} which is approximately equivalent to the dimmest sample with the known distance (GRB 970508). We would like to use the E_p values to estimate the redshift, but we failed measure them for 34 samples because of $\beta > -2$. We exclude these samples, and 745 samples are included in these selections.

In figure 5.3 (left), we show the α distribution of 745 samples. The distribution is similar to the Gaussian shape with a tail toward larger α. When we adopt the Gaussian function at the range between $-2 \leq \alpha \leq 0.4$, we obtained the mean value of $\bar{\alpha} = -0.77 \pm 0.03$ with the variance of $\sigma_\alpha = 0.47 \pm 0.03$. This result is consistent with $\bar{\alpha} \sim -0.8$ reported by Lloyd-Ronning et al. (2002a), but slightly larger than $\bar{\alpha} \sim -1$ of Preece et al. (2000). However, the sample of Lloyd-Ronning et al. (2002a) is one of brighter part of Preece et al. (2000). Therefore, the discrepancy among them may be due to the sample selection effect or the contamination of the ambiguities of the dimmer samples. In figure 5.3 (right), we show the β distribution of 779 samples (including the data with $\beta > -2$). The distribution is spreading to lower values, so we included all results with $\beta < -4$ into the lowest bin. Almost all samples showing the steep index are as dim as the flux limit of $F_{\mathrm{limit}} = 2.0 \times 10^{-7}$ ergs cm^{-2}s^{-1} . Therefore we conclude this fact comes from the poor statistics in high-energy photons. The mean of β value at the range of $-4 \leq \beta \leq -1$ is $\bar{\beta} = -2.23 \pm 0.05$, which is consistent with the results reported by Preece et al. (2000).

The β distribution in figure 5.3 (right) is one of the best fit result, and there are 34 samples with $\beta < -2.0$ within 1σ significance. We have to limit these samples, because the peak energy E_p can be determined only when β satisfies this criterion. After applying these criteria (F_{limit} and $\beta < -2.0$), 745 samples were remained. Hereafter we deal with these 745 samples, and discuss the GRB formation rate.

In figure 5.4, we show the E_p distribution of 745 samples. This distribution is well described by a lognormal distribution whose shape is the Gaussian distribution in the logarithmic horizontal scale. The probability density function of the lognormal distribution is described as

$$dP(x) = \frac{1}{\sqrt{2\pi}\sigma} \exp\left(-\frac{(\log x - \log\mu)^2}{2\sigma^2}\right) d(\log x), \qquad (5.1)$$

for the case of variable $x > 0$, and $dP(x) = 0$ for $x \leq 0$. Where $\log\mu$ and σ is the mean
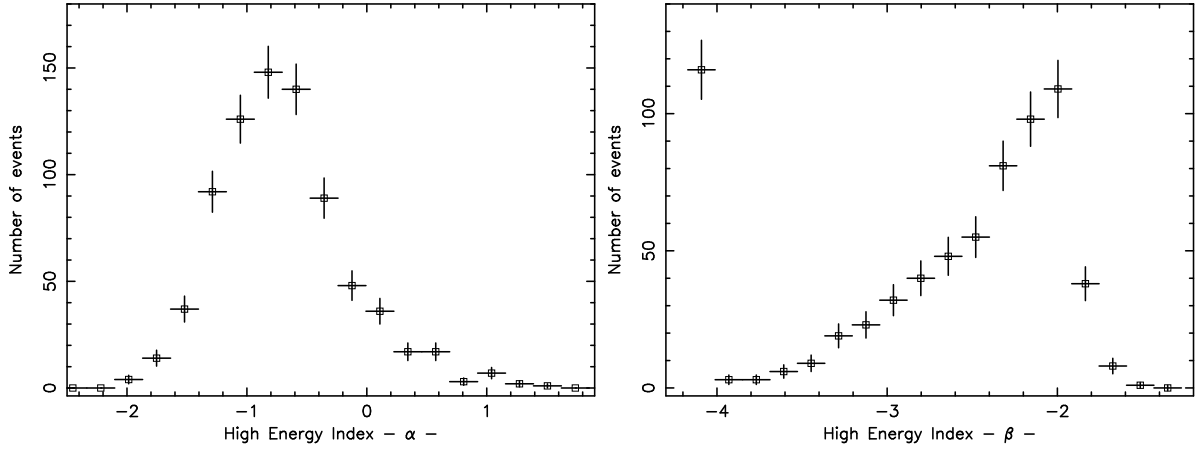
Figure 5.3: The distribution of the low-energy spectral index α (left) and the high-energy index β (right).

and the standard deviation, respectively. When we adopted the lognormal function to the E_p distribution, we obtained an acceptable fit of $\chi^2 = 6.94$ with 12 degree of freedom. The best-fit parameter is $\log \mu = 2.17 \pm 0.02$, which is equivalent to $\mu = 148$ keV, and $\log \sigma = 0.31 \pm 0.02$, respectively. The mean of the E_p distribution is remarkably smaller than the result of ~ 200 keV by Preece et al. (2000). This is because their E_p distribution is based on the brightest 157 samples and our results contains much dimmer samples achieving $F_{\rm limit} = 2.0 \times 10^{-7}$ ergs cm^{-2}s^{-1} . According to observations with the *HETE-2* satellite, which has the capability to detect the soft gamma-ray (X-ray) of a few keV, the E_p distribution is much softer than the result by Preece et al. (2000) and there are a lot of X-ray Flashes and X-ray Rich GRBs (Sakamoto, 2004, and the private communication with Prof. Kawai). Therefore, the lower end of the observed lognormal distribution is strongly restricted by the flux limit and the detector sensitivity at soft gamma-ray range. We cannot conclude whether the observed lognormal distribution of E_p values is the intrinsic property or the selection effect.

5.2   Redshift estimation

In the previous section, we confirmed that our fitting results were consistent with Preece et al. (2000) and Lloyd-Ronning et al. (2002a), including much dimmer samples compared with them. Using these 745 samples, we infer the GRB formation rate in the early universe.

We can rewrite equation (4.6):

$$\frac{d_L^2}{(1+z)^{2.0}} = \frac{2.34 \times 10^{47}}{4\pi F_p} \times E_p^{2.0} . \tag{5.2}$$

Once we obtained the peak flux (F_p) and E_p at the observer's rest frame, we can estimate the redshift and the luminosity. Although the left hand of equation (5.2) depends on both d_L and z, each parameter can be resolved numerically. In figure 5.5, we show the sample distribution in (z, L) plane, which is the optimum value, truncated by the above flux limit of $F_{\rm limit} = 2.0 \times 10^{-7}$ ergs cm^{-2}s^{-1} .
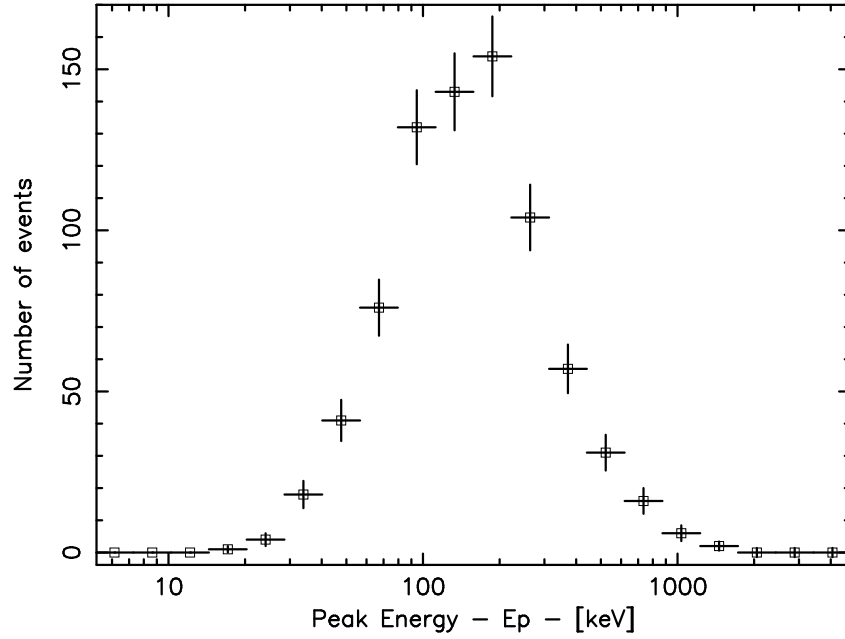
Figure 5.4: The distribution of the peak energy E_p. This distribution is formed by the data with $\alpha > -2$ and $\beta < -2$ within 1 σ uncertainty. The distribution is well represented by a lognormal distribution with the mean of $E_p \sim 200$ keV.

The estimated redshifts of the 41 samples are at the range of $12 < z < 20$, and the 14 samples show $z > 20$ (or no solution). These samples show large E_p at the observer's rest frame, but their peak fluxes are so dim. In this case, the redshifts become extremely large value and/or the solution cannot be obtained from our E_p–luminosity relation simply extended toward the larger E_p and the brighter luminosity range. Our E_p–luminosity relation can be certainly applied at the ranges of $50 < E_p < 2000$ keV and $10^{50} < L_p < 10^{54}$ ergs s^{-1} . However almost all samples with $z > 12$ are apart from this range. This might be caused by the simple linear extension of our E_p–luminosity relation toward the higher E_p and the brighter L end of the data. If the simple extension is incorrect, for example the luminosity saturates in the hard E_p region, the redshift estimation has to be improved. At present, we do not have enough information about the E_p–luminosity relation for much harder GRBs. Instead of using the "extended" E_p–luminosity relation as done by the previous works (Fenimore & Ramirez-Ruiz, 2000; Lloyd-Ronning et al., 2002a), we have shown all results in figure 5.5. In the following section, we will mention that the result of $z \leq 10$ is robust and $10 \leq z \leq 12$ may be marginal. Therefore, we may have to tread the 689 samples in $z \leq 12$. The list of the observed E_p, estimated redshift and luminosity with 1 σ error of 689 samples are summarized in Appendix B.

Each data point has uncertainty which comes from the error of the observed E_p and flux. We show the (z, L) distribution with error in figure 5.6. When we show all data points at once, it is difficult to recognize the uncertainty accompanying with each data because of large error bars of dim GRB samples. Therefore, dividing 689 samples into 4 parts based on the relative error of $\Delta z/z$, we show 4 distributions in figure 5.6. Since the data distributions are not biased in favor to some redshift range, we use all 689 samples in this analysis.
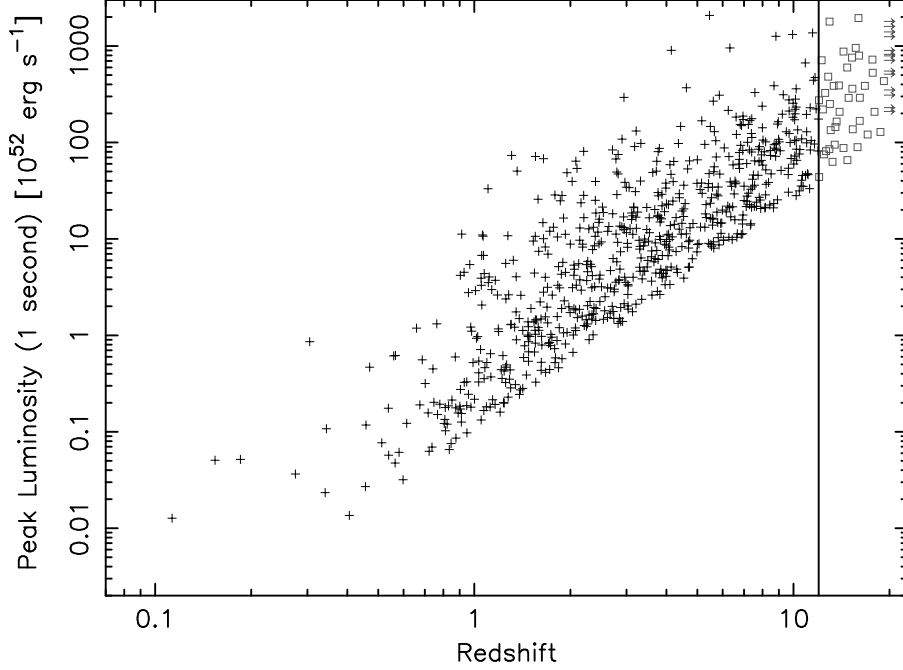
Figure 5.5: Redshift distribution based on the E_p-luminosity relation. The truncation is caused by the flux limit of $F_{\text{limit}} = 2 \times 10^{-7}$ ergs cm^{-2}s^{-1} . The open square shows the samples with their redshift of $12 < z < 20$. We failed determine the redshift of 14 samples, and they are plotted at $z = 20$ as a lower limit. We exclude these data because their redshift uncertainty is considerably large.

5.3   Luminosity Evolution

In the previous section, we show the (z, L) distributions estimated from the E_p–luminosity relation. For the purpose of considering the property of the distribution, we generate the luminosity function in each redshift interval. When we consider the redshift interval of $[z_i, z_{i+1}]$, there are two points crossing the flux truncation (luminosity limit), i.e. $L_{limit}(z_i)$ and $L_{limit}(z_{i+1})$. When we use only the luminosity range of $L > L_{limit}(z_{i+1})$, the luminosity function can be drawn free from the flux limit. In figure 5.7, we show the normalized luminosity functions for 5 redshift interval. The shape of these luminosity functions are similar to each other, but the break-luminosity seems to increase toward the higher redshift. This fact indicates that the luminosities correlate with the redshifts, so we can consider a luminosity evolution is hidden in the (z, L) plane in figure 5.5.

For the purpose of physical clarity, we would like to deal with the luminosity function and the GRB formation rate as a univariate function of the luminosity (L) and the redshift (z), respectively. In this section, using the τ statistical method (Efron & Petrosian, 1992; Petrosian, 1993; Maloney & Petrosian, 1999) (see Appendix A), which were used for the Quasar samples and first applied to the GRB samples by Lloyd-Ronning et al. (2002b), we quantitatively estimate the luminosity evolution as a function of the redshift. After removing this evolutionary effect from the data set, we discuss the luminosity function and the GRB formation rate. This
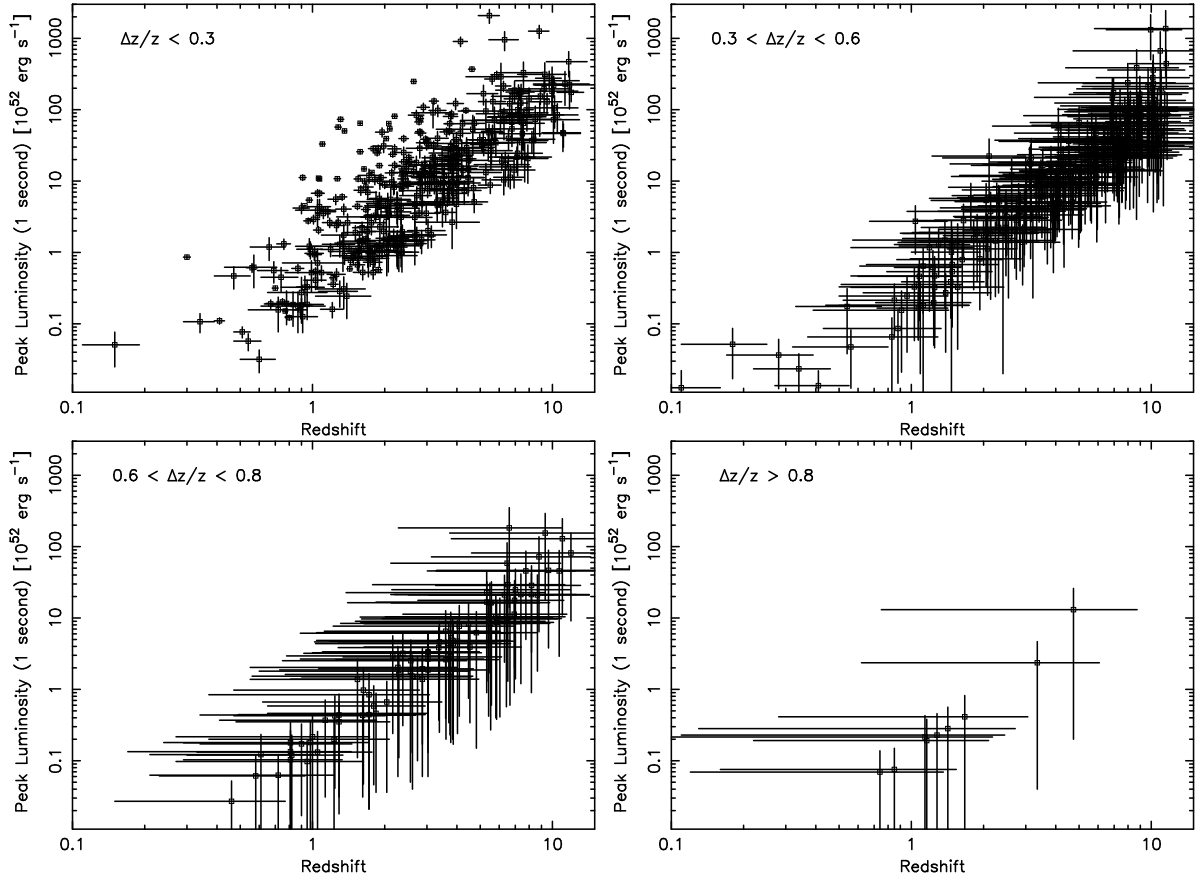
Figure 5.6: Detail distribution of estimated redshifts and luminosities. Each panel shows the (z, L) distribution with the redshift error displayed in it. The number of samples are 374 (top-left), 223(top-right), 83 (bottom-left), and 9 (bottom-right), respectively. For data in any significance, data distribution is not biased.
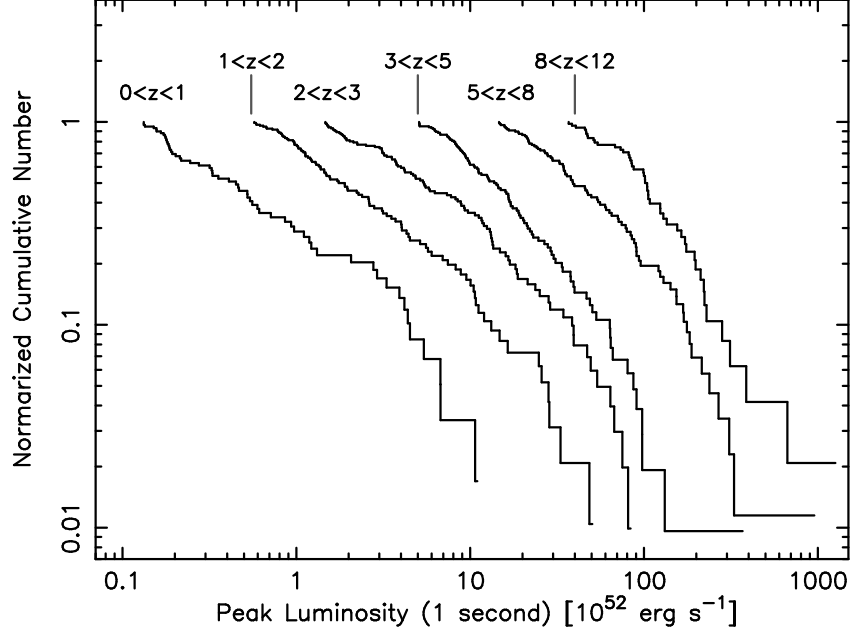
Figure 5.7: Normalized luminosity functions in cumulative form in each redshift interval. The shape of these luminosity functions are similar to each other, but the break-luminosity seems to increase toward the higher redshift. This indicates that a luminosity evolution is hidden in the (z, L) plane in figure 5.5.

is because the univariate distribution of the redshift and the luminosity can be estimated only when these two parameters are independent of each other.

The total luminosity function $\Psi(L, z)$ can be written as

$$\Psi(L, z) = \rho(z)\psi(L/g_k(z), \alpha_s)/g_k(z), \tag{5.3}$$

without the loss of generality (Caditz & Petrosian, 1990). Here, each function means the luminosity evolution $g_k(z)$, the density evolution $\rho(z)$ and the local luminosity function $\psi(L/g_k(z), \alpha_s)$, respectively. Although the parameter α_s represents the shape of the luminosity function, we will ignore the effect of this parameter because the shape of the luminosity function is approximately same as shown in figure 5.5. Assuming the functional form of the luminosity evolution as $g_k(z) = (1 + z)^k$, which is also used in discussions of QSO evolution by Maloney & Petrosian (1999) and the GRB evolution Lloyd-Ronning et al. (2002b), we convert the data set of (z, L) to (z, L'), where $L' \equiv L/g_k(z)$. We search the best value of index k giving the independent set of (z, L') within the significance of 1 σ error. The physical interpretation of the luminosity evolution will be given in Chapter 6.

We deal with the (z, L) data set truncated by the flux limit of $F_{\text{limit}} = 2 \times 10^{-7}$ ergs cm^{-2}s^{-1} as shown in figure 5.5. The test statistic τ of the *comparable* set of $J_i = \{j \mid L_j > L_i, L_j^- < L_i\}$ can be calculated by the following equation.

$$\tau = \frac{\sum_i (R_i - E_i)}{\sqrt{\sum_i V_i}}. \tag{5.4}$$

Here, $R_i = \text{number}\{j \in J_i \mid z_j \leq z_i\}$, $E_i = (N_i + 1)/2$ and $V_i = (N_i^2 - 1)/12$ is a rank of z_i in the *comparable* set, an expected mean and a variance of J_i, respectively. When L and z are

completely independent of each other, the value of τ is equivalent to be zero. Therefore we again and again calculate τ value to change the index k of the luminosity evolution ($g_k(z) = (1+z)^k$), and find the best index k giving $\tau = 0$. Then we can obtain the independent data set of (z, L') removed the luminosity evolution effect.
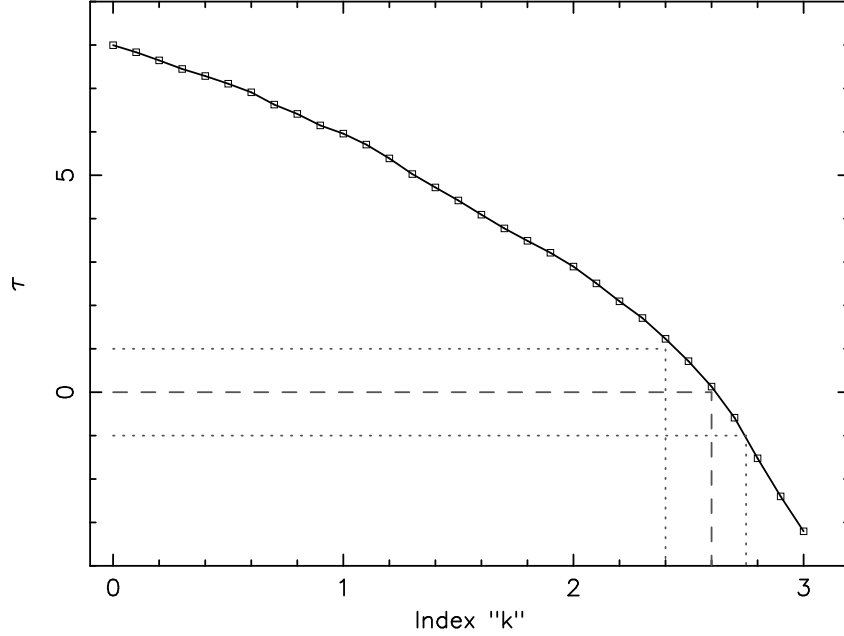
Figure 5.8: Determination of the parameter k of the luminosity evolution for the functional form of $g_k(z) = (1 + z)^k$. The correlation statistic τ is shown as a function of k. The parameter giving an optimum value of $|\tau|$ is $k = 2.60^{+0.15}_{-0.20}$ with $1\,\sigma$ statistical uncertainty, and $g_k(z) = (1+z)^{2.6}$ is the best function to describe the luminosity evolution. A hypothesis of no luminosity evolution (equivalent to $k = 0$) is reject with 8σ significance.

In figure 5.8, we show the variation of the test statistic τ as a function of the index k. The null-hypothesis of the luminosity evolution ($k = 0$) is rejected about 8σ significance. There is an optimum value with 1σ uncertainty at $k = 2.60^{+0.15}_{-0.20}$. Therefore, we conclude the luminosity evolution as $g_k(z) = (1 + z)^{2.60}$. This luminosity evolution is slightly larger than the previous value of $(1 + z)^{1.4\pm0.5}$ based on the variability–luminosity relation reported by Lloyd-Ronning et al. (2002b), and with $(1 + z)^{1.7\pm0.5}$ based on a numerical calculation by Wei & Gao (2002). However Caditz & Petrosian (1990); Maloney & Petrosian (1999) claimed the existence of strong luminosity evolution, $(1 + z)^3$, for QSOs. Therefore, there is a possibility that the progenitors of GRBs rapidly evolve as similar as QSOs.

In figure 5.9 (left), we show the distribution of the redshifts and the luminosities removed the evolutionary effect in (z, L') plane, where $L' = L/g_k(z) = L/(1 + z)^{2.6}$. If the effect of the luminosity evolution is completely removed and (z, L') are independent each other, some discrepancies of the luminosity functions as shown in figure 5.7 is expected to be disappeared. In figure 5.9 (right), we show the luminosity functions at the same redshift interval of figure 5.7, which is normalized to overlap each other. The figure shows that the shape of the luminosity functions and the break luminosities are approximately same. Therefore, the luminosity evolution shown in figure 5.7 is well removed by the form of $g_k(z) = (1 + z)^{2.6}$, and we can recognize

the (z, L') samples as independent data set. Hereafter, we use the (z, L') samples to estimate the luminosity function and the GRB formation rate.
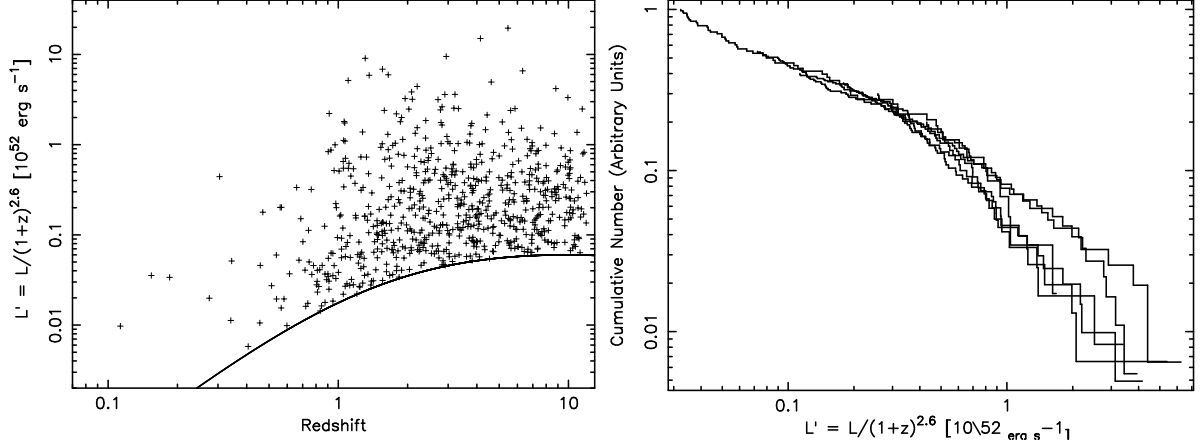
Figure 5.9: Left panel is the redshift and the luminosity distribution after removing the luminosity evolution of $g_k(z) = (1 + z)^{2.6}$. The luminosity functions in cumulative form at the same redshift interval of figure 5.7 are shown in the right panel. These luminosity functions are superimposed on each other for the purpose of easy comparison. Therefore the normalization is an arbitrary units. The shapes of these luminosity functions and the break luminosities are approximately same, so the effect of the luminosity evolution is cleanly removed, and the data set of (z, L') become independent each other.

5.4   Luminosity Function

Once we obtain the independent data set of (z, L'), we can generate the cumulative luminosity function $\psi(L'_i)$ as a function of univariate L' with following equation:

$$\ln \psi(L'_i) = \sum_{j<i} \ln(1 + \frac{1}{N_j}). \tag{5.5}$$

(see Appendix A in detail). Here, N_j is a number of samples in J_j, and the summation is performed for all points $L'_j < L'_i$. This luminosity function is equivalent to the local ($z = 0$) luminosity distribution. In figure 5.10, we show the cumulative luminosity function calculated with equation (5.5). The functional form is approximately described by broken power-law model with the break luminosity of $\sim 10^{51}\ ULUMI$.

It is difficult to determine the break luminosity because it has a smoothly broken power-low shape. Therefore, we show the power-law index at the dimmer and brighter ends of the function:

$$\psi(L'_i) \propto \begin{cases} L'^{-0.29\pm0.02} & \text{for } L'_{52} < 0.06, \\ L'^{-1.02\pm0.02} & \text{for } L'_{52} > 0.30. \end{cases} \tag{5.6}$$

This is the local luminosity function at $z = 0$, so the rest frame functional form is described as $\psi(L')(1 + z)^{2.6}$, and also the break luminosity is estimated as $L_{\text{break}} \sim 10^{51}(1 + z)^{2.6}$ ergs s^{-1} . In Chapter 6, we will give a possible interpretation about the shape of this luminosity function with the framework of GRB jet model.
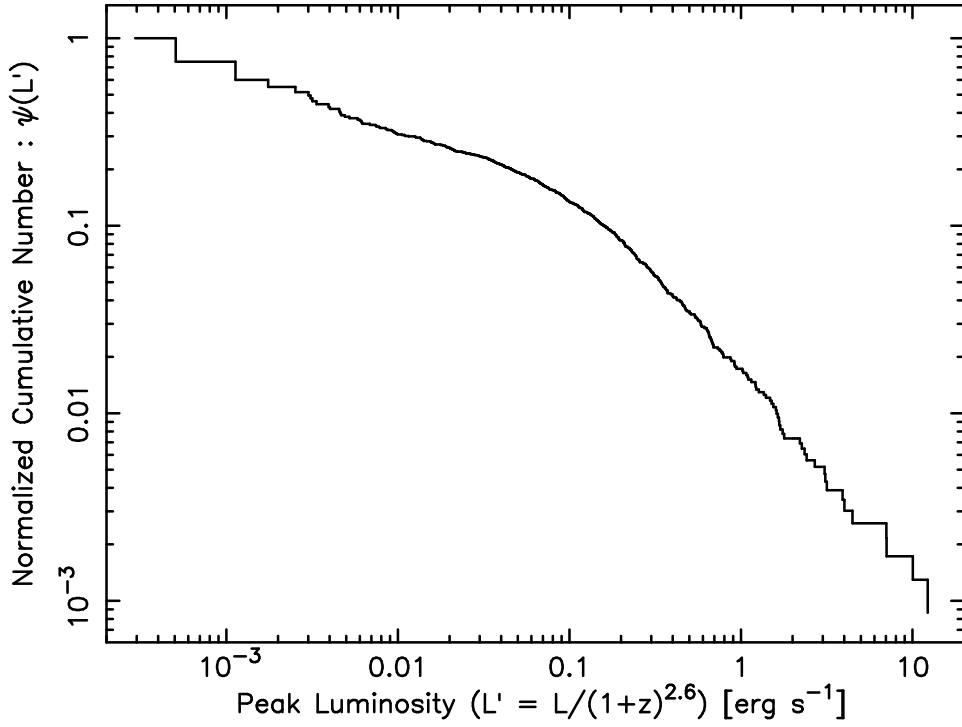
Figure 5.10: The local ($z = 0$) luminosity function of GRBs. This luminosity function is roughly broken power-law shape with the break luminosity of $L'_{\mathrm{break}} \sim 10^{52}$ ergs s^{-1} . The power-law dependence is summarized in equation (5.6).

5.5 Relative GRB Formation Rate

As already shown in equation (5.5), we can also generate the cumulative redshift distribution $\psi(z)$, GRB formation rate, as a univariate function of the redshift. In figure 5.11, we show the cumulative number count of the redshift distribution toward $z = 12$, which is normalized to unity. The differential (not the cumulative) form of the GRB formation rate is useful for the purpose of comparison with the star formation rates in UV, optical, infrared bands. Therefore we convert $\psi(z)$ into the differential form with the following equation:

$$\rho(z) = \frac{d\psi(z)}{dz}(1 + z)\left(\frac{dV(z)}{dz}\right)^{-1} , \tag{5.7}$$

where the additional factor of $(1 + z)$ comes from the cosmological time dilation, and $dV(z)/dz$ is a differential comoving volume.

In figure 5.12, we show the relative GRB formation rate $\rho(z)$. The solid line is the best result, and the dotted lines show the upper and the lower bound caused by the uncertainty of the E_p–luminosity relation. The results as shown in figure 5.12 indicates that the GRB formation rate rapidly increase up to $z = 1$, and keep rising toward the higher redshift. When we adopt broken power-law model to $\rho(z)$, we obtain the best result as

$$\rho(z) \propto \begin{cases} (1 + z)^{6.0 \pm 1.4} & \text{for } z < 1, \\ (1 + z)^{0.4 \pm 0.2} & \text{for } z > 1. \end{cases} \tag{5.8}$$
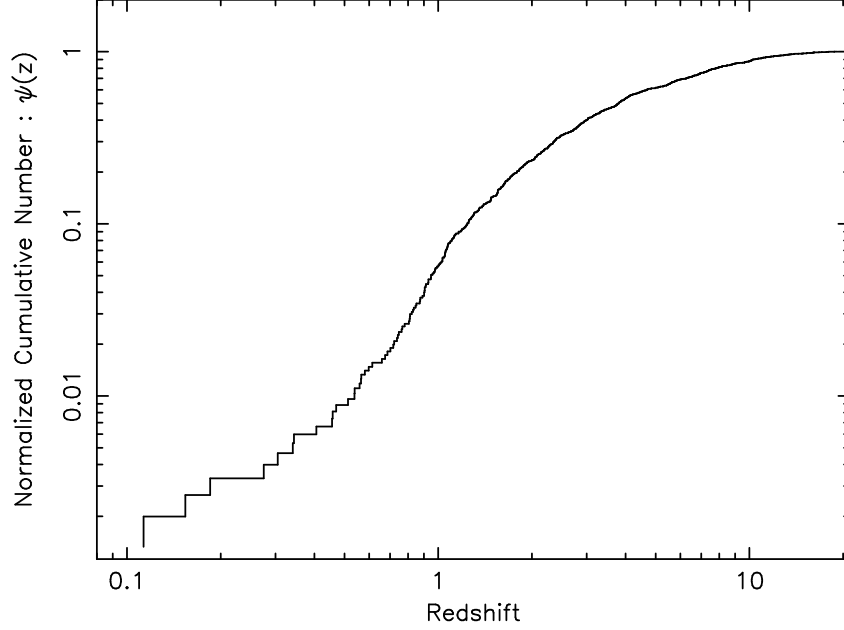
Figure 5.11: The cumulative number distribution of GRBs toward $z = 20$ calculated with equation (5.5).

Because of the mathematical reason, we can estimate only the functional form of the GRB formation rate and cannot give the normalization for it. In Chapter 6, considering the geometrical collimation appropriately, we try to estimate the absolute GRB formation rate. Anyway, the GRB formation rate at the early universe $z \sim 12$ is much larger than the present rate.

5.5.1   Effects of the E_p–Luminosity Deviations on the GRB Formation Rate

The GRB formation rate in figure 5.12 is based on the redshift estimation from the best-fit formula of the E_p–luminosity relation. As shown in figure 4.6, the deviations of E_p–luminosity relation directly reflect the ambiguity of the redshift estimation. There is a possibility to change the functional form of the GRB formation rate because of the redshift uncertainty. Thus we have to consider the effects of data deviations to the functional form of the GRB formation rate.

In figure 5.13 (upper), based on equation (5.2), we show the redshift estimated from the E_p–luminosity relation as a function of $E_p/F_p^{1/2}$ measured in the observer's rest frame. Here, F_p is 1 sec peak flux in units of ergs cm^{-2}s^{-1} . The solid line is the curve based on the best-fit E_p–luminosity relation, and two dotted lines are curves with 1 σ upper and lower bound. In the case of the high redshift, the difference between the upper and the lower bound is very large because of the deviations of the E_p–luminosity relation while it is negligible in the low redshift case. For example, the estimated redshift of $z = 10$ have ambiguity of $z = 10^{+10}_{-5}$. The one-side error reaches 100 % compared with the estimated redshift. Therefore, in the present work, we can assert the validity of the GRB formation rate at only $z \sim 10$ while we show the results toward $z = 20$ in figure 5.12.
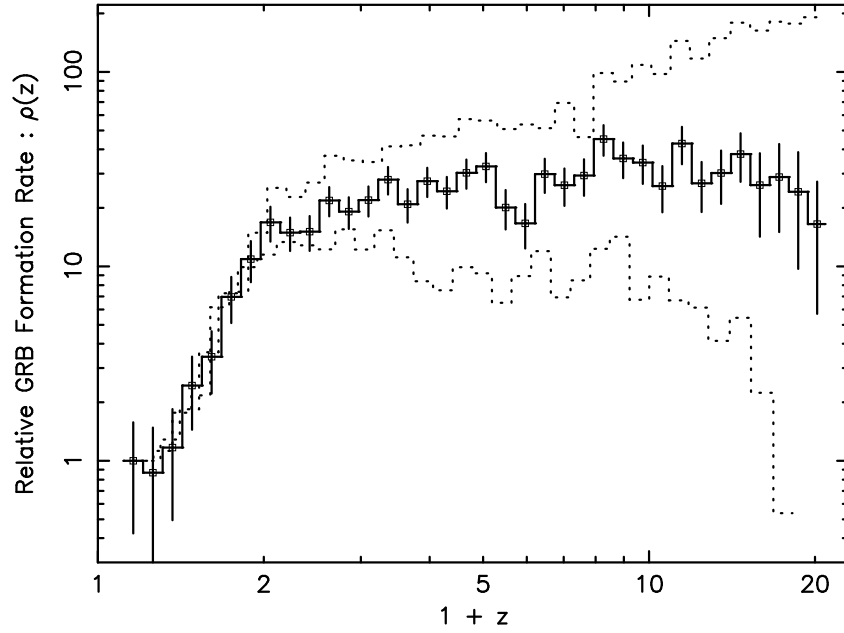
Figure 5.12: The relative GRB formation rate normalized at the first point. The solid line is the result based on the best fit of E_p–luminosity relation and two dotted lines indicate the upper and lower bounds caused by the uncertainty of E_p–luminosity relation. These dotted lines are also normalized and superposed on the best result. The error bars accompanying open squares represent the statistical uncertainty of each point.

If the GRBs distribute around the best-fit E_p–luminosity relation at random, it is expected that their estimated redshifts also randomly distribute around the solid line in figure 5.13. We consider two extremely biased cases at which all GRBs are ordered on the 1 σ upper or lower bound of the E_p–luminosity relation. Then we estimate the alteration of the functional form of the GRB formation rate. In figure 5.14, we show two boundary cases of the GRB formation rate with the best result as shown in figure 5.12. The solid lines marked by the open and filled squares are the upper and lower bound cases, respectively. These functions are normalized at the first point. For the lower bound case in figure 5.13 (left), the estimated redshifts are systematically biased toward small values. Therefore the GRB formation rate increases in the low redshift range compared with the best result. On the other hand, for the upper bound case, the GRB formation rate at high redshift increase but the one of the low redshift range is suppressed.

Again, we emphasize that the functional form of the GRB formation rate for the upper and the lower bound in figure 5.13 (right) is the extremely biased case, and they are never realized. Although the redshift estimation strongly depends on the deviation of the E_p–luminosity relation as shown in figure 5.13 (left), the upper and lower bounds within 1 σ deviation of the GRB formation rate are similar to the best result as shown in figure 5.12. We conclude the deviation of the E_p–luminosity relation do not significantly contribute to the functional form of the GRB formation rate.
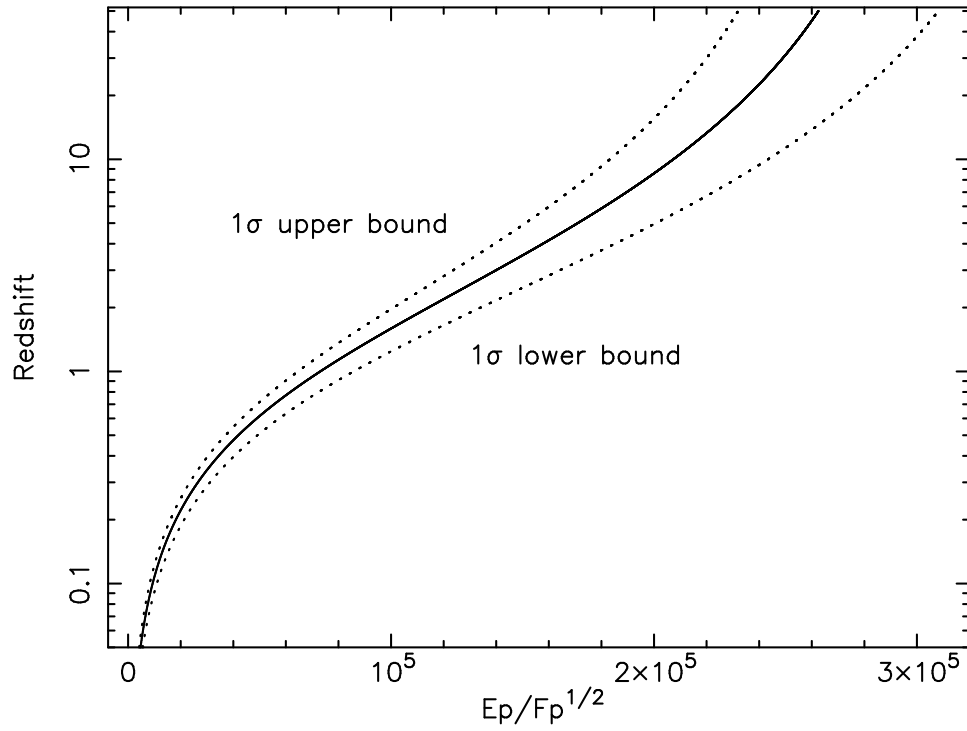
Figure 5.13: The redshift ambiguity comes from the E_p–luminosity deviations as a function of $E_p/F_\gamma^{1/2}$. The solid line is the estimated redshift with the best fit E_p–luminosity relation, and two dotted lines is 1 σ lower and upper bound.
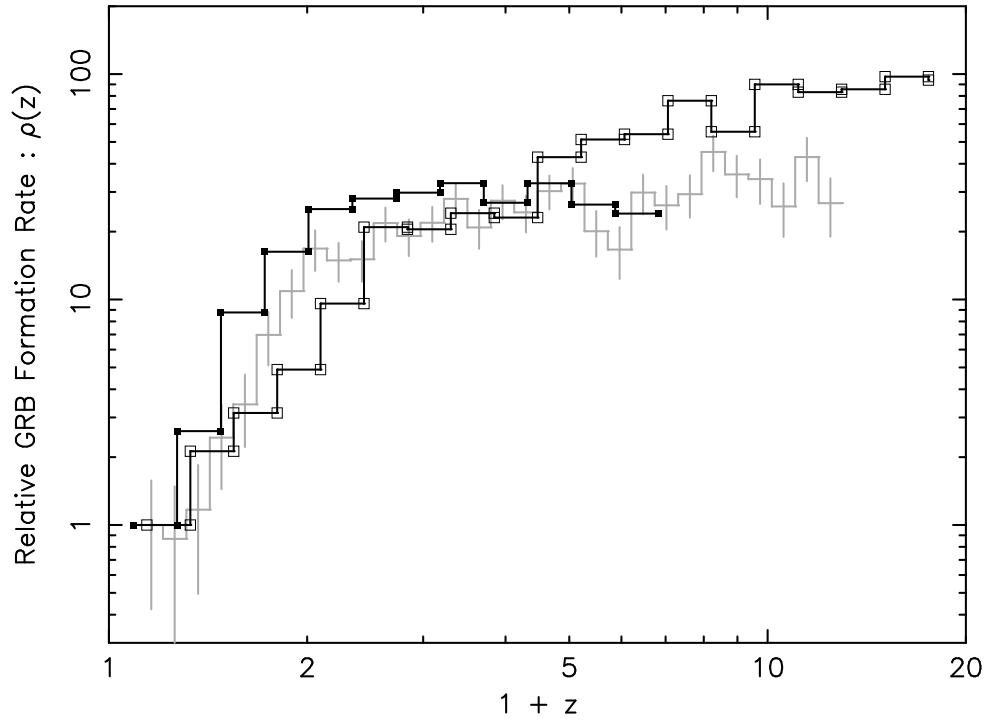
Figure 5.14: The change of the functional form of the GRB formation rate because of the redshift estimation with three lines of figure 5.13. The filled and open squares are the results corresponds to 1 σ lower and upper bound-curves, respectively.

5.5.2   GRB Formation Rate within Calibrated E_p–Luminosity Relation

The E_p–luminosity relation is confirmed within the luminosity range of $10^{51} < L < 10^{54}$ ergs s^{-1} as shown in figure 4.4. We simply extended it over the calibrated range when we estimate the redshift from observed E_p and flux. More rigid results may be obtained when we use only the data in the calibrated range.

In figure 5.15 (left), we show the redshift distribution within the luminosity range confirmed by the known redshift samples (marked "+"). Using only the data, we try to estimate the GRB formation with the same method described in Appendix A. When we use doubly truncated data (flux limit and the luminosity cut of $L = 10^{54}$ ergs s^{-1}), the τ-statistical method cannot be directly adopted to the data. Then we have to perform numerical simulation and generate pseudo events due to the luminosity function and the redshift distribution. However, we would like to discuss the GRB formation rate using only the observation data, so we do not perform such a simulation. For example, Maloney & Petrosian (1999) discussed the luminosity evolution of QSO samples with two cases, i.e., one-sided truncation (the flux limit) and doubly truncation (the flux limit and the limited observation band). As shown in table 1 by their results, the difference of the luminosity evolution by these two method is not so large (about 10 % differenece). Therefore, we assume the same luminosity evolution $g_k(z) = (1 + z)^{2.6}$ as shown in Section 5.3.

The relative GRB formation rate is shown in figure 5.15 (right). Since the $L = 10^{54}$ ergs s^{-1} line and the flux limit cross each other, we can measure the GRB formation rate until $z = 17$. The remotest two points contain only one event, respectively, so we can effectively trace it till $z \sim 12$. It shows similar tendency of the result in figure 5.12, and the GRB formation rate keeps flat toward higher redshifts. On the other hand, in figure 5.13, we have already shown that redshift estimations with the E_p–luminosity relation are reliable within $0 \le z \le 10$. Therefore, we consider the GRB formation rate of $z \sim 12$ are marginal results.
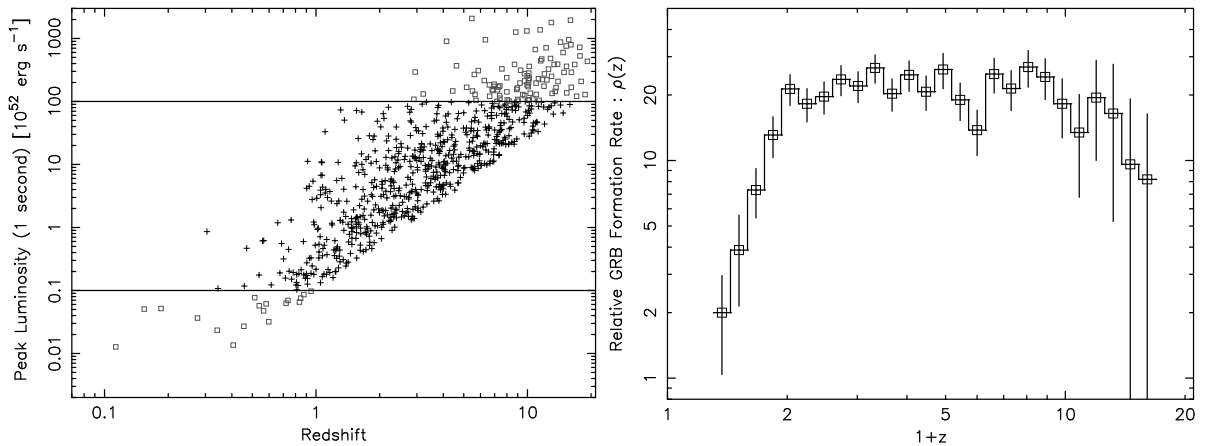
Figure 5.15: Left panel is (z, L) distribution of the data within the calibrated E_p–Luminosity range. The right panel is the GRB formation rate derived from the left panel.

5.5.3   Flux Limit Effects on the GRB Formation Rate

As shown in figure 5.6, the redshift estimation is quite sensitive to the accuracy of the determination of E_p values. Especially, for dim GRB samples, it is difficult to determine the E_p values with high precision. The incorrect estimation of redshifts may directly reflect to the GRB formation rate. Therefore we should confirm the functional form of the GRB formation rate with several flux-limit criteria. When we set the high flux-limit, we can exclude the samples with uncertain redshifts.

The GRB formation rate in figure 5.12 is derived from the 689 samples above flux limit of $F_{limit} = 2 \times 10^{-7}$ ergs cm^{-2}s^{-1} . In figure 5.16, we show the GRB formation rate derived from the samples above $F_{limit} = 2 \times 10^{-6}$ ergs cm^{-2}s^{-1} , which is one order of magnitude larger than the previous flux-limit used in figure 5.12. We obtained the result consistent with one of figure 5.12. We calculate the GRB formation rate with several flux-limit between 2×10^{-7} and 2×10^{-6}, and we confirmed that all results are consistent with one of figure 5.12. Since the functional forms are consistent with each other, we conclude the flux-limits do not give the strong effects for the GRB formation rate. In figure 5.17, we show the final result about the GRB formation rate.
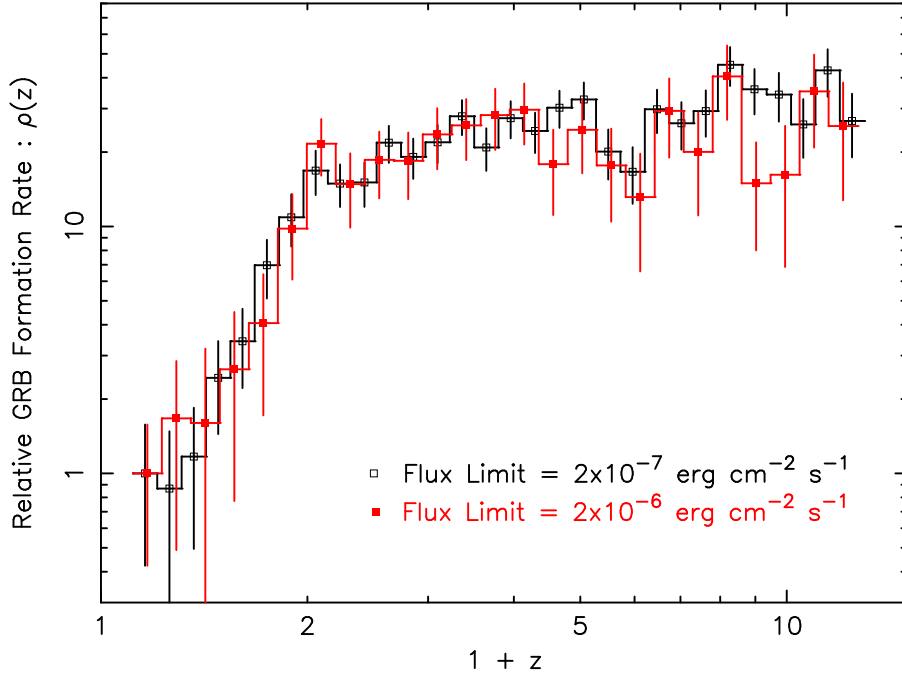
Figure 5.16: Flux limit effects on the GRB formation rate. The black and the red points are the GRB formation rate derived from the samples with the flux limit of $F_{limit} = 2 \times 10^{-7}$ ergs cm^{-2}s^{-1} and $F_{limit} = 2 \times 10^{-6}$ ergs cm^{-2}s^{-1} , respectively.
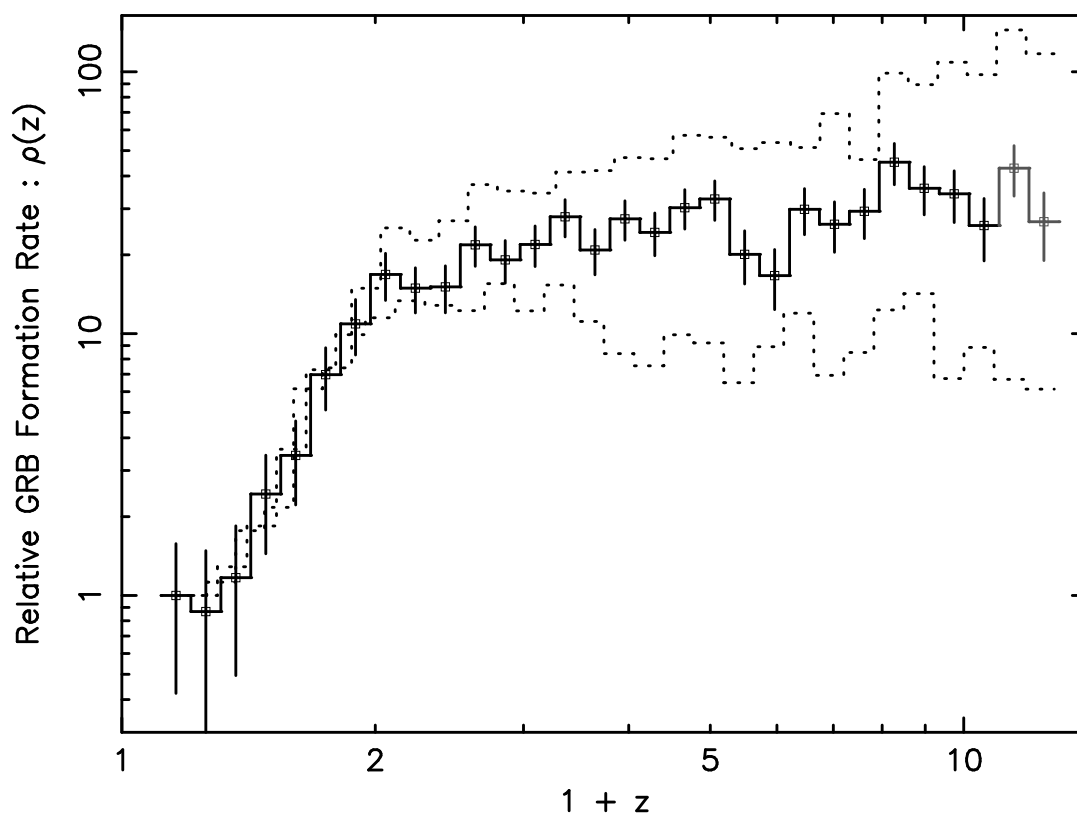
Figure 5.17: The relative GRB formation rate normalized at the first point. The solid line is the result based on the best fit of E_p–luminosity relation and two dotted lines indicate the upper and lower bounds caused by the uncertainty of E_p–luminosity relation. These dotted lines are also normalized and superposed on the best result. The error bars accompanying open squares represent the statistical uncertainty of each point. The functional form of $z < 10$

Chapter 6

Discussion

In this thesis, we investigated the spectral and the temporal properties of the prompt GRB emissions. Especially, we performed the spectral analyses for 12 samples with known redshifts detected by the *BATSE* instruments together with the *BeppoSAX* results, and found the E_p–luminosity relation among them. This E_p–luminosity relation is described as $L_{\gamma,52} \propto [E_p(1 + z)]^{2.0\pm0.2}$, and it is very tight with the chance probability of 5.31×10^{-9}. So this is much better indicator of the isotropic luminosity compared with the spectral time-lag and the variability of GRBs (Norris et al., 2000; Fenimore & Ramirez-Ruiz, 2000). Using the E_p–luminosity relation, we estimated the redshifts for 689 unknown redshift samples, and inferred the GRB formation rate in the early universe out to $z = 12$ as shown in figure 5.12.

In this chapter, first, we give physical interpretations for the observed E_p–luminosity relation in the framework of the standard internal shock model, and trace the physical condition in the internal shock. Second, applying the appropriate geometrical correction of the jet opening angle, we estimate the absolute GRB formation rate. Finally, based on the GRB formation rate, we explore the massive star formation in the early universe, and discuss the early-epoch reionization and the metal enrichment in the inter galactic medium.

6.1 Physical Conditions in the Internal Shock

The prompt gamma-ray emission and the following afterglow emission are well explained by the internal/external shock scenario in the framework of the fireball model (see Chapter 2). In this section, we briefly summarize the main features of the "standard" internal shock model.

The emission of the burst, which is generated by the conversion of bulk kinetic energy into thermal energy, has a duration which is determined by the activity of the central engine. In particular, in order to create complex variability patterns, the engine has to eject several shells of relativistic outflow. If they propagate with different Lorentz factors, a faster shell will catch up with a slower one, and an internal shock will develop. The electrons are accelerated to ultra-relativistic energies in the shock, and also the magnetic field is created as equipartition energy density. Then they lose energy by radiating synchrotron gamma-ray photons. If many internal shocks are generated, observed "spiky" burst may be realized.

6.1.1 Typical radii

Assuming two shells with an initial separation of R_0 and with different Lorentz factors Γ and $a\Gamma$ ($a > 1$), they interact at a distance R_i from the central engine, where

$$R_i = \frac{2a^2}{a^2 - 1} R_0 \Gamma^2. \tag{6.1}$$

When we assume $a = 2$ as a reference value, it corresponds to $R_i = (8/3)R_0\Gamma^2$. One of the typical distances characterizing the fireball evolution is the transparency radius R_t, at which an expanding shell becomes optically thin to Thomson scattering. Assuming that each shell carries an energy $E_s = 10^{50} E_{s,50}$ erg in bulk motion, $R_t = 6 \times 10^{12}(E_{s,50}/\Gamma_2)^{1/2}$ cm [1]. The standard scenario requires $R_i > R_t$ for the radiation produced to freely escape.

6.1.2 Typical synchrotron frequency

The electrons are instantaneously accelerated in a collision-less shock, and reach random Lorentz factors which corresponds to equipartition with the other forms of energy, i.e. $\gamma_{eq} = (\Gamma' - 1)n_p m_p/(n_e m_e)$, where Γ' is the Lorentz factor of faster shell in the rest frame of the slower one, and n_p (n_e) and m_p (m_e) are the proton (electron) density and mass, respectively. Deviations from the equipartition value are parametrized by a dimensionless coefficient $\epsilon_e = \gamma/\gamma_{eq}$. In this regime, the observed luminosity is equivalent to $L = \epsilon_e L_s$, where $L_s = 4\pi R^2 \Gamma^2 n_p' m_p c^3$ is the kinetic power carried by a single shell.

The outflowing plasma is magnetized, and a typical field value is estimated by assuming that the field energy in the emitting region constitutes some fraction (ϵ_B) of the randomized energy. In that case, at the distance where the shells interact, the Poynting flux carries a power of $L_B \equiv R^2 \Gamma^2 B'^2 c/2 \equiv \epsilon_B L_s$. This corresponds to

$$B' = [8\pi\epsilon_B n_p' m_p c^2]^{1/2} \tag{6.2}$$

$$= \left(\frac{2\epsilon_B L}{c\epsilon_e}\right)^{1/2} \frac{1}{\Gamma R}. \tag{6.3}$$

It follows that the typical synchrotron frequency is $\nu_{peak} = 2e\gamma^2 B'\Gamma/3\pi m_e c(1 + z)$ from the above estimation, which at R_i gives

$$h\nu_{peak} \equiv E_p = 450 \; \frac{\epsilon_e^{3/2}(\Gamma' - 1)^2 \epsilon_B^{1/2} L_{52}^{1/2}}{R_{i,14}(1 + z)} \; \text{keV}. \tag{6.4}$$

For the purpose of easy comparison with our observed E_p–luminosity relation, we change the formula of equation (6.4):

$$L_{52} = 4.94 \times 10^{-6} R_{i,14}^2 \epsilon_e^{-3} (\Gamma' - 1)^{-4} \epsilon_B^{-1} \left[\frac{E_p(1 + z)}{1 \; \text{keV}}\right]^2. \tag{6.5}$$

Note that the 'equipartition coefficients', ϵ_B and ϵ_e, are generally considered as about unity in the internal shocks. This is the theoretical solution about the relation between E_p and luminosity.

---

[1]Hereafter, we parametrize a quantity Q as $Q = 10^x Q_x$ in cgs units. We use primed values to describe the quantities in the comoving frame of the shock

6.1.3 Magnetic Field Strength in the Internal Shocks

We took into account 50 pulses from 11 cosmological GRBs, except for GRB 980425, and found all pulses are due to single formula of E_p–luminosity relation as $L = 2.72 \times 10^{-5}[E_p(1+z)]^{1.94}$. This observed E_p–luminosity relation is based on the single-pulse property, and each pulse represents individual internal shock (a shell–shell collision). On the other hand, assuming such a single collision and the synchrotron radiation, the theoretical solution can be given as equation (6.5) described above. Therefore we can say that the observed E_p–luminosity relation is naturally explained in the framework of the "standard" internal shock and synchrotron radiation scenario. Moreover, the observed E_p–luminosity relation is the universal relation for all cosmological GRBs. This fact indicates that some physical conditions (or couple of them) are finely tuned up via the physical process as the internal shock. This E_p–luminosity relation may play an important role for tracing the physical condition in the internal shocks. However, the case of GRB 980425 at $z = 0.0085$ is 4 orders of magnitude apart from the main population as shown in figure 4.33. We will give a possible interpretation about the *outlier* event in the latter section.

Comparing the observed E_p–luminosity relation by equation (4.6) with the theoretical solution of equation (6.5), we try to estimate several physical conditions in the internal shocks. Especially, we estimate the strength of the magnetic field in the relativistic internal shocks. When we describe the physical values, we assume $\Gamma = 100$ (typical Lorentz factor) and $\Gamma' = 2$ (the Lorenz factor of the faster-backward shell measured from the rest frame of the slower-forward shell), and normalize them with these values. We will rest their dependency explicitly.

First, comparing the normalization of both the observed and the theoretical power-law formula of E_p–luminosity relations, the collision radius of the internal shock is estimated as

$$R_i = 2.35 \times 10^{14} \ \epsilon_e^{3/2}(\Gamma'-1)^2\epsilon_B^{1/2} \ \text{cm,} \tag{6.6}$$

and the couple of these parameters $\epsilon_e^{3/2}(\Gamma'-1)^2\epsilon_B^{1/2}/R_i$ may keep constant for all internal shocks, since the observed E_p–luminosity relation is a universal formula. Using this result and equation (6.3), the magnetic field in the rest frame of internal shock can be also estimated as

$$B' \sim 10^3 \ \epsilon_e^{-2} \left(\frac{100}{\Gamma}\right)(\Gamma'-1)^{-2}\left[\frac{E_p(1+z)}{1 \ \text{keV}}\right]. \tag{6.7}$$

This formula indicates that the internal shocks emitting the synchrotron radiation with large E_p values are highly magnetized. When we consider the case with $E_p(1+z) = 1$ MeV, such as GRB 990123, the strength of the magnetic field may achieve 10^6 Gauss. According to equation (6.3) and equation (6.1), the magnetic field has a dependence of Γ^{-3}, because the shells with high Lorentz factors have to run far away until internal collision. Then the plasma density becomes small and the magnetic flux density decreases. On the other hand, according to equation (6.4) and equation (6.1), E_p shows the dependence of Γ^{-2}. One can think that the radiated photons from the relativistic shells with high Lorentz factor will be highly boosted with a factor of Γ. However, the synchrotron peak frequency linearly depends on the magnetic field, so the total dependence becomes Γ^{-2}. According to above estimation, the ultra-relativistic shell cannot be bright and also cannot emit the high-E_p synchrotron radiation.

6.2   Off-Axis Viewing Angle

GRB 980425 associated with SN 1998bw occurred at the redshift of $z = 0.0085$ which is two orders of magnitude closer than the other samples. The observed properties of GRB 980425 are $E_p = 55.1^{+11.6}_{-11.6}$ keV and $L_\gamma = (4.37 \pm 0.47) \times 10^{46}$ ergs s^{-1} , which is at least 10^{-4} times dimmer than the other populations as shown in figure 4.4. We have to mention about this discrepancy between the property of GRB 980425 and the standard E_p–luminosity relation.

Yamazaki, Yonetoku & Nakamura (2003) explained the low-luminosity of GRB 980425 as the effect of the off-axis viewing angle. The gamma-ray emissions are concentrated in the forward direction by the relativistic beaming effect. Therefore the peak energy is blueshifted by the Lorentz factor of the emitting material as $E_{p,obs} = \Gamma E_{p,0}$ and the luminosity becomes $L_{\gamma,obs} = \Gamma^4 L_{\gamma,0}$. Here $E_{p,obs}$ ($E_{p,0}$) and $L_{\gamma,obs}$ ($L_{\gamma,0}$) are the peak energy and the luminosity at the rest frame of observer (emitting material), respectively. If the observer stands at off-axis direction of the relativistic jet, the fraction component of the Lorentz factor toward the observer becomes small. Then the observed E_p is proportional to the *Doppler factor* $\delta \equiv \gamma[1 - \beta \cos(\theta_v - \Delta\theta)]$, and the luminosity depends on about $\propto \delta^4$.

Assuming the on-axis property of GRBs with the spectral shape of $\alpha = -1$, $\beta = -2.1$ and $E_p = 2.6$ MeV, they calculated the spectral property observed from off-axis direction. When the jet with the opening half-angle of $\Delta\theta \sim$10–30° is seen from the off-axis viewing angle of $\theta_v \sim \Delta\theta + 6°$, the observed quantities of GRB 980425 can be well explained. The detailed calculations are found in Yamazaki, Yonetoku & Nakamura (2003). If the observer exists at a few degree outside from the jet, the relativistic beaming effects rapidly decrease and the observed luminosity also rapidly becomes dim with δ^4. Therefore the effects of off-axis viewing angle are important only for the GRBs occurred at nearby galaxies because the cosmological event should not be observed. The GRB formation rate at high redshifts in figure 5.12 is not influenced by the off-axis viewing effects.

6.3   Physical Interpretation of $\psi(L')$, $g_k(z)$ and $\rho(z)$

6.3.1   The luminosity function : $\psi(L')$

As shown in figure 5.7, the shape of the cumulative luminosity function is independent of the redshift, except for the value of the break luminosity, which changes with z. We propose that the broken power-law shape in figure 5.10 suggests an important information on the jets parameters, which is responsible for the prompt gamma-ray emissions and a distribution of their opening angles. Let us consider a simple model for a uniform jet with an opening half-angle θ_j and a geometrically-corrected luminosity L_j, which is viewed from an angle of θ_v. Then, in a crude approximation the luminosity L is given by

$$L = \begin{cases} 2L_j\theta_j^{-2} & \text{for } \theta_v < \theta_j \\ 2L_j(\theta_j^6/\theta_v^8) & \text{for } \theta_v > \theta_j. \end{cases} \tag{6.8}$$

For the case of $\theta_v > \theta_j$, L is proportional to δ^4, where $\delta = [\gamma(1 - \beta \cos\theta_v)]^{-1} \propto \theta_v^{-2}$, so that the luminosity has the dependence of θ_v^{-8} (Ioka & Nakamura, 2001; Yamazaki et al., 2002;

Yamazaki, Yonetoku & Nakamura, 2003). The dependence of θ_j^6 is determined in order that two functions in equation (6.8) are continuously connected at $\theta_v = \theta_j$. We also consider the distribution of θ_j in the form $f(\theta_j)d\theta_j \propto \theta_j^{-q}d\theta_j$ when $\theta_{\min} < \theta_j < \theta_{\max}$. Then, in the case of $q < 5/2$, we have

$$
N(> L) \propto \begin{cases} L^{-1/4} & \text{for } L < 2L_j\theta_{\max}^{-2} \\ L^{(q-3)/2} & \text{for } 2L_j\theta_{\max}^{-2} < L < 2L_j\theta_{\min}^{-2}. \end{cases} \tag{6.9}
$$

This is a broken power-low with the break luminosity $2L_j\theta_{\max}^{-2}$. Then if $\theta_{\max}^{-2}L_j \propto g_k(z)$ with $q = 0.6$, we can roughly reproduce figure 5.10. According to equation (6.8), observed luminosity depends on the opening angle and the intrinsic luminosity within the collimated jet. This fact suggests that the luminosity evolution, $g_k(z) = (1 + z)^{2.6}$, comes from either the maximum opening half angle of the jet decreases or L_j increases as a function of the redshift (Yoneotku et al., 2004).

6.3.2 The luminosity evolution : $g_k(z)$

Probing the (z, L') independence with the τ statistical method, we estimated the luminosity evolution as $g_k(z) = (1+z)^{2.60}$. The luminosity evolution of $(1+z)^{1.4\pm0.5}$ and $(1+z)^{1.7\pm0.5}$ were suggested independently by Lloyd-Ronning et al. (2002b) and Wei & Gao (2002), respectively. We may enable to interpret the luminosity evolution as two cases; (1) the jet opening-angle is much narrowly collimated at the high redshift, and/or (2) the jet-corrected luminosity increases, for example the GRB progenitor evolution, at the high redshift. Although the jet opening angle evolution was suggested by Lloyd-Ronning et al. (2002b), our simple model of equation (6.8) gives either the maximum jet opening-angle (θ_j) decreases or the jet total energy (L_j) increases, and/or the both effect.

In the former case (jet opening-angle evolution), assuming that the maximum collimation angle of the relativistic jet decreases toward higher redshift, the energy density in the jet increases, so the gamma-ray luminosity also increases. On the other hand, in the latter case (progenitor evolution), if the average mass of the GRB progenitor increases, the total energy released by the gravitational collapse also increases.

We introduce a "κ" parameter, to separate the jet evolution and the progenitor evolution from equation (6.8),

$$
\bar{\theta}_j(z) = \bar{\theta}_{j,1}\left(\frac{1+z}{2}\right)^{-1.3\kappa} \tag{6.10}
$$

$$
\bar{L}_j(z) = \bar{L}_{j,1}\left(\frac{1+z}{2}\right)^{2.6(1-\kappa)}. \tag{6.11}
$$

Here, $\bar{\theta}_{j,1} \equiv 0.1$ (radian) and $\bar{L}_{j,1}$ are the mean jet opening angle and the mean geometrical corrected luminosity at $z = 1$. In figure 6.1, we show the each evolution as a function of the redshift. For $\kappa = 1.0$ (completely jet-evolution case), the mean opening angle evolves from 0.2 to 5×10^{-3} radian while $\bar{L}_j(z)$ keeps constant. It is difficult to consider such a strongly collimated jet. For $\kappa = 0.0$ (completely progenitor evolution case), the opening angle keeps constant, but the mean luminosity evolves from 0.1 to 400 times of $\bar{L}_{j,1}$. It is also unnatural. On the other hand, for $\kappa = 0.5$ (intermediate case), both $\bar{\theta}_j$ and $\bar{L}_j$ evolve in the range of 0.16–0.02 radian
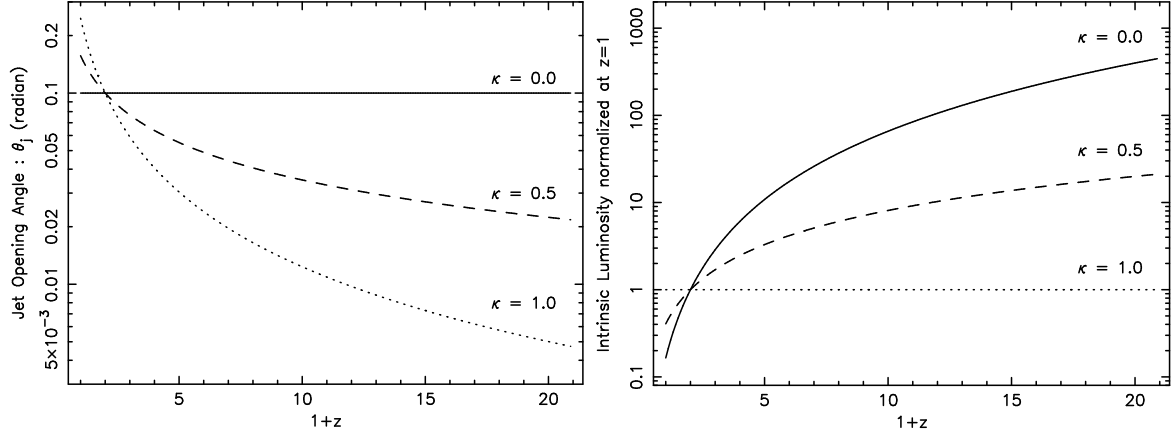
Figure 6.1: The left panel is the mean jet opening angle evolution and the right one is the progenitor (mean luminosity) evolution parametrized by κ. In the case of $\kappa = 1.0$ and $\kappa = 0.0$, the jet angle and the luminosity show quite strong evolution beyond natural extent, respectively. Therefore, we prefer the intermediate case, e.g. $\kappa = 0.5$, as a interpretation of the luminosity evolution.

and 0.4–21 times $\bar{L}_j$, respectively. We may recognize these evolution is acceptable value within the past observation results.

6.3.3   The GRB formation rate : $\rho(z)$

There are some luminosity indicators such as the variability–luminosity (V-L) relation (Fenimore & Ramirez-Ruiz, 2000), the spectral time lag–luminosity (lag-L) relation (Norris et al., 2000) and the E_p–E_{iso} and the E_p–luminosity relation (Amati et al., 2002; Sakamoto, 2004; Yoneotku et al., 2004). Using each luminosity indicator, several authors tried to estimate the GRB formation rate. Here, we summarize the preceding results.

The GRB formation rate derived by the V-L relation (see figure 5.1) are shown in figure 6.2. The left panel is a pioneering work by Fenimore & Ramirez-Ruiz (2000), and the right panel is reported by Lloyd-Ronning et al. (2002b) with the non-parametric method used in this thesis. On the other hand, using the lag-L relation (see figure 5.2), GRB formation rates are derived by Schaerer et al. (2002) and Murakami et al. (2003) as shown in figure 6.3 left and right, respectively. Murakami et al. (2003) noticed the off-axis viewing model by Ioka & Nakamura (2001), which can explain the observed lag-L property including GRB 980425 comprehensively, and they derived the GRB formation rate. These 4 results show the same tendency that the GRB formation rate monotonously increases toward the higher redshift. However all results are given as the relative GRB formation rate, and the absolute values have not been revealed yet.

In this thesis, as shown in figure 5.12, we derived the GRB formation rate with the E_p–luminosity relation. We succeeded in combining the results of *BATSE* and *BeppoSAX* , and the E_p–luminosity relation is much tighter than the previous V-L and lag-L relations. When we discuss the real GRB formation rate, it is important to deal with the geometrical effects of the jet opening-angle appropriately. As a first step to do this, we consider two extremely biased case for the luminosity evolution,
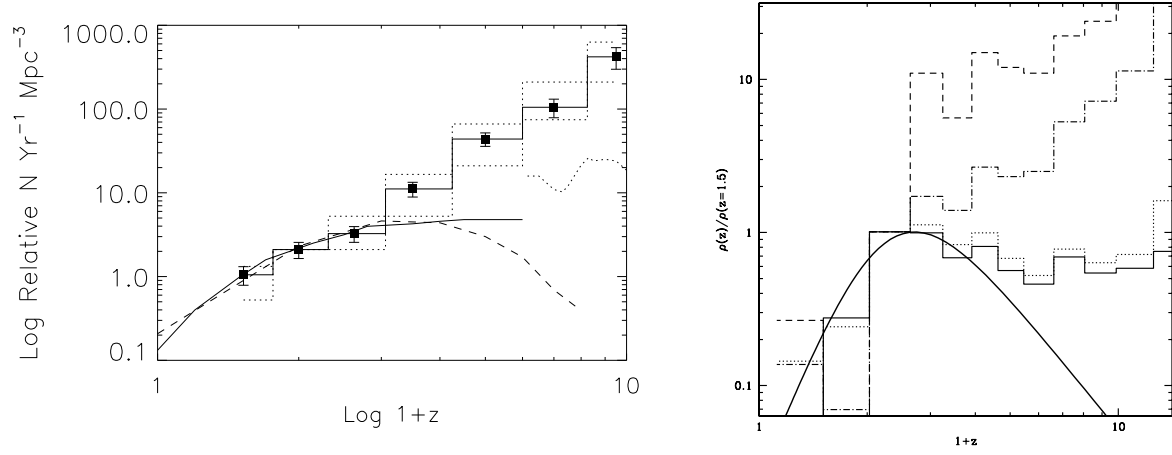
Figure 6.2: GRB formation rates derived by the variability–luminosity relation. The left and right figure is the result reported by Fenimore & Ramirez-Ruiz (2000) and Lloyd-Ronning et al. (2002b), respectively. These results are based on the same 220 samples.
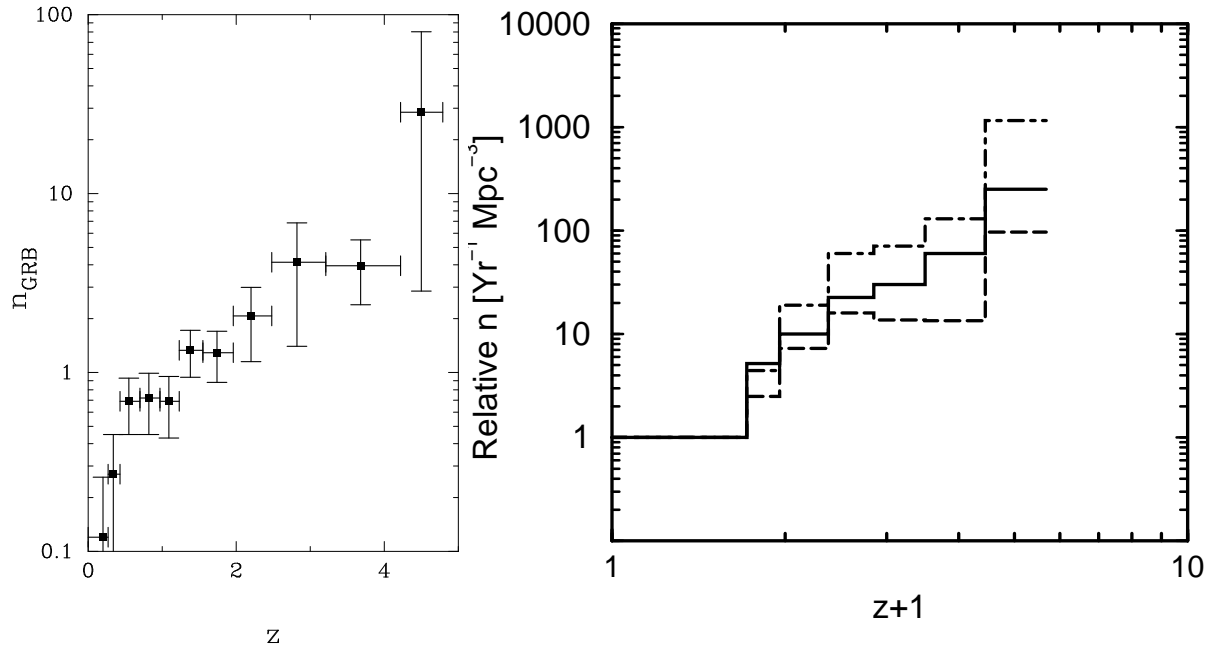
Figure 6.3: GRB formation rates derived by lag-L relation. The left and right figure is the result reported by Schaefer et al. (2001) and Murakami et al. (2003).

1. the case that the luminosity evolution is completely caused by the maximum jet opening-angle evolution ($\kappa = 1.0$) : $\theta_j^{-2} \propto (1 + z)^{2.6}$

2. the case that the luminosity evolution is completely caused by the progenitor evolution ($\kappa = 0.0$): $L_j \propto (1 + z)^{2.6}$.

In the former case the GRB formation rate shown in figure 5.12 is an underestimate, since the chance probability to observe the high-redshift GRB will decrease because the geometrical collimation becomes narrower toward higher redshift. If so, the GRB formation rate increases more rapidly toward the higher redshift. Quantitatively, $\rho(z)(1 + z)^{2.60}$ may be the improved GRB formation rate removed by the jet's geometrical effect. On the other hand, in the latter case, the functional form of the GRB formation rate in figure 5.12 is a reasonable estimate, because there is not the geometrical effect caused by jet opening-angle.

6.4 Absolute GRB Formation Rate

In Chapter 5, we show the relative GRB formation rate based on the redshift distribution derived by the E_p–luminosity relation, but we did not give the absolute value of the GRB formation rate because of the mathematical limitation (see Appendix A). In this section, using the functions of the luminosity function $\psi(L')$ and the luminosity evolution $g_k(z)$, we perform a numerical calculation to estimate absolute GRB formation rate.

6.4.1 Physical Parameters

To calculate the absolute GRB formation rate, we have to include several corrections. For example, the jet opening angle, luminosity evolution, selection effect, and so on. First, we summarize some physical parameters necessary to perform the numerical calculation.

(1) luminosity evolution $g_k(z)$ and jet correction factor $k(z)$
To estimate the absolute GRB formation rate, we have to correct the geometrical effect by the jet opening angle. Let us consider the jet opening angle with θ_j, then the beaming fraction is $(1 - \cos\theta_j) \sim \theta_j^2/2$ for $\theta_j \ll 1$. The chance probabilities to observe such GRBs reduces, so we correct the beaming effect multiplying by $2/\theta_j^2$. In this thesis, we found the luminosity evolution of $g_k(z) = (1 + z)^{2.6}$. This luminosity evolution is interpreted as the GRB progenitor evolution (mass evolution) or the jet opening angle evolution (Yoneotku et al., 2004). As already mentioned, if the luminosity evolution is resulted from the jet opening angle evolution, we have to correct the geometrical effect when we estimate the absolute GRB formation rate. Quantitatively, this correction factor is $k(z) = 2\bar{\theta_j}^{-2} g_k(z)$. Here, $\bar{\theta_j}$ is an average jet opening half angle. On the other hand, if the luminosity evolution is completely the progenitor evolution, then we do not require to include this evolution effect ($k(z) = 1$) in the calculation. Therefore, these two interpretations play different roles in the GRB formation rate. Taking into account these effects, we introduce κ parameter ($0 \leq \kappa \leq 1$), as already shown in equation (6.10), to describe the fraction of the jet opening angle evolution to the total luminosity evolution.

Using this κ parameter, we determine the jet correction factor, $k(z)$, including the jet opening angle evolution:

$$k(z) \equiv 2\bar{\theta}_j^{-2} g_k(z)^{\kappa} = 200 \Big(\frac{\bar{\theta}_{j,1}}{0.1}\Big)^{-2} \Big(\frac{1+z}{2}\Big)^{2.6\kappa}. \tag{6.12}$$

Here, we assume $\bar{\theta}_{j,1} = 0.1$ radian at $z = 1$ based on the results by Frail et al. (2001) and Bloom et al. (2003). We correct the geometrical effect by multiplying the factor $k(z)$ when we perform the numerical calculation.

(2) cumulative luminosity function $\psi(L')$
Based on the result by equation (5.6), we set the cumulative luminosity function:

$$\psi(L') \propto \begin{cases} L'^{-0.29} & \text{for } L' \leq 10^{51} \text{ erg s}^{-1}, \\ \alpha_b L'^{-1.02} & \text{for } L' \geq 10^{51} \text{ erg s}^{-1}. \end{cases} \tag{6.13}$$

Here, $L' = L/g_k(z)$ is the luminosity after removing the luminosity evolution. We set a coefficient α_b as 1.70×10^{37} to continuously connect two functional form at the break luminosity of $L' = 10^{51}$ ergs s^{-1} . This cumulative luminosity function $\psi(L')$ is normalized to unity at $L' = 10^{50}$ ergs s^{-1} .

(3) GRB formation rate $\rho(z)$
The functional form of the GRB formation rate as shown in figure 5.12 can be described below equation:

$$\rho(z) \propto \begin{cases} (1+z)^{6.0} & \text{for } z \leq 1, \\ \beta_b(1+z)^{0.4} & \text{for } z \geq 1. \end{cases} \tag{6.14}$$

Here, $\beta_b = 2^{5.4}$ is a coefficient to connect above two function at the break point of $z = 1$. This function is also normalized to unity because $\rho(z)$ describe only the shape of redshift distribution observed by *BATSE* .

(4) selection effect $P(L_{min})$
The relative GRB formation rate by equation (6.14) is derived from the flux limited samples, i.e. $F > F_{limit} = 2 \times 10^{-7}$ ergs cm^{-2}s^{-1} . Since we used the τ statistical method and the non-parametric method introduced in Appendix A, we could take into account the flux limit appropriately. However, we have no information below $L = 10^{50}$ ergs s^{-1} as shown in (z, L) diagram of figure 5.5, so we may have to include a correction factor when we calculate the absolute GRB formation rate.

We would like to estimate the absolute GRB formation rate between the luminosity range of L_{min} and L_{max}. For the purpose of easy calculation, we use the universal luminosity function $\psi(L')$ after removing the luminosity evolution. Instead of that, the integration should be performed from $L'_{max} = L_{max}/g_k(z)$ to $L'_{min} = L_{min}/g_k(z)$, and we can determine the correction factor:

$$P(L_{min}) \equiv \frac{\int_{L'_{min}}^{L'_{max}} \frac{d\psi(L')}{dL'} dL'}{\int_{L'_{lim,0}}^{L'_{max}} \frac{d\psi(L')}{dL'} dL'} = \frac{\psi(L'_{min}) - \psi(L'_{max})}{\psi(L'_{lim,0}) - \psi(L'_{max})} \tag{6.15}$$
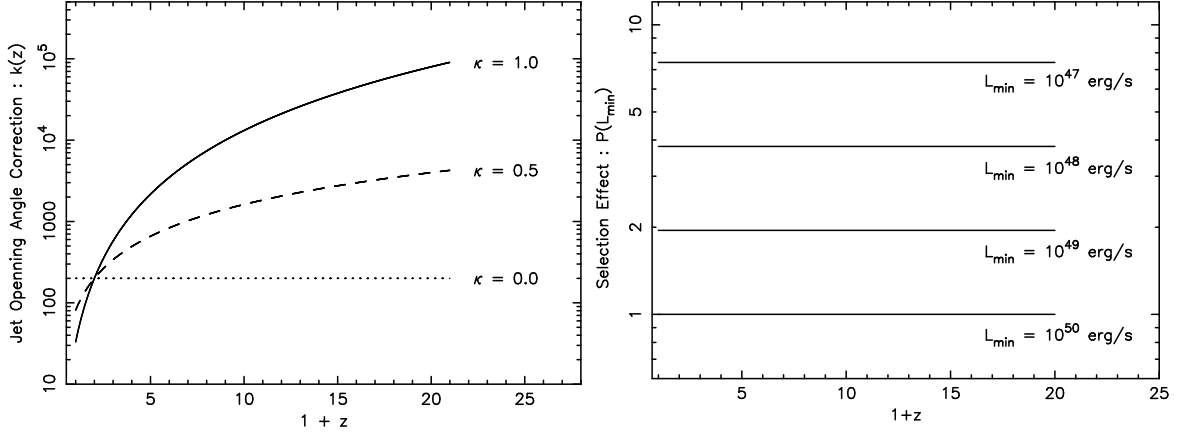
Figure 6.4: Correction factors $k(z)$ and $P(z)$ as a function of redshift. The left panel is the geometrical correction factor $k(z)$ of the jet opening angle evolution with three different cases of $\kappa = 1.0$, 0.5 and 0.0. We assume $\bar{\theta}_j = 0.1$ at $z = 1$. The right panel is the selection effect $P(L_{min})$ with four different cases of $L_{min} = 10^{50}$, 10^{49}, 10^{48} and 10^{47} ergs s^{-1} .

$$= \frac{\psi(L_{min}/g(z)) - \psi(L_{max}/g(z))}{\psi(L_{lim,0}/g(z)) - \psi(L_{max}/g(z))} = \frac{\psi(L_{min}/g(z)) - \psi(10^{55}/g(z))}{\psi(10^{50}/g(z)) - \psi(10^{55}/g(z))} \quad (6.16)$$

Here $L'_{lim,0}$ is the luminosity of the dimmest point at the redshift of $z \sim 0$ in our samples, and we set $L'_{lim,0} = L_{lim,0} = 10^{50}$ ergs s^{-1} . The numerator of equation (6.15) means the occurring probability of GRBs within the luminosity range of L'_{min}–L'_{max}. On the other hand, the denominator means the probability to detect GRBs brighter than the luminosity limit of $L'_{lim,0}$. Therefore the factor $P(L_{min})$ is the selection effect which shows the fraction of the real number of GRBs brighter than L_{min} to the observed GRBs above luminosity limit ($L_{lim,0}$). Setting $L_{max} = 10^{55}$ ergs s^{-1} , we investigate several cases of L_{min}, i.e. $L_{min} = 10^{50}, 10^{49}, 10^{48}$ and 10^{47} ergs s^{-1} . As shown in figure 6.4 (right), this selection effect $P(L_{min})$ is independent of the redshift.

6.4.2   Calculation of Absolute GRB Formation Rate

The number of GRBs brighter than $F_{limit} > 2 \times 10^{-7}$ ergs cm^{-2}s^{-1} is about 700 events during the entire *BATSE* life time (9 years). As shown in Chapter 3, the average fraction of the sky coverage is 0.483, so the observed GRB rate is $N(> L_{limit}) = 160$ events yr^{-1}. Generally, integrating the luminosity function over the entire luminosity and redshift ranges gives the total number count.

$$N(> L_{limit}) = \rho_0 \int_0^{z_{max}} dz \int_{L_{limit}(z)}^{L_{max}} \rho(z) \left(\frac{dV}{dz}\right) \frac{1}{1+z} \frac{d\psi(L/g_k(z))}{dL} \frac{dL}{g_k(z)} \quad (6.17)$$

$$= \rho_0 \int_0^{z_{max}} dz \int_{L'_{limit}(z)}^{L'_{max}} \rho(z) \left(\frac{dV}{dz}\right) \frac{1}{1+z} \frac{d\psi(L')}{dL'} \frac{dL'}{g_k(z)}. \quad (6.18)$$

Here ρ_0 is a normalization, one of the key parameter, which give the absolute value for the GRB formation rate. The term of dV/dz is the differential comoving volume and $1/(1 + z)$ describes the cosmological time dilation. Setting the above solution $N(> L_{limit})$ be the observed rate of 160 event yr^{-1}, we found the best result of $\rho_0 = 98.7$ events Gpc^{-3}yr^{-1}.

Using the ρ_0 value, we perform the calculations to estimate the absolute GRB formation rate with the luminosity above L_{min}. Then, introducing additional components of the geometrical correction (jet opening angle evolution) $k(z)$ and the selection effect $P(L_{min})$ described in the previous section, we derive the absolute GRB formation rate:

$$\rho(z)_{real} = \rho_0 \rho(z) k(z) P(L_{min}). \qquad (6.19)$$

In figure 6.5, we show the absolute GRB formation rate in units of events $Gpc^{-3}yr^{-1}$ as a function of $1 + z$. The data points with filled squares are the observed GRB rate corrected for $\kappa = 0.5$, and two dotted lines show the upper and lower bound based on the error of E_p–luminosity relation. Assuming the $L_{min} = 10^{50}$ ergs s^{-1} , in figure 6.5, we show three different cases at $\kappa = 0.0$, 0.5 and 1.0. Three functional forms are crossing at $z = 1$. This is because we assume the mean jet opening angle $\bar{\theta}_{j,1} = 0.1$ (radian) at $z = 1$. A local GRB formation rate (at $z = 0$) brighter than 10^{50} ergs s^{-1} is $\rho(0)_{real} \sim 10$ events $Gpc^{-3}yr^{-1}$, and $\rho(1)_{real} \sim 530$ events $Gpc^{-3}yr^{-1}$ at $z = 1$. At the higher redshift range, the GRB formation rate strongly depends on the κ parameter giving the jet opening angle evolution. In the case of $\kappa = 0.0$, the shape of the absolute GRB formation rate keeps the original form of equation (6.14). Then, the GRB formation rate is $\sim 10^3$ events $Gpc^{-3}yr^{-1}$ at $z = 12$. On the other hand, in the case of $\kappa = 1.0$, it is $\sim 10^5$ events $Gpc^{-3}yr^{-1}$ at $z = 12$. This is the first work to estimate the absolute GRB formation rate, and also the star formation rate at the cosmological reionization epoch. This absolute GRB formation rate are reported in Murakami, Yonetoku et al. (2004); Matsubayashi, Yamazaki, Yonetoku et al. (2004).

6.4.3 GRB Formation Rate and Star Formation Rate

As already shown in figure 1.12, the star formation rate has been measured as a function of the redshift. The initial mass function (IMF) at present is well described by the single power-law in mass with the index of -2.35. This is frequently called the Salpeter type IMF (Salpeter, 1955). Integrating over the mass range between 0.1–1000 $M_{\odot}$, and comparing the observed star formation rate, we can obtain the IMF at $z = 1$:

$$\frac{dN}{dm} = 1.63 \times 10^{-2} m^{-2.35} \quad (\text{at } z = 1). \qquad (6.20)$$

Based on the above IMF, we can estimate the total number of star in the mass range of 40–1000 $M_{\odot}$ which is thought to be the GRB candidates.

$$M_{star}(> 40 \ M_{\odot}) = \int_{40M_{\odot}}^{1000M_{\odot}} 1.63 \times 10^{-2} m^{-2.35} dm \qquad (6.21)$$
$$= 8.19 \times 10^4 \quad (\text{stars } Gpc^{-3}yr^{-1} \text{ at } z = 1). \qquad (6.22)$$

Comparing the observed GRB formation rate in figure 6.5 and the above estimate, we can say GRBs are produced by about 1 % of stars with the mass above 40 $M_{\odot}$. The energetic supernova (Hypernova) associated with GRBs are thought to be CO-stars without hydrogen envelope. Since the stellar form at the final stage of their life-time depends on the stellar evolutions, all stars with the mass above 40 $M_{\odot}$ may not enable to produce GRBs.
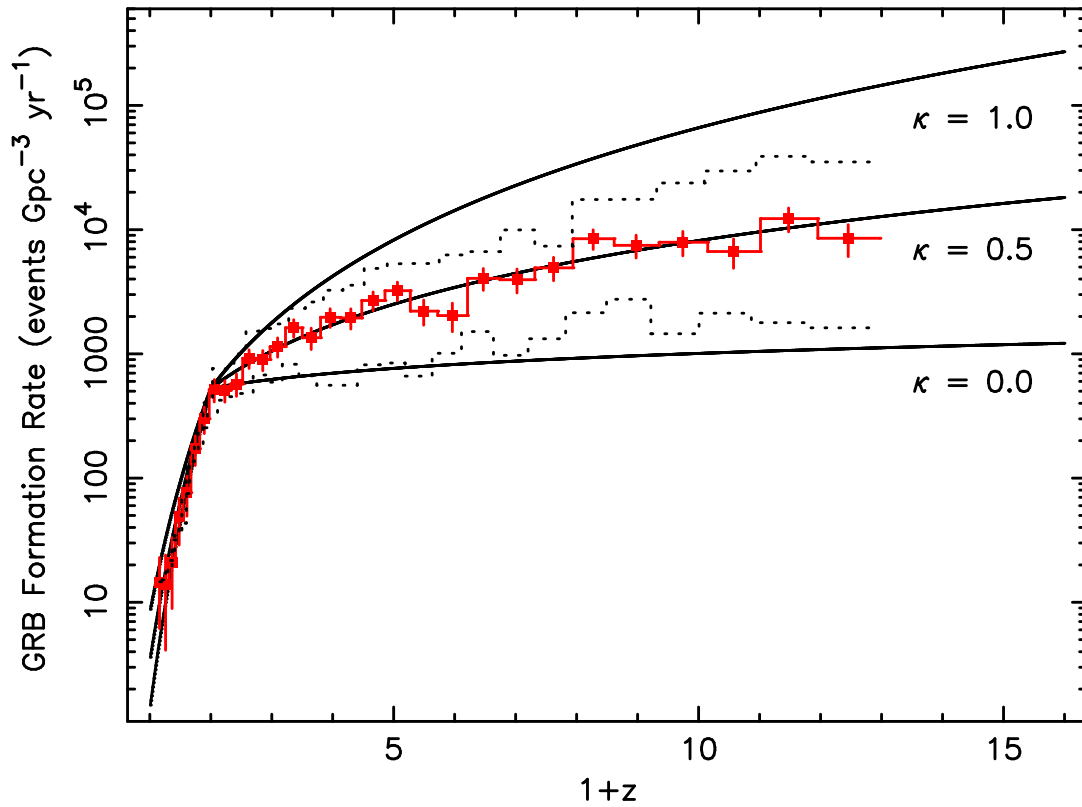
Figure 6.5: Absolute GRB formation rate after the beaming correction. The red marked points are observed GRB event-rate including the jet angle evolution with $\kappa = 0.5$, and two dotted lines indicate upper- and lower-bound comes from the error of the E_p–luminosity relation. Three different cases with the jet opening angle evolution ($\kappa = 1.0$, 0.5 and 0.0) are shown as the solid lines. In the figure, we assume $L_{min} = 10^{50}$ ergs s^{-1} and $L_{max} = 10^{55}$, respectively.

6.5 Cosmological Influence by Population III Stars

We have already shown that the GRB formation rate is significantly larger than the present local value. Recently, connections between long duration GRBs and SNe are confirmed by the observations of GRB 030329/SN 2003dh and GRB 980425/SN 1998bw. Therefore GRBs are triggered by the massive star explosion. On the other hand, numerical simulations of the formation of the first generation stars, so called population III stars (Pop-III stars), show that they are quite massive beyond 50 $M_\odot$. Therefore, we can consider that GRBs are produced by massive Pop-III stars in the early universe. In this section, based on the GRB formation rate in figure 6.5, we estimate the star formation rate of Pop-III stars, and discuss about a cosmic reionization and a metal enrichment into the intergalactic medium in view of the influence from Pop-III stars. These phase transitions are the most important events in the cosmological history, and they must influence the following cosmic fates, such as formation of stars, galaxies, large scale structures, and so on.

6.5.1 Initial Mass Function of Population III Stars

According to recent hydrodynamical simulations (e.g. Gnedin, 2000; Nakamura & Umemura, 2001), primordial gaseous clouds gravitationally condense like filaments and zero-metal stars (population III stars: composed by only H and He) are formed in the early universe. Especially, Nakamura & Umemura (2001) suggested the initial mass function (IMF) of Pop-III stars are due to bimodal distribution because it is highly dependent on the initial density. In high density case with $n > 10^5$ cm^{-3}, effective H$_2$ cooling stops the radial contraction of the primordial gas. Then the density of the gas clumps are relatively low, so the Pop-III stars with a few $M_\odot$ are formed. On the other hand, in low density case with $n < 10^5$ cm^{-3}, the cooling by H$_2$ molecules does not significantly contribute the hydrodynamics of the primordial gas condensation. Thus the gas clouds grow to dense clumps, and *massive* Pop-III stars are formed.

By the recent works of the stellar evolution of the Pop-III stars (e.g. Portinari et al., 1998; Heger & Woosley, 2002), their fates can be classified as following 6 patterns, i.e.,

1. $m \leq 10\ M_\odot$ stars form white dwarfs, so they do not explode and emit any heavy metals.

2. $10\ M_\odot \leq m \leq 25\ M_\odot$ stars form neutron stars through type-II supernova explosions. The majority of the ejecta are hydrogen and helium with small amount of heavy metals. The metal mass is generally thought to be 10 % of all exploded mass.

3. $25\ M_\odot \leq m \leq 100\ M_\odot$ stars form black holes, and the stellar matters are involved into BH. No matter is emitted into the intergalactic medium (IGM).

4. $100\ M_\odot \leq m \leq 140\ M_\odot$ stars can produce GRBs as Hypernovae, which is the key interest in this thesis. These stars also generate black holes, but the 10 % of the exploded matters contribute the metal enrichment into the IGM.

5. $140\ M_\odot \leq m \leq 260\ M_\odot$ stars do not form any compact object via the stellar collapse. The core completely disrupts, and the whole core involving large amount of heavy elements is
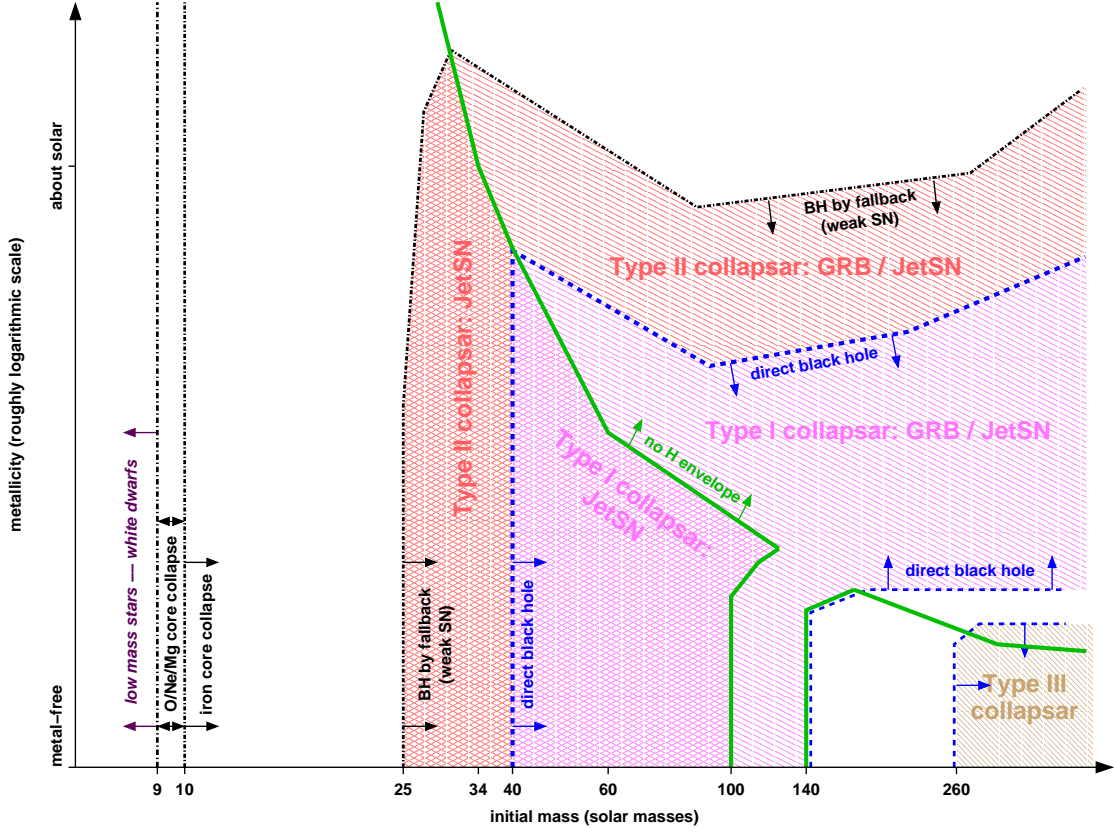
Figure 6.6: Fate of massive stars as a function of metallicity at the end of their lifetime by Heger et al. (2003).

injected into the IGM. Since the metal fraction of the exploded mass is about 50 %, the strong metal enrichment are expected from these events.

6. $m \geq 260$ $M_\odot$ stars collapse completely into a black hole without ejecting any heavy elements.

In figure 6.6, we show the stellar fate as the function of the metallicity (Heger & Woosley, 2002). In figure 6.7, we also show a schematic IMF assuming the power-law distributions with index α and β, and cut-off mass of 50 $M_\odot$ and 1 $M_\odot$ for high-mass and low-mass part, respectively. At present, this type of IMF is independently reconstructed by simulations in several works, and widely believed that the Pop-III stars are heavier than 50 $M_\odot$ while the existence or absence of the low-mass part of the bimodal IMF in figure 6.7 is still in debate. In this section, we also based on the IMF in figure 6.7 and discuss about cosmological influences by the Pop-III stars. We consider the both IMFs in the following calculation, but the number and the total mass of the low-mass stars are quite small, and their contributions to the early epoch reionization and the metal enrichment are negligible.

As shown in figure 6.7, assuming the IMF of double power-law shapes with peaks of 50 $M_\odot$
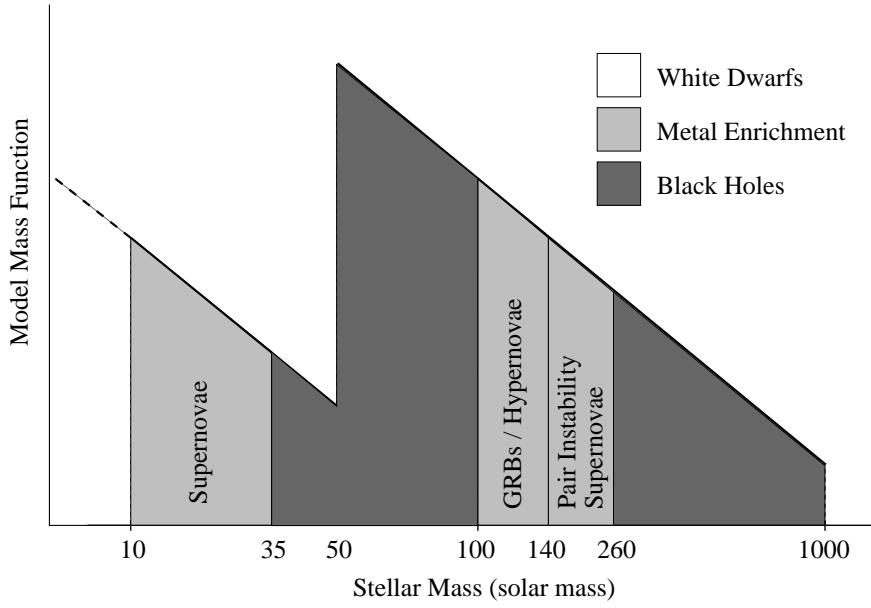
Figure 6.7: Schematic view of the initial mass function (IMF). we assume bimodal distribution of the IMF to refer to Nakamura & Umemura (2001). The functional form of the IMF is given by equation (6.23), (6.24) and (6.25). The two parts denoted as "SNe" and "GRBs" contribute for the cosmic metal enrichment, and the other parts do not intersperse any heavy elements during their own lifetime.

and 1 $M_\odot$ for the high-mass and the low-mass parts, respectively, we set the functional form of the IMF:

$$\frac{dN}{dm} = \frac{d(N_{high} + N_{low})}{dm},$$ (6.23)

where

$$\frac{dN_{high}}{dm} = \begin{cases} Am^{-\alpha} & \text{for} \quad 50\ M_\odot \le m \le 1000\ M_\odot, \\ 0 & \text{for} \quad \text{otherwise}, \end{cases}$$ (6.24)

$$\frac{dN_{low}}{dm} = \begin{cases} Bm^{-\beta} & \text{for} \quad 1\ M_\odot \le m \le 50\ M_\odot, \\ 0 & \text{for} \quad \text{otherwise}. \end{cases}$$ (6.25)

Here α and β are the power-law indices of IMF for high-mass and low-mass parts, respectively. The observed GRB formation rate in figure 6.5 corresponds to the region between 100 and 140 $M_\odot$ denoted as "GRBs/Hypernovae". We have no information about the lower part of the IMF, so we introduce a parameter q to determine the relative value to the higher part IMF, and that satisfy a condition of $B(1M_\odot)^{-\beta} = qA(50M_\odot)^{-\alpha}$. Although the IMF is generally described in units of [stars $M_\odot^{-1}$], we set it as in [stars Gpc^{-3}yr^{-1} $M_\odot^{-1}$] to compare the absolute GRB formation rate in units of [events Gpc^{-3}yr^{-1}] in figure 6.5.

Let us determine the normalization A (and also B) from the observed GRB formation rate as shown in figure 6.5. To do so, integrating the IMF of equation (6.23) over 100–140 $M_\odot$, we determine the normalization A:

$$\rho_{GRB} = \int_{100M_\odot}^{140M_\odot} \frac{dN_{high}}{dm} dm = \int_{100M_\odot}^{140M_\odot} Am^{-\alpha} dm$$ (6.26)

$$= \ A \ \frac{(140 M_\odot)^{1-\alpha} - (100 M_\odot)^{1-\alpha}}{1-\alpha} \quad \text{(events Gpc}^{-3}\text{yr}^{-1}). \tag{6.27}$$

Thus the normalization A and B can be described as a function of ρ_{GRB}, and the IMFs of equation (6.24) and (6.25) can be rewritten:

$$\frac{dN_{high}}{dm} \ = \ \frac{(1-\alpha) \ \rho_{GRB}}{(140 M_\odot)^{1-\alpha} - (100 M_\odot)^{1-\alpha}} m^{-\alpha}, \tag{6.28}$$

$$\frac{dN_{low}}{dm} \ = \ q(50 M_\odot)^{-\alpha} \frac{(1-\alpha) \ \rho_{GRB}}{(140 M_\odot)^{1-\alpha} - (100 M_\odot)^{1-\alpha}} m^{-\beta}. \tag{6.29}$$

In the following section, based on the above functional form of IMF, we discuss about the cosmological influence from Pop-III stars and GRBs.

6.5.2   Cosmological Reionization by Population III Stars

Cosmic reionization is one of the most important event in cosmology. By the recent observations with the *WMAP* satellite, Bennett et al. (2003); Spergel et al. (2003) reported that the cosmic reionization (*early epoch reionization*) started at $z = 17 \pm 5$ ($\sim$ 200 million years after the big bang) which implies the Pop-III stars have already brightened before at least this epoch (e.g. Miralda-Escudé, 2003; Yoshida et al., 2004). They may significantly urge the cosmic reionization at the early universe[2]. Using the absolute GRB formation rate, we investigate contributions from Pop-III stars for the early epoch reionization.

Massive Pop-III stars ($50 M_\odot \leq M \leq 1000 M_\odot$) radiate almost at the Eddington limit of $L = 1.3 \times 10^{38} \ (M/M_\odot)$ erg s^{-1} with a blackbody temperature of $\sim 10^5$ K during a main-sequence lifetime of $\sim 3 \times 10^{13}$ s (e.g. Couchman and Rees, 1986; Schaerer et al., 2002). The typical properties of Pop-III stars are summarized in table 6.1 (Schaerer et al., 2002). The surface temperature and the lifetime scarcely depend on the stellar mass while luminosity is proportional to mass. On the surface condition of 10^5 K, about 90 % photons radiated via blackbody are above 13.6 eV, thus they can ionize hydrogen atoms effectively with the photo-ionization process.

Using the above properties of massive Pop-III stars, we estimate the photon emission rate above > 13.6 eV:

$$Q_i = 1.3 \times 10^{38} \left(\frac{M}{M_\odot}\right) \frac{\int_{\nu_i}^{\infty} d\nu F_\nu/(h\nu)}{\int_0^{\infty} d\nu F_\nu} \sim 3 \times 10^{48} \left(\frac{M}{M_\odot}\right) \quad \text{(photons s}^{-1}). \tag{6.30}$$

Here, F_ν is the spectral flux distribution (Planck law) in units of erg cm^{-2}s^{-1}Hz^{-1}, and $\nu_i = 13.6$ eV$/h$ is the critical frequency which enables it to ionize Hydrogen atoms. Therefore, the total number of photon produced in the lifetime (3×10^{13} s) is roughly 10^{62} ($M/M_\odot$) photons (10^{62} photons per unit solar mass). The total photon emission rate above 13.6 eV produced by

---

[2]A scenario that the universe has been reionized twice are suggested. Actually the existence of neutral Hydrogens in the IGM at $z \sim 6$ are pointed out by the QSO observation while the *WMAP* satellite measured the reionization epoch of $z = 17 \pm 5$. We separate these two reionization and discuss one of the earlier epoch in this thesis.

Initial Mass	Luminosity	Temperature	lifetime[1]	lifetime[2]
$M_\odot$	$L_\odot$	K	yr	yr
1000	2.87×10^7	1.06×10^5	—	2.43×10^6
500	1.28×10^7	1.07×10^5	1.90×10^6	2.45×10^6
400	9.64×10^6	1.07×10^5	1.97×10^6	—
300	6.60×10^6	1.02×10^5	2.05×10^6	2.15×10^6
200	3.75×10^6	9.98×10^4	2.20×10^6	2.63×10^6
120	1.75×10^6	9.57×10^4	2.52×10^6	2.95×10^6
80	8.85×10^5	9.33×10^4	3.01×10^6	3.72×10^6
60	5.19×10^5	8.77×10^4	3.46×10^6	—
40	2.64×10^5	7.94×10^4	3.86×10^6	—
25	7.76×10^4	7.08×10^4	6.46×10^6	—
15	2.11×10^4	5.74×10^4	1.04×10^7	—
9	5.12×10^3	4.19×10^4	2.02×10^7	—
5	7.41×10^2	2.75×10^4	6.19×10^7	—

Table 6.1: Properties of population III stars by Schaerer et al. (2002). The stellar lifetime is summarized both for no mass-loss[1] and strong mass-loss[2] cases.

the Pop-III stars with 50–1000 $M_\odot$ is estimated as

$$\dot{N}_{UV} = \int_{50M_\odot}^{1000M_\odot} 10^{62}(M/M_\odot)\frac{dN_{high}}{dm}dm = \int_{50M_\odot}^{1000M_\odot} 10^{62}m\frac{dN_{high}}{dm}dm \qquad (6.31)$$

$$= 10^{62}\frac{1-\alpha}{2-\alpha}\frac{(1000M_\odot)^{2-\alpha} - (50M_\odot)^{2-\alpha}}{(140M_\odot)^{1-\alpha} - (100M_\odot)^{1-\alpha}}\,\rho_{GRB} \quad \text{(photons Gpc}^{-3}\text{yr}^{-1}). \quad (6.32)$$

If we assume IMF index as the traditional Salpeter value of $\alpha = 2.35$ (Salpeter, 1955), we have estimated the total UV photon emission rate as $\dot{N}_{UV} = 8.75 \times 10^{64}\rho_{GRB}$ photons Gpc^{-3}yr^{-1}.

The neutral hydrogens are ionized by the UV photons, but they recombine into the neutral state again. The Pop-III stars have to continuously irradiate the IGM to keep ionizing all hydrogens. Then we have to estimate the recombination timescale and the UV photon emission rate minimally required to remain the ionization equilibrium. The recombination timescale is generally determined by the density and the temperature as

$$\bar{t}_{rec} = [(1+2\chi)\bar{n}_{\rm H}\alpha_B]^{-1} = 0.5\Big(\frac{\Omega_b h^2}{0.0224}\Big)^{-1}\Big(\frac{1+z}{16}\Big)^{-3} \quad \text{(Gyr)}, \qquad (6.33)$$

where $\chi \sim 0.25$ is the helium to hydrogen cosmic abundance ratio, and α_B is the recombination coefficient at $\sim 10^4$ K. The $\bar{n}_{\rm H}$ is the mean hydrogen density of the expanding IGM, and we set $\bar{n}_{\rm H} = 3.36 \times 10^{-7}(\Omega_b h^2/0.0224)$ cm^{-3} to refer to Madau et al. (1999). By use of the recombination timescale $\bar{t}_{rec}$, the minimum photon emission rate to keep the fully ionization state of the IGM is estimated as

$$\dot{N}_{min} = \frac{\bar{n}_{\rm H}}{\bar{t}_{rec}} = 1.15 \times 10^{67}\Big(\frac{\Omega_b h^2}{0.0224}\Big)^2\Big(\frac{1+z}{16}\Big)^3 \quad \text{(photons Gpc}^{-3}\text{yr}^{-1}). \qquad (6.34)$$

Only in the case where the photon emission rate brighter than equation (6.34), the IGM is held in fully ionization state by Pop-III stars. Based on the above estimate of $\dot{N}_{UV}$ and $\dot{N}_{min}$, effective photon luminosity contributes the early epoch reionization is about $\dot{N}_{UV} - \dot{N}_{min}$.

The cosmological parameter for the baryon density is measured as $\Omega_b = 0.047$ by the CMB observations with the *WMAP* satellite (Spergel et al., 2003). This is equivalent to the baryon mass density of $\rho_b = \Omega_b \rho_{cr} = 6.0 \times 10^{18}\ M_\odot\ \mathrm{Gpc}^{-3}$, where $\rho_{cr} \equiv 3H^2/8\pi G$ is the critical density. When we assume all baryons in the primordial gas are hydrogen atoms in the early universe, the number of Hydrogen is estimated as $N_b \sim \rho_b/m_p = 7.66 \times 10^{75}\ \mathrm{Gpc}^{-3}$. Then the required time to ionize all hydrogens is

$$t_{reionize} \sim \frac{N_b}{(\dot{N}_{UV} - \dot{N}_{min})} = \frac{7.66 \times 10^{75}}{8.75 \times 10^{64}\rho_{GRB} - 1.15 \times 10^{67}}\quad (\mathrm{yr}) \tag{6.35}$$

Substituting the absolute GRB rate in figure 6.5 for equation (6.35), we estimate the required time-interval to ionize the IGM completely:

$$t_{reionize} = \begin{cases} 1.0 \times 10^8\ \mathrm{yr} & \text{for}\quad \rho_{GRB} = 1 \times 10^3 & (\kappa = 0.0), \\ 4.4 \times 10^6\ \mathrm{yr} & \text{for}\quad \rho_{GRB} = 2 \times 10^4 & (\kappa = 0.5), \\ 2.9 \times 10^5\ \mathrm{yr} & \text{for}\quad \rho_{GRB} = 3 \times 10^5 & (\kappa = 1.0). \end{cases} \tag{6.36}$$

From this estimation, the neutral hydrogen in the primordial IGM can be promptly ionized, such as $z > 12$, by the strong UV radiation from Pop-III stars.

The Pop-III stars generally belong to the dense filament or the primordial galaxies. To ionize the entire IGM, the UV photons emitted by the Pop-III stars must escape from them and achieve the IGM. Even if the escape fraction is 1 %, UV photon luminosity ($\dot{N}_{UV}$ for $\kappa = 0.5$) is 2 orders of magnitude larger than the minimum value ($\dot{N}_{min}$), so the IGM is effectively reionized by the UV photon from Pop-III stars.

6.5.3   Metal Products and Cosmic Pollution by Population III Stars

In this section, we consider a heavy-element synthesis at the early universe based on the absolute GRB formation rate. As shown in figure 6.7, only the Pop-III stars with the mass range of 100–140 $M_\odot$ (GRBs/Hypernovae), 140–260 $M_\odot$ (pair instability SNe) and 10–25 $M_\odot$ (type-II SNe) can contribute the metal enrichment at the end of their lifetime. The mass production rate (including Hydrogen, Helium as well as heavy elements) for each mass range can be estimated as:

$$\dot{M}_{GRB} = \int_{100M_\odot}^{140M_\odot} m \frac{dN_{high}}{dm} dm \tag{6.37}$$

$$= \frac{1-\alpha}{2-\alpha} \frac{(140M_\odot)^{2-\alpha} - (100M_\odot)^{2-\alpha}}{(140M_\odot)^{1-\alpha} - (100M_\odot)^{1-\alpha}}\ \rho_{GRB}\quad (M_\odot\ \mathrm{Gpc}^{-3}\mathrm{yr}^{-1}), \tag{6.38}$$

$$\dot{M}_{pair} = \int_{140M_\odot}^{260M_\odot} m \frac{dN_{high}}{dm} dm \tag{6.39}$$

$$= \frac{1-\alpha}{2-\alpha} \frac{(260M_\odot)^{2-\alpha} - (140M_\odot)^{2-\alpha}}{(140M_\odot)^{1-\alpha} - (100M_\odot)^{1-\alpha}}\ \rho_{GRB}\quad (M_\odot\ \mathrm{Gpc}^{-3}\mathrm{yr}^{-1}), \tag{6.40}$$

$$\dot{M}_{SN} = \int_{10M_\odot}^{25M_\odot} m \frac{dN_{low}}{dm} dm \tag{6.41}$$

$$= \frac{q}{(50M_\odot)^\alpha} \frac{1-\alpha}{2-\beta} \frac{(25M_\odot)^{2-\beta} - (10M_\odot)^{2-\beta}}{(140M_\odot)^{1-\alpha} - (100M_\odot)^{1-\alpha}}\ \rho_{GRB}\quad (M_\odot\ \mathrm{Gpc}^{-3}\mathrm{yr}^{-1}). \tag{6.42}$$

Again, assuming the Salpeter value for $\alpha = \beta = 2.35$ (Salpeter, 1955) and $q = 1.0$, we calculate the above mass production rate is $\dot{M}_{GRB} = 117 \ \rho_{GRB}$, $\dot{M}_{pair} = 183 \ \rho_{GRB}$ and $\dot{M}_{SN} = 0.07 \ \rho_{GRB} \ M_\odot \mathrm{Gpc}^{-3}\mathrm{yr}^{-1}$, respectively [3]. Since the fraction of the metal mass to the exploded total mass is 10 %, 50 % and 10 % for $\dot{M}_{GRB}$, $\dot{M}_{pair}$ and $\dot{M}_{SN}$ (Nakamura & Umemura, 2001), the total metal production rate is estimated as $\dot{M}_{metal} = 103.2 \ \rho_{GRB} \ M_\odot \ \mathrm{Gpc}^{-3}\mathrm{yr}^{-1}$. The total number of metal in the IGM increase with $\dot{N}_{metal} = \dot{M}_{metal}/(\mu m_p)$, where μ is the mean mass number of the heavy elements, and we set $\mu = 16.54$ in the solar value.

As a reference value, we consider the time interval injecting the heavy elements into the space as $\Delta t = 10^7$ yr, then the total number of heavy elements are estimated as

$$N_{metal} \sim \dot{N}_{metal}\Delta t = 1.23 \times 10^{66} \ \rho_{GRB} \quad \mathrm{Gpc}^{-3}. \tag{6.43}$$

Therefore, the abundance ratio Z (metallicity) of the heavy elements to the Hydrogen and Helium can be estimated as

$$Z = \frac{N_{metal}}{N_b} = \frac{1.23 \times 10^{66} \ \rho_{GRB}}{7.66 \times 10^{75}} = 1.61 \times 10^{-10} \rho_{GRB}. \tag{6.44}$$

Using the absolute GRB formation rate in figure 6.5, metal pollutions by the Pop-III stars at the early universe are summarized as following:

$$Z = 6.1 \times 10^{-6} Z_\odot \quad \text{for} \quad \rho_{GRB} = 1 \times 10^3 \quad (\kappa = 0.0), \tag{6.45}$$

$$Z = 1.2 \times 10^{-4} Z_\odot \quad \text{for} \quad \rho_{GRB} = 2 \times 10^4 \quad (\kappa = 0.5), \tag{6.46}$$

$$Z = 1.8 \times 10^{-3} Z_\odot \quad \text{for} \quad \rho_{GRB} = 3 \times 10^5 \quad (\kappa = 1.0). \tag{6.47}$$

Here, $Z_\odot = 1.6 \times 10^{-3}$ is the solar abundance, and κ is the parameter to describe the jet opening angle evolution in equation (6.12). At the most preferable case of $\kappa = 0.5$, the metal abundance in the IGM rapidly increase $Z \sim 10^{-4} Z_\odot$. These discussions are reported in Murakami, Yonetoku et al. (2004).

---

[3]Since Pop-III stars are generally thought to be massive object, we should assume $q \leq 1$. Even if the q value is order of unity, we can neglect the contribution from supernova.

Chapter 7

Conclusion

We studied the spectral properties of the prompt GRB emissions with the known redshifts detected by the *BATSE* instruments aboard the *CGRO* satellite. Combining the results with the *BeppoSAX* results by Amati et al. (2002), we showed the strong correlation between the spectral peak energy (E_p) and the peak luminosity. As a further analysis, we also performed time resolved spectral analyses in view of the individual pulses. Based on the E_p–luminosity relation, we estimated the redshifts for the majority of GRBs without known distances, and derived the absolute GRB formation rate from the redshift distribution. This is the first work to estimate the absolute GRB formation rate up to $z = 12$, which is comparable to the early epoch reionization measured by the WMAP satellite (Bennett et al., 2003; Spergel et al., 2003). In this chapter, we summarize the important results of this thesis.

1. On the spectral analyses for the prompt emission of known redshift GRBs, we found the tight correlation between the E_p and the 1 sec peak luminosity (L_γ) as shown in figure 4.4. This relation can be described as the formula:

$$\frac{L_\gamma}{10^{52} \text{ ergs s}^{-1}} = (2.34^{+2.29}_{-1.75}) \times 10^{-5} \left[\frac{E_p(1+z)}{1 \text{ keV}} \right]^{2.0 \mp 0.2}. \tag{7.1}$$

   Here we measured the E_p from the spectra averaged over the entire T_{90} duration of GRBs. We proposed that the E_p–luminosity relation is useful to estimate the redshifts and luminosities of GRBs without known distance.

2. We performed the spectral analyses for a lot of GRBs without known redshifts. Using the above E_p–luminosity relation as the redshift indicator, we estimated their redshifts and luminosities for brighter 689 GRBs.

3. We found the luminosity evolution as $g_k(z) = (1+z)^{2.6^{+0.15}_{-0.20}}$ from the redshift distribution of 689 GRBs with the τ statistical method described in Appendix A. We suggested that there are two possibility to interpret this luminosity evolution. One is the jet opening angle evolution, and another is the progenitor evolution. The former case means the collimation angles of the relativistic jets are narrower than the present ones. Then the energy density in the GRB jets increase, so the luminosity also increase. On the other hand, the latter case means that the GRB progenitor itself (e.g. mass) evolves toward the higher redshifts, and intrinsic luminosity becomes brighter.

4. As shown in figure 6.5, we derived the absolute GRB formation rate from the flux-limited 689 samples with the non-parametric method described in Appendix A. Then we properly correct the geometrical effect of the jet collimation including also the jet opening angle evolution. The GRB formation rate rapidly increase at $z \leq 1$ and keeps rising toward the higher redshift up to $z = 12$. The local GRB event rate is about 10 events $\mathrm{Gpc^{-3}yr^{-1}}$. This rate is equivalent to 10^{-7} events yr per galaxy. At the early universe of $z = 12$, the GRB rate is 10^3 times larger than the present value. This result indicates that the explosive massive star formation (population-III star formation) has happened at the extremely early universe.

5. Assuming the initial mass function of Nakamura & Umemura (2001), we calculate the star formation rate with the observed GRB formation rate. Based on the star formation rate, we investigated two fundamental issues of the early epoch reionization and the metal abundance in the intergalactic medium (IGM). The ultra-violet photons are effectively produced by massive Pop-III stars. The UV photon luminosity is quite strong enough to reionize the primordial gas. From our estimation, the universe was instantaneously reionized with the timescale of 10^7 yr. The Pop-III stars supply heavy elements into the space via the supernova explosion. The metal abundance reaches 10^{-4} $Z_\odot$ within 10^7 yr, which is comparable to the observed abundance measured by the absorption in the quasar spectra.

Appendix A

τ Statistics and Non-Parametric Method

The statistical problem at hand is the determination of the true distribution of luminosities and redshifts of the sources from a biased or truncated data set, such as a flux limited sample. Several different techniques exist that give the data and fit to some parametric forms of the luminosity functions and the density functions. However, it is preferable to use a *non-parametric* methods. In this chapter, we briefly introduce the way how to deal with the flux-limited samples with the non-parametric method.

A.1   Probing Data Independent

A.1.1   Untruncated Data

Suppose an untruncated data samples on (z, L) plane, and the total number of sample N. If L and z are independent of each other, then the number of samples R_i of z_i will be distributed uniformly between 1 and N with an expected mean $E = (N+1)/2$ and variance $V = (N^2-1)/12$. Then, one may normalize R_i to have a mean of 0 and a variance of 1 by defining a test statistic $T_i = (R_i - E)/\sqrt{V}$. One then can judge whether to reject or to accept the hypothesis of independence based on the distribution of the T_i.

Generally, to quantify the data correlation degree, the test statistic τ is introduced as

$$\tau = \frac{\sum_i (R_i - E)}{\sqrt{\sum_i V}}. \tag{A.1}$$

This τ value is normalized by the square root of variance, so the data correlation degree between z and L can be measured in unit of the standard deviation. Additionally, this τ is equivalent to Kendell's τ statistic, which is defined in the following manner. Consider possible pairings $P = (i, j)$ between data points and call a pairing (i, j) positive if $(z_i - zj)(L_i - L_j) > 0$ and negative if $(z_i - zj)(L_i - L_j) < 0$. If there are no truncation on the (z, L) plane, the τ of equation (A.1) is equivalent to Kendell's τ statistic

$$\tau = \frac{\text{number positive}(i, j) \in P \ - \ \text{number negative}(i, j) \in P}{\text{number}(i, j) \in P}. \tag{A.2}$$

A.1.2   Data with One-sided Truncation

It is rare to obtain the untruncated data samples as described above from the real observation. At almost all cases, the data samples are restricted by some kind of the truncation, such as the flux limit caused by the detector sensitivity. Therefore, it is useful to generalize the above method for the truncated samples.

For example, if the data is truncated by the flux limit, the above procedure is modified as follows. When we notice the i-th sample of (z_i, L_i), as shown in figure A.1, we can consider an associated set of

$$\mathbf{J_i} = \{ j \mid L_j > L_i, z_j < z_{i,\mathrm{lim}} \}, \quad \text{for } 1 \le i \le 470, \tag{A.3}$$

and define the number of samples in $\mathbf{J_i}$ as N_i. Here, $z_{i,\mathrm{lim}}$ is a crossing point between two lines of the flux limit and the $L = L_i$. As far as considering the region in $\mathbf{J_i}$, we can equivalently compare each of them, because the number distribution in the associated set is unrelated to the flux limit. Then, if z_i and L_i are independent of each other, we expect the number of sample $\mathbf{R_i}$ of z_i in the eligible set,

$$\mathbf{R_i} = \text{number } \{ j \in \mathbf{J_i} \mid z_j \le z_i \} \tag{A.4}$$

to be uniformly distributed between 1 and N_i. The improved τ statistic value is defined as

$$\tau = \frac{\sum_i (R_i - E_i)}{\sqrt{\sum_i V_i}}, \tag{A.5}$$

where $E_i = (N_i + 1)/2$ and $V_i = (N_i^2 - 1)/12$. The summation is performed for all points. If R_i is completely due to the uniform distribution, we again expect the τ value to be zero.

We used the above τ statistics to estimate the luminosity evolution. If the data correlation is found, assuming the arbitrary functional form $g_k(z)$ parametrized by k, we can convert the data set (z, L) into $(z, L/g_k(z)) \equiv (z, L')$. For such data set (z, L'), we estimate the τ values with the method described above. Giving the requirement of $\tau = 0$, the best parameter $k = k_0$ can be determined. Then, the functional form of the luminosity evolution $g_{k_0(z)}$ and the independent data set $(z, L/g_{k_0}(z))$ can be obtained.

A.1.3   Multiply Truncated Data

A generalization of the above method to doubly (or multiply) truncated data was developed by Efron & Petrosian (1992). The method is equivalent to the previous method, with the eligible set defined as

$$\mathbf{J_i} = \{ j \mid L_j > L_i, z_j \in (z_{i,\mathrm{lim}}^-, z_{i,\mathrm{lim}}^+) \}, \tag{A.6}$$

where $z_{i,\mathrm{lim}}^-$ and $z_{i,\mathrm{lim}}^+$ is the point determined at the crossing between the $L = L_i$ and each truncation limit, respectively. Then, the set of allowed pairings

$$P = \{ (i,j) \mid z_i \in (z_{j,\mathrm{lim}}^-, z_{j,\mathrm{lim}}^+), z_j \in (z_{i,\mathrm{lim}}^-, z_{i,\mathrm{lim}}^+) \} \tag{A.7}$$
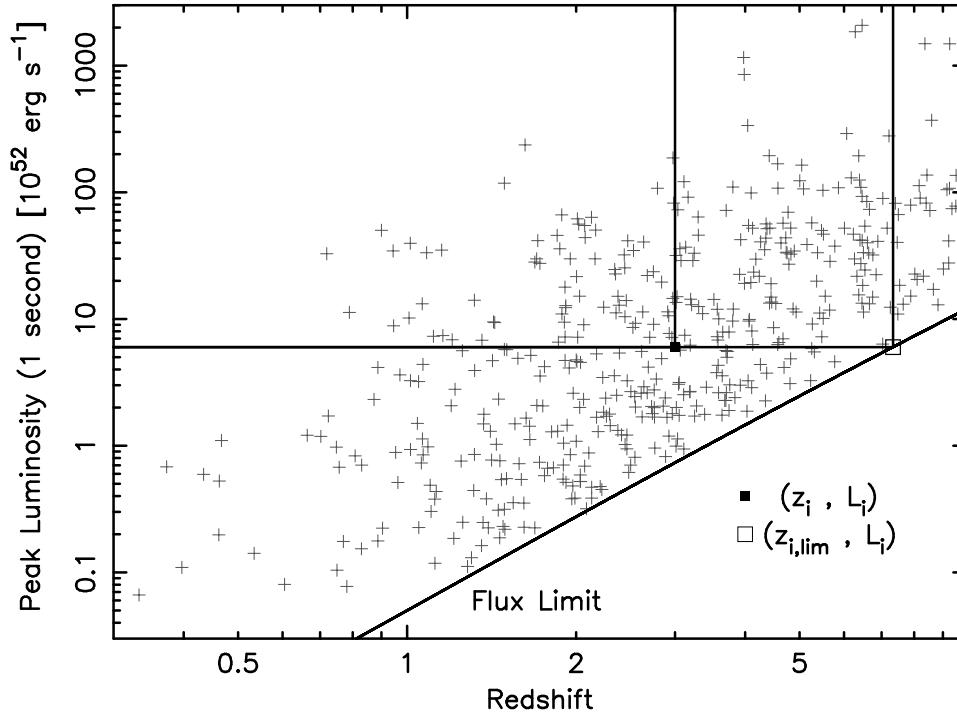
Figure A.1: An example of the associated set. When we notice the i-th sample of (z_i, L_i), the associated set can be determined as the region of both $L > L_i$ and $z < z_{i,\text{lim}}$. The data in this set is free from the flux limit, so they can be equivalently compare to each other.

can be defined such that each object lies within the truncation region of the other.

In this case, however, the distribution of the number of samples (or τ) is unknown. If the data are uncorrelated, then τ must still have a mean of zero, and a numerical simulation may be used to determine the variance V_τ as follows. By assuming the data $\{z_i, L_i\}$ are uncorrelated, one can use the methods of the next section to determine $\Psi(L)$, the underlying probability distribution of L. Once $\Psi(L)$ is found, one can simulate N_{sim} sets of data with underlying probability density $\Psi(L)$ and truncation limits $[z_{i,\text{lim}}^-, z_{i,\text{lim}}^+]$ for the i-th object in each set. For each simulated set of data D_k, one may find τ_k as in equation (A.2) and estimate V_τ from the distribution of $\{\tau_k\}_{k=1}^{N_{\text{sim}}}$. For large numbers of simulations N_{sim}, the error in this determination of V_τ is approximately $V_\tau/\sqrt{N_{\text{sim}}}$. Given V_τ, one can define a normalized test statistic τ/V_τ with a mean of 0 and a variance of 1.

A.2   Estimate The Distribution Function

We deal with the flux-limited samples, and estimate the sample distribution from these truncated data. Moreover, although they are discrete data, we derive the parent distribution which are generally continuous function. Here, we introduce a useful method which minimizes numerical fluctuations when deriving the luminosity functions and the density evolutions (e.g. GRB formation rate). This method is first developed by Lynden-Bell (1971), and it was frequently used to astrophysical objects such as QSOs (e.g. Caditz & Petrosian, 1990; Efron & Petrosian, 1992; Maloney & Petrosian, 1999), GRBs (e.g. Lloyd-Ronning et al., 2001, 2002a) and so on.
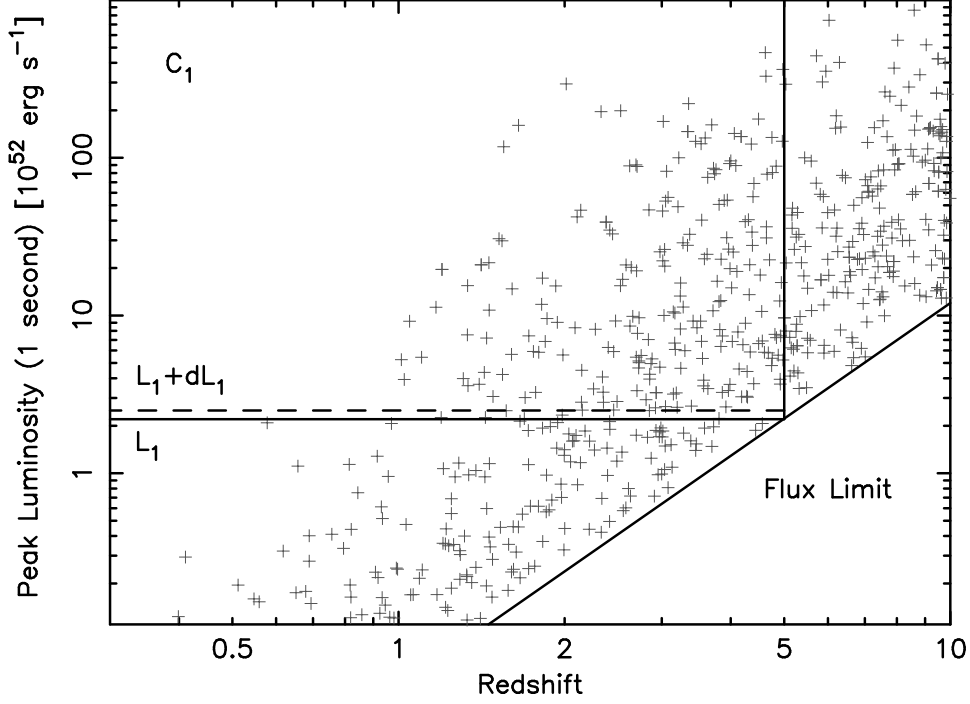
Figure A.2: An example of the sample distribution truncated by the flux limit.

We wish to know the distribution function $\phi(L)$ of an observable L in a population. As shown in figure A.2, we have a number of individual samples of the population each taken above a flux limit (F_{limit}), so we can consider only the range of $L \geq 4\pi d_L^2 F_{\text{limit}}$. The true distribution in L is of course independent of our observational selection represented here by F_{limit}. Let $\psi(L_1)$ be the parent distribution of sources with $L \geq L_1$ in the cumulative form, so that $\phi(L) \equiv -d\psi(L)/dL$ is the desired true distribution function. Let $X(L_1)$ be the observed number of points with $L \geq L_1$; then $-dX$ is the number of points in the infinitesimal column between L_1 and $L_1 + dL_1$. The ratio of this number to the number of points C_{L_1} in the rectangular area C_1 of figure A.2, is equivalent to the ratio of the increment $(-d\psi)$ to the cumulative distribution function, to $\psi(L_1)$ itself. This is equivalent to compare the parent (continuous) distribution with the sample (discrete) distribution, and this can be described as

$$\frac{dX}{C} = \frac{d\psi}{\psi}. \qquad (A.8)$$

Integrating this, we obtain

$$\psi(L_1) = A \exp \int \frac{dX}{C} = A \exp \int_{L_0}^{L_1} \frac{1}{C(L)} \frac{dX}{dL} dL \qquad (A.9)$$

Here, A is the constant of integration.

When one chooses L_0 to be a value of L well within the observed range of points, A determines the normalization of ψ. However, in the case where parts of the distribution have not been observed, it is best to use a non-normalized distribution and a convenient one is got by choosing an L_0 and then using $A = 1$.

In practice our observations give us discrete points so X will jump at discrete values L_i at which GRBs are actually observed. Thus $-dX/dL$ will be a sum of Dirac delta functions

$$-\frac{dX}{dL} = \sum_i \delta(L - L_i). \tag{A.10}$$

However, when the equation (A.10) is substituted into equation (A.9) we find that $C(L_i)$ has to be evaluated. That is the number of points in the box C_1 has to be evaluated again and again when one point (with $L = L_i$) is on the side of the box. When the number of points in C_1 is not large, error could be generated in the choice of whether to include, exclude, or half include the point on the edge. To discover the correct weight to give such an edge point we discuss the transition from the continuous to the discrete distribution by assuming that $-dX/dL$ becomes large in the neighborhood of each of the points L_i with unit integral across each neighborhood. To evaluate equation (A.9), we wish to know the behavior of $C(L)$ when L is close to L_i. Clearly $C(L)$ will include only the fraction

$$x = X(L) - X(L_i^+) \tag{A.11}$$

of the point at L_i where L_i^+ is taken just to the right of where the i-th point contributes to X. If the define $C^-(L_i)$ to be the value of C at L_i with the contribution of the point i itself omitted, then in the neighborhood of $L = L_i$ we have

$$C(L) = C^-(L_i) + x. \tag{A.12}$$

In equation (A.9), we require the contribution from the neighborhood of $L = L_i$ to the integral

$$\int_{L_i^-}^{L_i^+} \frac{1}{C} \frac{dX}{dL} dL = \int_0^1 \frac{dx}{C^- + x} = \ln\left(1 + \frac{1}{C^-}\right) \tag{A.13}$$

where, we remember that the number of points contributing to X increases by 1 as we cross L_i. The equation (A.13) may be substituted into equation (A.9) to yield the expression

$$\ln \psi(L_i) = A \sum_i \ln\left(1 + \frac{1}{C^-(L_i)}\right). \tag{A.14}$$

Here, $\sum$ is executed over all i with $L_0 < L_i < L$ whenever $L_0 < L$. The differential form $\phi(L)$ is easily calculated to differentiate the derived $\psi(L)$. Based on the above theoretical descriptions, we applied this non-parametric method to the GRB data for estimating the luminosity evolution, the luminosity function and the GRB formation rate.

Appendix B

Estimated Redshifts and Luminosities of 689 GRBs

Table B.1: Redshifts and luminosities estimated by E_p–L relation

Trigger Number	E_p keV	redshift	luminosity erg s^{-1}
105	$141.4^{+7.8}_{-7.5}$	$1.26^{+0.11}_{-0.10}$	$(2.39^{+0.52}_{-0.43}) \times 10^{52}$
109	$385.4^{+20.7}_{-18.8}$	$1.98^{+0.20}_{-0.17}$	$(3.10^{+0.82}_{-0.60}) \times 10^{53}$
111	$97.2^{+21.7}_{-20.6}$	$11.23^{+33.87}_{-6.51}$	$(3.32^{+67.19}_{-2.87}) \times 10^{53}$
130	$182.2^{+7.4}_{-7.1}$	$5.17^{+0.68}_{-0.57}$	$(2.97^{+0.99}_{-0.71}) \times 10^{53}$
133	$73.9^{+25.4}_{-28.3}$	$4.53^{+9.47}_{-2.89}$	$(3.92^{+48.15}_{-3.58}) \times 10^{52}$
143	$620.8^{+10.8}_{-10.5}$	$1.36^{+0.04}_{-0.03}$	$(5.04^{+0.33}_{-0.31}) \times 10^{53}$
160	$207.9^{+16.5}_{-15.2}$	$4.39^{+1.10}_{-0.78}$	$(2.94^{+2.03}_{-1.10}) \times 10^{53}$
179	$198.2^{+29.4}_{-27.6}$	$8.46^{+8.12}_{-3.41}$	$(8.24^{+29.32}_{-5.74}) \times 10^{53}$
219	$20.9^{+9.2}_{-9.6}$	$0.11^{+0.05}_{-0.05}$	$(1.27^{+1.58}_{-0.94}) \times 10^{50}$
222	$280.7^{+41.1}_{-45.3}$	$9.70^{+10.46}_{-4.55}$	$(2.12^{+8.76}_{-1.62}) \times 10^{54}$
228	$42.1^{+14.9}_{-21.9}$	$1.09^{+0.65}_{-0.65}$	$(1.82^{+3.90}_{-1.62}) \times 10^{51}$
249	$261.1^{+10.5}_{-10.0}$	$1.05^{+0.06}_{-0.06}$	$(6.75^{+0.99}_{-0.83}) \times 10^{52}$
332	$84.0^{+17.3}_{-14.8}$	$3.88^{+2.90}_{-1.38}$	$(3.95^{+10.65}_{-2.56}) \times 10^{52}$
351	$59.4^{+40.5}_{-26.1}$	$1.07^{+1.47}_{-0.56}$	$(3.56^{+25.82}_{-2.96}) \times 10^{51}$
394	$323.6^{+9.0}_{-8.8}$	$7.30^{+0.80}_{-0.68}$	$(1.69^{+0.46}_{-0.34}) \times 10^{54}$
398	$122.9^{+39.7}_{-34.6}$	$5.11^{+11.11}_{-2.79}$	$(1.32^{+17.09}_{-1.12}) \times 10^{53}$
408	$75.1^{+14.0}_{-13.2}$	$2.34^{+1.03}_{-0.68}$	$(1.47^{+2.08}_{-0.84}) \times 10^{52}$
451	$134.4^{+8.3}_{-7.8}$	$0.76^{+0.06}_{-0.05}$	$(1.32^{+0.27}_{-0.22}) \times 10^{52}$
467	$311.3^{+25.6}_{-22.9}$	$7.22^{+2.69}_{-1.65}$	$(1.54^{+1.63}_{-0.69}) \times 10^{54}$
469	$227.8^{+166.6}_{-84.9}$	$3.16^{+25.84}_{-1.81}$	$(2.11^{+326.44}_{-1.84}) \times 10^{53}$
493	$144.2^{+25.4}_{-33.0}$	$11.94^{+22.92}_{-7.34}$	$(8.16^{+78.59}_{-7.25}) \times 10^{53}$
501	$72.5^{+10.2}_{-6.7}$	$2.40^{+0.77}_{-0.40}$	$(1.43^{+1.37}_{-0.51}) \times 10^{52}$
503	$494.7^{+65.1}_{-52.3}$	$6.10^{+3.65}_{-1.74}$	$(2.90^{+5.60}_{-1.58}) \times 10^{54}$
543	$253.0^{+8.7}_{-8.3}$	$2.54^{+0.18}_{-0.16}$	$(1.88^{+0.35}_{-0.28}) \times 10^{53}$
548	$158.3^{+13.4}_{-12.5}$	$10.10^{+5.08}_{-2.86}$	$(7.24^{+10.87}_{-3.86}) \times 10^{53}$
577	$117.0^{+36.2}_{-27.2}$	$5.58^{+12.48}_{-2.76}$	$(1.39^{+18.63}_{-1.11}) \times 10^{53}$
647	$200.6^{+6.0}_{-5.9}$	$3.11^{+0.22}_{-0.20}$	$(1.59^{+0.28}_{-0.23}) \times 10^{53}$
658	$88.1^{+25.4}_{-31.2}$	$3.91^{+4.96}_{-2.29}$	$(4.39^{+25.05}_{-3.87}) \times 10^{52}$
659	$62.2^{+1.6}_{-15.6}$	$2.82^{+0.16}_{-1.18}$	$(1.33^{+0.19}_{-0.97}) \times 10^{52}$

Table B.1: Redshifts and luminosities estimated by E_p–L relation

Trigger Number	E_p keV	redshift	luminosity erg s^{-1}
660	$282.8^{+27.2}_{-24.1}$	$9.23^{+5.11}_{-2.66}$	$(1.96^{+3.34}_{-1.06}) \times 10^{54}$
676	$321.1^{+10.1}_{-9.9}$	$9.69^{+1.47}_{-1.19}$	$(2.76^{+1.04}_{-0.71}) \times 10^{54}$
680	$82.1^{+30.0}_{-26.0}$	$4.33^{+9.59}_{-2.43}$	$(4.49^{+61.16}_{-3.87}) \times 10^{52}$
692	$107.1^{+25.0}_{-21.9}$	$9.65^{+25.63}_{-5.23}$	$(3.05^{+50.85}_{-2.55}) \times 10^{53}$
704	$132.7^{+30.5}_{-13.6}$	$3.69^{+3.10}_{-0.82}$	$(9.09^{+28.80}_{-4.10}) \times 10^{52}$
764	$100.6^{+11.4}_{-29.6}$	$5.93^{+2.85}_{-3.46}$	$(1.14^{+1.68}_{-1.00}) \times 10^{53}$
773	$70.9^{+21.4}_{-9.9}$	$2.25^{+1.79}_{-0.53}$	$(1.24^{+3.82}_{-0.60}) \times 10^{52}$
795	$109.3^{+32.6}_{-31.7}$	$6.95^{+20.01}_{-4.20}$	$(1.77^{+35.18}_{-1.57}) \times 10^{53}$
825	$71.1^{+36.9}_{-27.8}$	$3.21^{+9.82}_{-1.91}$	$(2.10^{+51.85}_{-1.87}) \times 10^{52}$
829	$127.7^{+0.8}_{-1.2}$	$1.85^{+0.02}_{-0.03}$	$(3.11^{+0.08}_{-0.13}) \times 10^{52}$
841	$102.2^{+12.8}_{-11.1}$	$1.30^{+0.26}_{-0.20}$	$(1.30^{+0.75}_{-0.44}) \times 10^{52}$
869	$235.2^{+28.7}_{-25.8}$	$8.03^{+5.50}_{-2.66}$	$(1.06^{+2.39}_{-0.64}) \times 10^{54}$
907	$211.9^{+7.4}_{-7.1}$	$4.98^{+0.55}_{-0.47}$	$(3.77^{+1.05}_{-0.78}) \times 10^{53}$
914	$88.8^{+17.3}_{-16.3}$	$1.70^{+0.64}_{-0.46}$	$(1.35^{+1.60}_{-0.73}) \times 10^{52}$
973	$289.4^{+11.9}_{-11.4}$	$4.72^{+0.60}_{-0.50}$	$(6.44^{+2.08}_{-1.48}) \times 10^{53}$
999	$262.8^{+17.8}_{-16.1}$	$1.72^{+0.21}_{-0.17}$	$(1.20^{+0.38}_{-0.27}) \times 10^{53}$
1025	$153.2^{+7.5}_{-7.1}$	$1.18^{+0.09}_{-0.08}$	$(2.62^{+0.50}_{-0.40}) \times 10^{52}$
1036	$99.7^{+33.2}_{-28.7}$	$3.14^{+3.97}_{-1.51}$	$(4.00^{+23.27}_{-3.18}) \times 10^{52}$
1039	$93.9^{+3.8}_{-3.5}$	$5.51^{+0.76}_{-0.60}$	$(8.78^{+3.08}_{-2.09}) \times 10^{52}$
1042	$47.9^{+7.4}_{-6.4}$	$1.30^{+0.33}_{-0.24}$	$(2.85^{+2.11}_{-1.14}) \times 10^{51}$
1085	$227.2^{+1.9}_{-1.8}$	$0.93^{+0.01}_{-0.01}$	$(4.50^{+0.12}_{-0.12}) \times 10^{52}$
1114	$106.2^{+8.1}_{-7.6}$	$4.29^{+1.00}_{-0.75}$	$(7.39^{+4.72}_{-2.69}) \times 10^{52}$
1122	$170.7^{+4.7}_{-4.5}$	$1.54^{+0.07}_{-0.07}$	$(4.42^{+0.50}_{-0.44}) \times 10^{52}$
1141	$417.6^{+9.9}_{-9.6}$	$6.25^{+0.52}_{-0.46}$	$(2.15^{+0.44}_{-0.35}) \times 10^{54}$
1145	$77.7^{+28.6}_{-48.2}$	$2.56^{+3.07}_{-1.96}$	$(1.80^{+9.87}_{-1.75}) \times 10^{52}$
1148	$191.6^{+33.7}_{-39.1}$	$9.77^{+14.63}_{-5.31}$	$(9.98^{+66.86}_{-8.36}) \times 10^{53}$
1150	$66.5^{+3.6}_{-3.0}$	$1.54^{+0.14}_{-0.11}$	$(6.71^{+1.57}_{-1.10}) \times 10^{51}$
1156	$87.6^{+33.0}_{-29.5}$	$6.93^{+38.83}_{-4.55}$	$(1.13^{+73.50}_{-1.04}) \times 10^{53}$
1157	$236.8^{+9.5}_{-9.1}$	$1.82^{+0.13}_{-0.12}$	$(1.05^{+0.19}_{-0.16}) \times 10^{53}$
1159	$254.4^{+23.1}_{-20.1}$	$9.96^{+5.45}_{-2.80}$	$(1.82^{+3.04}_{-0.97}) \times 10^{54}$
1190	$121.9^{+12.5}_{-11.7}$	$2.67^{+0.64}_{-0.48}$	$(4.70^{+3.18}_{-1.80}) \times 10^{52}$
1197	$92.3^{+32.6}_{-39.8}$	$3.70^{+6.25}_{-2.42}$	$(4.43^{+39.50}_{-4.09}) \times 10^{52}$
1200	$90.1^{+18.3}_{-11.6}$	$3.98^{+3.01}_{-1.11}$	$(4.72^{+12.91}_{-2.56}) \times 10^{52}$
1218	$116.1^{+5.0}_{-5.0}$	$11.11^{+2.64}_{-1.98}$	$(4.64^{+2.85}_{-1.67}) \times 10^{53}$
1235	$122.1^{+11.5}_{-9.9}$	$2.25^{+0.44}_{-0.32}$	$(3.70^{+2.02}_{-1.17}) \times 10^{52}$
1244	$30.7^{+39.0}_{-23.9}$	$0.85^{+2.47}_{-0.69}$	$(7.55^{+204.68}_{-7.40}) \times 10^{50}$
1288	$354.7^{+24.3}_{-22.8}$	$9.29^{+3.34}_{-2.13}$	$(3.13^{+3.14}_{-1.41}) \times 10^{54}$
1303	$195.5^{+31.6}_{-52.9}$	$11.00^{+16.12}_{-7.21}$	$(1.29^{+8.27}_{-1.18}) \times 10^{54}$
1384	$103.5^{+15.1}_{-20.7}$	$8.14^{+7.34}_{-4.13}$	$(2.10^{+6.87}_{-1.70}) \times 10^{53}$
1396	$105.9^{+23.5}_{-24.3}$	$4.05^{+3.53}_{-1.78}$	$(6.70^{+22.19}_{-5.04}) \times 10^{52}$
1406	$106.9^{+10.8}_{-13.4}$	$1.91^{+0.37}_{-0.39}$	$(2.28^{+1.23}_{-0.97}) \times 10^{52}$
1416	$104.3^{+32.4}_{-28.7}$	$2.96^{+3.15}_{-1.34}$	$(4.00^{+18.13}_{-3.08}) \times 10^{52}$
1419	$145.6^{+32.5}_{-27.3}$	$2.31^{+1.27}_{-0.71}$	$(5.46^{+10.19}_{-3.24}) \times 10^{52}$

Table B.1: Redshifts and luminosities estimated by E_p–L relation

Trigger Number	E_p keV	redshift	luminosity erg s^{-1}
1425	$185.9^{+9.3}_{-8.9}$	$2.19^{+0.21}_{-0.19}$	$(8.23^{+2.11}_{-1.63}) \times 10^{52}$
1432	$62.3^{+22.5}_{-16.0}$	$2.91^{+3.88}_{-1.25}$	$(1.39^{+8.85}_{-1.04}) \times 10^{52}$
1440	$271.2^{+6.7}_{-6.5}$	$2.52^{+0.13}_{-0.12}$	$(2.14^{+0.28}_{-0.24}) \times 10^{53}$
1443	$163.3^{+29.0}_{-25.1}$	$3.47^{+1.95}_{-1.06}$	$(1.25^{+2.32}_{-0.73}) \times 10^{53}$
1467	$140.8^{+47.6}_{-30.3}$	$2.33^{+2.25}_{-0.81}$	$(5.15^{+20.77}_{-3.34}) \times 10^{52}$
1472	$142.7^{+21.7}_{-19.5}$	$9.64^{+10.99}_{-4.04}$	$(5.41^{+24.24}_{-3.86}) \times 10^{53}$
1533	$149.9^{+25.3}_{-23.2}$	$3.28^{+1.65}_{-0.98}$	$(9.68^{+15.70}_{-5.57}) \times 10^{52}$
1540	$112.7^{+16.8}_{-20.5}$	$7.54^{+6.53}_{-3.51}$	$(2.17^{+6.76}_{-1.67}) \times 10^{53}$
1541	$39.8^{+48.8}_{-15.5}$	$0.18^{+0.26}_{-0.07}$	$(5.17^{+33.14}_{-3.47}) \times 10^{50}$
1574	$98.5^{+20.7}_{-7.2}$	$6.92^{+9.62}_{-1.54}$	$(1.43^{+8.83}_{-0.63}) \times 10^{53}$
1578	$179.8^{+9.4}_{-8.9}$	$3.75^{+0.54}_{-0.43}$	$(1.71^{+0.64}_{-0.43}) \times 10^{53}$
1579	$314.0^{+169.9}_{-88.5}$	$2.11^{+3.90}_{-0.89}$	$(2.24^{+24.82}_{-1.65}) \times 10^{53}$
1614	$144.8^{+31.7}_{-35.7}$	$7.56^{+12.58}_{-4.26}$	$(3.60^{+29.05}_{-3.09}) \times 10^{53}$
1625	$580.6^{+8.4}_{-8.2}$	$2.20^{+0.06}_{-0.06}$	$(8.10^{+0.56}_{-0.51}) \times 10^{53}$
1626	$157.7^{+36.7}_{-29.8}$	$7.45^{+13.67}_{-3.54}$	$(4.16^{+39.19}_{-3.24}) \times 10^{53}$
1628	$133.1^{+44.2}_{-50.0}$	$5.33^{+13.01}_{-3.49}$	$(1.67^{+25.92}_{-1.54}) \times 10^{53}$
1651	$56.3^{+17.7}_{-24.8}$	$0.54^{+0.21}_{-0.26}$	$(1.75^{+2.17}_{-1.37}) \times 10^{51}$
1652	$184.8^{+7.6}_{-7.3}$	$2.95^{+0.28}_{-0.24}$	$(1.25^{+0.30}_{-0.23}) \times 10^{53}$
1660	$90.4^{+33.4}_{-18.9}$	$2.00^{+1.91}_{-0.64}$	$(1.72^{+6.92}_{-1.06}) \times 10^{52}$
1663	$448.7^{+8.9}_{-8.3}$	$2.78^{+0.12}_{-0.11}$	$(6.74^{+0.72}_{-0.61}) \times 10^{53}$
1683	$353.2^{+17.1}_{-16.2}$	$11.69^{+3.26}_{-2.26}$	$(4.71^{+3.47}_{-1.81}) \times 10^{54}$
1709	$204.6^{+5.6}_{-5.5}$	$2.00^{+0.10}_{-0.10}$	$(8.83^{+1.13}_{-0.99}) \times 10^{52}$
1712	$212.3^{+23.1}_{-21.5}$	$10.31^{+7.46}_{-3.57}$	$(1.35^{+3.23}_{-0.84}) \times 10^{54}$
1717	$166.4^{+15.7}_{-14.0}$	$4.48^{+1.39}_{-0.91}$	$(1.95^{+1.72}_{-0.81}) \times 10^{53}$
1734	$90.0^{+22.2}_{-20.3}$	$3.81^{+3.66}_{-1.63}$	$(4.40^{+16.84}_{-3.24}) \times 10^{52}$
1807	$149.6^{+14.9}_{-21.5}$	$4.11^{+1.28}_{-1.27}$	$(1.37^{+1.22}_{-0.81}) \times 10^{53}$
1815	$201.1^{+24.8}_{-20.8}$	$3.21^{+1.08}_{-0.68}$	$(1.68^{+1.67}_{-0.73}) \times 10^{53}$
1883	$211.6^{+10.6}_{-10.2}$	$3.25^{+0.40}_{-0.34}$	$(1.90^{+0.61}_{-0.44}) \times 10^{53}$
1885	$103.8^{+30.8}_{-41.8}$	$8.17^{+30.64}_{-6.05}$	$(2.13^{+65.28}_{-2.04}) \times 10^{53}$
1886	$488.8^{+6.5}_{-6.4}$	$2.10^{+0.05}_{-0.05}$	$(5.38^{+0.33}_{-0.31}) \times 10^{53}$
1922	$170.0^{+27.6}_{-25.4}$	$10.21^{+13.88}_{-4.63}$	$(8.52^{+49.17}_{-6.40}) \times 10^{53}$
1924	$80.0^{+22.8}_{-41.2}$	$2.29^{+1.71}_{-1.52}$	$(1.62^{+4.58}_{-1.51}) \times 10^{52}$
1956	$143.8^{+18.5}_{-16.5}$	$4.47^{+2.02}_{-1.19}$	$(1.45^{+2.02}_{-0.76}) \times 10^{53}$
1967	$119.5^{+7.8}_{-7.0}$	$5.28^{+1.20}_{-0.85}$	$(1.32^{+0.80}_{-0.45}) \times 10^{53}$
1974	$53.8^{+3.3}_{-2.5}$	$0.67^{+0.05}_{-0.04}$	$(1.90^{+0.38}_{-0.26}) \times 10^{51}$
1989	$97.4^{+24.0}_{-11.6}$	$1.98^{+1.10}_{-0.38}$	$(1.97^{+3.76}_{-0.81}) \times 10^{52}$
1993	$57.1^{+2.8}_{-12.4}$	$1.62^{+0.14}_{-0.50}$	$(5.25^{+1.14}_{-3.15}) \times 10^{51}$
1997	$31.0^{+14.5}_{-11.4}$	$0.28^{+0.14}_{-0.11}$	$(3.65^{+6.11}_{-2.42}) \times 10^{50}$
2018	$53.4^{+3.6}_{-2.7}$	$1.79^{+0.22}_{-0.15}$	$(5.22^{+1.67}_{-1.01}) \times 10^{51}$
2037	$103.9^{+35.1}_{-22.2}$	$0.57^{+0.24}_{-0.14}$	$(6.20^{+8.67}_{-3.00}) \times 10^{51}$
2047	$70.0^{+18.6}_{-24.5}$	$1.63^{+0.87}_{-0.76}$	$(7.94^{+14.55}_{-6.25}) \times 10^{51}$
2053	$186.6^{+17.4}_{-21.6}$	$7.93^{+3.74}_{-2.72}$	$(6.51^{+9.17}_{-4.05}) \times 10^{53}$
2061	$223.8^{+58.8}_{-56.1}$	$4.53^{+5.75}_{-2.21}$	$(3.60^{+20.28}_{-2.87}) \times 10^{53}$

Table B.1: Redshifts and luminosities estimated by E_p–L relation

Trigger Number	E_p keV	redshift	luminosity erg s^{-1}
2067	$271.2^{+2.3}_{-2.3}$	$1.77^{+0.03}_{-0.03}$	$(1.32^{+0.05}_{-0.05}) \times 10^{53}$
2074	$139.8^{+57.3}_{-41.1}$	$5.30^{+21.63}_{-3.00}$	$(1.82^{+69.21}_{-1.57}) \times 10^{53}$
2080	$345.8^{+30.0}_{-27.6}$	$11.55^{+6.69}_{-3.49}$	$(4.42^{+7.84}_{-2.47}) \times 10^{54}$
2083	$332.5^{+4.9}_{-4.8}$	$1.06^{+0.02}_{-0.02}$	$(1.10^{+0.06}_{-0.05}) \times 10^{53}$
2090	$230.1^{+8.6}_{-8.3}$	$2.46^{+0.19}_{-0.17}$	$(1.48^{+0.29}_{-0.24}) \times 10^{53}$
2102	$134.2^{+27.4}_{-20.5}$	$4.84^{+4.40}_{-1.68}$	$(1.44^{+4.98}_{-0.92}) \times 10^{53}$
2106	$174.8^{+28.2}_{-19.6}$	$8.01^{+8.35}_{-2.69}$	$(5.83^{+23.34}_{-3.56}) \times 10^{53}$
2111	$105.5^{+5.1}_{-16.2}$	$7.90^{+1.68}_{-3.32}$	$(2.07^{+1.14}_{-1.49}) \times 10^{53}$
2119	$136.9^{+7.6}_{-9.0}$	$8.36^{+2.18}_{-1.87}$	$(3.85^{+2.67}_{-1.70}) \times 10^{53}$
2122	$101.9^{+39.0}_{-26.8}$	$1.30^{+0.94}_{-0.45}$	$(1.29^{+3.62}_{-0.84}) \times 10^{52}$
2123	$104.3^{+15.7}_{-14.8}$	$3.48^{+1.59}_{-1.00}$	$(5.12^{+7.32}_{-2.84}) \times 10^{52}$
2138	$238.4^{+19.9}_{-12.0}$	$2.46^{+0.45}_{-0.24}$	$(1.60^{+0.80}_{-0.35}) \times 10^{53}$
2148	$90.0^{+54.4}_{-56.9}$	$2.27^{+5.65}_{-1.72}$	$(2.03^{+36.89}_{-1.97}) \times 10^{52}$
2151	$146.8^{+3.6}_{-3.5}$	$0.30^{+0.01}_{-0.01}$	$(8.60^{+0.53}_{-0.51}) \times 10^{51}$
2156	$381.2^{+9.8}_{-9.4}$	$2.40^{+0.12}_{-0.11}$	$(3.94^{+0.51}_{-0.44}) \times 10^{53}$
2188	$97.7^{+14.5}_{-22.2}$	$10.20^{+11.82}_{-5.97}$	$(2.81^{+12.83}_{-2.44}) \times 10^{53}$
2197	$50.5^{+35.3}_{-30.5}$	$1.72^{+3.96}_{-1.23}$	$(4.43^{+72.63}_{-4.22}) \times 10^{51}$
2211	$103.0^{+2.3}_{-14.4}$	$2.78^{+0.14}_{-0.72}$	$(3.55^{+0.44}_{-1.83}) \times 10^{52}$
2213	$300.5^{+27.3}_{-25.5}$	$9.97^{+5.45}_{-2.96}$	$(2.55^{+4.24}_{-1.41}) \times 10^{54}$
2228	$192.7^{+14.7}_{-13.3}$	$2.18^{+0.34}_{-0.27}$	$(8.83^{+3.69}_{-2.41}) \times 10^{52}$
2232	$228.3^{+35.4}_{-32.6}$	$3.87^{+1.99}_{-1.16}$	$(2.90^{+4.77}_{-1.67}) \times 10^{53}$
2253	$117.2^{+13.1}_{-22.2}$	$7.86^{+4.69}_{-3.81}$	$(2.53^{+4.78}_{-1.99}) \times 10^{53}$
2254	$147.6^{+23.4}_{-34.5}$	$3.41^{+1.64}_{-1.44}$	$(9.96^{+15.18}_{-7.31}) \times 10^{52}$
2267	$83.6^{+42.5}_{-43.9}$	$3.03^{+8.03}_{-2.14}$	$(2.66^{+51.53}_{-2.53}) \times 10^{52}$
2276	$32.3^{+15.4}_{-14.7}$	$0.88^{+0.66}_{-0.45}$	$(8.60^{+25.57}_{-7.13}) \times 10^{50}$
2277	$157.4^{+10.0}_{-30.4}$	$9.83^{+3.37}_{-5.19}$	$(6.81^{+6.45}_{-5.61}) \times 10^{53}$
2287	$139.9^{+35.8}_{-31.9}$	$3.81^{+3.86}_{-1.63}$	$(1.06^{+4.38}_{-0.79}) \times 10^{53}$
2309	$207.4^{+28.1}_{-37.0}$	$8.70^{+7.47}_{-4.19}$	$(9.49^{+28.89}_{-7.43}) \times 10^{53}$
2315	$165.4^{+9.9}_{-9.4}$	$10.48^{+3.48}_{-2.30}$	$(8.46^{+7.67}_{-3.64}) \times 10^{53}$
2316	$138.6^{+1.5}_{-1.3}$	$2.05^{+0.04}_{-0.03}$	$(4.19^{+0.21}_{-0.17}) \times 10^{52}$
2321	$208.0^{+7.8}_{-7.5}$	$2.64^{+0.21}_{-0.19}$	$(1.35^{+0.28}_{-0.22}) \times 10^{53}$
2328	$125.4^{+21.6}_{-17.9}$	$5.60^{+4.54}_{-1.96}$	$(1.61^{+4.68}_{-1.02}) \times 10^{53}$
2329	$896.8^{+12.2}_{-11.9}$	$2.64^{+0.07}_{-0.07}$	$(2.49^{+0.17}_{-0.16}) \times 10^{54}$
2340	$109.7^{+5.9}_{-6.3}$	$3.88^{+0.58}_{-0.52}$	$(6.73^{+2.64}_{-1.96}) \times 10^{52}$
2345	$129.4^{+25.4}_{-20.5}$	$4.17^{+3.12}_{-1.40}$	$(1.05^{+2.81}_{-0.65}) \times 10^{53}$
2346	$116.7^{+24.7}_{-22.1}$	$2.46^{+1.32}_{-0.78}$	$(3.83^{+6.89}_{-2.32}) \times 10^{52}$
2362	$65.0^{+5.0}_{-5.7}$	$1.03^{+0.11}_{-0.12}$	$(4.09^{+1.20}_{-1.07}) \times 10^{51}$
2367	$134.2^{+10.2}_{-16.6}$	$3.83^{+0.84}_{-1.02}$	$(9.88^{+5.88}_{-5.15}) \times 10^{52}$
2380	$89.5^{+40.3}_{-42.9}$	$4.02^{+12.71}_{-2.84}$	$(4.73^{+119.38}_{-4.49}) \times 10^{52}$
2387	$181.7^{+8.4}_{-8.0}$	$3.76^{+0.47}_{-0.39}$	$(1.76^{+0.56}_{-0.40}) \times 10^{53}$
2393	$53.2^{+2.0}_{-2.1}$	$0.75^{+0.04}_{-0.04}$	$(2.02^{+0.25}_{-0.23}) \times 10^{51}$
2394	$161.9^{+31.2}_{-33.0}$	$8.19^{+11.83}_{-4.22}$	$(5.20^{+33.52}_{-4.23}) \times 10^{53}$
2423	$67.6^{+26.2}_{-33.5}$	$2.74^{+3.83}_{-1.84}$	$(1.50^{+10.34}_{-1.40}) \times 10^{52}$

Table B.1: Redshifts and luminosities estimated by E_p–L relation

Trigger Number	E_p keV	redshift	luminosity erg s^{-1}
2429	$127.3^{+52.4}_{-61.1}$	$5.57^{+25.58}_{-4.17}$	$(1.64^{+76.72}_{-1.58}) \times 10^{53}$
2430	$53.5^{+27.1}_{-28.9}$	$1.29^{+1.34}_{-0.81}$	$(3.51^{+16.56}_{-3.20}) \times 10^{51}$
2431	$96.2^{+15.3}_{-14.0}$	$0.47^{+0.09}_{-0.08}$	$(4.68^{+2.41}_{-1.61}) \times 10^{51}$
2432	$61.1^{+33.6}_{-21.8}$	$1.48^{+1.93}_{-0.69}$	$(5.38^{+35.50}_{-4.22}) \times 10^{51}$
2435	$105.2^{+19.8}_{-26.3}$	$2.50^{+1.18}_{-1.00}$	$(3.19^{+4.84}_{-2.27}) \times 10^{52}$
2436	$320.2^{+49.0}_{-73.8}$	$6.88^{+5.68}_{-3.62}$	$(1.49^{+4.39}_{-1.23}) \times 10^{54}$
2438	$64.1^{+3.6}_{-3.8}$	$1.26^{+0.11}_{-0.11}$	$(4.94^{+1.10}_{-0.97}) \times 10^{51}$
2443	$180.9^{+28.2}_{-22.1}$	$3.08^{+1.33}_{-0.74}$	$(1.28^{+1.72}_{-0.62}) \times 10^{53}$
2446	$276.0^{+11.8}_{-11.4}$	$10.12^{+2.23}_{-1.65}$	$(2.21^{+1.25}_{-0.74}) \times 10^{54}$
2451	$153.9^{+43.2}_{-36.1}$	$5.49^{+9.83}_{-2.72}$	$(2.34^{+21.93}_{-1.88}) \times 10^{53}$
2453	$81.9^{+12.7}_{-15.0}$	$4.68^{+2.82}_{-1.84}$	$(5.09^{+10.11}_{-3.54}) \times 10^{52}$
2458	$28.7^{+40.4}_{-11.2}$	$0.56^{+1.36}_{-0.24}$	$(4.74^{+91.21}_{-3.49}) \times 10^{50}$
2460	$73.0^{+27.9}_{-48.3}$	$3.35^{+5.77}_{-2.73}$	$(2.36^{+22.08}_{-2.32}) \times 10^{52}$
2476	$65.3^{+1.3}_{-1.4}$	$1.43^{+0.04}_{-0.05}$	$(5.89^{+0.46}_{-0.46}) \times 10^{51}$
2477	$118.0^{+4.1}_{-7.0}$	$11.06^{+2.02}_{-2.59}$	$(4.75^{+2.18}_{-2.16}) \times 10^{53}$
2482	$118.3^{+8.4}_{-7.1}$	$7.11^{+2.21}_{-1.36}$	$(2.16^{+1.86}_{-0.84}) \times 10^{53}$
2500	$118.5^{+18.8}_{-20.2}$	$7.29^{+6.71}_{-3.20}$	$(2.26^{+7.69}_{-1.68}) \times 10^{53}$
2510	$68.5^{+46.2}_{-31.0}$	$1.48^{+2.67}_{-0.83}$	$(6.76^{+75.12}_{-5.86}) \times 10^{51}$
2511	$59.6^{+48.0}_{-39.0}$	$1.29^{+2.73}_{-0.95}$	$(4.38^{+64.15}_{-4.20}) \times 10^{51}$
2519	$148.4^{+27.5}_{-25.9}$	$10.24^{+17.93}_{-5.15}$	$(6.53^{+55.23}_{-5.22}) \times 10^{53}$
2530	$205.8^{+52.6}_{-53.8}$	$5.88^{+9.60}_{-3.19}$	$(4.70^{+37.82}_{-3.96}) \times 10^{53}$
2533	$380.4^{+5.7}_{-5.6}$	$4.36^{+0.18}_{-0.17}$	$(9.76^{+1.00}_{-0.88}) \times 10^{53}$
2537	$103.6^{+6.1}_{-5.3}$	$0.56^{+0.04}_{-0.03}$	$(6.11^{+1.08}_{-0.86}) \times 10^{51}$
2570	$212.6^{+20.8}_{-17.2}$	$3.47^{+0.94}_{-0.61}$	$(2.12^{+1.62}_{-0.78}) \times 10^{53}$
2586	$297.9^{+12.7}_{-12.1}$	$6.63^{+1.09}_{-0.86}$	$(1.21^{+0.51}_{-0.33}) \times 10^{54}$
2593	$72.3^{+4.2}_{-4.0}$	$2.21^{+0.26}_{-0.22}$	$(1.26^{+0.39}_{-0.28}) \times 10^{52}$
2600	$102.9^{+4.6}_{-11.7}$	$4.69^{+0.65}_{-1.26}$	$(8.04^{+2.86}_{-4.21}) \times 10^{52}$
2603	$82.2^{+1.3}_{-1.4}$	$1.48^{+0.04}_{-0.04}$	$(9.72^{+0.59}_{-0.64}) \times 10^{51}$
2611	$550.4^{+15.4}_{-15.2}$	$2.90^{+0.18}_{-0.17}$	$(1.08^{+0.17}_{-0.15}) \times 10^{54}$
2620	$73.7^{+4.6}_{-4.7}$	$2.72^{+0.39}_{-0.34}$	$(1.77^{+0.66}_{-0.49}) \times 10^{52}$
2628	$170.5^{+9.1}_{-9.2}$	$1.90^{+0.19}_{-0.17}$	$(5.72^{+1.48}_{-1.19}) \times 10^{52}$
2634	$51.0^{+6.8}_{-13.9}$	$0.78^{+0.14}_{-0.25}$	$(1.93^{+0.96}_{-1.18}) \times 10^{51}$
2640	$30.1^{+36.8}_{-20.1}$	$0.72^{+1.71}_{-0.51}$	$(6.28^{+116.82}_{-5.94}) \times 10^{50}$
2660	$88.2^{+12.6}_{-14.2}$	$5.63^{+3.51}_{-2.16}$	$(8.03^{+16.48}_{-5.45}) \times 10^{52}$
2662	$123.4^{+40.3}_{-28.7}$	$4.62^{+8.91}_{-2.15}$	$(1.13^{+12.17}_{-0.88}) \times 10^{53}$
2665	$98.6^{+5.9}_{-6.3}$	$1.19^{+0.11}_{-0.11}$	$(1.10^{+0.26}_{-0.23}) \times 10^{52}$
2696	$116.8^{+14.3}_{-13.6}$	$7.67^{+5.06}_{-2.61}$	$(2.41^{+5.19}_{-1.49}) \times 10^{53}$
2697	$93.5^{+24.0}_{-25.9}$	$4.98^{+6.74}_{-2.67}$	$(7.34^{+45.08}_{-6.16}) \times 10^{52}$
2700	$197.6^{+67.4}_{-47.4}$	$2.62^{+2.85}_{-1.03}$	$(1.20^{+5.70}_{-0.84}) \times 10^{53}$
2703	$236.2^{+56.2}_{-63.1}$	$6.94^{+12.16}_{-4.00}$	$(8.25^{+72.85}_{-7.16}) \times 10^{53}$
2706	$157.4^{+23.5}_{-20.3}$	$10.43^{+12.52}_{-4.32}$	$(7.59^{+36.45}_{-5.36}) \times 10^{53}$
2709	$189.6^{+14.4}_{-13.0}$	$10.20^{+4.49}_{-2.58}$	$(1.06^{+1.34}_{-0.51}) \times 10^{54}$
2711	$101.7^{+38.0}_{-23.6}$	$5.06^{+14.89}_{-2.42}$	$(8.91^{+191.99}_{-7.02}) \times 10^{52}$

Table B.1: Redshifts and luminosities estimated by E_p–L relation

Trigger Number	E_p keV	redshift	luminosity erg s^{-1}
2728	$159.5^{+46.0}_{-44.8}$	$7.75^{+24.43}_{-4.74}$	$(4.57^{+104.51}_{-4.07}) \times 10^{53}$
2736	$185.4^{+38.0}_{-34.8}$	$3.53^{+2.43}_{-1.27}$	$(1.66^{+4.03}_{-1.09}) \times 10^{53}$
2749	$48.9^{+29.9}_{-8.1}$	$1.35^{+1.89}_{-0.31}$	$(3.08^{+23.10}_{-1.47}) \times 10^{51}$
2760	$65.7^{+3.9}_{-10.9}$	$2.85^{+0.39}_{-0.85}$	$(1.50^{+0.54}_{-0.87}) \times 10^{52}$
2774	$63.5^{+20.9}_{-22.4}$	$1.93^{+1.53}_{-0.94}$	$(8.13^{+25.12}_{-6.56}) \times 10^{51}$
2790	$217.1^{+16.0}_{-15.6}$	$6.77^{+2.11}_{-1.47}$	$(6.68^{+5.77}_{-2.90}) \times 10^{53}$
2797	$273.7^{+9.8}_{-9.3}$	$3.20^{+0.27}_{-0.24}$	$(3.10^{+0.67}_{-0.53}) \times 10^{53}$
2798	$536.3^{+5.6}_{-5.5}$	$2.08^{+0.04}_{-0.04}$	$(6.40^{+0.30}_{-0.29}) \times 10^{53}$
2799	$164.5^{+17.6}_{-16.6}$	$2.81^{+0.73}_{-0.54}$	$(9.23^{+6.85}_{-3.75}) \times 10^{52}$
2812	$235.7^{+7.4}_{-7.1}$	$1.93^{+0.11}_{-0.10}$	$(1.12^{+0.16}_{-0.14}) \times 10^{53}$
2815	$91.4^{+5.4}_{-5.8}$	$6.27^{+1.43}_{-1.18}$	$(1.04^{+0.63}_{-0.40}) \times 10^{53}$
2831	$766.1^{+15.9}_{-15.5}$	$1.31^{+0.04}_{-0.04}$	$(7.34^{+0.58}_{-0.54}) \times 10^{53}$
2852	$437.3^{+29.8}_{-27.3}$	$7.57^{+2.33}_{-1.54}$	$(3.30^{+2.79}_{-1.35}) \times 10^{54}$
2855	$318.2^{+6.7}_{-6.5}$	$2.16^{+0.09}_{-0.08}$	$(2.37^{+0.24}_{-0.21}) \times 10^{53}$
2877	$48.6^{+1.8}_{-1.8}$	$0.41^{+0.02}_{-0.02}$	$(1.10^{+0.11}_{-0.11}) \times 10^{51}$
2880	$137.1^{+23.5}_{-21.2}$	$3.39^{+1.77}_{-1.03}$	$(8.49^{+14.47}_{-4.93}) \times 10^{52}$
2889	$248.9^{+48.5}_{-39.0}$	$4.20^{+3.12}_{-1.40}$	$(3.93^{+10.44}_{-2.44}) \times 10^{53}$
2891	$747.5^{+19.7}_{-18.9}$	$8.81^{+1.03}_{-0.86}$	$(1.26^{+0.36}_{-0.26}) \times 10^{55}$
2894	$217.3^{+9.5}_{-8.9}$	$1.59^{+0.12}_{-0.10}$	$(7.44^{+1.40}_{-1.14}) \times 10^{52}$
2897	$45.4^{+0.9}_{-1.2}$	$0.77^{+0.02}_{-0.03}$	$(1.51^{+0.09}_{-0.12}) \times 10^{51}$
2913	$121.6^{+17.0}_{-15.7}$	$2.09^{+0.61}_{-0.45}$	$(3.31^{+2.86}_{-1.47}) \times 10^{52}$
2919	$315.6^{+23.4}_{-21.4}$	$4.22^{+0.95}_{-0.69}$	$(6.36^{+3.89}_{-2.20}) \times 10^{53}$
2924	$101.4^{+8.5}_{-8.9}$	$10.43^{+5.33}_{-3.25}$	$(3.15^{+4.81}_{-1.81}) \times 10^{53}$
2925	$73.5^{+39.4}_{-30.6}$	$3.74^{+16.43}_{-2.40}$	$(2.85^{+131.22}_{-2.62}) \times 10^{52}$
2929	$460.5^{+15.6}_{-14.8}$	$3.95^{+0.37}_{-0.31}$	$(1.22^{+0.29}_{-0.22}) \times 10^{54}$
2945	$42.8^{+14.8}_{-7.9}$	$1.39^{+0.92}_{-0.36}$	$(2.44^{+6.09}_{-1.26}) \times 10^{51}$
2950	$120.3^{+25.8}_{-32.0}$	$8.18^{+14.36}_{-4.92}$	$(2.86^{+24.88}_{-2.53}) \times 10^{53}$
2951	$148.6^{+51.9}_{-63.1}$	$6.52^{+25.25}_{-4.74}$	$(2.93^{+98.27}_{-2.80}) \times 10^{53}$
2953	$196.3^{+5.2}_{-5.0}$	$1.11^{+0.04}_{-0.04}$	$(4.03^{+0.39}_{-0.35}) \times 10^{52}$
2958	$144.6^{+17.0}_{-14.7}$	$2.87^{+0.84}_{-0.57}$	$(7.35^{+6.27}_{-3.03}) \times 10^{52}$
2988	$199.1^{+34.3}_{-28.5}$	$7.94^{+9.11}_{-3.19}$	$(7.44^{+34.23}_{-5.18}) \times 10^{53}$
2998	$72.8^{+5.3}_{-7.8}$	$3.03^{+0.54}_{-0.64}$	$(2.02^{+0.97}_{-0.88}) \times 10^{52}$
3001	$219.3^{+20.8}_{-19.5}$	$7.40^{+3.36}_{-2.00}$	$(7.96^{+10.75}_{-4.12}) \times 10^{53}$
3003	$326.5^{+13.9}_{-13.1}$	$7.40^{+1.31}_{-1.00}$	$(1.77^{+0.80}_{-0.50}) \times 10^{54}$
3011	$178.4^{+42.7}_{-39.6}$	$1.77^{+0.88}_{-0.58}$	$(5.73^{+9.53}_{-3.56}) \times 10^{52}$
3012	$76.8^{+42.0}_{-28.1}$	$2.24^{+4.55}_{-1.17}$	$(1.45^{+18.67}_{-1.21}) \times 10^{52}$
3015	$170.5^{+29.3}_{-24.1}$	$11.37^{+19.51}_{-5.18}$	$(1.04^{+8.48}_{-0.78}) \times 10^{54}$
3032	$103.1^{+15.1}_{-9.8}$	$3.31^{+1.40}_{-0.65}$	$(4.63^{+6.06}_{-1.90}) \times 10^{52}$
3035	$167.1^{+76.6}_{-47.2}$	$1.04^{+0.82}_{-0.37}$	$(2.73^{+8.70}_{-1.78}) \times 10^{52}$
3039	$132.9^{+6.4}_{-6.3}$	$1.83^{+0.16}_{-0.14}$	$(3.31^{+0.75}_{-0.60}) \times 10^{52}$
3042	$303.1^{+14.1}_{-13.3}$	$2.99^{+0.33}_{-0.28}$	$(3.44^{+0.97}_{-0.72}) \times 10^{53}$
3055	$73.4^{+1.9}_{-2.7}$	$1.75^{+0.08}_{-0.11}$	$(9.57^{+1.08}_{-1.35}) \times 10^{51}$
3056	$125.9^{+16.8}_{-13.7}$	$2.34^{+0.70}_{-0.45}$	$(4.16^{+3.65}_{-1.68}) \times 10^{52}$

Table B.1: Redshifts and luminosities estimated by E_p–L relation

Trigger Number	E_p keV	redshift	luminosity erg s^{-1}
3057	$683.9^{+14.4}_{-13.9}$	$1.28^{+0.04}_{-0.04}$	$(5.71^{+0.46}_{-0.41}) \times 10^{53}$
3067	$380.4^{+12.5}_{-11.8}$	$1.88^{+0.11}_{-0.10}$	$(2.82^{+0.42}_{-0.36}) \times 10^{53}$
3068	$132.4^{+26.2}_{-38.5}$	$9.63^{+17.80}_{-6.34}$	$(4.65^{+43.07}_{-4.27}) \times 10^{53}$
3070	$171.2^{+23.7}_{-33.5}$	$11.00^{+12.34}_{-6.06}$	$(9.91^{+42.96}_{-8.34}) \times 10^{53}$
3072	$55.5^{+16.4}_{-31.2}$	$2.04^{+1.47}_{-1.42}$	$(6.66^{+17.94}_{-6.30}) \times 10^{51}$
3075	$49.7^{+31.5}_{-37.5}$	$1.67^{+3.10}_{-1.39}$	$(4.13^{+47.39}_{-4.08}) \times 10^{51}$
3076	$93.0^{+38.5}_{-38.2}$	$3.36^{+6.75}_{-2.08}$	$(3.85^{+46.14}_{-3.48}) \times 10^{52}$
3084	$166.6^{+35.3}_{-37.0}$	$6.57^{+8.70}_{-3.32}$	$(3.73^{+21.55}_{-3.02}) \times 10^{53}$
3085	$91.3^{+24.4}_{-40.9}$	$6.04^{+11.13}_{-4.44}$	$(9.70^{+94.06}_{-9.29}) \times 10^{52}$
3093	$128.6^{+31.5}_{-36.9}$	$6.45^{+10.93}_{-3.80}$	$(2.15^{+18.15}_{-1.89}) \times 10^{53}$
3096	$240.9^{+34.7}_{-47.8}$	$10.99^{+13.12}_{-6.10}$	$(1.96^{+9.27}_{-1.65}) \times 10^{54}$
3100	$54.2^{+2.0}_{-1.2}$	$1.88^{+0.13}_{-0.07}$	$(5.73^{+0.98}_{-0.51}) \times 10^{51}$
3101	$107.5^{+5.4}_{-5.5}$	$1.69^{+0.15}_{-0.14}$	$(1.96^{+0.44}_{-0.38}) \times 10^{52}$
3105	$259.7^{+8.3}_{-7.5}$	$8.91^{+1.30}_{-0.98}$	$(1.55^{+0.56}_{-0.36}) \times 10^{54}$
3109	$111.1^{+12.0}_{-10.8}$	$7.66^{+4.24}_{-2.25}$	$(2.17^{+3.74}_{-1.20}) \times 10^{53}$
3115	$310.8^{+7.0}_{-6.8}$	$3.72^{+0.22}_{-0.20}$	$(5.04^{+0.73}_{-0.61}) \times 10^{53}$
3119	$52.4^{+13.8}_{-14.8}$	$1.46^{+0.72}_{-0.55}$	$(3.88^{+6.49}_{-2.68}) \times 10^{51}$
3120	$108.8^{+46.7}_{-41.4}$	$4.47^{+15.08}_{-2.83}$	$(8.32^{+231.45}_{-7.57}) \times 10^{52}$
3128	$382.1^{+7.1}_{-6.9}$	$2.80^{+0.11}_{-0.11}$	$(4.94^{+0.50}_{-0.44}) \times 10^{53}$
3129	$72.5^{+9.8}_{-12.3}$	$2.26^{+0.67}_{-0.63}$	$(1.31^{+1.15}_{-0.72}) \times 10^{52}$
3131	$40.0^{+1.0}_{-2.2}$	$0.80^{+0.03}_{-0.06}$	$(1.22^{+0.10}_{-0.20}) \times 10^{51}$
3132	$81.5^{+4.0}_{-4.3}$	$4.72^{+0.73}_{-0.65}$	$(5.11^{+2.04}_{-1.51}) \times 10^{52}$
3138	$217.6^{+6.5}_{-6.2}$	$1.33^{+0.06}_{-0.06}$	$(6.00^{+0.70}_{-0.62}) \times 10^{52}$
3142	$248.9^{+45.9}_{-61.7}$	$9.33^{+14.42}_{-5.60}$	$(1.55^{+10.94}_{-1.37}) \times 10^{54}$
3143	$130.6^{+43.4}_{-35.4}$	$1.65^{+1.17}_{-0.62}$	$(2.80^{+7.55}_{-1.93}) \times 10^{52}$
3153	$28.8^{+11.9}_{-14.1}$	$0.83^{+0.52}_{-0.46}$	$(6.55^{+14.94}_{-5.59}) \times 10^{50}$
3159	$43.3^{+31.5}_{-38.6}$	$1.28^{+2.23}_{-1.17}$	$(2.29^{+24.45}_{-2.28}) \times 10^{51}$
3166	$41.4^{+43.9}_{-25.4}$	$1.23^{+4.11}_{-0.86}$	$(2.00^{+66.64}_{-1.89}) \times 10^{51}$
3177	$197.8^{+29.4}_{-24.5}$	$8.75^{+8.72}_{-3.29}$	$(8.72^{+32.60}_{-5.78}) \times 10^{53}$
3193	$121.7^{+34.1}_{-28.8}$	$7.81^{+23.20}_{-4.34}$	$(2.70^{+55.61}_{-2.29}) \times 10^{53}$
3212	$105.8^{+36.8}_{-51.1}$	$1.38^{+0.92}_{-0.81}$	$(1.49^{+3.72}_{-1.32}) \times 10^{52}$
3217	$51.6^{+47.5}_{-16.7}$	$0.85^{+1.50}_{-0.33}$	$(2.14^{+23.69}_{-1.48}) \times 10^{51}$
3220	$78.8^{+22.5}_{-18.5}$	$2.70^{+2.33}_{-1.06}$	$(2.00^{+6.77}_{-1.40}) \times 10^{52}$
3227	$222.2^{+10.6}_{-10.2}$	$1.67^{+0.14}_{-0.12}$	$(8.25^{+1.76}_{-1.43}) \times 10^{52}$
3237	$97.3^{+14.9}_{-20.4}$	$1.34^{+0.34}_{-0.38}$	$(1.22^{+0.90}_{-0.68}) \times 10^{52}$
3238	$95.4^{+67.2}_{-51.2}$	$1.54^{+3.12}_{-0.99}$	$(1.38^{+18.53}_{-1.27}) \times 10^{52}$
3241	$297.2^{+10.1}_{-9.9}$	$3.05^{+0.24}_{-0.22}$	$(3.41^{+0.69}_{-0.56}) \times 10^{53}$
3242	$23.6^{+13.2}_{-7.7}$	$0.34^{+0.22}_{-0.12}$	$(2.34^{+5.41}_{-1.46}) \times 10^{50}$
3245	$342.9^{+13.4}_{-11.6}$	$2.20^{+0.17}_{-0.14}$	$(2.83^{+0.56}_{-0.41}) \times 10^{53}$
3246	$119.5^{+17.9}_{-36.9}$	$10.67^{+13.24}_{-7.40}$	$(4.56^{+22.91}_{-4.27}) \times 10^{53}$
3247	$211.7^{+59.6}_{-77.0}$	$6.47^{+14.59}_{-4.35}$	$(5.86^{+78.13}_{-5.45}) \times 10^{53}$
3255	$91.4^{+12.5}_{-11.6}$	$0.69^{+0.12}_{-0.10}$	$(5.58^{+2.69}_{-1.85}) \times 10^{51}$
3256	$141.8^{+6.1}_{-6.6}$	$3.42^{+0.38}_{-0.36}$	$(9.23^{+2.60}_{-2.15}) \times 10^{52}$

Table B.1: Redshifts and luminosities estimated by E_p–L relation

Trigger Number	E_p keV	redshift	luminosity erg s^{-1}
3257	$210.5^{+6.3}_{-5.9}$	$11.97^{+1.98}_{-1.52}$	$(1.75^{+0.72}_{-0.46}) \times 10^{54}$
3259	$265.4^{+68.7}_{-48.1}$	$8.96^{+27.42}_{-4.41}$	$(1.64^{+34.96}_{-1.30}) \times 10^{54}$
3279	$76.3^{+17.6}_{-17.6}$	$2.95^{+2.05}_{-1.17}$	$(2.13^{+5.32}_{-1.50}) \times 10^{52}$
3283	$185.8^{+32.0}_{-29.4}$	$10.61^{+16.86}_{-5.07}$	$(1.09^{+7.93}_{-0.85}) \times 10^{54}$
3287	$198.1^{+15.0}_{-13.9}$	$4.00^{+0.89}_{-0.66}$	$(2.31^{+1.39}_{-0.81}) \times 10^{53}$
3290	$144.3^{+5.2}_{-5.1}$	$1.06^{+0.05}_{-0.05}$	$(2.06^{+0.27}_{-0.24}) \times 10^{52}$
3292	$97.3^{+38.0}_{-43.4}$	$5.81^{+24.78}_{-4.23}$	$(1.03^{+41.83}_{-0.99}) \times 10^{53}$
3306	$130.8^{+24.5}_{-22.6}$	$2.80^{+1.42}_{-0.86}$	$(5.79^{+9.61}_{-3.43}) \times 10^{52}$
3307	$46.1^{+26.3}_{-20.5}$	$1.56^{+2.26}_{-0.87}$	$(3.27^{+25.29}_{-2.83}) \times 10^{51}$
3319	$207.2^{+36.6}_{-38.2}$	$9.03^{+12.42}_{-4.50}$	$(1.01^{+6.02}_{-0.81}) \times 10^{54}$
3320	$115.5^{+17.6}_{-10.5}$	$6.36^{+4.86}_{-1.64}$	$(1.70^{+4.51}_{-0.85}) \times 10^{53}$
3330	$434.3^{+25.4}_{-23.3}$	$5.16^{+1.02}_{-0.76}$	$(1.68^{+0.88}_{-0.52}) \times 10^{54}$
3336	$104.3^{+41.5}_{-37.7}$	$2.84^{+4.33}_{-1.55}$	$(3.77^{+29.61}_{-3.22}) \times 10^{52}$
3345	$201.5^{+12.3}_{-10.8}$	$1.70^{+0.18}_{-0.15}$	$(6.95^{+1.98}_{-1.38}) \times 10^{52}$
3351	$159.3^{+45.7}_{-45.0}$	$4.29^{+5.95}_{-2.23}$	$(1.67^{+10.80}_{-1.38}) \times 10^{53}$
3352	$149.1^{+9.6}_{-8.2}$	$1.87^{+0.22}_{-0.17}$	$(4.30^{+1.35}_{-0.91}) \times 10^{52}$
3356	$100.5^{+25.3}_{-26.1}$	$2.62^{+1.84}_{-1.10}$	$(3.10^{+7.96}_{-2.27}) \times 10^{52}$
3364	$105.1^{+12.4}_{-17.3}$	$8.91^{+6.33}_{-4.11}$	$(2.54^{+5.98}_{-1.93}) \times 10^{53}$
3369	$83.7^{+22.7}_{-14.0}$	$3.99^{+4.66}_{-1.38}$	$(4.09^{+20.64}_{-2.61}) \times 10^{52}$
3370	$41.9^{+35.8}_{-31.4}$	$1.16^{+2.41}_{-0.94}$	$(1.92^{+27.68}_{-1.89}) \times 10^{51}$
3403	$87.1^{+17.1}_{-34.2}$	$6.43^{+7.31}_{-4.48}$	$(9.82^{+45.51}_{-9.25}) \times 10^{52}$
3407	$112.5^{+58.7}_{-52.8}$	$4.09^{+20.06}_{-2.87}$	$(7.69^{+427.25}_{-7.27}) \times 10^{52}$
3408	$348.7^{+6.3}_{-6.3}$	$3.73^{+0.17}_{-0.16}$	$(6.39^{+0.73}_{-0.65}) \times 10^{53}$
3415	$205.9^{+7.0}_{-6.8}$	$2.44^{+0.17}_{-0.15}$	$(1.18^{+0.21}_{-0.17}) \times 10^{53}$
3436	$193.0^{+15.7}_{-14.9}$	$8.85^{+3.81}_{-2.31}$	$(8.48^{+10.60}_{-4.24}) \times 10^{53}$
3448	$176.1^{+72.8}_{-56.8}$	$3.00^{+5.20}_{-1.53}$	$(1.16^{+11.13}_{-0.96}) \times 10^{53}$
3458	$236.7^{+8.2}_{-7.9}$	$2.14^{+0.14}_{-0.13}$	$(1.30^{+0.22}_{-0.18}) \times 10^{53}$
3480	$370.8^{+10.0}_{-9.6}$	$2.82^{+0.17}_{-0.15}$	$(4.71^{+0.70}_{-0.59}) \times 10^{53}$
3481	$395.5^{+10.4}_{-10.1}$	$1.79^{+0.08}_{-0.08}$	$(2.85^{+0.33}_{-0.29}) \times 10^{53}$
3485	$113.2^{+19.6}_{-17.7}$	$10.61^{+16.98}_{-5.02}$	$(4.05^{+29.76}_{-3.12}) \times 10^{53}$
3488	$321.8^{+32.3}_{-28.9}$	$5.28^{+1.99}_{-1.23}$	$(9.57^{+10.51}_{-4.45}) \times 10^{53}$
3489	$327.7^{+10.4}_{-10.0}$	$6.81^{+0.83}_{-0.69}$	$(1.54^{+0.47}_{-0.34}) \times 10^{54}$
3491	$221.8^{+13.3}_{-12.4}$	$0.90^{+0.07}_{-0.07}$	$(4.19^{+0.88}_{-0.71}) \times 10^{52}$
3503	$106.1^{+19.3}_{-22.6}$	$10.57^{+18.64}_{-6.03}$	$(3.54^{+30.18}_{-3.04}) \times 10^{53}$
3511	$45.0^{+13.2}_{-19.7}$	$1.39^{+0.76}_{-0.76}$	$(2.72^{+5.18}_{-2.32}) \times 10^{51}$
3512	$223.2^{+13.6}_{-12.4}$	$2.36^{+0.30}_{-0.24}$	$(1.32^{+0.44}_{-0.31}) \times 10^{53}$
3514	$128.6^{+33.5}_{-42.5}$	$5.49^{+8.53}_{-3.36}$	$(1.63^{+12.26}_{-1.46}) \times 10^{53}$
3516	$261.3^{+40.7}_{-37.0}$	$10.12^{+12.66}_{-4.42}$	$(1.98^{+10.12}_{-1.45}) \times 10^{54}$
3523	$642.5^{+8.6}_{-8.5}$	$1.58^{+0.03}_{-0.03}$	$(6.46^{+0.36}_{-0.34}) \times 10^{53}$
3527	$215.1^{+54.4}_{-50.9}$	$9.69^{+31.81}_{-5.73}$	$(1.24^{+29.53}_{-1.08}) \times 10^{54}$
3567	$108.6^{+21.7}_{-9.1}$	$6.55^{+7.85}_{-1.59}$	$(1.58^{+7.89}_{-0.75}) \times 10^{53}$
3569	$216.1^{+47.8}_{-36.6}$	$3.11^{+2.13}_{-0.98}$	$(1.85^{+4.52}_{-1.11}) \times 10^{53}$
3588	$60.2^{+28.2}_{-31.9}$	$1.24^{+1.12}_{-0.77}$	$(4.27^{+16.47}_{-3.86}) \times 10^{51}$

Table B.1: Redshifts and luminosities estimated by E_p–L relation

Trigger Number	E_p keV	redshift	luminosity erg s^{-1}
3598	$235.5^{+17.5}_{-16.2}$	$6.77^{+2.13}_{-1.41}$	$(7.85^{+6.86}_{-3.29}) \times 10^{53}$
3608	$44.8^{+24.9}_{-27.4}$	$0.61^{+0.47}_{-0.40}$	$(1.22^{+3.73}_{-1.12}) \times 10^{51}$
3618	$252.9^{+12.9}_{-12.3}$	$7.18^{+1.52}_{-1.14}$	$(1.00^{+0.55}_{-0.33}) \times 10^{54}$
3634	$254.8^{+40.1}_{-34.3}$	$6.83^{+5.83}_{-2.47}$	$(9.35^{+28.76}_{-6.07}) \times 10^{53}$
3637	$164.9^{+11.2}_{-10.1}$	$7.49^{+2.29}_{-1.49}$	$(4.60^{+3.86}_{-1.85}) \times 10^{53}$
3648	$199.0^{+7.4}_{-7.2}$	$3.88^{+0.39}_{-0.34}$	$(2.21^{+0.57}_{-0.43}) \times 10^{53}$
3649	$239.7^{+21.0}_{-20.1}$	$6.28^{+2.28}_{-1.50}$	$(7.14^{+7.42}_{-3.36}) \times 10^{53}$
3658	$247.2^{+5.9}_{-5.7}$	$1.65^{+0.07}_{-0.06}$	$(1.00^{+0.10}_{-0.09}) \times 10^{53}$
3662	$224.0^{+15.6}_{-13.6}$	$1.91^{+0.25}_{-0.20}$	$(9.96^{+3.47}_{-2.31}) \times 10^{52}$
3663	$197.2^{+22.1}_{-19.1}$	$2.86^{+0.80}_{-0.54}$	$(1.36^{+1.09}_{-0.54}) \times 10^{53}$
3664	$79.4^{+6.2}_{-4.4}$	$2.37^{+0.39}_{-0.24}$	$(1.67^{+0.75}_{-0.39}) \times 10^{52}$
3765	$298.1^{+5.7}_{-5.6}$	$1.27^{+0.04}_{-0.04}$	$(1.08^{+0.08}_{-0.07}) \times 10^{53}$
3776	$180.0^{+7.6}_{-6.9}$	$2.50^{+0.22}_{-0.18}$	$(9.31^{+2.14}_{-1.58}) \times 10^{52}$
3788	$204.8^{+5.7}_{-5.5}$	$2.14^{+0.11}_{-0.10}$	$(9.70^{+1.31}_{-1.12}) \times 10^{52}$
3811	$55.6^{+1.8}_{-2.1}$	$1.22^{+0.06}_{-0.07}$	$(3.58^{+0.44}_{-0.46}) \times 10^{51}$
3815	$46.3^{+11.8}_{-11.3}$	$0.87^{+0.32}_{-0.26}$	$(1.77^{+2.06}_{-1.02}) \times 10^{51}$
3843	$193.6^{+10.1}_{-29.4}$	$7.56^{+1.69}_{-3.10}$	$(6.45^{+3.79}_{-4.56}) \times 10^{53}$
3866	$310.7^{+61.4}_{-41.3}$	$10.15^{+20.01}_{-4.25}$	$(2.81^{+28.71}_{-2.00}) \times 10^{54}$
3869	$77.7^{+41.5}_{-47.3}$	$1.63^{+2.22}_{-1.16}$	$(9.76^{+68.37}_{-9.29}) \times 10^{51}$
3870	$135.8^{+30.6}_{-19.2}$	$0.66^{+0.19}_{-0.11}$	$(1.19^{+1.04}_{-0.42}) \times 10^{52}$
3875	$77.3^{+4.6}_{-4.8}$	$1.48^{+0.15}_{-0.14}$	$(8.60^{+2.24}_{-1.88}) \times 10^{51}$
3879	$95.6^{+16.2}_{-18.3}$	$2.75^{+1.21}_{-0.91}$	$(3.01^{+4.20}_{-1.89}) \times 10^{52}$
3886	$160.4^{+44.7}_{-33.7}$	$5.81^{+11.06}_{-2.72}$	$(2.80^{+28.73}_{-2.17}) \times 10^{53}$
3890	$104.2^{+19.9}_{-20.5}$	$10.72^{+21.12}_{-5.87}$	$(3.50^{+35.48}_{-2.94}) \times 10^{53}$
3891	$216.2^{+11.4}_{-10.5}$	$1.25^{+0.10}_{-0.09}$	$(5.57^{+1.16}_{-0.91}) \times 10^{52}$
3892	$32.4^{+31.4}_{-18.4}$	$0.58^{+0.86}_{-0.35}$	$(6.13^{+50.79}_{-5.44}) \times 10^{50}$
3893	$168.7^{+3.8}_{-3.7}$	$4.53^{+0.29}_{-0.27}$	$(2.05^{+0.33}_{-0.28}) \times 10^{53}$
3900	$87.8^{+116.0}_{-317.4}$	$1.11^{+5.13}_{8.75}$	$(8.09^{+503.70}_{1450.37}) \times 10^{51}$
3905	$228.8^{+15.6}_{-14.3}$	$3.77^{+0.72}_{-0.54}$	$(2.80^{+1.43}_{-0.87}) \times 10^{53}$
3906	$120.3^{+9.9}_{-9.2}$	$3.73^{+0.87}_{-0.64}$	$(7.59^{+4.90}_{-2.76}) \times 10^{52}$
3909	$58.2^{+26.9}_{-25.3}$	$1.03^{+0.82}_{-0.53}$	$(3.29^{+10.54}_{-2.71}) \times 10^{51}$
3912	$198.0^{+17.6}_{-16.2}$	$4.39^{+1.25}_{-0.87}$	$(2.67^{+2.14}_{-1.09}) \times 10^{53}$
3916	$101.8^{+28.5}_{-26.8}$	$5.00^{+7.95}_{-2.59}$	$(8.74^{+68.74}_{-7.21}) \times 10^{52}$
3918	$273.7^{+19.2}_{-17.5}$	$7.99^{+2.65}_{-1.70}$	$(1.42^{+1.31}_{-0.60}) \times 10^{54}$
3929	$274.9^{+12.0}_{-11.2}$	$4.13^{+0.51}_{-0.42}$	$(4.67^{+1.49}_{-1.05}) \times 10^{53}$
3930	$512.1^{+12.3}_{-11.9}$	$5.61^{+0.44}_{-0.39}$	$(2.69^{+0.52}_{-0.42}) \times 10^{54}$
3936	$182.9^{+6.5}_{-6.2}$	$2.78^{+0.22}_{-0.19}$	$(1.12^{+0.23}_{-0.18}) \times 10^{53}$
3954	$304.9^{+13.9}_{-13.4}$	$2.40^{+0.23}_{-0.20}$	$(2.51^{+0.62}_{-0.48}) \times 10^{53}$
4048	$355.9^{+20.1}_{-18.6}$	$6.95^{+1.62}_{-1.15}$	$(1.88^{+1.16}_{-0.65}) \times 10^{54}$
4157	$85.3^{+6.4}_{-5.0}$	$2.37^{+0.38}_{-0.26}$	$(1.94^{+0.83}_{-0.48}) \times 10^{52}$
4216	$56.9^{+10.9}_{-15.7}$	$0.90^{+0.25}_{-0.30}$	$(2.75^{+2.23}_{-1.73}) \times 10^{51}$
4312	$109.6^{+10.4}_{-10.1}$	$0.98^{+0.13}_{-0.12}$	$(1.11^{+0.40}_{-0.30}) \times 10^{52}$
4350	$85.2^{+27.9}_{-19.6}$	$1.05^{+0.55}_{-0.30}$	$(7.13^{+13.15}_{-4.06}) \times 10^{51}$

Table B.1: Redshifts and luminosities estimated by E_p–L relation

Trigger Number	E_p keV	redshift	luminosity erg s^{-1}
4556	$264.1^{+6.6}_{-6.1}$	$1.55^{+0.06}_{-0.06}$	$(1.07^{+0.11}_{-0.09}) \times 10^{53}$
4701	$238.2^{+8.1}_{-7.8}$	$3.76^{+0.34}_{-0.30}$	$(3.02^{+0.68}_{-0.54}) \times 10^{53}$
4710	$99.0^{+5.0}_{-5.3}$	$1.02^{+0.07}_{-0.07}$	$(9.33^{+1.72}_{-1.59}) \times 10^{51}$
4814	$217.4^{+28.3}_{-37.2}$	$7.76^{+5.63}_{-3.49}$	$(8.51^{+20.83}_{-6.40}) \times 10^{53}$
5080	$43.2^{+2.7}_{-2.3}$	$0.89^{+0.08}_{-0.06}$	$(1.57^{+0.35}_{-0.25}) \times 10^{51}$
5304	$471.7^{+17.9}_{-17.0}$	$3.33^{+0.31}_{-0.27}$	$(9.77^{+2.34}_{-1.79}) \times 10^{53}$
5389	$182.7^{+8.5}_{-8.0}$	$3.95^{+0.51}_{-0.42}$	$(1.92^{+0.64}_{-0.45}) \times 10^{53}$
5415	$125.3^{+13.6}_{-11.3}$	$7.16^{+3.77}_{-1.92}$	$(2.45^{+3.99}_{-1.27}) \times 10^{53}$
5416	$117.2^{+17.7}_{-16.4}$	$10.91^{+13.97}_{-4.86}$	$(4.57^{+24.02}_{-3.38}) \times 10^{53}$
5417	$176.6^{+9.6}_{-8.9}$	$1.35^{+0.11}_{-0.10}$	$(4.05^{+0.90}_{-0.71}) \times 10^{52}$
5419	$97.2^{+52.8}_{-30.3}$	$1.56^{+2.09}_{-0.65}$	$(1.45^{+9.93}_{-1.07}) \times 10^{52}$
5428	$73.5^{+6.9}_{-14.6}$	$2.67^{+0.58}_{-0.91}$	$(1.70^{+1.03}_{-1.08}) \times 10^{52}$
5429	$78.1^{+21.6}_{-29.7}$	$1.12^{+0.51}_{-0.52}$	$(6.45^{+9.68}_{-5.04}) \times 10^{51}$
5433	$194.6^{+14.9}_{-14.1}$	$6.78^{+2.21}_{-1.48}$	$(5.38^{+4.89}_{-2.34}) \times 10^{53}$
5434	$97.9^{+28.3}_{-29.0}$	$8.66^{+33.64}_{-5.60}$	$(2.10^{+68.06}_{-1.92}) \times 10^{53}$
5439	$266.0^{+45.5}_{-34.0}$	$4.66^{+3.18}_{-1.38}$	$(5.32^{+12.46}_{-3.01}) \times 10^{53}$
5447	$37.9^{+18.6}_{-2.6}$	$0.51^{+0.32}_{-0.04}$	$(7.70^{+17.50}_{-1.36}) \times 10^{50}$
5451	$193.1^{+7.6}_{-7.3}$	$5.10^{+0.65}_{-0.54}$	$(3.25^{+1.05}_{-0.75}) \times 10^{53}$
5463	$103.0^{+10.1}_{-25.5}$	$8.68^{+4.71}_{-5.10}$	$(2.33^{+3.89}_{-2.04}) \times 10^{53}$
5472	$133.6^{+26.6}_{-23.1}$	$6.23^{+7.01}_{-2.61}$	$(2.19^{+10.03}_{-1.58}) \times 10^{53}$
5474	$37.4^{+2.7}_{-2.9}$	$1.21^{+0.13}_{-0.13}$	$(1.60^{+0.47}_{-0.39}) \times 10^{51}$
5476	$167.4^{+30.5}_{-26.2}$	$6.60^{+6.83}_{-2.63}$	$(3.80^{+15.32}_{-2.64}) \times 10^{53}$
5477	$1456.8^{+73.8}_{-50.2}$	$5.46^{+0.95}_{-0.55}$	$(2.08^{+0.94}_{-0.46}) \times 10^{55}$
5478	$178.2^{+9.9}_{-10.3}$	$5.81^{+1.17}_{-0.97}$	$(3.45^{+1.83}_{-1.20}) \times 10^{53}$
5479	$170.8^{+23.3}_{-21.2}$	$3.86^{+1.68}_{-1.03}$	$(1.62^{+2.17}_{-0.85}) \times 10^{53}$
5486	$262.4^{+8.4}_{-8.0}$	$2.20^{+0.14}_{-0.12}$	$(1.66^{+0.26}_{-0.22}) \times 10^{53}$
5489	$312.0^{+8.2}_{-8.0}$	$3.62^{+0.24}_{-0.22}$	$(4.88^{+0.82}_{-0.68}) \times 10^{53}$
5493	$91.6^{+40.2}_{-45.7}$	$5.53^{+30.71}_{-4.22}$	$(8.40^{+556.70}_{-8.13}) \times 10^{52}$
5504	$91.7^{+44.8}_{-33.5}$	$1.82^{+2.41}_{-0.90}$	$(1.57^{+10.39}_{-1.27}) \times 10^{52}$
5508	$76.2^{+11.9}_{-11.4}$	$3.96^{+2.10}_{-1.24}$	$(3.35^{+5.72}_{-1.99}) \times 10^{52}$
5515	$91.8^{+63.6}_{-50.5}$	$2.57^{+10.82}_{-1.82}$	$(2.52^{+114.74}_{-2.39}) \times 10^{52}$
5517	$138.7^{+31.5}_{-24.8}$	$3.31^{+2.47}_{-1.12}$	$(8.37^{+22.87}_{-5.27}) \times 10^{52}$
5518	$163.3^{+15.6}_{-13.9}$	$5.54^{+2.03}_{-1.26}$	$(2.67^{+2.84}_{-1.22}) \times 10^{53}$
5523	$135.2^{+21.5}_{-20.2}$	$2.26^{+0.81}_{-0.57}$	$(4.57^{+4.99}_{-2.32}) \times 10^{52}$
5530	$71.3^{+5.8}_{-5.6}$	$1.09^{+0.13}_{-0.12}$	$(5.23^{+1.67}_{-1.27}) \times 10^{51}$
5531	$131.9^{+16.9}_{-16.2}$	$5.99^{+3.41}_{-1.91}$	$(1.99^{+3.63}_{-1.18}) \times 10^{53}$
5539	$112.2^{+15.7}_{-18.0}$	$4.73^{+2.48}_{-1.69}$	$(9.70^{+16.16}_{-6.29}) \times 10^{52}$
5541	$145.7^{+31.2}_{-28.3}$	$9.15^{+18.60}_{-4.74}$	$(5.12^{+55.54}_{-4.18}) \times 10^{53}$
5542	$219.5^{+7.9}_{-7.5}$	$5.63^{+0.69}_{-0.57}$	$(4.97^{+1.54}_{-1.10}) \times 10^{53}$
5548	$165.2^{+20.8}_{-18.1}$	$1.84^{+0.44}_{-0.32}$	$(5.15^{+3.59}_{-1.94}) \times 10^{52}$
5551	$68.1^{+24.4}_{-11.6}$	$2.04^{+1.91}_{-0.56}$	$(1.01^{+3.91}_{-0.54}) \times 10^{52}$
5563	$184.1^{+10.5}_{-9.9}$	$1.16^{+0.10}_{-0.09}$	$(3.72^{+0.82}_{-0.65}) \times 10^{52}$
5567	$359.8^{+8.5}_{-8.3}$	$1.86^{+0.08}_{-0.07}$	$(2.48^{+0.26}_{-0.23}) \times 10^{53}$

Table B.1: Redshifts and luminosities estimated by E_p–L relation

Trigger Number	E_p keV	redshift	luminosity erg s^{-1}
5568	$509.3^{+19.6}_{-18.5}$	$2.71^{+0.23}_{-0.20}$	$(8.38^{+1.81}_{-1.42}) \times 10^{53}$
5571	$147.0^{+62.6}_{-49.2}$	$3.02^{+5.60}_{-1.59}$	$(8.19^{+87.14}_{-6.87}) \times 10^{52}$
5572	$189.6^{+18.3}_{-20.4}$	$2.95^{+0.71}_{-0.62}$	$(1.31^{+0.88}_{-0.57}) \times 10^{53}$
5575	$215.6^{+16.9}_{-16.0}$	$2.94^{+0.56}_{-0.44}$	$(1.69^{+0.87}_{-0.55}) \times 10^{53}$
5585	$153.2^{+29.1}_{-38.1}$	$7.00^{+8.27}_{-3.88}$	$(3.52^{+17.13}_{-2.99}) \times 10^{53}$
5593	$228.3^{+8.6}_{-8.1}$	$7.28^{+1.10}_{-0.88}$	$(8.37^{+3.20}_{-2.15}) \times 10^{53}$
5601	$279.8^{+57.1}_{-46.6}$	$5.00^{+4.69}_{-1.87}$	$(6.61^{+23.81}_{-4.44}) \times 10^{53}$
5603	$160.5^{+28.1}_{-25.7}$	$11.64^{+21.30}_{-5.78}$	$(9.65^{+86.42}_{-7.65}) \times 10^{53}$
5604	$273.6^{+22.7}_{-19.8}$	$6.07^{+2.01}_{-1.26}$	$(8.79^{+8.22}_{-3.68}) \times 10^{53}$
5606	$165.4^{+22.9}_{-36.2}$	$6.40^{+4.28}_{-3.18}$	$(3.51^{+7.84}_{-2.82}) \times 10^{53}$
5608	$202.9^{+20.7}_{-33.4}$	$8.10^{+4.36}_{-3.61}$	$(8.00^{+13.26}_{-5.97}) \times 10^{53}$
5621	$259.1^{+8.6}_{-8.1}$	$1.07^{+0.05}_{-0.05}$	$(6.74^{+0.80}_{-0.71}) \times 10^{52}$
5624	$226.4^{+49.5}_{-44.2}$	$8.18^{+14.98}_{-4.10}$	$(1.01^{+9.41}_{-0.81}) \times 10^{54}$
5628	$237.4^{+12.6}_{-12.0}$	$2.71^{+0.32}_{-0.27}$	$(1.82^{+0.57}_{-0.41}) \times 10^{53}$
5637	$154.4^{+82.1}_{-47.9}$	$4.53^{+29.95}_{-2.54}$	$(1.71^{+163.40}_{-1.47}) \times 10^{53}$
5640	$69.7^{+11.0}_{-10.0}$	$3.82^{+1.96}_{-1.14}$	$(2.65^{+4.38}_{-1.52}) \times 10^{52}$
5644	$301.9^{+16.2}_{-14.9}$	$3.32^{+0.45}_{-0.36}$	$(3.98^{+1.41}_{-0.96}) \times 10^{53}$
5645	$101.3^{+36.2}_{-50.6}$	$3.38^{+5.20}_{-2.36}$	$(4.62^{+36.04}_{-4.37}) \times 10^{52}$
5654	$255.1^{+4.7}_{-4.6}$	$3.98^{+0.20}_{-0.18}$	$(3.79^{+0.46}_{-0.40}) \times 10^{53}$
5655	$74.3^{+41.8}_{-32.8}$	$2.87^{+8.85}_{-1.81}$	$(1.94^{+49.25}_{-1.77}) \times 10^{52}$
5667	$136.4^{+45.5}_{-29.3}$	$4.02^{+6.74}_{-1.68}$	$(1.10^{+9.63}_{-0.80}) \times 10^{53}$
5697	$50.4^{+6.8}_{-6.6}$	$0.34^{+0.05}_{-0.05}$	$(1.07^{+0.42}_{-0.32}) \times 10^{51}$
5704	$175.5^{+8.2}_{-7.7}$	$1.01^{+0.07}_{-0.06}$	$(2.91^{+0.48}_{-0.41}) \times 10^{52}$
5706	$155.6^{+51.6}_{-74.3}$	$5.32^{+12.92}_{-3.94}$	$(2.27^{+35.00}_{-2.18}) \times 10^{53}$
5711	$487.4^{+18.4}_{-17.6}$	$1.95^{+0.14}_{-0.12}$	$(4.85^{+0.87}_{-0.71}) \times 10^{53}$
5713	$41.0^{+20.1}_{-13.8}$	$1.24^{+1.19}_{-0.53}$	$(1.98^{+8.35}_{-1.48}) \times 10^{51}$
5719	$186.5^{+45.8}_{-38.3}$	$7.80^{+17.10}_{-3.97}$	$(6.32^{+78.61}_{-5.11}) \times 10^{53}$
5726	$113.7^{+8.5}_{-8.1}$	$1.51^{+0.19}_{-0.16}$	$(1.90^{+0.64}_{-0.47}) \times 10^{52}$
5729	$86.0^{+14.5}_{-8.3}$	$1.55^{+0.47}_{-0.23}$	$(1.13^{+1.03}_{-0.36}) \times 10^{52}$
5731	$175.8^{+36.9}_{-20.7}$	$6.33^{+7.92}_{-2.00}$	$(3.90^{+20.79}_{-2.29}) \times 10^{53}$
5773	$182.9^{+1.7}_{-1.7}$	$1.05^{+0.01}_{-0.01}$	$(3.30^{+0.11}_{-0.10}) \times 10^{52}$
5867	$207.1^{+31.0}_{-29.4}$	$8.83^{+9.00}_{-3.67}$	$(9.74^{+37.47}_{-6.92}) \times 10^{53}$
5989	$40.3^{+11.5}_{-10.9}$	$0.15^{+0.05}_{-0.04}$	$(5.07^{+3.96}_{-2.58}) \times 10^{50}$
5995	$706.5^{+8.5}_{-8.3}$	$4.62^{+0.16}_{-0.15}$	$(3.70^{+0.31}_{-0.28}) \times 10^{54}$
6004	$48.1^{+33.3}_{-32.0}$	$1.00^{+1.33}_{-0.73}$	$(2.17^{+15.05}_{-2.07}) \times 10^{51}$
6082	$63.2^{+3.1}_{-9.4}$	$1.79^{+0.16}_{-0.41}$	$(7.28^{+1.64}_{-3.44}) \times 10^{51}$
6083	$100.6^{+7.0}_{-3.8}$	$3.42^{+0.63}_{-0.30}$	$(4.64^{+2.29}_{-0.90}) \times 10^{52}$
6090	$165.7^{+23.8}_{-20.4}$	$3.82^{+1.76}_{-1.01}$	$(1.50^{+2.16}_{-0.78}) \times 10^{53}$
6098	$113.7^{+19.0}_{-16.4}$	$5.91^{+4.81}_{-2.13}$	$(1.45^{+4.23}_{-0.94}) \times 10^{53}$
6100	$562.1^{+10.9}_{-10.7}$	$3.21^{+0.15}_{-0.14}$	$(1.32^{+0.15}_{-0.13}) \times 10^{54}$
6113	$155.5^{+21.2}_{-18.8}$	$2.12^{+0.61}_{-0.43}$	$(5.53^{+4.69}_{-2.36}) \times 10^{52}$
6124	$405.4^{+7.4}_{-7.3}$	$1.58^{+0.05}_{-0.05}$	$(2.58^{+0.19}_{-0.18}) \times 10^{53}$
6128	$38.4^{+4.4}_{-5.7}$	$0.91^{+0.14}_{-0.17}$	$(1.26^{+0.55}_{-0.51}) \times 10^{51}$

Table B.1: Redshifts and luminosities estimated by E_p–L relation

Trigger Number	E_p keV	redshift	luminosity erg s^{-1}
6141	$89.8^{+62.5}_{-38.9}$	$2.14^{+6.58}_{-1.24}$	$(1.86^{+49.49}_{-1.64}) \times 10^{52}$
6147	$85.8^{+3.3}_{-6.3}$	$3.59^{+0.35}_{-0.59}$	$(3.64^{+0.91}_{-1.26}) \times 10^{52}$
6152	$130.0^{+62.3}_{-84.6}$	$4.74^{+24.61}_{-3.99}$	$(1.31^{+78.65}_{-1.29}) \times 10^{53}$
6159	$76.3^{+3.0}_{-13.1}$	$1.74^{+0.12}_{-0.45}$	$(1.02^{+0.18}_{-0.53}) \times 10^{52}$
6167	$59.6^{+11.7}_{-6.5}$	$2.29^{+1.07}_{-0.44}$	$(9.02^{+13.66}_{-3.63}) \times 10^{51}$
6186	$45.0^{+52.8}_{-25.0}$	$0.90^{+2.48}_{-0.56}$	$(1.72^{+41.40}_{-1.55}) \times 10^{51}$
6190	$88.9^{+48.6}_{-27.5}$	$2.48^{+5.70}_{-1.17}$	$(2.24^{+35.08}_{-1.77}) \times 10^{52}$
6194	$136.2^{+19.5}_{-18.4}$	$4.39^{+2.24}_{-1.33}$	$(1.26^{+2.05}_{-0.73}) \times 10^{53}$
6198	$361.4^{+11.5}_{-9.8}$	$0.91^{+0.04}_{-0.03}$	$(1.12^{+0.12}_{-0.10}) \times 10^{53}$
6206	$46.6^{+3.6}_{-3.9}$	$0.90^{+0.10}_{-0.10}$	$(1.84^{+0.51}_{-0.45}) \times 10^{51}$
6216	$108.4^{+15.9}_{-7.4}$	$3.30^{+1.39}_{-0.49}$	$(5.09^{+6.62}_{-1.62}) \times 10^{52}$
6222	$51.9^{+25.1}_{-28.5}$	$1.62^{+1.90}_{-1.07}$	$(4.34^{+24.12}_{-4.03}) \times 10^{51}$
6226	$206.1^{+24.0}_{-38.6}$	$6.74^{+3.73}_{-3.08}$	$(5.98^{+10.39}_{-4.54}) \times 10^{53}$
6235	$388.5^{+11.7}_{-11.2}$	$3.77^{+0.30}_{-0.26}$	$(8.04^{+1.60}_{-1.27}) \times 10^{53}$
6241	$98.9^{+20.3}_{-34.1}$	$1.88^{+0.80}_{-0.89}$	$(1.90^{+2.62}_{-1.51}) \times 10^{52}$
6266	$208.1^{+66.1}_{-70.6}$	$3.14^{+3.68}_{-1.69}$	$(1.74^{+9.03}_{-1.47}) \times 10^{53}$
6272	$61.9^{+1.2}_{-1.4}$	$1.22^{+0.04}_{-0.04}$	$(4.41^{+0.33}_{-0.35}) \times 10^{51}$
6273	$113.5^{+31.6}_{-31.6}$	$5.96^{+11.70}_{-3.37}$	$(1.47^{+15.74}_{-1.26}) \times 10^{53}$
6274	$184.0^{+9.6}_{-8.9}$	$1.11^{+0.08}_{-0.07}$	$(3.52^{+0.69}_{-0.55}) \times 10^{52}$
6280	$121.3^{+24.7}_{-18.3}$	$4.00^{+3.03}_{-1.27}$	$(8.63^{+23.66}_{-5.17}) \times 10^{52}$
6285	$41.4^{+13.6}_{-27.4}$	$1.12^{+0.62}_{-0.82}$	$(1.81^{+3.50}_{-1.73}) \times 10^{51}$
6288	$32.1^{+28.4}_{-3.4}$	$0.54^{+0.69}_{-0.07}$	$(5.72^{+36.85}_{-1.53}) \times 10^{50}$
6295	$84.5^{+7.1}_{-5.9}$	$1.60^{+0.23}_{-0.17}$	$(1.13^{+0.45}_{-0.28}) \times 10^{52}$
6303	$194.1^{+12.2}_{-11.3}$	$4.06^{+0.74}_{-0.57}$	$(2.26^{+1.09}_{-0.68}) \times 10^{53}$
6304	$128.8^{+33.3}_{-48.4}$	$7.01^{+14.70}_{-4.87}$	$(2.49^{+29.27}_{-2.35}) \times 10^{53}$
6309	$33.1^{+43.6}_{-21.9}$	$0.95^{+3.40}_{-0.68}$	$(9.75^{+384.32}_{-9.29}) \times 10^{50}$
6315	$99.0^{+10.4}_{-9.5}$	$2.67^{+0.66}_{-0.48}$	$(3.10^{+2.17}_{-1.19}) \times 10^{52}$
6317	$88.8^{+30.1}_{-39.6}$	$5.85^{+17.28}_{-4.26}$	$(8.68^{+184.54}_{-8.30}) \times 10^{52}$
6319	$113.4^{+36.0}_{-42.4}$	$7.39^{+27.70}_{-5.19}$	$(2.13^{+66.09}_{-2.01}) \times 10^{53}$
6320	$72.7^{+13.8}_{-23.6}$	$1.23^{+0.38}_{-0.50}$	$(6.17^{+5.79}_{-4.48}) \times 10^{51}$
6321	$154.0^{+13.3}_{-12.3}$	$3.02^{+0.65}_{-0.49}$	$(8.98^{+5.31}_{-3.12}) \times 10^{52}$
6322	$83.8^{+21.6}_{-19.6}$	$1.47^{+0.71}_{-0.47}$	$(1.01^{+1.64}_{-0.62}) \times 10^{52}$
6323	$95.3^{+11.1}_{-13.6}$	$5.61^{+2.68}_{-1.96}$	$(9.33^{+13.67}_{-5.93}) \times 10^{52}$
6329	$229.8^{+5.7}_{-5.5}$	$3.16^{+0.18}_{-0.17}$	$(2.14^{+0.31}_{-0.26}) \times 10^{53}$
6335	$147.9^{+13.1}_{-11.7}$	$2.25^{+0.41}_{-0.32}$	$(5.41^{+2.74}_{-1.67}) \times 10^{52}$
6344	$59.1^{+47.0}_{-33.0}$	$1.13^{+2.02}_{-0.72}$	$(3.70^{+41.73}_{-3.39}) \times 10^{51}$
6349	$111.9^{+79.4}_{-54.9}$	$2.16^{+7.11}_{-1.38}$	$(2.94^{+87.81}_{-2.70}) \times 10^{52}$
6351	$45.8^{+5.4}_{-6.5}$	$0.95^{+0.16}_{-0.17}$	$(1.87^{+0.85}_{-0.73}) \times 10^{51}$
6353	$281.4^{+43.0}_{-47.3}$	$10.20^{+12.43}_{-5.00}$	$(2.33^{+11.45}_{-1.83}) \times 10^{54}$
6369	$56.5^{+35.2}_{-29.3}$	$1.80^{+3.52}_{-1.15}$	$(5.85^{+72.83}_{-5.39}) \times 10^{51}$
6397	$198.7^{+5.5}_{-5.3}$	$2.39^{+0.13}_{-0.12}$	$(1.07^{+0.15}_{-0.13}) \times 10^{53}$
6399	$36.5^{+43.4}_{-21.3}$	$0.81^{+2.04}_{-0.52}$	$(1.03^{+21.15}_{-0.93}) \times 10^{51}$
6404	$175.5^{+5.2}_{-5.1}$	$0.96^{+0.04}_{-0.04}$	$(2.77^{+0.28}_{-0.26}) \times 10^{52}$

Table B.1: Redshifts and luminosities estimated by E_p–L relation

Trigger Number	E_p keV	redshift	luminosity erg s^{-1}
6405	$85.7^{+28.0}_{-18.1}$	$4.31^{+7.57}_{-1.83}$	$(4.86^{+45.41}_{-3.56}) \times 10^{52}$
6413	$61.0^{+9.6}_{-10.0}$	$0.93^{+0.21}_{-0.19}$	$(3.25^{+2.09}_{-1.41}) \times 10^{51}$
6422	$68.4^{+1.5}_{-1.4}$	$0.70^{+0.02}_{-0.02}$	$(3.17^{+0.22}_{-0.19}) \times 10^{51}$
6436	$156.5^{+47.3}_{-43.4}$	$2.05^{+1.52}_{-0.84}$	$(5.35^{+15.03}_{-3.88}) \times 10^{52}$
6440	$47.7^{+12.5}_{-10.4}$	$0.72^{+0.25}_{-0.18}$	$(1.57^{+1.72}_{-0.80}) \times 10^{51}$
6453	$118.1^{+6.8}_{-6.4}$	$1.61^{+0.16}_{-0.14}$	$(2.22^{+0.58}_{-0.44}) \times 10^{52}$
6472	$470.2^{+46.2}_{-42.2}$	$3.18^{+0.82}_{-0.59}$	$(9.06^{+6.57}_{-3.51}) \times 10^{53}$
6489	$123.9^{+1.4}_{-1.4}$	$3.95^{+0.12}_{-0.12}$	$(8.81^{+0.65}_{-0.60}) \times 10^{52}$
6504	$154.8^{+4.0}_{-4.0}$	$1.67^{+0.07}_{-0.07}$	$(4.00^{+0.44}_{-0.41}) \times 10^{52}$
6521	$133.4^{+24.3}_{-25.7}$	$7.15^{+8.07}_{-3.39}$	$(2.78^{+12.59}_{-2.16}) \times 10^{53}$
6522	$98.1^{+21.4}_{-83.0}$	$1.47^{+0.59}_{-1.31}$	$(1.38^{+1.76}_{-1.37}) \times 10^{52}$
6523	$92.4^{+58.6}_{-27.5}$	$1.48^{+2.40}_{-0.59}$	$(1.23^{+11.51}_{-0.88}) \times 10^{52}$
6525	$349.9^{+25.2}_{-36.6}$	$10.19^{+4.18}_{-3.60}$	$(3.60^{+4.21}_{-2.27}) \times 10^{54}$
6528	$222.4^{+16.1}_{-15.3}$	$7.83^{+2.66}_{-1.76}$	$(9.04^{+8.56}_{-4.01}) \times 10^{53}$
6531	$66.2^{+4.7}_{-5.0}$	$3.13^{+0.55}_{-0.49}$	$(1.76^{+0.83}_{-0.59}) \times 10^{52}$
6538	$48.6^{+6.9}_{-10.1}$	$0.83^{+0.16}_{-0.21}$	$(1.86^{+1.01}_{-0.94}) \times 10^{51}$
6539	$310.4^{+64.2}_{-76.9}$	$4.10^{+3.26}_{-1.92}$	$(5.89^{+17.14}_{-4.59}) \times 10^{53}$
6546	$73.6^{+3.6}_{-3.6}$	$1.55^{+0.13}_{-0.12}$	$(8.30^{+1.75}_{-1.48}) \times 10^{51}$
6552	$36.7^{+15.0}_{-22.8}$	$1.05^{+0.73}_{-0.72}$	$(1.32^{+3.50}_{-1.25}) \times 10^{51}$
6554	$69.3^{+10.8}_{-9.8}$	$1.71^{+0.50}_{-0.37}$	$(8.26^{+7.24}_{-3.72}) \times 10^{51}$
6560	$177.9^{+4.0}_{-3.9}$	$2.46^{+0.11}_{-0.11}$	$(8.89^{+1.02}_{-0.90}) \times 10^{52}$
6564	$117.0^{+21.3}_{-17.5}$	$5.79^{+5.26}_{-2.12}$	$(1.48^{+5.04}_{-0.98}) \times 10^{53}$
6578	$107.2^{+54.3}_{-60.7}$	$3.77^{+14.34}_{-2.88}$	$(6.12^{+217.26}_{-5.94}) \times 10^{52}$
6582	$69.6^{+53.9}_{-47.9}$	$1.72^{+4.83}_{-1.35}$	$(8.42^{+195.73}_{-8.21}) \times 10^{51}$
6583	$90.4^{+4.9}_{-4.2}$	$6.67^{+1.45}_{-0.98}$	$(1.13^{+0.64}_{-0.35}) \times 10^{53}$
6585	$48.2^{+41.4}_{-28.4}$	$0.81^{+1.25}_{-0.52}$	$(1.78^{+15.83}_{-1.63}) \times 10^{51}$
6587	$326.5^{+4.4}_{-4.6}$	$1.07^{+0.02}_{-0.02}$	$(1.07^{+0.05}_{-0.05}) \times 10^{53}$
6593	$261.4^{+5.7}_{-5.6}$	$2.40^{+0.11}_{-0.10}$	$(1.86^{+0.20}_{-0.18}) \times 10^{53}$
6598	$73.2^{+24.2}_{-8.6}$	$1.90^{+1.50}_{-0.36}$	$(1.06^{+3.25}_{-0.42}) \times 10^{52}$
6601	$39.3^{+49.2}_{-22.5}$	$0.82^{+2.28}_{-0.52}$	$(1.20^{+29.77}_{-1.09}) \times 10^{51}$
6605	$117.9^{+8.9}_{-8.6}$	$2.86^{+0.51}_{-0.42}$	$(4.86^{+2.35}_{-1.54}) \times 10^{52}$
6610	$72.4^{+5.5}_{-4.4}$	$1.95^{+0.28}_{-0.20}$	$(1.07^{+0.42}_{-0.25}) \times 10^{52}$
6611	$112.3^{+43.5}_{-25.8}$	$3.50^{+6.53}_{-1.47}$	$(5.98^{+63.28}_{-4.37}) \times 10^{52}$
6621	$115.4^{+13.2}_{-10.9}$	$0.97^{+0.16}_{-0.12}$	$(1.22^{+0.55}_{-0.34}) \times 10^{52}$
6625	$81.7^{+7.9}_{-7.4}$	$2.18^{+0.43}_{-0.34}$	$(1.58^{+0.88}_{-0.54}) \times 10^{52}$
6629	$419.2^{+95.7}_{-77.4}$	$8.69^{+18.91}_{-4.29}$	$(3.87^{+47.02}_{-3.07}) \times 10^{54}$
6630	$288.4^{+5.3}_{-5.2}$	$1.90^{+0.06}_{-0.06}$	$(1.65^{+0.14}_{-0.12}) \times 10^{53}$
6631	$92.7^{+35.2}_{-33.5}$	$2.74^{+3.71}_{-1.49}$	$(2.83^{+18.48}_{-2.41}) \times 10^{52}$
6641	$42.5^{+42.0}_{-21.3}$	$0.91^{+1.89}_{-0.52}$	$(1.55^{+22.67}_{-1.34}) \times 10^{51}$
6649	$87.1^{+21.9}_{-33.8}$	$6.65^{+12.29}_{-4.64}$	$(1.04^{+10.03}_{-0.98}) \times 10^{53}$
6657	$93.8^{+34.2}_{-41.7}$	$3.03^{+4.28}_{-1.93}$	$(3.36^{+23.20}_{-3.07}) \times 10^{52}$
6666	$88.5^{+42.0}_{-49.0}$	$4.82^{+25.14}_{-3.78}$	$(6.23^{+377.00}_{-6.08}) \times 10^{52}$
6672	$116.2^{+15.9}_{-15.4}$	$1.35^{+0.31}_{-0.26}$	$(1.75^{+1.14}_{-0.71}) \times 10^{52}$

Table B.1: Redshifts and luminosities estimated by E_p–L relation

Trigger Number	E_p keV	redshift	luminosity erg s^{-1}
6683	$188.3^{+15.7}_{-14.9}$	$5.40^{+1.65}_{-1.14}$	$(3.41^{+2.92}_{-1.46}) \times 10^{53}$
6762	$129.6^{+36.7}_{-39.0}$	$6.31^{+13.92}_{-3.80}$	$(2.11^{+27.16}_{-1.87}) \times 10^{53}$
6763	$155.0^{+32.4}_{-21.2}$	$3.54^{+2.50}_{-0.99}$	$(1.16^{+2.92}_{-0.63}) \times 10^{53}$
6767	$88.9^{+32.7}_{-46.3}$	$3.86^{+7.40}_{-2.83}$	$(4.38^{+47.81}_{-4.21}) \times 10^{52}$
6802	$123.1^{+36.1}_{-40.8}$	$3.60^{+4.26}_{-1.97}$	$(7.51^{+39.12}_{-6.42}) \times 10^{52}$
6814	$197.6^{+28.0}_{-23.8}$	$4.19^{+2.03}_{-1.13}$	$(2.47^{+3.76}_{-1.30}) \times 10^{53}$
6816	$85.3^{+3.5}_{-6.9}$	$0.87^{+0.05}_{-0.09}$	$(5.97^{+0.84}_{-1.39}) \times 10^{51}$
6830	$93.6^{+28.0}_{-18.1}$	$7.36^{+23.36}_{-3.53}$	$(1.43^{+33.44}_{-1.12}) \times 10^{53}$
6877	$143.8^{+11.2}_{-12.6}$	$7.44^{+2.66}_{-1.99}$	$(3.46^{+3.48}_{-1.78}) \times 10^{53}$
6882	$44.7^{+35.8}_{-50.1}$	$1.14^{+2.09}_{-1.04}$	$(2.15^{+25.10}_{-2.14}) \times 10^{51}$
6892	$196.8^{+58.0}_{-61.2}$	$5.42^{+10.52}_{-3.19}$	$(3.74^{+39.94}_{-3.30}) \times 10^{53}$
6904	$1206.0^{+32.8}_{-31.5}$	$4.14^{+0.31}_{-0.28}$	$(9.03^{+1.69}_{-1.36}) \times 10^{54}$
6917	$153.0^{+27.7}_{-29.3}$	$2.27^{+0.95}_{-0.71}$	$(5.86^{+7.77}_{-3.51}) \times 10^{52}$
6930	$100.4^{+7.4}_{-6.9}$	$1.02^{+0.11}_{-0.09}$	$(9.70^{+2.72}_{-2.04}) \times 10^{51}$
6963	$199.3^{+36.8}_{-29.7}$	$1.05^{+0.29}_{-0.20}$	$(3.91^{+3.27}_{-1.61}) \times 10^{52}$
7012	$300.4^{+5.1}_{-4.9}$	$1.64^{+0.05}_{-0.04}$	$(1.48^{+0.10}_{-0.10}) \times 10^{53}$
7028	$208.2^{+20.7}_{-17.8}$	$1.07^{+0.16}_{-0.12}$	$(4.38^{+1.74}_{-1.14}) \times 10^{52}$
7030	$52.2^{+29.4}_{-23.8}$	$1.25^{+1.48}_{-0.69}$	$(3.24^{+18.51}_{-2.78}) \times 10^{51}$
7087	$197.3^{+57.4}_{-48.7}$	$7.14^{+20.09}_{-3.96}$	$(6.05^{+115.22}_{-5.14}) \times 10^{53}$
7207	$136.8^{+41.7}_{-31.0}$	$7.23^{+23.49}_{-3.82}$	$(2.98^{+72.29}_{-2.47}) \times 10^{53}$
7209	$81.9^{+37.1}_{-13.7}$	$1.56^{+1.61}_{-0.38}$	$(1.03^{+4.74}_{-0.51}) \times 10^{52}$
7213	$72.5^{+19.3}_{-31.4}$	$3.60^{+3.68}_{-2.35}$	$(2.61^{+10.95}_{-2.41}) \times 10^{52}$
7228	$175.8^{+26.8}_{-21.6}$	$3.22^{+1.40}_{-0.79}$	$(1.29^{+1.75}_{-0.63}) \times 10^{53}$
7230	$190.1^{+37.4}_{-27.8}$	$10.08^{+19.57}_{-4.49}$	$(1.04^{+10.37}_{-0.77}) \times 10^{54}$
7240	$612.0^{+101.8}_{-98.1}$	$11.48^{+18.71}_{-5.68}$	$(1.37^{+10.26}_{-1.08}) \times 10^{55}$
7250	$134.6^{+12.3}_{-11.1}$	$3.30^{+0.80}_{-0.57}$	$(7.85^{+5.33}_{-2.88}) \times 10^{52}$
7255	$240.5^{+23.5}_{-21.8}$	$3.98^{+1.19}_{-0.82}$	$(3.37^{+2.85}_{-1.43}) \times 10^{53}$
7263	$41.9^{+54.3}_{-31.6}$	$0.81^{+2.34}_{-0.64}$	$(1.34^{+36.03}_{-1.31}) \times 10^{51}$
7285	$93.1^{+36.7}_{-33.9}$	$2.05^{+2.20}_{-1.04}$	$(1.89^{+9.02}_{-1.56}) \times 10^{52}$
7293	$186.5^{+17.9}_{-16.1}$	$8.48^{+4.35}_{-2.38}$	$(7.33^{+11.42}_{-3.89}) \times 10^{53}$
7295	$353.4^{+16.9}_{-15.7}$	$5.65^{+0.95}_{-0.73}$	$(1.30^{+0.56}_{-0.36}) \times 10^{54}$
7298	$141.4^{+42.7}_{-15.1}$	$7.35^{+23.97}_{-2.29}$	$(3.27^{+79.81}_{-1.90}) \times 10^{53}$
7301	$564.8^{+10.6}_{-10.3}$	$1.10^{+0.03}_{-0.03}$	$(3.31^{+0.23}_{-0.20}) \times 10^{53}$
7319	$164.9^{+37.4}_{-26.6}$	$5.75^{+7.39}_{-2.22}$	$(2.91^{+16.29}_{-1.98}) \times 10^{53}$
7323	$96.4^{+40.1}_{-43.2}$	$5.42^{+24.31}_{-3.91}$	$(8.99^{+404.36}_{-8.57}) \times 10^{52}$
7328	$103.4^{+28.1}_{-10.9}$	$6.92^{+15.93}_{-2.08}$	$(1.57^{+21.53}_{-0.89}) \times 10^{53}$
7374	$193.4^{+8.3}_{-6.8}$	$2.90^{+0.28}_{-0.21}$	$(1.34^{+0.34}_{-0.22}) \times 10^{53}$
7390	$254.4^{+18.8}_{-17.1}$	$11.28^{+5.17}_{-2.95}$	$(2.29^{+3.04}_{-1.14}) \times 10^{54}$
7403	$144.8^{+25.7}_{-22.6}$	$10.02^{+15.75}_{-4.65}$	$(5.98^{+42.94}_{-4.56}) \times 10^{53}$
7429	$223.5^{+9.2}_{-8.7}$	$9.50^{+1.91}_{-1.43}$	$(1.29^{+0.66}_{-0.40}) \times 10^{54}$
7446	$138.8^{+15.3}_{-14.4}$	$1.40^{+0.26}_{-0.21}$	$(2.60^{+1.32}_{-0.86}) \times 10^{52}$
7452	$90.8^{+21.2}_{-167.4}$	$4.14^{+3.95}_{-1.38}$	$(5.10^{+19.22}_{-3.16}) \times 10^{52}$
7464	$367.2^{+92.9}_{-126.1}$	$6.61^{+12.29}_{-4.33}$	$(1.83^{+17.84}_{-1.69}) \times 10^{54}$

Table B.1: Redshifts and luminosities estimated by E_p–L relation

Trigger Number	E_p keV	redshift	luminosity erg s^{-1}
7469	$67.5^{+39.6}_{-24.6}$	$1.08^{+1.20}_{-0.48}$	$(4.63^{+24.34}_{-3.52}) \times 10^{51}$
7475	$149.4^{+14.9}_{-13.1}$	$1.93^{+0.37}_{-0.28}$	$(4.50^{+2.41}_{-1.44}) \times 10^{52}$
7477	$232.2^{+35.5}_{-29.7}$	$5.65^{+3.90}_{-1.81}$	$(5.59^{+13.10}_{-3.34}) \times 10^{53}$
7481	$114.9^{+32.3}_{-54.5}$	$3.59^{+3.98}_{-2.47}$	$(6.53^{+30.82}_{-6.14}) \times 10^{52}$
7487	$79.2^{+7.4}_{-7.0}$	$2.34^{+0.47}_{-0.37}$	$(1.64^{+0.91}_{-0.56}) \times 10^{52}$
7491	$428.6^{+6.1}_{-6.0}$	$2.03^{+0.05}_{-0.05}$	$(3.94^{+0.26}_{-0.24}) \times 10^{53}$
7494	$111.0^{+16.1}_{-14.9}$	$4.69^{+2.57}_{-1.45}$	$(9.36^{+16.51}_{-5.46}) \times 10^{52}$
7497	$133.0^{+16.0}_{-19.7}$	$5.76^{+2.92}_{-2.09}$	$(1.89^{+2.98}_{-1.24}) \times 10^{53}$
7502	$110.2^{+47.0}_{-41.3}$	$3.69^{+9.00}_{-2.21}$	$(6.26^{+102.51}_{-5.57}) \times 10^{52}$
7503	$198.2^{+13.5}_{-12.8}$	$3.68^{+0.69}_{-0.54}$	$(2.02^{+1.01}_{-0.64}) \times 10^{53}$
7504	$116.6^{+21.9}_{-22.4}$	$4.07^{+2.80}_{-1.57}$	$(8.20^{+19.72}_{-5.65}) \times 10^{52}$
7515	$221.2^{+13.0}_{-12.0}$	$5.44^{+1.12}_{-0.83}$	$(4.76^{+2.61}_{-1.53}) \times 10^{53}$
7527	$400.7^{+9.9}_{-9.6}$	$3.80^{+0.25}_{-0.22}$	$(8.69^{+1.39}_{-1.16}) \times 10^{53}$
7528	$70.7^{+31.2}_{-45.8}$	$2.61^{+4.33}_{-2.05}$	$(1.53^{+13.85}_{-1.49}) \times 10^{52}$
7529	$177.8^{+11.5}_{-10.6}$	$2.38^{+0.32}_{-0.26}$	$(8.47^{+3.05}_{-2.10}) \times 10^{52}$
7530	$146.9^{+6.4}_{-6.2}$	$1.28^{+0.09}_{-0.08}$	$(2.63^{+0.45}_{-0.38}) \times 10^{52}$
7548	$184.2^{+21.2}_{-17.6}$	$5.57^{+2.59}_{-1.40}$	$(3.44^{+4.87}_{-1.70}) \times 10^{53}$
7550	$120.4^{+21.6}_{-16.1}$	$2.03^{+0.78}_{-0.44}$	$(3.12^{+3.76}_{-1.42}) \times 10^{52}$
7551	$71.1^{+35.0}_{-14.7}$	$2.08^{+3.20}_{-0.67}$	$(1.12^{+9.29}_{-0.69}) \times 10^{52}$
7564	$82.1^{+3.4}_{-5.7}$	$2.10^{+0.16}_{-0.25}$	$(1.53^{+0.31}_{-0.41}) \times 10^{52}$
7566	$40.7^{+8.6}_{-11.1}$	$1.07^{+0.35}_{-0.37}$	$(1.66^{+1.66}_{-1.07}) \times 10^{51}$
7567	$68.9^{+5.3}_{-5.8}$	$1.82^{+0.25}_{-0.25}$	$(8.84^{+3.33}_{-2.66}) \times 10^{51}$
7568	$49.4^{+25.8}_{-25.6}$	$1.84^{+2.74}_{-1.19}$	$(4.61^{+36.68}_{-4.25}) \times 10^{51}$
7573	$52.2^{+16.2}_{-23.8}$	$0.96^{+0.46}_{-0.51}$	$(2.45^{+3.96}_{-2.05}) \times 10^{51}$
7575	$467.9^{+6.2}_{-6.1}$	$2.82^{+0.08}_{-0.08}$	$(7.51^{+0.54}_{-0.50}) \times 10^{53}$
7579	$31.3^{+32.8}_{-25.3}$	$0.74^{+1.40}_{-0.62}$	$(6.94^{+87.92}_{-6.83}) \times 10^{50}$
7588	$74.7^{+2.6}_{-11.5}$	$1.44^{+0.08}_{-0.32}$	$(7.79^{+1.12}_{-3.57}) \times 10^{51}$
7598	$109.3^{+15.6}_{-15.0}$	$2.34^{+0.75}_{-0.55}$	$(3.12^{+2.99}_{-1.50}) \times 10^{52}$
7603	$93.6^{+20.2}_{-39.2}$	$2.31^{+1.21}_{-1.33}$	$(2.24^{+3.94}_{-1.97}) \times 10^{52}$
7605	$136.2^{+27.1}_{-17.3}$	$4.06^{+3.02}_{-1.13}$	$(1.12^{+2.97}_{-0.60}) \times 10^{53}$
7607	$60.9^{+4.0}_{-5.0}$	$0.95^{+0.09}_{-0.10}$	$(3.29^{+0.79}_{-0.80}) \times 10^{51}$
7608	$92.4^{+23.9}_{-20.1}$	$7.33^{+16.46}_{-3.79}$	$(1.39^{+18.13}_{-1.14}) \times 10^{53}$
7630	$127.2^{+24.2}_{-31.1}$	$4.09^{+2.88}_{-1.89}$	$(9.85^{+24.37}_{-7.63}) \times 10^{52}$
7638	$66.8^{+3.3}_{-3.3}$	$1.74^{+0.15}_{-0.14}$	$(7.83^{+1.79}_{-1.45}) \times 10^{51}$
7645	$70.7^{+15.9}_{-25.8}$	$2.54^{+1.51}_{-1.36}$	$(1.47^{+3.01}_{-1.24}) \times 10^{52}$
7657	$74.7^{+2.7}_{-2.9}$	$1.03^{+0.05}_{-0.05}$	$(5.41^{+0.70}_{-0.67}) \times 10^{51}$
7677	$73.4^{+7.3}_{-17.7}$	$2.07^{+0.41}_{-0.76}$	$(1.19^{+0.66}_{-0.80}) \times 10^{52}$
7678	$323.5^{+7.4}_{-7.2}$	$2.96^{+0.15}_{-0.14}$	$(3.86^{+0.50}_{-0.43}) \times 10^{53}$
7688	$258.0^{+30.9}_{-27.6}$	$5.73^{+2.87}_{-1.60}$	$(7.07^{+10.98}_{-3.80}) \times 10^{53}$
7695	$871.4^{+42.4}_{-39.8}$	$6.32^{+1.17}_{-0.89}$	$(9.56^{+4.57}_{-2.84}) \times 10^{54}$
7701	$185.3^{+33.6}_{-29.8}$	$9.09^{+13.18}_{-4.16}$	$(8.20^{+52.62}_{-6.20}) \times 10^{53}$
7703	$174.6^{+81.4}_{-54.4}$	$3.82^{+12.03}_{-2.04}$	$(1.66^{+41.97}_{-1.40}) \times 10^{53}$
7705	$44.3^{+59.0}_{-31.1}$	$0.98^{+3.72}_{-0.74}$	$(1.80^{+79.57}_{-1.74}) \times 10^{51}$

Table B.1: Redshifts and luminosities estimated by E_p–L relation

Trigger Number	E_p keV	redshift	luminosity erg s^{-1}
7707	$62.8^{+37.2}_{-34.2}$	$2.87^{+9.96}_{-2.06}$	$(1.39^{+43.50}_{-1.33}) \times 10^{52}$
7711	$206.6^{+11.4}_{-10.9}$	$5.15^{+0.96}_{-0.74}$	$(3.79^{+1.85}_{-1.16}) \times 10^{53}$
7727	$126.6^{+12.3}_{-14.4}$	$4.00^{+1.18}_{-1.00}$	$(9.40^{+7.91}_{-4.69}) \times 10^{52}$
7744	$79.5^{+2.4}_{-2.7}$	$1.85^{+0.10}_{-0.11}$	$(1.20^{+0.16}_{-0.16}) \times 10^{52}$
7750	$90.9^{+74.0}_{-37.4}$	$2.08^{+8.90}_{-1.16}$	$(1.84^{+89.71}_{-1.59}) \times 10^{52}$
7762	$103.9^{+16.3}_{-30.3}$	$2.83^{+1.17}_{-1.33}$	$(3.72^{+4.76}_{-2.93}) \times 10^{52}$
7769	$120.1^{+43.8}_{-31.4}$	$3.33^{+5.23}_{-1.51}$	$(6.34^{+51.18}_{-4.87}) \times 10^{52}$
7770	$121.9^{+51.1}_{-37.6}$	$2.48^{+3.53}_{-1.16}$	$(4.21^{+30.22}_{-3.32}) \times 10^{52}$
7781	$121.2^{+12.4}_{-11.3}$	$1.76^{+0.33}_{-0.26}$	$(2.61^{+1.36}_{-0.85}) \times 10^{52}$
7785	$148.3^{+8.8}_{-4.3}$	$4.24^{+0.75}_{-0.31}$	$(1.41^{+0.66}_{-0.24}) \times 10^{53}$
7786	$101.9^{+31.4}_{-49.8}$	$1.19^{+0.63}_{-0.69}$	$(1.17^{+2.14}_{-1.02}) \times 10^{52}$
7788	$244.4^{+28.4}_{-31.8}$	$10.08^{+7.86}_{-4.15}$	$(1.72^{+4.54}_{-1.21}) \times 10^{54}$
7803	$97.5^{+7.0}_{-6.7}$	$2.98^{+0.52}_{-0.42}$	$(3.54^{+1.64}_{-1.08}) \times 10^{52}$
7818	$178.8^{+38.9}_{-52.0}$	$8.79^{+17.56}_{-5.66}$	$(7.19^{+76.01}_{-6.55}) \times 10^{53}$
7822	$96.7^{+10.8}_{-10.4}$	$1.57^{+0.31}_{-0.26}$	$(1.44^{+0.79}_{-0.51}) \times 10^{52}$
7831	$92.3^{+43.7}_{-44.1}$	$3.03^{+6.94}_{-2.03}$	$(3.26^{+49.05}_{-3.04}) \times 10^{52}$
7840	$172.1^{+8.5}_{-8.1}$	$6.56^{+1.26}_{-0.97}$	$(3.97^{+1.98}_{-1.23}) \times 10^{53}$
7841	$109.2^{+56.8}_{-49.1}$	$2.38^{+4.74}_{-1.46}$	$(3.20^{+39.51}_{-2.89}) \times 10^{52}$
7845	$448.6^{+103.4}_{-92.8}$	$10.90^{+34.18}_{-6.18}$	$(6.68^{+145.13}_{-5.71}) \times 10^{54}$
7858	$96.4^{+2.5}_{-2.6}$	$1.67^{+0.07}_{-0.07}$	$(1.55^{+0.17}_{-0.16}) \times 10^{52}$
7868	$214.8^{+56.9}_{-32.1}$	$8.98^{+29.20}_{-3.89}$	$(1.08^{+25.51}_{-0.79}) \times 10^{54}$
7886	$126.8^{+7.1}_{-62.1}$	$4.45^{+0.75}_{-3.24}$	$(1.12^{+0.50}_{-1.07}) \times 10^{53}$
7929	$684.4^{+83.7}_{-70.9}$	$9.94^{+8.28}_{-3.45}$	$(1.32^{+3.80}_{-0.82}) \times 10^{55}$
7932	$140.8^{+20.4}_{-16.2}$	$3.51^{+1.53}_{-0.84}$	$(9.47^{+12.78}_{-4.56}) \times 10^{52}$
7934	$45.4^{+40.8}_{-39.5}$	$1.42^{+4.10}_{-1.29}$	$(2.82^{+71.22}_{-2.81}) \times 10^{51}$
7938	$149.1^{+38.8}_{-30.3}$	$8.51^{+24.17}_{-4.43}$	$(4.72^{+89.27}_{-3.86}) \times 10^{53}$
7954	$244.2^{+5.4}_{-5.3}$	$0.97^{+0.03}_{-0.03}$	$(5.41^{+0.41}_{-0.38}) \times 10^{52}$
7969	$83.2^{+11.5}_{-6.1}$	$1.36^{+0.31}_{-0.15}$	$(9.00^{+5.92}_{-2.19}) \times 10^{51}$
7976	$171.6^{+2.4}_{-2.0}$	$2.35^{+0.07}_{-0.05}$	$(7.75^{+0.54}_{-0.41}) \times 10^{52}$
7987	$292.0^{+20.0}_{-17.8}$	$2.80^{+0.44}_{-0.34}$	$(2.88^{+1.23}_{-0.78}) \times 10^{53}$
7992	$23.0^{+33.4}_{-3.3}$	$0.60^{+1.57}_{-0.10}$	$(3.18^{+71.91}_{-1.12}) \times 10^{50}$
7994	$274.0^{+5.6}_{-5.5}$	$7.38^{+0.59}_{-0.52}$	$(1.24^{+0.24}_{-0.19}) \times 10^{54}$
7998	$90.6^{+2.3}_{-3.1}$	$1.42^{+0.06}_{-0.07}$	$(1.13^{+0.11}_{-0.14}) \times 10^{52}$
8001	$136.1^{+6.6}_{-6.4}$	$8.21^{+1.81}_{-1.36}$	$(3.69^{+2.11}_{-1.26}) \times 10^{53}$
8004	$74.9^{+24.0}_{-13.3}$	$0.99^{+0.50}_{-0.22}$	$(5.22^{+9.02}_{-2.44}) \times 10^{51}$
8008	$529.5^{+9.3}_{-9.1}$	$5.86^{+0.35}_{-0.32}$	$(3.09^{+0.44}_{-0.37}) \times 10^{54}$
8012	$93.9^{+46.2}_{-48.3}$	$3.84^{+14.01}_{-2.80}$	$(4.85^{+158.89}_{-4.65}) \times 10^{52}$
8019	$95.9^{+3.6}_{-3.5}$	$1.62^{+0.10}_{-0.10}$	$(1.48^{+0.24}_{-0.21}) \times 10^{52}$
8022	$136.0^{+25.3}_{-23.8}$	$1.70^{+0.61}_{-0.44}$	$(3.15^{+3.51}_{-1.65}) \times 10^{52}$
8026	$70.0^{+34.1}_{-41.3}$	$3.03^{+7.38}_{-2.30}$	$(1.87^{+31.24}_{-1.81}) \times 10^{52}$
8030	$166.7^{+13.7}_{-13.1}$	$3.14^{+0.65}_{-0.51}$	$(1.12^{+0.64}_{-0.39}) \times 10^{53}$
8036	$106.7^{+4.9}_{-4.8}$	$3.65^{+0.44}_{-0.38}$	$(5.79^{+1.80}_{-1.35}) \times 10^{52}$
8049	$23.3^{+45.6}_{-15.4}$	$0.46^{+1.55}_{-0.31}$	$(2.70^{+97.79}_{-2.51}) \times 10^{50}$

Table B.1: Redshifts and luminosities estimated by E_p–L relation

Trigger Number	E_p keV	redshift	luminosity erg s^{-1}
8050	$81.7^{+3.2}_{-3.2}$	$1.49^{+0.10}_{-0.09}$	$(9.74^{+1.61}_{-1.38}) \times 10^{51}$
8059	$62.7^{+39.2}_{-28.8}$	$1.25^{+1.72}_{-0.69}$	$(4.68^{+33.74}_{-4.02}) \times 10^{51}$
8063	$260.7^{+47.3}_{-43.4}$	$7.41^{+8.59}_{-3.22}$	$(1.13^{+5.30}_{-0.83}) \times 10^{54}$
8064	$61.9^{+5.0}_{-19.6}$	$2.36^{+0.41}_{-1.11}$	$(1.01^{+0.48}_{-0.80}) \times 10^{52}$
8066	$83.5^{+19.1}_{-63.4}$	$2.41^{+1.40}_{-2.06}$	$(1.90^{+3.82}_{-1.88}) \times 10^{52}$
8073	$127.5^{+80.3}_{-50.9}$	$2.14^{+5.37}_{-1.18}$	$(3.76^{+69.54}_{-3.23}) \times 10^{52}$
8075	$138.8^{+11.7}_{-10.8}$	$2.72^{+0.54}_{-0.41}$	$(6.26^{+3.38}_{-2.04}) \times 10^{52}$
8084	$126.0^{+4.9}_{-4.9}$	$6.15^{+0.88}_{-0.74}$	$(1.91^{+0.69}_{-0.49}) \times 10^{53}$
8087	$341.3^{+43.5}_{-38.5}$	$6.96^{+4.46}_{-2.21}$	$(1.73^{+3.63}_{-1.02}) \times 10^{54}$
8098	$148.6^{+19.3}_{-16.3}$	$2.06^{+0.55}_{-0.38}$	$(4.85^{+3.78}_{-1.90}) \times 10^{52}$
8099	$79.5^{+12.1}_{-11.3}$	$0.74^{+0.15}_{-0.13}$	$(4.49^{+2.54}_{-1.66}) \times 10^{51}$
8105	$17.1^{+5.5}_{-5.4}$	$0.41^{+0.15}_{-0.14}$	$(1.36^{+1.55}_{-0.84}) \times 10^{50}$
8111	$354.5^{+46.6}_{-88.3}$	$7.98^{+6.05}_{-4.60}$	$(2.38^{+6.15}_{-2.06}) \times 10^{54}$
8116	$241.2^{+30.7}_{-18.2}$	$11.78^{+12.32}_{-3.44}$	$(2.23^{+8.69}_{-1.21}) \times 10^{54}$
8121	$103.8^{+24.7}_{-20.9}$	$8.43^{+19.23}_{-4.34}$	$(2.25^{+29.58}_{-1.83}) \times 10^{53}$

Appendix C

Luminosity Evolution

In Chapter 5, we proposed the existence of the luminosity evolution of $(1 + z)^{2.6}$ in prompt GRBs (the luminosity increase as the function of redshift) using τ-statistical method introduced in Appendix A. Lloyd-Ronning et al. (2002a) and Wei & Gao (2002) independently reported the luminosity evolution as $(1 + z)^{1.4}$ and $(1 + z)^{1.8}$, respectively. As already discussed in Chapter 6, observed luminosity is described as $L_{obs} = 2L_j\theta_j^{-2}$. Therefore, we can give two probable interpretations for the luminosity evolution as the progenitor evolution (e.g. mass evolution) and the jet opening-angle evolution. In this chapter, based on the recent theory of the star formation rate and the observed jet opening angle, we show how each part contributes to the observed luminosity evolution.

C.1 Progenitor Evolution

As shown in figure 6.6, we show the stellar fate as the function of the metallicity. Generally, GRBs are produced vir the massive star collapse having ~ 40 $M_\odot$. This is correspond to the case with the metallicity of solar abundance. GRBs from these objects averagely occur at $z \sim 1$. Moreover, assuming Salpeter-type IMF, stars heavier than 100 $M_\odot$ is hard to form because of metal cooling. Probably, almost all GRBs at $z \sim 1$ are triggered by several times 10 $M_\odot$. On the other hand, metal-free stars (pop-III stars) in the mass range of 100–140 $M_\odot$ may occur GRBs, which can be formed only in the early universe such as $z > 12$.

If the luminosity of the prompt GRBs associates with the stellar mass, we can naturally introduce mass evolution for the purpose of explaining the luminosity evolution. When we consider the luminosity L_* from 40 $M_\odot$ progenitor at $z = 1$, the luminosity from $z \sim 12$ is expected as $3L_*$ because the mass of progenitor is 120 $M_\odot$. Then the evolution is quantitatively described as $(1 + z)^{0.6}$.

C.2 Jet Opening-Angle Evolution

In figure C.1, we show the jet opening angle as the function of redshift measured from the break time of afterglows. The filled squares are the measured opening-angle and the cursors mean the upper or lower value. The total gamma-ray energy released in the jet is

$$E_\gamma = \frac{\theta_j^2}{2}E_{obs} = \frac{\theta_j^2}{2}\frac{4\pi d_L^2 F}{(1 + z)}. \tag{C.1}$$

Here, d_L is the luminosity distance and the F is the observed fluence in units of erg cm^{-2}. The additional term of $(1 + z)$ comes from the cosmological time dilation. Adopting the geometrical correction of the jet, Frail et al. (2001) and Bloom et al. (2003) reported the distribution of E_γ as the standard candle of $E_\gamma = 10^{51}$ erg (see figure 1.9 right). When we set the fluence limit as 1×10^{-7} erg cm^{-2}, which correspond to the detector sensitivity of *BATSE* , we can estimate the maximum jet opening-angle as the function of redshift (solid line in figure C.1).
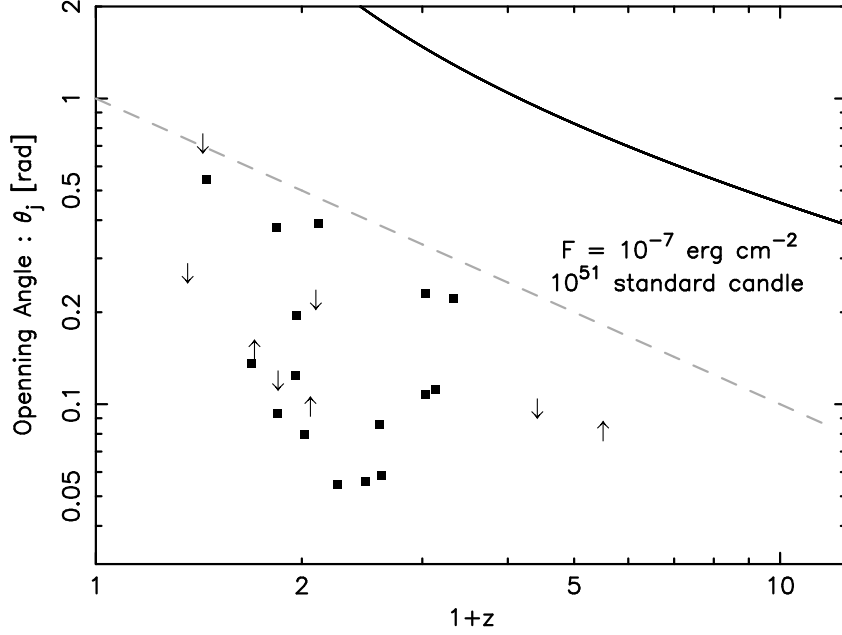
Figure C.1: Observed jet opening-angle distribution reported by Bloom et al. (2003). The filled squares are the measured opening-angle and the cursors mean the upper or lower value. The solid line is the maximum opening angle of detectable GRBs in stand on the the standard candle as $E_{iso} = 10^{51}$ erg. The dashed line is a reference of $\theta_j \propto (1 + z)^{-1}$.

It is difficult to give quantitative arguments about the jet opening-angle evolution from the small data samples shown in figure C.1. But we can recognize a tendency of the evolution, i.e., the near events have large opening angle and the remote ones are narrowly collimated. We superposed a reference line as $\theta_j \propto (1 + z)^{-1}$ on the same figure. If such evolution exists, the luminosity evolution as the jet opening-angle evolution is $L_{obs} \propto \theta_j^{-2} \propto (1 + z)^2$.

It is hard to consider that the sensitivity of the *BATSE* detectors limit the determination of the jet opening-angle, because the truncation of such effect is far from the observation. On the other hand, we cannot determine the flux limit of the optical observations because afterglows are observed different telescopes with different sensitivity in the world. It is an actual fact that the events measured the jet break are considerably bright case. Therefore there is a possibility that the plots in figure C.1 is truncated by some observational limitations. We cannot strongly assert about the jet opening angle evolution of $\theta_j \propto (1 + z)^{-1}$, it is not impossible to explain the luminosity evolution of $(1 + z)^{2.6}$ in total.

Appendix D

Data Analysis of X-ray Afterglows

GRB afterglows are the phenomena following the prompt gamma-ray emission of GRBs. The afterglows, generally, are brightening in X-ray, optical and radio band, decaying their flux with the power-law in time. In the framework of the fireball model, afterglows are thought to be generated by the external shock (the relativistic flow interacts with the inter stellar medium).

In this chapter, we perform X-ray spectral and temporal analysis for each X-ray afterglows, noticing the X-ray emission lines. We used 3 data (GRB 970828, 990123 and 990704; Murakami et al., 1997c, 1999a,b) observed with *ASCA* [1], and 5 data (GRB 001025A, 011211, 020322, 030227 and 031203; Altieri et al., 2000; Santos-Lleo et al., 2001; Ehle et al., 2002; Loiseau et al., 2003; Santos-Lleo et al., 2003) observed with *XMM-Newton* , respectively. In table D.1, we summarized the basic informations about each GRB.

GRB	Satellite	GRB Time (UT)	TSTART (UT)	EXP.	R.A.	DEC.
970828	*ASCA*	1997/08/28.74	1997/08/29.92	40.0 ks	18h08m29.4s	$+59^o18'39.7"$
990123	*ASCA*	1999/01/23.56	1999/01/25.70	39.8 ks	15h25m32.0s	$+44^o45'28.9"$
990704	*ASCA*	1999/07/04.73	1999/07/05.36	29.0 ks	12h19m20.7s	$-03^o50'10.6"$
001025A	*XMM*	2000/10/25.13	2000/10/27.25	18.0 ks	08h36m35.9s	$-13^o04'09.1"$
011211	*XMM*	2001/12/11.80	2001/12/12.30	28.8 ks	11h15m17.9s	$-21^o56'57.5"$
020322	*XMM*	2002/03/22.16	2002/03/22.80	26.3 ks	18h01m03.4s	$+81^o06'30.7"$
030227	*XMM*	2003/02/27.36	2003/02/27.77	31.8 ks	04h57m33.0s	$+20^o29'09.0"$
031203-1	*XMM*	2003/12/03.92	2003/12/04.19	56.2 ks	08h22m30.3s	$-39^o51'02.4"$
031203-2	*XMM*	2003/12/03.92	2003/12/06.77	52.6 ks	08h22m30.3s	$-39^o51'02.4"$

Table D.1: The basic information of X-ray afterglow samples taking into account in this thesis. For each GRB, this table contain the information about the GRB trigger time, the exposure start time (TSTART) for X-ray afterglow, total exposure duration (EXP.) and the coordinate (R.A., Dec.), respectively.

---

[1] *ASCA* observed the positions of the other 4 GRBs (GRB 970228, GRB 970402, GRB 970616 and GRB 970815), but the no new X-ray source was detected. The detail description about the follow-up observations are found in IAUC 6593, IAUC 6687 and IAUC 6732 (Yoshida et al., 1997; Murakami et al., 1997a,b).

D.1   Individual target – Events with Emission Lines

Noticing spectral features, we show the spectral property of X-ray afterglows observed with *ASCA* and *XMM-Newton* . In this section, we summarize the events with the emission lines and/or the edge structures. In the next section, the cases without emission lines are introduced.

D.1.1   GRB 970828

An X-ray afterglow accompanying GRB 970828 was observed with *ASCA* . This is the first event to obtain the X-ray spectrum with good statistics by *ASCA* . A radio flare was observed within the error circle of the X-ray transient, and the redshift was measured as $z = 0.9578$ from the spectral absorption lines of the host galaxy (Djorgovski et al., 2001).

We show the X-ray image of the X-ray afterglow of GRB 970828 observed with *ASCA* GIS2 detector in figure D.1 (within the circle). In figure D.2, we show the lightcurve of the source after subtracting the background. The lightcurve shows power-law decline with $\propto t^{-1.44\pm0.06}$, and a flare structure around 1.2×10^5 sec. We divide the entire observation into three parts before/in/after the flare, and perform the spectral analysis.
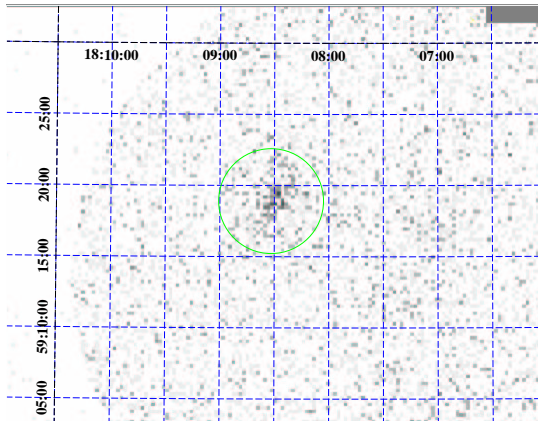
Figure D.1: The image of the X-ray afterglow of GRB 970828 (*ASCA* GIS2). The source in the center circle is the X-ray counterpart of this event. The horizontal and the vertical axis means R.A. and Dec., respectively.
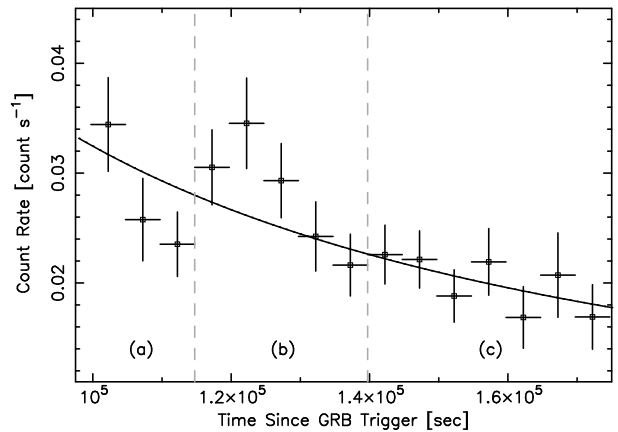
Figure D.2: The lightcurve of X-ray afterglow of GRB 970828. The solid line is the best fit result with $\propto t^{-1.44}$. The spectral analysis is performed for two intervals as divided by the dashed lines.

Yoshida et al. (1999) interpreted the spectral feature in spectrum (b) as the He-like iron emission line (6.7 keV), and measured the redshift as $z = 0.33$. However, this redshift is inconsistent with the optically measured redshift of $z = 0.9578$. Therefore, we reanalyzed the spectrum and interpreted it as the radiative recombination edge and continuum (RRC) of the fully ionized iron ($E_{RRC} = 9.28$ keV). The model function of the RRC is described below.

$$N(E) = \begin{cases} 0 & \text{for } E \geq E_{RRC} \\ N_0(kT)^{-3/2}\exp(-\frac{E-E_{RRC}}{kT}) & \text{for } E \leq E_{RRC}, \end{cases} \tag{D.1}$$

Introducing the three parameters for the RRC, i.e., E_{RRC}, kT_e, and normalization, we achieve a significant reduction of χ^2, $\Delta\chi^2 = 13.2$. Hence, the confidence level of the RRC model is found by an F-test to be 99.3 %. The best fit gives an edge energy of $E_{RRC} = 4.76^{+0.19}_{-0.25}$ keV, an electron temperature at the rest frame of $kT_e = 0.8^{+1.0}_{-0.2}$, and an integrated RRC flux of $F_{RRC} = 1.7^{+6.4}_{-1.3} \times 10^{-5}$ photons cm^{-2} s^{-1} . The above 90 % error range of E_{RRC} is consistent with the expected RRC-edge energy of H-like iron at 4.74 keV and He-like iron at 4.51 keV with a redshift of $z = 0.9578$.Thus, the spectral feature could be explained as the RRC above the edge energy in highly ionized plasma.

It should be notable that there is no redshifted iron emission line seen at the expected energy for such ionized plasma. We searched for an H-like iron emission line (6.97 keV at the rest frame) in the spectrum at (b). As shown in figure D.3-(b), we found no emission line around $6.97/(1 + z) = 3.56$ keV with an upper limit of $F_{line} \leq 1.5 \times 10^{-6}$ photons cm^{-2} s^{-1} . No significant line structure was found in (a) or (c). Yoneotku et al. (2001) suggested that these cases can realize in the plasma with the non-equilibrium ionization (NEI) state. We will mention about this point in Chapter 6. The best-fit parameters and the upper limits on the iron emission line and the RRC intensities are summarized in table D.2 and table D.3 (Yoshida, Namiki, Yonetoku et al., 2001).
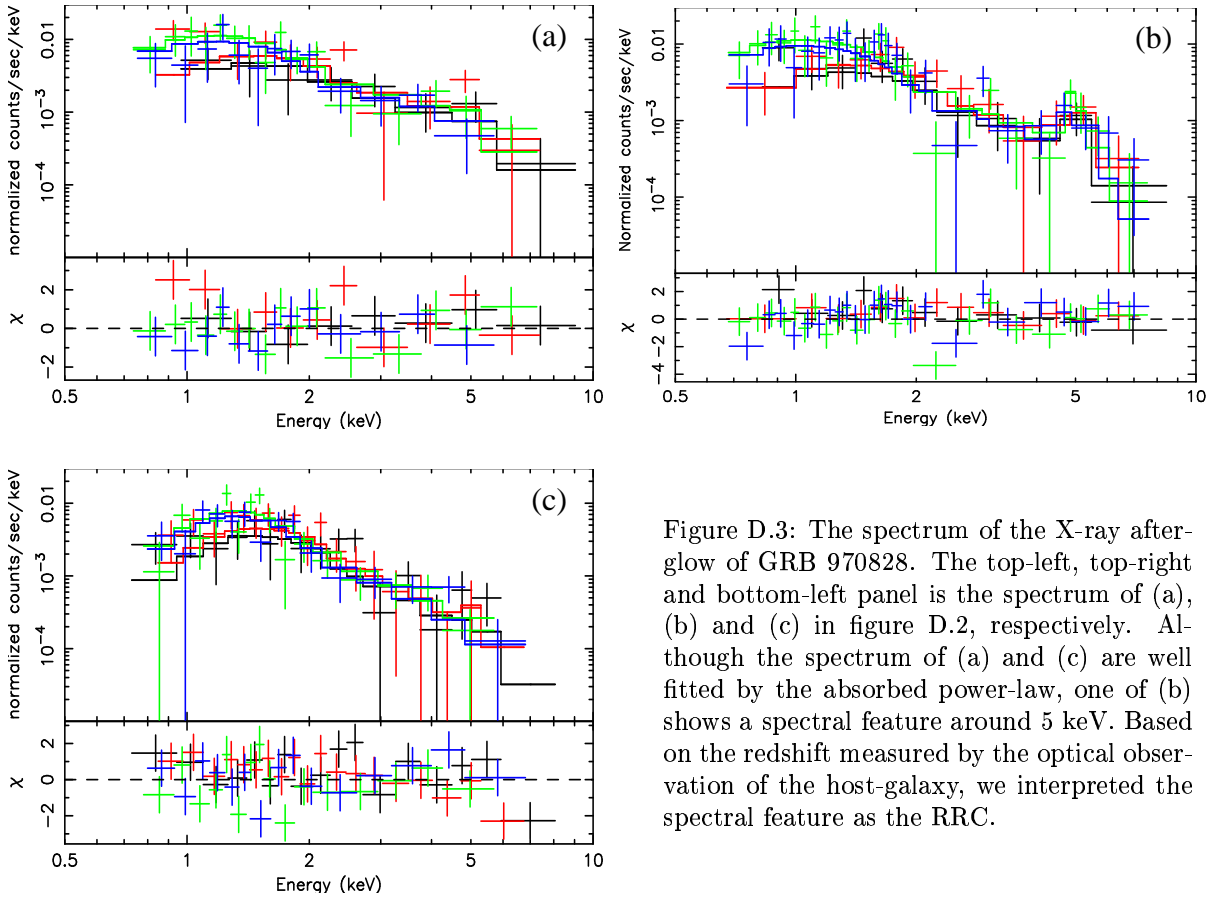

Figure D.3: The spectrum of the X-ray afterglow of GRB 970828. The top-left, top-right and bottom-left panel is the spectrum of (a), (b) and (c) in figure D.2, respectively. Although the spectrum of (a) and (c) are well fitted by the absorbed power-law, one of (b) shows a spectral feature around 5 keV. Based on the redshift measured by the optical observation of the host-galaxy, we interpreted the spectral feature as the RRC.

Period	N_{H}^{gal} $(\times 10^{20}$ cm$^{-2})$	N_{H} $(\times 10^{20}$ cm$^{-2})$	power-law index	E_{RRC} keV	kT_e keV	$\chi^2/$d.o.f
(a)	3.4 (fixed)	< 36.5	$1.6^{+0.2}_{-0.3}$	...	...	34.7/48
(b)	3.4 (fixed)	< 55.4	$2.1^{+0.3}_{-0.3}$	$4.76^{+0.19}_{-0.25}$	$0.8^{+1.0}_{-0.2}$	70.3/72
(c)	3.4 (fixed)	$70.8^{+32.1}_{-27.5}$	$2.9^{+0.7}_{-0.4}$	...	...	94.0/84

Table D.2: Fitting results of X-ray afterglow of GRB 970828.

Period	Line (6.97 keV) photons cm^{-2} s^{-1}	RRC (9.28 keV) photons cm^{-2} s^{-1}
(a)	$< 4.7 \times 10^{-6}$	$< 1.2 \times 10^{-5}$
(b)	$< 1.5 \times 10^{-6}$	$1.7^{+6.4}_{-1.2} \times 10^{-5}$
(c)	$< 3.0 \times 10^{-5}$	$< 7.0 \times 10^{-6}$

Table D.3: Iron Line and RRC Flux of X-ray afterglow of GRB 970828.

D.1.2   GRB 001025A

GRB 001025 was detected by the All-Sky Monitor aboard the *RXTE* satellite at about 03:10:05 (UT) on 25 Oct 2000, and determined its position by the inter planetary network (IPN) (Smith et al., 2000). The peak flux of this event was ~ 4 Crab in 5–12 keV band, and ~ 1.5 Crab in 1.5–3 band, respectively. The optical counterpart of this event is not found, thus the redshift is unknown.

In figure D.4, we show the image of X-ray afterglow detected by the PN detector aboard *XMM* . The point source shown in the circle is the X-ray afterglow. The lightcurve of this source is shown in figure D.5. When we adopt the power-law model to the lightcurve, we obtained the best result as $\propto t^{-2.9\pm1.0}$ with $\chi^2 = 9.38$ for 12 d.o.f. There is large error in the decay index. This is because this observation has been done after 2.1 days since the GRB trigger, so the source is dimmer than the other samples, and the photon flux is not enough to determine the decay index.

We divided the entire observation into 2 parts (a) and (b) as shown in figure D.5. In figure D.6, we show the source spectrum of GRB 001025A. The left and the right panel is the fitting result with the absorbed power-law model including the galactic absorption ($N_{\mathrm{H}} = 6.1 \times 10^{20}$ cm^{-2}). There are some discrepancies between the data and the model functions in 0.6–2.2 keV range. Including additional line components into the spectrum (b), we improved the fitting significantly as shown in figure D.7. Two lines are about 3 σ confidence and the other two are marginal detection. When we consider the detected lines as the H-like elements (Mg XII, Si XIV, S XVI, Ar XVIII), the redshift can be determined as $z = 0.79 \pm 0.07$. Including the line model components to the spectrum (a), we could not obtain the significant reduction of χ^2, and set only upper-limits of the line fluxes. The best-fit continuum and the line parameters are summarized in table D.4 and table D.5.
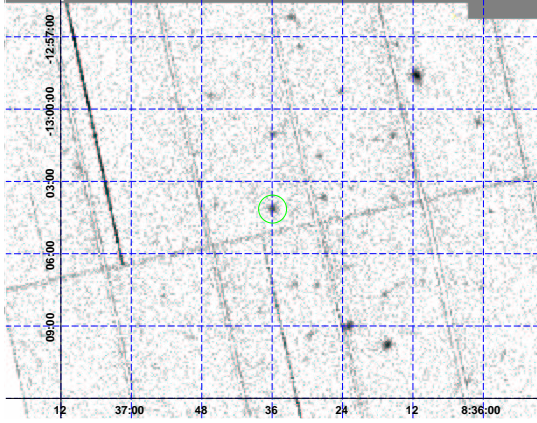
Figure D.4: The image of the X-ray afterglow of GRB 001025A (XMM-PN). The source in the center circle is the X-ray counterpart of this event. The horizontal and the vertical axis means R.A. and Dec., respectively.
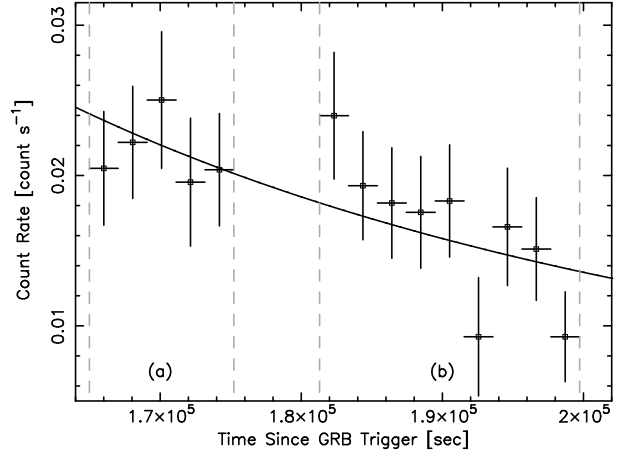

Figure D.5: The lightcurve of the X-ray afterglow of GRB 001025A. The solid line is the best-fit result with $\propto t^{-2.9\pm1.0}$. The spectral analysis is performed for two intervals as divided by the dashed lines.
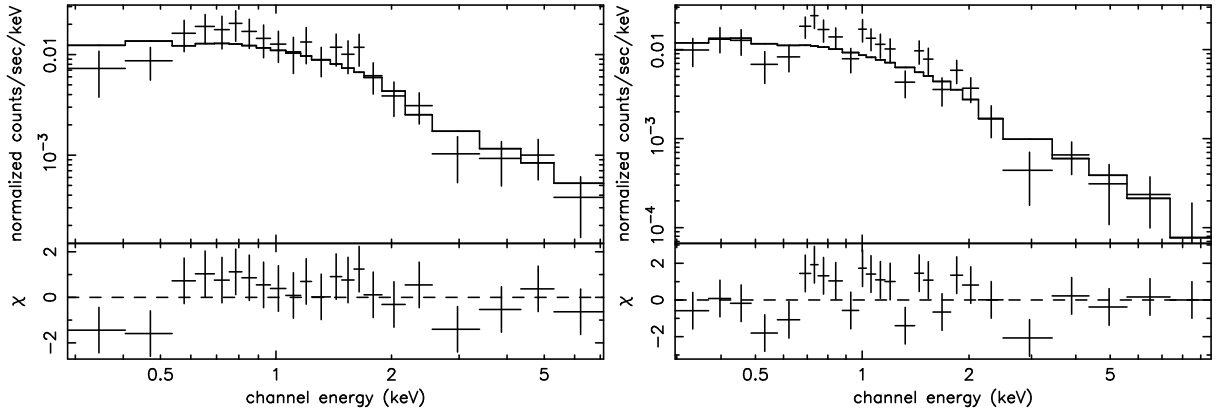

Figure D.6: The spectrum of the X-ray afterglow of GRB 001025A. The left and right panel is the spectrum of (a) and (b), respectively. There are discrepancies between the data and the model component around 0.5 keV and 2.0 keV, especially in the right panel.
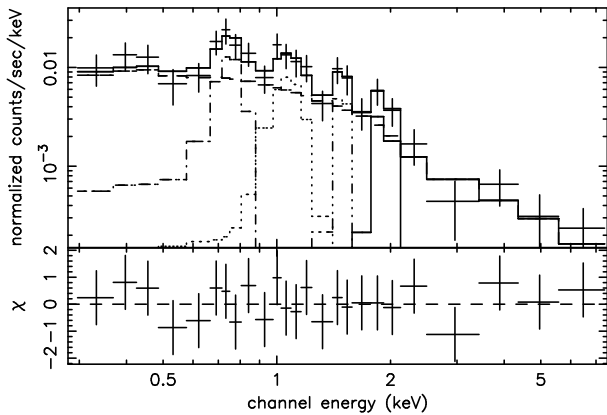
Figure D.7: The spectrum of X-ray afterglow of GRB 001025A. The left panel is the fitting result with the absorbed power-law model. There are discrepancies between the data and the model component around 0.7 keV and 1.1 keV. The right panel is the same data but including the 4 Gaussian models to represent the emission lines.

Interval	N_{H} 10^{20} cm^{-2}	power-law index	energy flux (2–10 keV) ergs cm^{-2}s^{-1}	χ^2	d.o.f
(a) PL	6.1 (fix)	1.61 ± 0.17	$(7.25 \pm 0.94) \times 10^{-14}$	15.9	20
(b) PL	6.1 (fix)	1.96 ± 0.19	$(3.55 \pm 0.41) \times 10^{-14}$	33.7	24
(b) PL+line	6.1 (fix)	1.88 ± 0.33	$(2.69 \pm 0.79) \times 10^{-14}$	8.62	14

Table D.4: Fitting results for the continuum spectrum of GRB 001025A. When we estimate the energy flux, the galactic absorption (N_{H}) was corrected.

Element	Energy keV	σ keV	Photon Flux photon cm^{-2}s^{-1}	Energy Flux erg cm^{-2}s^{-1}	Significance
(a) line-1 (Mg XII)	0.77 (fix)	0 (fix)	$< 3.57 \times 10^{-6}$	$< 4.37 \times 10^{-15}$	...
(a) line-2 (Si XIV)	1.08 (fix)	0 (fix)	$< 1.81 \times 10^{-6}$	$< 3.12 \times 10^{-15}$	...
(a) line-3 (S XVI)	1.49 (fix)	0 (fix)	$< 1.95 \times 10^{-6}$	$< 4.63 \times 10^{-15}$	...
(a) line-4 (Ar XVIII)	1.90 (fix)	0 (fix)	$< 1.01 \times 10^{-6}$	$< 3.12 \times 10^{-15}$	...
(b) line-1 (Mg XII)	0.77 ± 0.04	0 (fix)	$(2.65^{+2.11}_{-1.16}) \times 10^{-6}$	$(3.28^{+2.59}_{-1.43}) \times 10^{-15}$	3.1 σ
(b) line-2 (Si XIV)	1.08 ± 0.08	0 (fix)	$(2.05^{+1.59}_{-1.55}) \times 10^{-6}$	$(3.54^{+2.74}_{-2.67}) \times 10^{-15}$	2.9 σ
(b) line-3 (S XVI)	1.49 ± 0.05	0 (fix)	$(8.71^{+6.59}_{-5.85}) \times 10^{-7}$	$(2.07^{+1.57}_{-1.39}) \times 10^{-15}$	$\sim$90 %
(b) line-4 (Ar XVIII)	1.90 ± 0.12	0 (fix)	$(9.86^{+6.52}_{-7.27}) \times 10^{-7}$	$(3.02^{+1.99}_{-2.22}) \times 10^{-15}$	$\sim$90 %

Table D.5: The best fit results of the line components of GRB 001025A.

D.1.3   GRB 011211

GRB 011211 was detected by *BeppoSAX* , and the burst duration was 270 s (the longest burst observed by *BeppoSAX*) with a peak flux of 5×10^{-8} ergs cm^{-2}s^{-1} . The redshift of GRB 011211 was measured as $z = 2.141 \pm 0.01$ (Fruchter et al., 2001; Holland et al., 2001).

The X-ray image of GRB 011211 is shown in figure D.8. Unfortunately, at the first pointing of this observation, the source is located close to the edge of the PN chip. Therefore, after ~ 5 ks since the exposure start, *XMM-Newton* was maneuvered into the position that the source is well located on the PN detector (see the right panel (a) and (b) of figure D.8). The lightcurve of the source is shown in figure D.9. The best fit power-law model is $\propto t^{-1.66 \pm 0.22}$ with $\chi^2 = 14.2$ for 12 d.o.f. We performed the spectral analysis for the intervals of (a) and (b) as shown in figure D.9

In figure D.10, we show the spectra of both (a) and (b) with the absorbed power-law model. In the first 5 ksec observation (a), some spectral features are found around 0.7 keV, 0.9 keV and 1.2 keV. On the other hand, in the following 22 ksec observation (b), the lines are disappeared and we can obtain the acceptable fit only with the single power-law with the galactic absorption. Adopting three Gaussian components to represent the spectral features in (a), we can improve the fit as shown in figure D.11 (two are about 3 σ confidence and one is marginal). Although Reeves et al. (2002, 2003) reported *five* emission lines in the X-ray spectrum of GRB 011211, we confirmed only *three* of them. The parameters of detected three emission lines, i.e. E_{line} and

the flux, are consistent with their results. The best-fit parameters are summarized in table D.6 for the continuum and table D.7 for the emission lines, respectively.

In the time interval detected the emission lines, the source are located near the detector edge. Therefore, the background, especially caused by the mount plate of the PN detector, should be considered as claimed by Borozdin & Trudolyubov (2003). In Reeves et al. (2003), they show the detail analysis taking into account the background, the calibration, and so on. Considering several observational effects, the detected emission lines appears robust (Reeves et al., 2003).
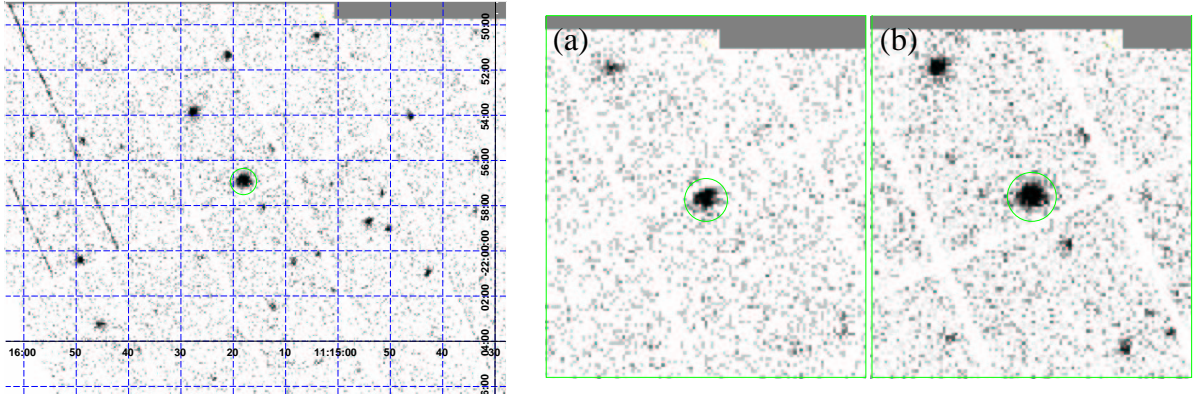
Figure D.8: The left panel is the image of the X-ray afterglow of GRB 011211 (XMM-PN). The right panel is the source image (a): at the first pointing, (b): after maneuvering, respectively.
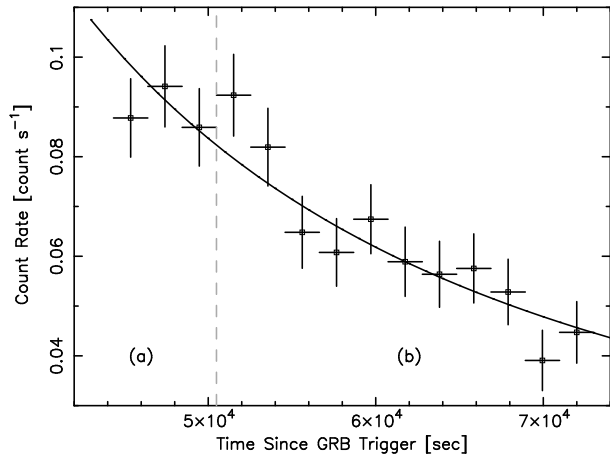

Figure D.9: The lightcurve of X-ray afterglow of GRB 011211. The interval assigned (a) and (b) is correspond to one of figure D.8 (right), respectively. The solid line is the best fit power-law model as $\propto t^{-1.66 \pm 0.22}$.

D.1.4 GRB 030227

GRB 030227 was detected by the *INTEGRAL* satellite and its position was determined within a few arcsec accuracy. The burst duration was about 20 second and the peak flux over 2 seconds is about 6×10^{-8} ergs cm^{-2}s^{-1} in the 25–100 keV energy range. *XMM-Newton* began observing
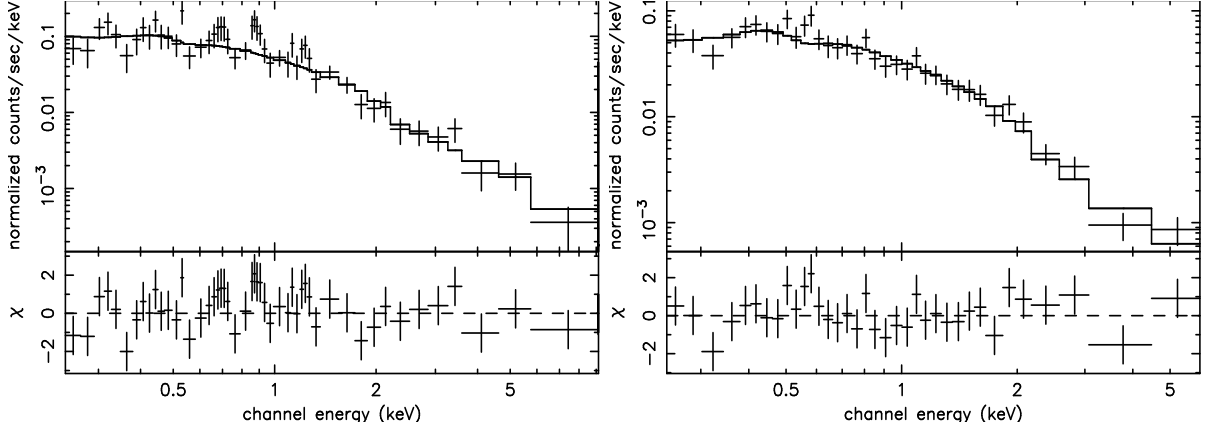
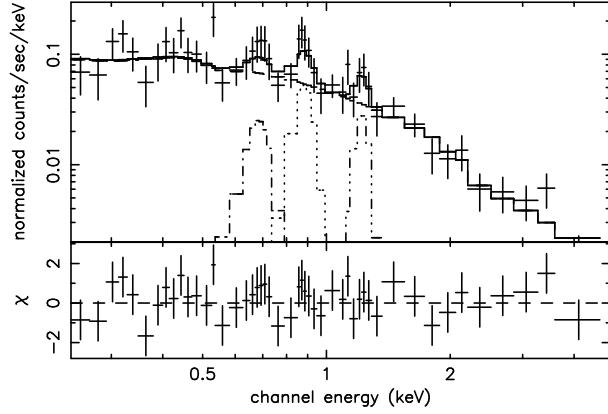Figure D.10: The spectrum of X-ray afterglow of GRB 011211.

Figure D.11: The spectrum of X-ray afterglow of GRB 011211. The left panel is the fitting result with the absorbed power-law model. There are discrepancies between the data and the model component around 0.7 keV and 1.1 keV. The right panel is the same data but including the 4 Gaussian models to represent the emission lines.

Interval	N_H 10^{20} cm^{-2}	power-law index	energy flux (2–10 keV) ergs cm^{-2}s^{-1}	χ^2	d.o.f
(a) PL	4.27 (fix)	2.13 ± 0.11	$(1.45 \pm 0.11) \times 10^{-13}$	51.9	54
(b) PL	4.27 (fix)	2.17 ± 0.09	$(8.08 \pm 0.49) \times 10^{-14}$	34.0	34
(a) PL+line	4.27 (fix)	2.10 ± 0.08	$(1.38 \pm 0.26) \times 10^{-13}$	33.8	48

Table D.6: Fitting results for the continuum spectrum of GRB 011211. When we estimate the energy flux, the galactic absorption (N_H) was corrected.

Element	Energy [keV]	σ [keV]	Photon Flux [photon cm^{-2}s^{-1}]	Energy Flux [erg cm^{-2}s^{-1}]	Significance
(a) line-1 (Si XIV)	0.70 ± 0.04	0 (fix)	$(4.14^{+11.1}_{-2.95}) \times 10^{-6}$	$(4.63^{+12.4}_{-3.30}) \times 10^{-15}$	~90 %
(a) line-2 (S XVI)	0.89 ± 0.02	0 (fix)	$(7.04^{+7.31}_{-3.01}) \times 10^{-6}$	$(1.01^{+1.05}_{-0.43}) \times 10^{-14}$	3.1 σ
(a) line-3 (Ar XVIII)	1.22 ± 0.04	0 (fix)	$(3.50^{+3.50}_{-2.56}) \times 10^{-6}$	$(6.84^{+6.83}_{-5.02}) \times 10^{-15}$	2.7 σ
(b) line-1 (Si XIV)	0.70 (fix)	0 (fix)	$< 1.87 \times 10^{-6}$	$< 2.10 \times 10^{-15}$	...
(b) line-2 (S XVI)	0.89 (fix)	0 (fix)	$< 6.51 \times 10^{-7}$	$< 9.33 \times 10^{-16}$	...
(b) line-3 (Ar XVIII)	1.22 (fix)	0 (fix)	$< 1.01 \times 10^{-6}$	$< 1.99 \times 10^{-15}$	...

Table D.7: The best fit results of the line components of GRB 011211.

the error-box of GRB 030227 about eight hours after the burst. This X-ray afterglow was pretty bright, so the detail analysis was performed by Watson et al. (2003).

In figure D.12, we show the image of the X-ray afterglow of GRB 030227. The X-ray afterglow is clearly detected within the circle. The X-ray flux is decaying with a power-law of $\propto t^{-1.0\pm0.1}$ as shown in figure D.13. We divided the entire data into 4 parts (a), (b), (c) and (d), and performed spectral analyses.

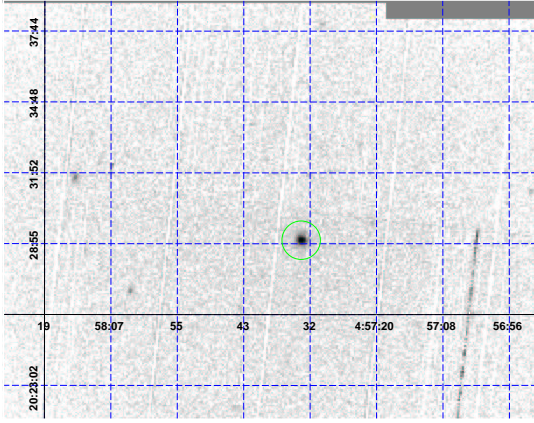We show four time-resolved spectra in figure D.14.

Figure D.12: The image of the X-ray afterglow of GRB 030227 (XMM-PN). The source in the center circle is the X-ray counterpart of this event.
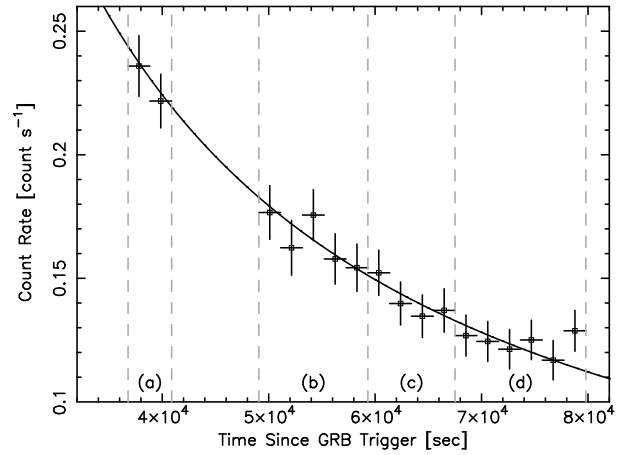

Figure D.13: The lightcurve of X-ray afterglow of GRB 030227. The solid line is the best fit result with $\propto t^{-1.0}$. The spectral analysis is performed for two intervals as divided by the dashed lines.
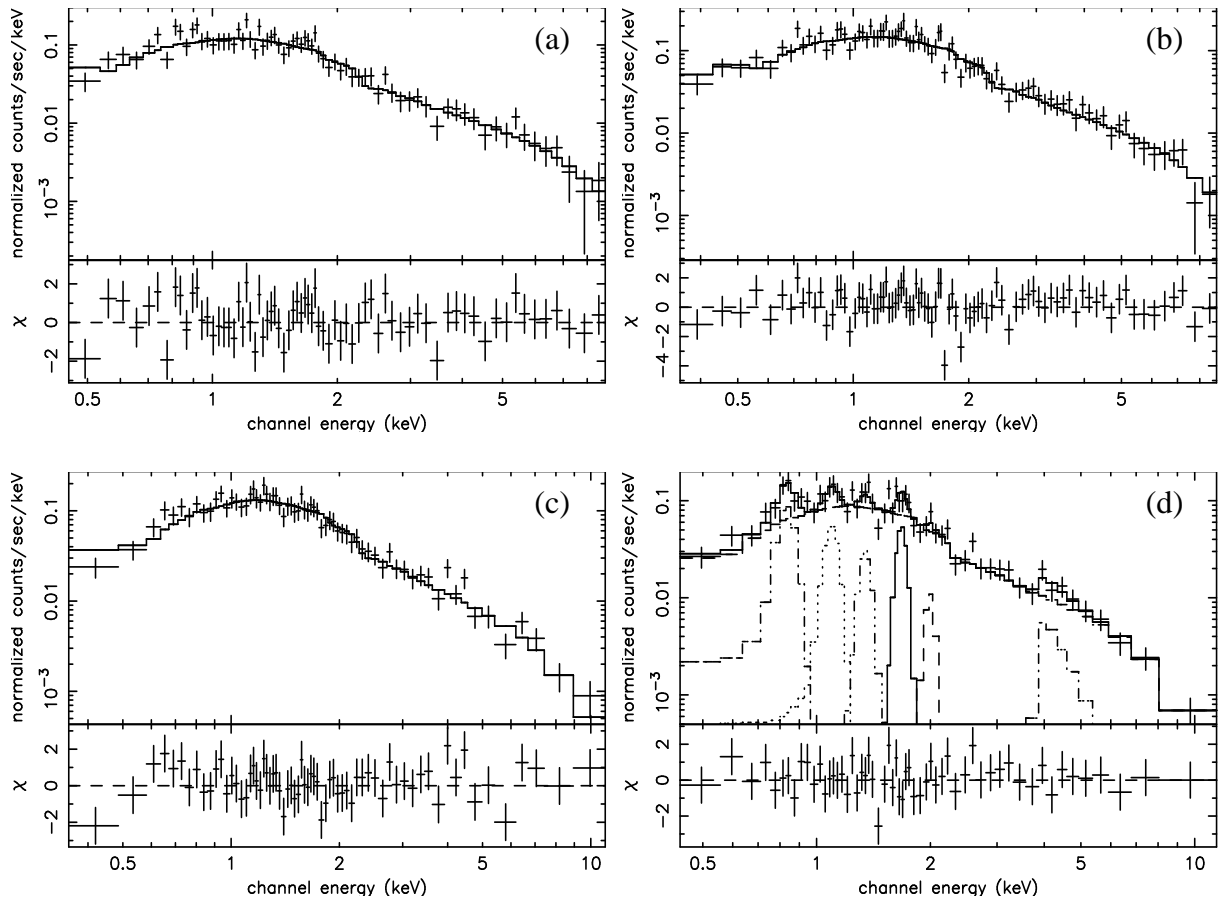
Figure D.14: The spectrum of X-ray afterglow of GRB 030227.

Element	Energy [keV]	σ/kT_e [keV]	Photon Flux [photon cm^{-2}s^{-1}]	Energy Flux [erg cm^{-2}s^{-1}]	Significance
(a) line-1 (Si XIV)	0.85 (fix)	0 (fix)	$< 7.89 \times 10^{-6}$	$< 1.08 \times 10^{-14}$	...
(a) line-2 (S XVI)	1.10 (fix)	0 (fix)	$< 3.10 \times 10^{-6}$	$< 5.47 \times 10^{-15}$	...
(a) line-3 (Ar XVIII)	1.33 (fix)	0 (fix)	$< 3.63 \times 10^{-6}$	$< 7.74 \times 10^{-15}$	...
(a) line-4 (Ca XX)	1.66 (fix)	0 (fix)	$< 7.55 \times 10^{-6}$	$< 2.02 \times 10^{-14}$	...
(a) RRC (Fe XXVI)	3.85 (fix)	0.56 (fix)	$< 7.65 \times 10^{-6}$	$< 5.41 \times 10^{-14}$	...
(b) line-1 (Si XIV)	0.85 (fix)	0 (fix)	$< 4.24 \times 10^{-6}$	$< 5.79 \times 10^{-15}$	...
(b) line-2 (S XVI)	1.10 (fix)	0 (fix)	$< 6.31 \times 10^{-6}$	$< 1.11 \times 10^{-15}$	...
(b) line-3 (Ar XVIII)	1.33 (fix)	0 (fix)	$< 9.50 \times 10^{-6}$	$< 2.03 \times 10^{-14}$	...
(b) line-4 (Ca XX)	1.66 (fix)	0 (fix)	$< 2.14 \times 10^{-6}$	$< 5.74 \times 10^{-15}$	...
(b) RRC (Fe XXVI)	3.85 (fix)	0.56 (fix)	$< 1.09 \times 10^{-5}$	$< 7.72 \times 10^{-14}$	...
(c) line-1 (Si XIV)	0.85 (fix)	0 (fix)	$< 3.19 \times 10^{-5}$	$< 4.35 \times 10^{-15}$	...
(c) line-2 (S XVI)	1.10 (fix)	0 (fix)	$< 2.75 \times 10^{-6}$	$< 4.85 \times 10^{-15}$	...
(c) line-3 (Ar XVIII)	1.33 (fix)	0 (fix)	$< 4.46 \times 10^{-6}$	$< 9.51 \times 10^{-15}$	...
(c) line-4 (Ca XX)	1.66 (fix)	0 (fix)	$< 5.04 \times 10^{-6}$	1.35×10^{-14}	...
(c) RRC (Fe XXVI)	3.85 (fix)	0.56 (fix)	$< 9.59 \times 10^{-6}$	$< 6.78 \times 10^{-14}$	...
(d) line-1 (Si XIV)	0.85 ± 0.02	0 (fix)	$(1.15^{+0.43}_{-0.71}) \times 10^{-5}$	$(1.55^{+0.58}_{-0.96}) \times 10^{-14}$	3.5 σ
(d) line-2 (S XVI)	1.10 ± 0.03	0 (fix)	$(6.58^{+3.44}_{-4.12}) \times 10^{-6}$	$(1.16^{+0.61}_{-0.74}) \times 10^{-14}$	3.0 σ
(d) line-3 (Ar XVIII)	$1.33^{+0.05}_{-0.04}$	0 (fix)	$(3.46^{+4.59}_{-2.21}) \times 10^{-6}$	$(7.35^{+9.76}_{-4.71}) \times 10^{-15}$	$\sim$ 90 %
(d) line-4 (Ca XX)	1.66 ± 0.04	0 (fix)	$(6.57^{+1.95}_{-4.68}) \times 10^{-6}$	$(1.76^{+0.52}_{-1.25}) \times 10^{-14}$	2.5 σ
(d) RRC (Fe XXVI)	$3.85^{+0.16}_{-0.27}$	$0.56^{+1.10}_{-0.50}$	$(6.76^{+4.96}_{-4.17}) \times 10^{-6}$	$(4.90^{+3.59}_{-3.02}) \times 10^{-14}$	$\sim$ 90 %

Table D.8: The best fit results of the line components of GRB 030227.

D.2   Events with Emission Lines Detected by *Chandra* and *BeppoSAX*

In this section, we briefly summarize past observations detected the emission lines and the RRC structure. *BeppoSAX* detected the iron emission line in the X-ray afterglow of GRB 970508 (Piro et al., 1999) and GRB 000214 (Antonelli et al., 2000). *Chandra* also detected the iron emission line and the RRC in the X-ray afterglow of GRB 991216 (Piro et al., 2000).

D.2.1   GRB 970508 (*BeppoSAX*)

The first detection of the emission line in the X-ray afterglow of GRB 970508 was reported by Piro et al. (1999). In figure D.15, we show the lightcurve of the X-ray afterglow of GRB 970508. There is a flare-like behavior 6×10^4 sec after the burst trigger. The spectrum before/after the flare (1a and 1b; top and bottom) is shown in figure D.16, respectively. In the pre-flare phase, a strong emission line is detected around 3.5 keV, and it is interpreted as the iron emission line based on the optically measured redshift ($z = 0.835$). The best-fit line flux is $F_{line} = (5 \pm 2) \times 10^{-5}$ photons cm^{-2} s^{-1} , and the power-law index is 1.5 ± 0.9. On the other hand, after the flare, the iron emission line was disappeared with the upper-limit flux of $F_{line} < 2 \times 10^{-5}$ photons cm^{-2} s^{-1} as shown in figure D.16 (bottom). The continuum parameter is 1.7 ± 1.0 which is consistent with the spectrum of pre-flare phase.
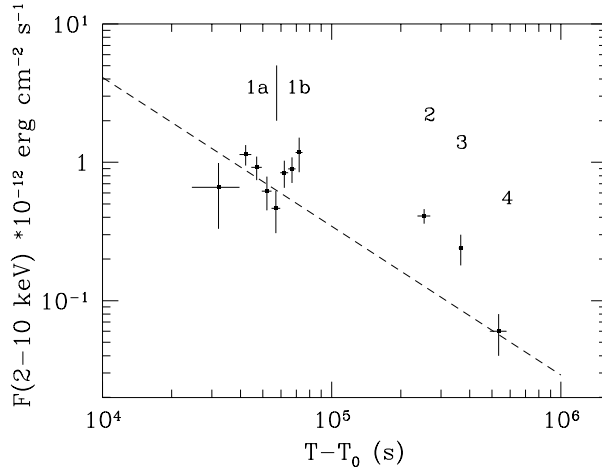

Figure D.15:   The lightcurve of the X-ray afterglow of GRB 970508 detected by the *BeppoSAX* satellite (Piro et al., 1999). A X-ray flare was detected about 6×10^4 sec after the GRB trigger.

D.2.2   GRB 000214 (*BeppoSAX*)

Antonelli et al. (2000) reported the detection of the strong and significant iron emission line in the X-ray afterglow of GRB 000214. The follow-up observation with *BeppoSAX* began about 12 hours after the GRB trigger, and lasted 104 ksec. The decay index of the X-ray flux is $\propto$ $t^{-1.41 \pm 0.03}$. The X-ray spectrum of this event is shown in figure D.17, and the line emission was clearly shown around 4.7 keV. The power-law index of the continuum spectrum is 2.2 ± 0.3, and the flux of $F = 2.9 \pm 0.9$ ergs cm^{-2}s^{-1} in 2–10 keV range. Adopting the Gaussian model to
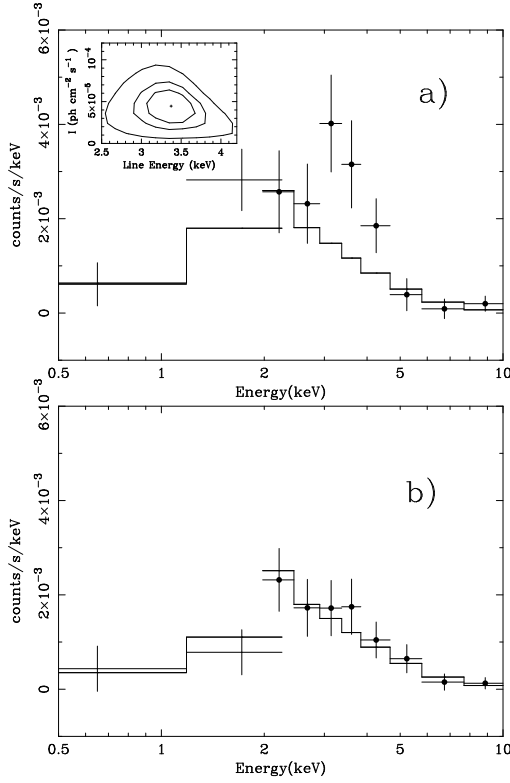
Figure D.16: The spectrum of the X-ray afterglow of GRB 970508 detected by the *BeppoSAX* satellite (Piro et al., 1999). The upper and lower panel is the spectrum between time interval of 1a and 1b in figure D.15, respectively. The iron emission line was detected in 1a with 99.3 % confidence level.
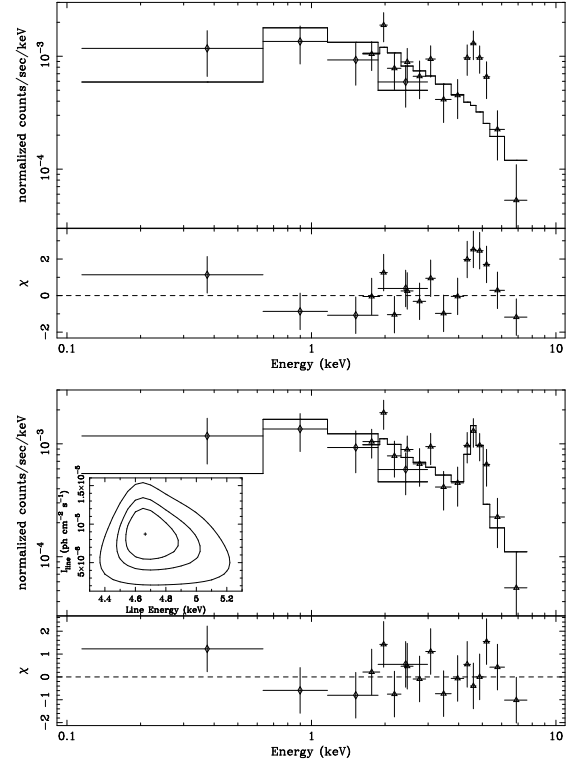
Figure D.17: The spectrum of the X-ray afterglow of GRB 000214 detected by the *BeppoSAX* satellite (Antonelli et al., 2000). The upper and lower panel is the spectrum excluding/including the emission line component. Antonelli et al. (2000) interpreted the spectral structure as the redshifted iron emission line, they measured the redshift as $z \sim$ 0.33. The confidence of the line component achieves 3.2 σ level.

the spectral structure, Antonelli et al. (2000) reported the line energy of $E_{line} = 4.7 \pm 0.2$ keV, and the line flux $F_{line} = (9 \pm 3) \times 10^{-6}$ photons cm^{-2} s^{-1} with 3.2 σ confidence level. Antonelli et al. (2000) identified the emission feature as the iron K$_\alpha$ line, the redshift of GRB 000214 was measured between 0.37 to 0.47.

D.2.3 GRB 991216 (*Chandra*)

GRB 991216 was one of the brightest GRBs detected by *BATSE* . The *RXTE* satellite discovered an X-ray afterglow of this event, and observed (scanned) in the error circle of the burst direction twice at 4.02 and 10.90 hours after the burst trigger, respectively. The afterglow flux was measured as $(1.24 \pm 0.04) \times 10^{-10}$ ergs cm^{-2}s^{-1} and $(0.25 \pm 0.01) \times 10^{-10}$ ergs cm^{-2}s^{-1} , so the decline was described by $\propto t^{-1.64}$ (Takeshima et al., 1999).

The first observation for the X-ray afterglow with *Chandra* was performed for GRB 991216 with the High Energy Transmission Grating (HETG). In figure D.18, we show the X-ray

spectrum observed by the HETG (left) and ACIS-CCD (right) detectors (Piro et al., 2000). As shown the left panel, a spectral feature is clearly shown $E_{line} = 3.49 \pm 0.06$ keV which is interpreted as the redshifted emission line of fully ionized iron. The line flux is $F_{line} = (3.2 \pm 0.8) \times 10^{-5}$ photons cm^{-2} s^{-1} with the standard deviation of $\sigma_{line} = 0.23 \pm 0.07$ keV. The confidence level of the emission line achieves 4.7 σ. This broad emission line is considered as the cause of the moving ejecta with the velocity of $v \sim 0.1\ c$.

Moreover, the RRC component was detected around 4.5 keV in the spectrum observed by the ACIS-CCD detector (the right panel of figure D.18). The best-fit parameters for the RRC structure is $E_{RRC} = 4.4 \pm 0.5$, $\sigma_{RRC} > 1.0$ keV, and $F_{RRC} = (3.8 \pm 2.0) \times 10^{-5}$ photons cm^{-2} s^{-1}. The significance of this RRC component is $\sim 3\ \sigma$. The continuum is described with the single power-law with the photon index of 2.2 ± 0.2, and the flux of $F = 2.3 \times 10^{-12}$ ergs cm^{-2}s^{-1} in 2–10 keV.
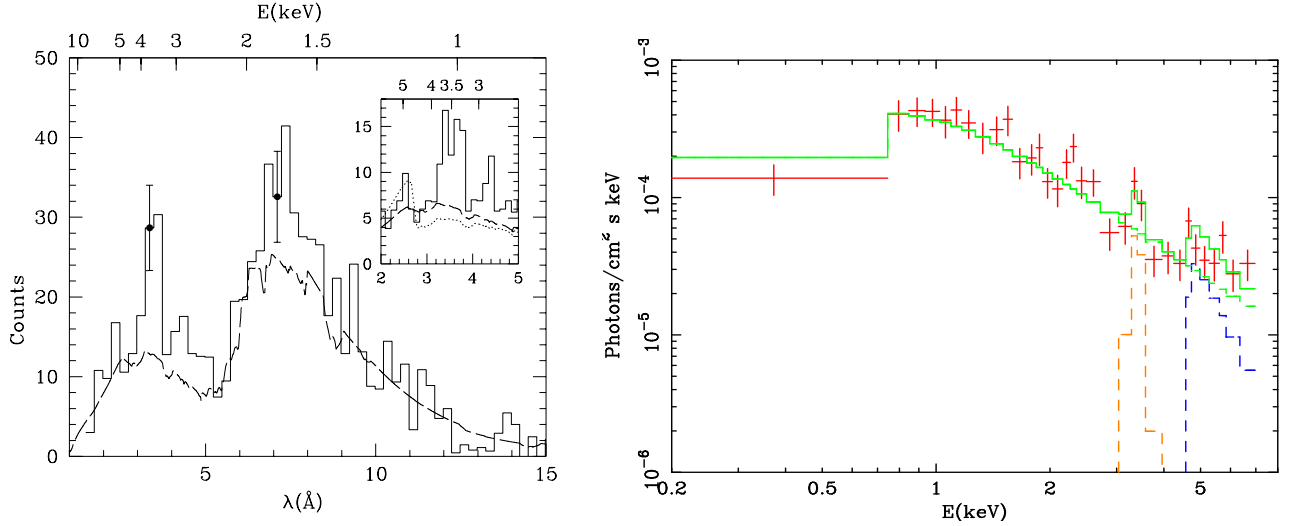

Figure D.18: The spectra of the X-ray afterglow of GRB 991216 observed with *Chandra* . The left and right panel is the spectrum by the High Energy Transmission Grating (HETG) and the ACIS-CCD detector, respectively (Piro et al., 2000). In left panel, the iron emission line is clearly detected around 3.5 keV with 4.2 σ confidence level. in left panel, and the RRC structure also detected around 4.6 keV in right panel.

D.3   Individual target – Event without Emission Lines

We introduced detail analyses for the events with the emission lines and/or the RRC structure in previous section. However, the spectral structures have not been detected in the major part of the X-ray afterglow. For example, in 38 X-ray afterglows observed by *BeppoSAX* , only two case show the spectral structures (Piro et al., 1999; Antonelli et al., 2000). In this section, we show the temporal and the spectral properties of X-ray afterglow without emission lines.

D.3.1 GRB 990123

GRB 990123 was detected by *BeppoSAX* on 1999 January 23.408 (UT). The X-ray flux of the GRB was 8.2×10^{-8} ergs cm^{-2}s^{-1} in 1.5-20 keV range, and the duration was ~ 100 s by *BeppoSAX* . The ground based optical observations discovered an OT associated with the GRB (Odewahn et al., 1999). Remarkably and surprisingly enough, this burst was also detected as a 8.95 magnitude optical flash by ROTSE simultaneously with the burst (Akerlof et al., 1999). The Keck observation revealed a red-shift of 1.600 (Andersen et al., 1999).

ASCA started observation of the afterglow with a delay of ~ 57.4 hours and monitored for 80 ks (Murakami et al., 1999a). In the field of view of the GIS detectors, there were a few nearby X-ray sources. To subtract background, we had to consider these nearby X-ray sources. The lightcurve of this event is shown in figure D.19 (left). The intensity of the flux decayed during the observation with a power-law index of about -1.4. The background subtracted X-ray flux during the ASCA observation was $(6.2^{+1.2}_{-1.1}) \times 10^{-13}$ ergs cm^{-2}s^{-1} .
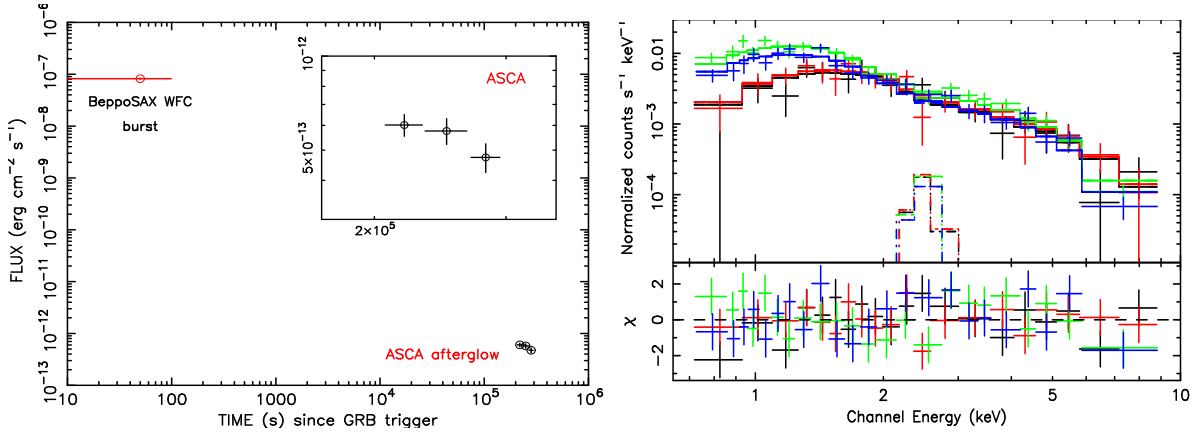

Figure D.19: The left panel is the X-ray lightcurve of GRB 990123 in the 2–10 keV band after subtracting the background. The X-ray flux of the *BeppoSAX* WFC averaged over the burst in the 2–10 keV is also plotted in the same figure. The right panel is the X-ray spectrum combined with the four ASCA detectors into one figure. The spectrum can be explained without any iron structure at $z = 1.60$. 90 % upper limit for the 6.4 keV line is 3.3×10^{-6} photons cm^{-2} s^{-1} or EW = 100 eV.

An X-ray spectrum combined with the four ASCA GIS and SIS detectors is shown in figure D.19 (right). The spectrum was fitted by a single power-law model with a Gaussian line. The absorptions by line of sight material in our own galaxy and in a host galaxy are also considered. It is clear that there is no noticeable iron emission line in the spectrum. Independently from the excess absorption at low energy which will be discuss later, we set an upper limit to the line flux. Assuming the line center to be at 6.4 keV at $z = 1.60$, the 90 % upper limit for the line flux is 3.3×10^{-6} photons cm^{-2} s^{-1} or 1.3×10^{-14} ergs cm^{-2}s^{-1} or 100 eV in EW. The reduced $\chi^2(\nu)$ of 79.0(79) without the line structure is already acceptable and the $\Delta\chi^2$ for the additional one parameter for the line is only 1.0. So we do not require iron line emission from statistical point of view, and only an upper limit can be set. Considering the strong iron line observed only during the flare state of GRB 970828, we divided the data into six parts and carried out a sliding scan over the data to search for a flare and the line.

An iron line emission was not apparent in each spectrum at any time more than ~ 300 eV in EW. The power-law photon index of -1.8 ± 0.1 is typical of X-ray afterglows and the X-ray flux was $F_X = (9.0^{+1.8}_{-1.5}) \times 10^{-6}$ photons cm^{-2} s^{-1} or $F_X = (6.2^{+1.2}_{-1.1}) \times 10^{-13}$ ergs cm^{-2}s^{-1} in the 2–10 keV band.

One thing noticeable is an excess absorption in the low energy spectrum. Although a single power-law model, with column density fixed to the galactic value of $N_{\mathrm{H}} = 2.09 \times 10^{20}$ cm^{-2} (Dickey & Lockman, 1990) shows an acceptable fit with χ^2 of 89.7 for 81 d.o.f., we have a significant reduction of χ^2 of 79.2 for 80 d.o.f. in case of the free column density at $N_{\mathrm{H}} = (1.5^{+0.7}_{-0.6}) \times 10^{21}$cm^{-2}. The improvement of such a large reduction corresponds to a confidence level of 99.8 %. The large reduction in χ^2 suggests an excess absorption in the low energy part of the spectrum. If we attribute this excess absorption to the host galaxy at $z = 1.6$, $N_{\mathrm{H}} = (1.2 \pm 0.6) \times 10^{22}$ cm^{-2} is required for the rest frame at the host galaxy. The fitting results are summarized in table D.9, and these results are published as Yoneotku et al. (2000).

D.3.2 GRB 990704

The ASCA observation of GRB 990704, following the detection by *BeppoSAX* (Piro et al., 1999), started 16 hours after the burst and monitored the afterglow for 63 ksec (Murakami et al., 1999b). Follow-up optical observations discovered an OT (Alain, 1999) but the redshift is unknown. The burst was bright in X-ray with a flux of 1.5×10^{-7} ergs cm^{-2}s^{-1} (6.2 Crab) in 2–10 keV band during the burst, and the burst duration was ~ 40 sec. GRB 990704 was much brighter than GRB 990123. Although ASCA started the observation of this much quicker than GRB 990123, but due to the faster decay with an index of about -1.5, the flux at the time of the ASCA observation was half of the GRB 990123. The light curve after subtracting the background is shown in figure D.20 (left).

A spectrum of GRB 990704 is also fitted by a simple power-law with a fixed galactic column density of $N_{\mathrm{H}} = 3.06 \times 10^{20}$ cm^{-2}. The power-law photon index of -1.7 ± 0.1 is typical of X-ray afterglows. The X-ray flux is $F_X = (7.6 \pm 2.3) \times 10^{-5}$ photons cm^{-2} s^{-1} or $F_X = (5.2^{+1.7}_{-1.6}) \times 10^{-13}$ ergs cm^{-2}s^{-1} in the 2–10 keV range. The redshift of the burst is not known, so we searched for a probable line emission between 0.7 and 6.7 keV. However no line was detected in the energy range. An upper limit of the line flux is set to be 4.7×10^{-6} photons cm^{-2} s^{-1} or 2.2×10^{-14} ergs cm^{-2}s^{-1} or 250 eV in EW. Due to poorer S/N of the X-ray afterglow compared to GRB 990123, we cannot say about the excess absorption for this case. The fitting results are summarized in table D.9, and these results are also published as Yoneotku et al. (2000).

GRB	N_{H}^{gal} 10^{20} cm^{-2}	N_{H} 10^{20} cm^{-2}	power-law index	F_{line} photons cm^{-2} s^{-1}	F_{line} ergs cm^{-2}s^{-1}	χ^2/d.o.f
990123	2.09	120 ± 60	1.8 ± 0.1	$< 3.3 \times 10^{-6}$	$< 1.3 \times 10^{-14}$	79.0/79
990704	3.06	...	1.7 ± 0.1	$< 4.7 \times 10^{-6}$	2.2×10^{-14}	46.1/52

Table D.9: Fitting results of the X-ray afterglow of GRB 990123 and GRB 990704.
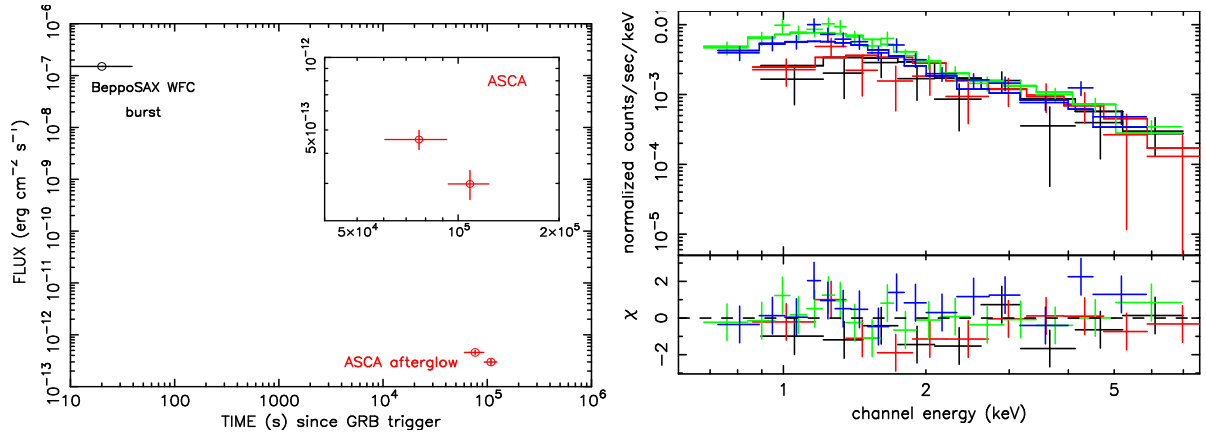
Figure D.20: The left panel is the lightcurve of GRB 990704. The ASCA window is divided into two intervals. The X-ray flux during the burst by the *BeppoSAX* WFC is also plotted in the same figure. The right panel is the spectrum fitted with the absorbed power-law model. There is no significant spectral feature in the entire energy range.

D.3.3   GRB 020322

GRB 020322 was detected by *BeppoSAX* WFC on Mar. 22, 03:51:30 UT. A follow up observation was done by *BeppoSAX* 7.5 hours after the burst trigger, and it found the X-ray counterpart of this event. After that, *XMM-Newton* starts to observe the X-ray counterpart 15.4 hours after the trigger. A very faint optical afterglow, the *R*-band magnitude of 23.26 mag (Bloom et al., 2002), was also found in the *XMM* error circle, but the redshift could not be measured.

We show the image of the X-ray afterglow of this event in figure D.21 obtained by the *XMM-Newton* observation. The source in the circle is the X-ray afterglow of GRB 020322. The background-subtracted lightcurve of the source was shown in figure D.22. This source is clearly decaying, and its decline is described by $\propto t^{-1.31 \pm 0.32}$.
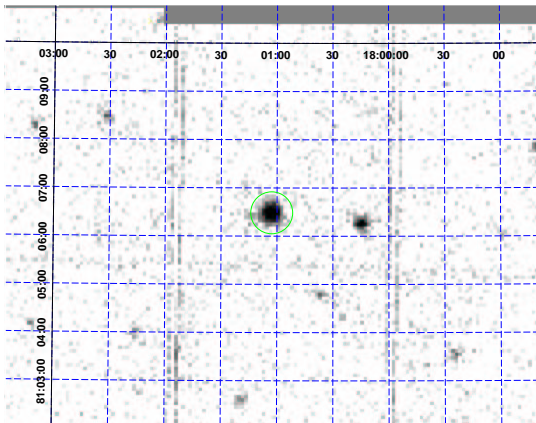

Figure D.21: The image of the X-ray afterglow of GRB 020322 (XMM-PN). The source in the center circle is the X-ray counterpart of this event.
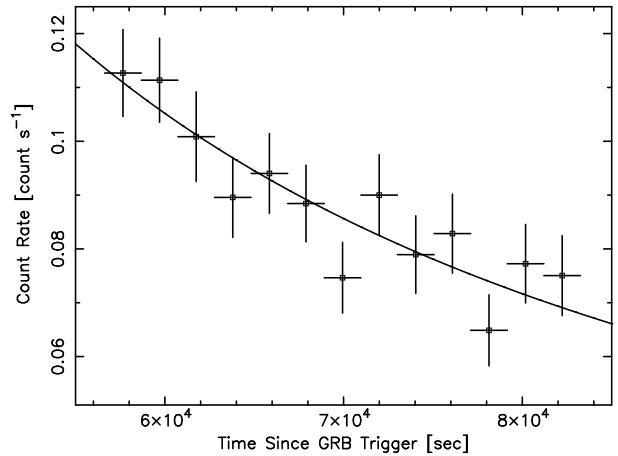

Figure D.22: The lightcurve of X-ray afterglow of GRB 020322. The solid line is the best fit result with $\propto t^{-1.31 \pm 0.32}$.

Although we performed time-dividing spectral analysis for the purpose of finding X-ray emission lines, we failed to detect the significant emission lines in the data. In figure D.23, we show the spectrum of the entire observation. When we adopt the power-law model with the galactic absorption of $N_H = 4.57 \times 10^{20}$ cm^{-2} , we cannot obtain the acceptable fit as shown in figure D.23 (left). There is a large discrepancy below 0.6 keV range, and this fact indicates that the extra-galactic absorption should be considered. Including the additional absorption component, the fitting results are significantly improved as shown in figure D.23 (right). The $\Delta\chi^2 = 115.6$ for an additional d.o.f.
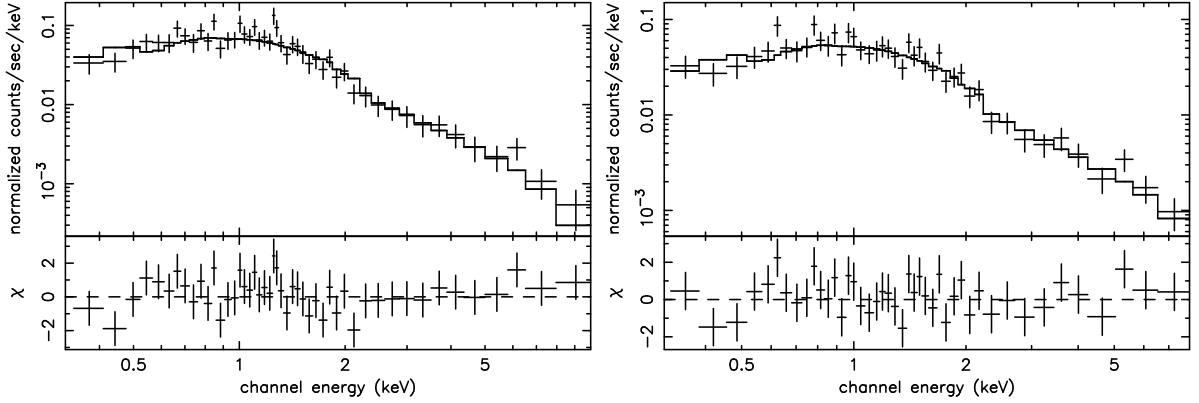

Figure D.23: The spectrum of X-ray afterglow of GRB 020322. The left panel is the spectrum fitted by the power-law model with the galactic absorption, and the right one is the improved spectrum with the additional extra-galactic absorption $N_H = 17.1 \times 10^{20}$ cm^{-2} .

Interval	N_H^{gal} 10^{20} cm^{-2}	N_H 10^{20} cm^{-2}	power-law index	energy flux (2–10 keV) ergs cm^{-2}s^{-1}	χ^2	d.o.f
PL	4.57 (fix)	...	1.58	2.83×10^{-13}	236.2	116
PL*phabs	4.57 (fix)	17.1 ± 2.9	2.23 ± 0.12	$(2.10 \pm 0.23) \times 10^{-13}$	120.6	115

Table D.10: Fitting results for the continuum spectrum of GRB 020322. When we adopt the power-law model (PL) with the galactic absorption, the reduced χ^2 is above 2.0, so the error calculation cannot be performed because of the software restriction.

D.3.4   GRB 031203

GRB 031203 was detected by the *INTEGRAL* satellite. A peak flux of this event is about 1.2 photons cm^{-2} s^{-1} and 1.3×10^{-7} ergs cm^{-2}s^{-1} in the 20–200 keV energy range. The burst consists of a single peak lasting about 30 sec (Gotz et al., 2003; Mereghetti & Gotz, 2003). *XMM-Newton* began observing the *INTEGRAL* error region 7.0 hours after the GRB trigger, and detected a considerably bright X-ray afterglow of GRB 031203. Therefore, *XMM-Newton* performed second pointing observation 2.88 days after the trigger.

We show the image of the first and the second observation by *XMM* in figure D.24–left and –right, respectively. The source flux is clearly decaying. The lightcurve of the source is

shown in figure D.25. The power-law index of the first epoch (a) is $\propto t^{-0.4\pm0.1}$, but the single power-law model cannot continuously describe the second epoch (b) as shown in figure D.25. The decay-index becomes steeper than the epoch (a), and we require the index of < -1.47. Therefore, the break point of the flux decline may exist between two epochs (a) and (b) as suggested by Watson et al. (2004).

We divided the entire observation of the epoch (a) into 4 parts, and integrated the total exposure time for the epoch (b), and performed the spectral analyses to search the emission lines and the RRC component in the observed spectrum. However, we failed to detect any spectral features. In figure D.26, we show the observed spectra integrating the entire exposure of (a) and (b), respectively. We cannot obtain acceptable fits with a single power-law with the galactic absorption ($N_{\rm H} = 6.21 \times 10^{20}$ cm^{-2}), so additional extra-galactic absorption was required. The spectral parameters of both (a) and (b) are consistent with each other except for the flux, and the fitting results are summarized in table D.11.
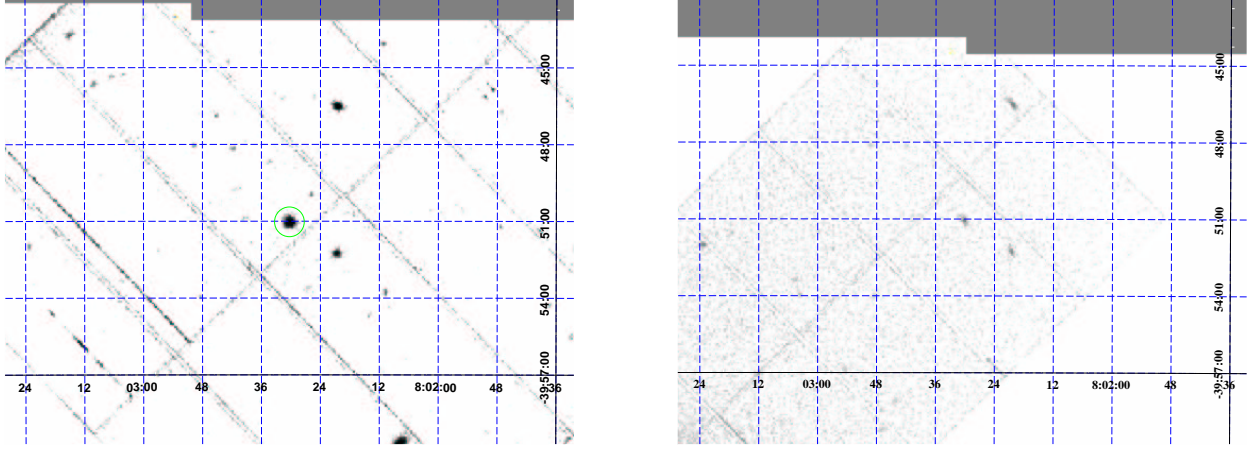

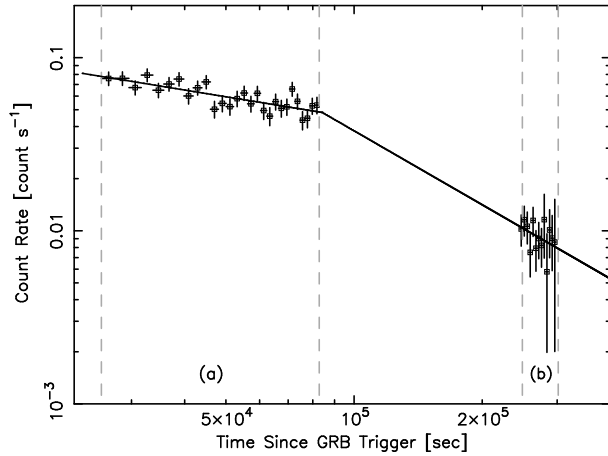Figure D.24: The image of the X-ray afterglow of GRB 001025A (XMM-PN).

Figure D.25: The lightcurve of X-ray afterglow of GRB 031203. The data is fitted by the broken power-law model with $\propto t^{-0.4}$ and $\propto t^{-1.47}$ continuously jointed at the end of epoch (a).
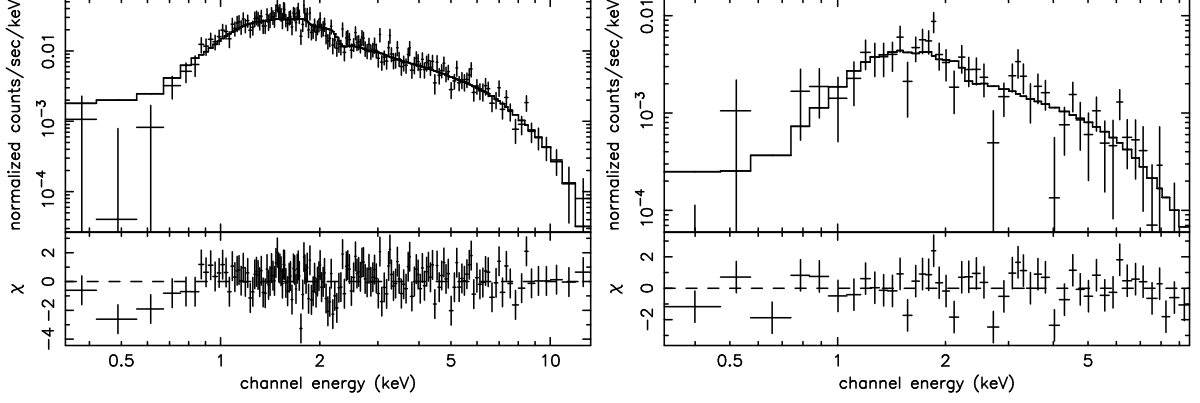
Figure D.26: The spectrum of X-ray afterglow of GRB 031203. The left panel is the spectrum fitted by the power-law model with the galactic absorption, and the right one is the improved spectrum with the additional extra-galactic absorption $N_{\rm H} = 17.1 \times 10^{20}$ cm^{-2} .

Interval	$N_{\rm H}^{gal}$ 10^{20} cm^{-2}	$N_{\rm H}$ 10^{20} cm^{-2}	power-law index	energy flux (2–10 keV) ergs cm^{-2}s^{-1}	χ^2	d.o.f
(a) PL	62.1 (fix)	...	1.62 ± 0.05	$(4.19 \pm 0.21) \times 10^{-13}$	191.6	166
(a) PL*phabs	62.1 (fix)	18.5 ± 6.2	1.83 ± 0.08	$(4.11 \pm 0.45) \times 10^{-13}$	163.6	165
(b) PL	62.1 (fix)	...	1.49 ± 0.20	$(1.56 \pm 0.81) \times 10^{-13}$	57.3	47
(b) PL*phabs	62.1 (fix)	30.9 ± 15.5	1.82 ± 0.22	$(1.47 \pm 0.73) \times 10^{-13}$	54.6	46

Table D.11: Fitting results for the continuum spectrum of GRB 031203.

D.4   Summary of the X-ray Afterglow Analysis

ASCA and *XMM-Newton* detected the emission lines of Si, S, Ar, Ca, and Fe materials and/or the RRC component of the fully ionized iron in 4 GRBs (GRB 970828, GRB 001025A, GRB 011211, and GRB 030227), and *BeppoSAX* and *Chandra* independently detected iron emission line in 3 GRBs (GRB 970508, GRB 991216, and GRB 000214). At present, in total, we know 7 GRBs with the emission lines and the RRC structure. However, these spectral features were not detected in major part of GRBs. For example, 36 cases[2] in 38 GRBs observed with *BeppoSAX* set only upper-limits for the emission lines. We introduced 4 of the no-emission line cases (GRB 990123, GRB 990704, GRB 020322, and GRB 031203) with high quality data in view of the photon statistics.

As already shown in this chapter, the emission features show the temporal behavior, and they appear only in a part of the entire observation time. Therefore, even if we observe a bright afterglow, we cannot always detect the emission feature because of its transience. This fact restricts and makes difficult to deal with the emission line phenomena quantitatively. In table D.12, we summarized the line detected time-interval (t_{line}) at the rest frame of GRBs, the temporal and the spectral index, respectively.

In figure D.27 (left and right), we show the decaying index and the spectral index as a function of t_{line}, respectively. As shown in the left panel of figure D.27, we can recognize a

---

[2]Because of poor statistics, the spectral analysis can be performed sufficiently only for 14 cases.

weak correlation between the decaying index and t_{line}, while the significant correlation between the spectral index and t_{line} could not be found. In figure D.28, we show the distribution of the decaying index and the spectral index, respectively. The gray and the white cells with GRB number are samples, which are taken into account in this chapter, with and without the evidence of the emission features, respectively. The other part of the distribution is the *BeppoSAX* results reported by Piro et al. (2004). As shown in figure D.28, the possibility to detect the emission features rises in below two cases. (1) at the case where the time decaying index is large, and (2) the index of the spectral continuum is steep. Based on the results, one possible interpretation about the existence or lack of the spectral features will be discussed in Chapter 6.

GRB	t_{line} 10^4 second	afterglow decay index	afterglow spectral index
970508	2.2 ± 0.8	~ 1.1	1.5 ± 0.9
970828	6.5 ± 0.6	1.44 ± 0.06	2.1 ± 0.3
991216	6.9 ± 0.3	~ 1.64	2.2 ± 0.2
000214	6.7 ± 3.7	1.41 ± 0.03	2.2 ± 0.3
001025A	10.8 ± 0.5	2.9 ± 1.0	1.88 ± 0.33
011211	1.6 ± 0.2	1.66 ± 0.22	2.10 ± 0.08
030227	3.0 ± 0.2	1.0 ± 0.1	1.96 ± 0.20

Table D.12: The basic information of X-ray afterglow samples taking into account in this thesis. For each GRB, this table contain the information about the GRB trigger time, the exposure start time (TSTART) for X-ray afterglow, total exposure duration (EXP.) and the coordinate (R.A., Dec.), respectively.
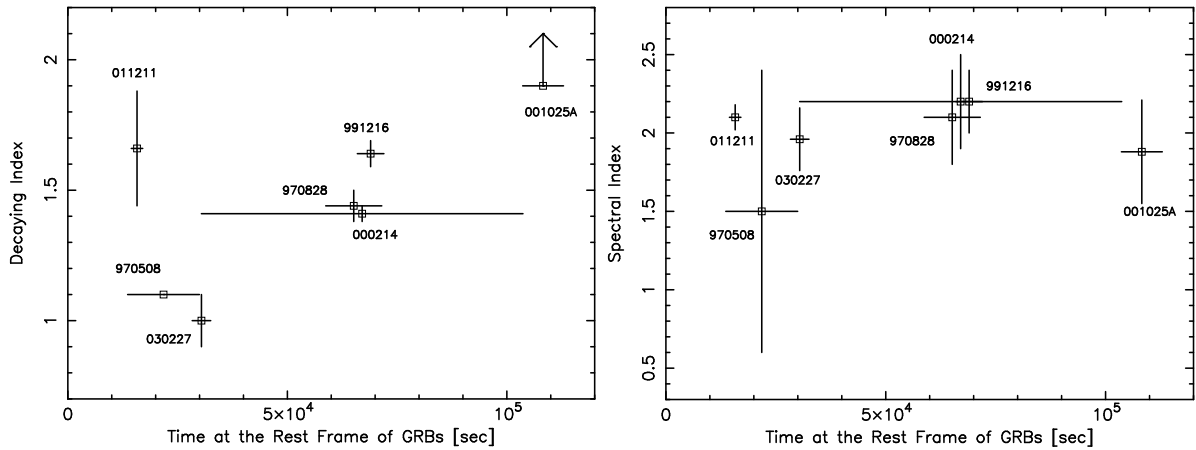

Figure D.27: The left and right panel is the decaying index and the spectral index of the sample detected the spectral features as a function of the line-detected time interval. We can recognize a weak correlation in the left panel, but the any correlation cannot be found in the right one.

Number of Events

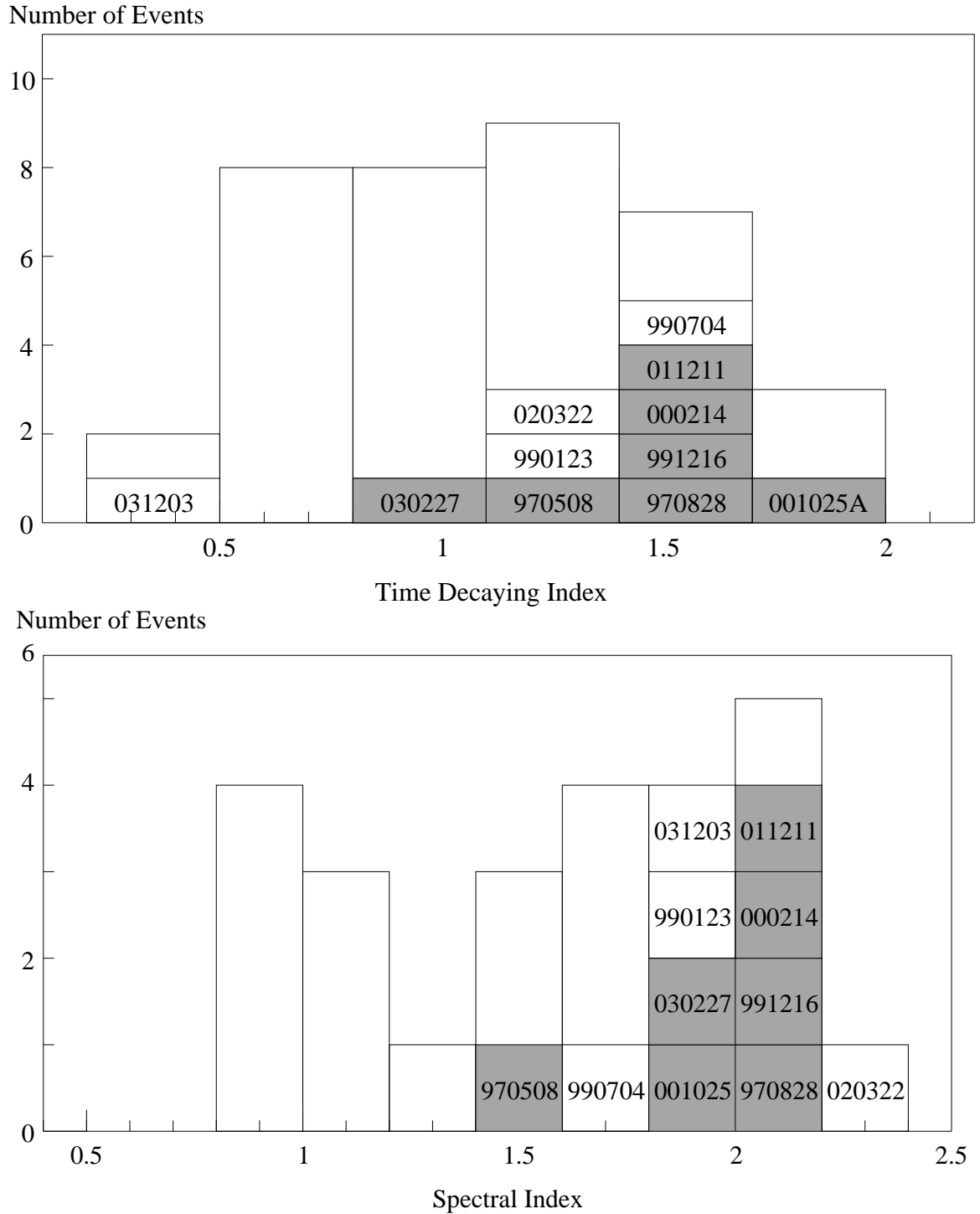Time Decaying Index

Number of Events

Spectral Index

Figure D.28: The distribution of the time decaying index and the spectral photon-index of X-ray afterglows. The cells with GRB number are the samples shown in this chapter. The gray and white parts are the events with or without the emission lines and the RRC component, respectively. The other parts are the events detected by *BeppoSAX* , and only upper-limit flux of the emission line is set for them.

Bibliography

Akerlof, C. W., Balsano, R., Barthelmy, S., et al. 1999, Nature, 398, 400

Alain, M., 1999, GCN, #363

Altieri, B. et al. 2000, GCN, #869

Amati, L., Frontera. F., Tavani. M., et al. 2002, A&A, 390, 81

Andersen M. I., Castro-Tirado, A. J., Hjorth, J., et al. 1999, Science, 283, 2075

Andersen M. I., Hjorth, J., Pedersen, H., et al. 2000, A & A, 364, L54

Antonelli, L. A., et al. 2000, ApJ, 545, L39

Atteia, J-L. 2003, astro-ph/0304327

Band, D.L., Matteson, J., Ford, L., et al. 1993, ApJ, 413, 281

Band, D.L. 2003, ApJ, 588, 945

Barger, A. J., Cowie, L. L., & Richards, E. A. 2000, AJ, 119, 2092

Bennett, C. L., Halpern, M., Hinshaw, G., et al. 2003, ApJS, 148, 1

Bevington, P. R. & Robinson, D. K. 1992, *WCB/McGraw-Hill*, Data Reduction and Error
  Analysis for the Physical Sciences

Blandford, R. D., & McKee, C. F. 1976, Physics of Fluids, 19, 1130

Bloom, J. S., et al. 1999, Nature, 401, 453

Bloom, J. S., Frail, D. A., & Sari, R. 2001, AJ, 121, 2879

Bloom, J. S. et al. 2002, GCN, #1294

Bloom, J. S., Frail, D. A., & Kulkarni, S. R. 2003, astro-ph/0302210

Borgonovo, L. & Ryde, F., 2001, ApJ, 548, 770

Borozdin, K. N., & Trudolyubov, S. P. 2003, ApJL, 583, 57

Briggs, M. S., Band, D. L., Kippen, R. M., et al. 1999, ApJ, 524, 82

Bunker A. J., Stanway E. R., Ellis R. S., & McMahon R. G. 2004, astro-ph/0403223

Burke, B. E., Mountain, R. W., Harrison, D. C., Bautz, M. W., Doty, J. P., Ricker, G. R., & Daniels, P. J. 1991, *IEEE Trans. Nucl. Sci.*, 38, 1069

Burke, B. E., Mountain, R. W., Daniels, P. J., Cooper, M. J., & Dolat, V. S. 1994, *IEEE Trans. Nucl. Sci.*, 41, 375

Caditz, D. & Petrosian, V. 1990, ApJ, 357, 326

Cen, R. 2003, ApJ, 591, 12

Costa, E., et al. 1997, Nature, 287, 783

Couchman, H. M. P. & Rees, M. J. 1986, MNRAS, 221, 53

Cowie, L. L. & Songaila, A. 1998, Nature, 394, 44

Cowie, L. L., Songaila, A., & Barger, A. J. 1999, AJ, 118, 603

Crider, A., Liang, E. P., Preece, R. D., et al. 1999 ApJ, 519, 206

Dickey, J. M., & Lockman, J. F., 1990, ARA&A, 28, 215

Djorgovski, S. G., et al. 2001, ApJ, 562, 654

Dotani, T., Yamashita, A., Rasmussen, A., & the SIS team 1995, *ASCA* News, 3, 25 (http://heasarc.gsfc.nasa.gov/docs/asca/newsletters/Contents3.html)

Dotani, T., et al. 1996, *ASCA* News, 4, 3 (http://heasarc.gsfc.nasa.gov/docs/asca/newsletters/Contents4.html)

Dotani, T., Yamashita, A., Ezuka, H., Takahashi, K., Crew, G., Mukai, K., & the SIS team 1997, *ASCA* News, 5, 14 (http://heasarc.gsfc.nasa.gov/docs/asca/newsletters/Contents5.html)

Efron, B. & Petrosian, V., 1992, ApJ, 399, 345

Ehle, M., et al. 2002, GCN, #1293

Ford, L. A., Band, D. L., Matteson J. L., et al. 1995, ApJ, 439, 307

Fenimore, E. E., & Ramirez-Ruiz, E. 2000, astro-ph/0004176

Fontana, A., Poli, F., Menci, N., et al. 2003, ApJ, 587, 544

Frail, D. A., Kulkarni, S. R., Sari, R., et al. 2001, ApJ, 562, L55

Frontera, F., Amati, L., Costa, J. M., et al. 2000, ApJ, 127, 59

Fruchter, A., et al. 2001, GCN, #1200

Galama, T. J., Briggs, M. S., Wijers, R. A. M., et al. 1999, Natur, 398, 394

Gendreau, K. C. et al. 1994, PASJ, 47, L5

Gendreau, K., & Yaqoob, Y., 1997, *ASCA* News, 5, 8
(http://heasarc.gsfc.nasa.gov/docs/asca/newsletters/Contents5.html)

Giavalisco M., Dickinson M., Ferguson, H. C., et al. 2004, ApJL, 600, 103

Glazebrook, K., et al. 2003, ApJ, 587, 55

Gnedin, N. Y. 2000, ApJ, 535, 530

Gotz, D., Mereghetti, S., Beck, M., & Borkowski, J., 2003, GCN, #2459

Harrison, F. A., et al. 2001, 1ApJ, 559, 123

Heger, A. & Woosley, S. E. 2002, ApJ, 567, 532

Heger, A., Fryer, C.L., Woosley, S. E. et al. 2003, ApJ, 591, 288

Hjorth, J., et al. 2003, Nature, 423, 847

Holland, S., et al., 2002, AJ, 124, 639

Ishisaki, Y. 1997, Ph.D. thesis, Tokyo University

Ishisaki, Y., Ueda, Y., Kubo, H., Ikebe, Y., Makishima, K., & the GIS team 1997, *ASCA*
News, 5, 26
(http://heasarc.gsfc.nasa.gov/docs/asca/newsletters/Contents5.html)

Kaneda, H. 1998, Ph.D. thesis, Tokyo University

Kaneda, H., Makishima, K., Yamauchi, S., Koyama, K., Matsuzaki, K., & Yamasaki, N. Y.
1997, ApJ, 491, 638

Kashikawa, N., Takata, T., Ohyama, Y., et al. 2002, 125, 53

Klebesadel, R. W., et al. 1973, ApJ, 182, L85

Kodaira K., et al. 2003, PASJ, 55, 17

Kulkarni, S., et al. 1999, Nature, 398, 389

Lamb, D. Q. et al. 1999, AAS, 138, 479

Lamb, D. Q. et al. 2003, astro-ph/0310414

Lilly, S. J., LeFevre, O., Hammer, F., & Crampton, D. 1996, ApJ, 460, L1

Loiseau, N., et al. 2003, GCN, #1901

Lloyd-Ronning, N. M., Petrosian, V. & Mallozzi, R. S. 2001, ApJ, 534, 227

Lloyd-Ronning, N. M. & Petrosian, V. 2002, ApJ, 565, 182

Lloyd-Ronning, N. M., Fryer, C. L. & Ramirez-Ruiz, E. 2002, ApJ, 574, 554

Lynden-Bell, D. 1971, MNRAS, 155, 95

Ioka, K., & Nakamura, T. 2001, ApJL, 554, 163

Madau, P., Ferguson, H. C., Dickinson, M. E., et al. 1996, MNRAS, 283, 1388

Madau, P., Haardt, F., & Rees, M. J. 1999, ApJ, 514, 648

Makishima, K. et al. 1996, PASJ, 48, 171

Maloney, A. & Petrosian, V. 1999, ApJ, 518, 32

Matsubayashi, T., Yamazaki, R., Yonetoku, D. & Ebisuzaki, T. 2004, ApJ, submitted

Mereghetti, S., & Gotz, D., 2003, GCN, #2460

Miralda-Escudé, J., 2003, ApJ, 591, L91

Murakami, T., et al., 1997, IAUC, #6687

Murakami, T., et al., 1997, IAUC, #6722

Murakami, T., et al., 1997, IAUC, #6732

Murakami, T., et al., 1999, GCN, #228

Murakami, T., et al., 1999, GCN, #372

Murakami, T., Yonetoku, D., Izawa, H., et al. 2003, GCN, #2044

Murakami, T., Yonetoku, D., Izawa, H. & Ioka, K. 2003, PASJ, 55, 65

Murakami, T., Yonetoku, D., Umemura, M., et al. 2004, ApJL, submitted

Nakamura, F. & Umemura, M., 2001, ApJ, 548, 19

Norris, J. et al. 1986, ApJ, 301, 213

Norris, J. et al. 1996, ApJ, 459, 393

Norris,J., Marani, G.,& Bonnell, J. 2000, ApJ, 534, 248

Norris, J. 2002, ApJ, 579, 386

Odewahn, S. C., Bloom, J. S., & Kulkarni, S. R., 1999, GCN, #201

Ohashi, T. et al. 1996, PASJ, 48, 157

Peebles, P. J. E. *Princeton University Press*, Principles of Physical Cosmology

Peterson, B. A. & Price, P. A. 2003, GCN, #1985

Petrosian, V. 1993, ApJ, 402, L33

Piran, T. 1999, Physics Report, 314, 575

Piro, L., et al. 1999, ApJ, 514, L73

Piro, L., et al. 1999, GCN, #199

Piro, L., et al. 2000, Science, 290, 955

Piro, L. 2004, astro-ph/0402638

Portinari, L., Chiosi, C., & Bressan, A. 1998, A&A, 334, 505

Preece, R. D., Briggs, M. S., Mallozzi, G. N., et al. 2000, ApJS, 126, 19

Rees M. J. & Mészáros P. 1992, MNRAS, 258, L41

Reeves, J. N., Watson, D., Osborne, J. P., et al. 2002, Nature, 416, 512

Reeves, J. N., Watson, D., Osborne, J. P., et al. 2003, A&A, 403, 463

Rutledge, S. & Sako, M. 2003, MNRAS, 339, 600

Rybicki, G. B. & Lightman, A. P. 1979, *WILEY INTER SCIENCE*, Radiative Processes in
    Astrophysics

Sakamoto T. 2004, Ph.D. thesis, Tokyo Institute of Technology

Salpeter, E. E. 1955, ApJ, 121, 161

Santos-Lleo, M., et al. GCN, #1192

Santos-Lleo, M., et al. GCN, #2462

Sato, R., Yatsu, Y., Suzuki, M., and Kawai, N. 2003, GCN, #2080

Schaefer, B. E., Deng, M. & Band, D. L. 2001 ApJ, 563, L123

Schaerer, D. 2002, A&A, 382, 28

Serlemitsos, P. J., et al. 1995, PASJ, 47, 105

Shapiro, S. L. & Teukolsky, S. A. 1983, *Jhon Wiley & Sons, Inc.*, Black Holes, White Dwarfs
    and Neutron Stars – The Physics of Compact Objects

Smith, D. A., Levine A. M., Remillard R., et al. 2000, GCN notice #861

Songaila, A. 2001, ApJ, 561, L153

Spergel, D. N., Verde, L., Peiris, H. V., et al. 2003, astro-ph/0302209

Stanway, E. R., Bunker, A. J. & McMahon, R. G. 2003, MNRAS, 342, 439

Takagi, R. 2000, Master Thesis

Takeshima, T., et al. 1999, GCN notice #478

Tanaka, Y., Inoue, H., & Holt, S. S. 1994, PASJ, 46, L37

Torii, K. 2003, GCN, #1986

Uemura, M. 2003, GCN, #1989

Watson, D., Reeves, J. N., Hjorth, J., et al. 2003, astro-ph/0306284

Watson, D., Hjorth, J., Levan, A., et al. 2004, astro-ph/0401225

Waxman, E., Kulkarni, S. R. & Frail, D. A. 1998, ApJ, 497, 288

Wei, D. M. & Gao, D. H. 2002, submitted to MNRAS (astro-ph/0212513)

Yamashita, A. 1998, Ph.D. thesis, Tokyo University

Yamashita, A., Dotani, T., Ezuka, H., Kawasaki, M., & Takahashi, K. 1999, NIM A, 436, 68

Yamazaki, R., Ioka, K., & Nakamura, T. 2002, ApJ, 571, L31

Yamazaki, R., Yonetoku, D. & Nakamura, T. 2003, ApJ, 594, L79

Yoshida, A., et al. 1997, IAU Circ. #6593

Yoshida, A., et al. 1999, A&AS, 138, 433

Yoshida, A., Namiki, M., Yonetoku, D., Murakami, T., et al. 2001, ApJ, 557, 27

Yoshida, N., Bromm, V. & Hernquist, L. 2004, ApJ, 605, 579

Yonetoku, D., Murakami, Y., Ueda, Y. et al. 2000, PASJ, 52, 509

Yonetoku, D., Murakami, T., Masai, K., et al. 2001, ApJ, 557, 23

Yonetoku, D. 2001, Master Thesis

Yonetoku, D., Murakami, T., et al. 2004, ApJ, 609, 935

Acknowledgment

I gratefully thank Prof. Toshio Murakami for his guidance to the frontiers of Gamma-Ray Burst and afterglow sciences. He always supports me to advance in the proper direction when I stray off into scientific and experimental difficulties. I could not complete this thesis without his continuous encouragements. He eternally consider what is the most important and the most interesting topics in science, and I frequently discuss about them together with him. I have learned a lot of physics in great environments.

I would like to thank Prof. Takashi Nakamura, Dr. Kunihito Ioka and Dr. Ryo Yamazaki for meaningful theoretical discussions. I always learn about the latest theories in personal discussions and many scientific meetings. I am grateful to Prof. Masayuki Umemura for guiding me into the new field "the early universe". He also gave me a lot of useful suggestions to improve this thesis.

I have learned a lot of astrophysics from all of the best friends. Especially, I expanded my knowledge of the astrophysics through useful discussions and trivial talks with Dr. Naohisa Anabuki. I would like to keep in touch with all of them.

Finally, I gratefully thank my mother for supporting my educations and school life.

The referees of this thesis
Prof. Nobuyuki Kawai (TITech),
Prof. Akio Hosoya (TITech),
Prof. Yasushi Watanabe (TITech)
Prof. Hideyo Kunieda (ISAS/JAXA),
Dr. Hideo Matsuhara (ISAS/JAXA).